Old Dominion University

ODU Digital Commons

Spring 2003

Measurments of Correlated Pair Momentum Distributions in 3He(e,e'pp)n With CLAS

Rustam Niyazov
Old Dominion University

Follow this and additional works at: https://digitalcommons.odu.edu/physics_etds

Part of the Nuclear Commons

Recommended Citation

MEASUREMENTS OF CORRELATED PAIR MOMENTUM DISTRIBUTIONS IN ^{3}He(e,e′pp)n WITH CLAS

by

Rustam Niyazov
M.S. June 1986, Minsk Radiotechnical Institute
M.S. December 1997, Old Dominion University

A Dissertation Submitted to the Faculty of
Old Dominion University in Partial Fullfillment of the
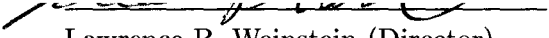Requirement for the Degree of

DOCTOR OF PHILOSOPHY

PHYSICS

OLD DOMINION UNIVERSITY
May 2003

Approved by:

Lawrence B. Weinstein (Director)

John Adam

Sebastian Kuhn

Rocco Schiavilla

Charles I. Sukenik

ABSTRACT

MEASUREMENTS OF CORRELATED PAIR MOMENTUM DISTRIBUTIONS IN ^{3}He(e,e′pp)n WITH CLAS

Rustam Niyazov
Old Dominion University, 2003
Director: Dr. Lawrence B. Weinstein

We have measured the ^{3}He(e,e′pp)n reaction at 2.2 and 4.4 GeV over a wide kinematic range. The kinetic energy distribution for 'fast' nucleons ($p > 250$ MeV/c) peaks where two nucleons each have 20% or less and the third or 'leading' nucleon carries most of the transferred energy. These fast nucleon pairs (both pp and pn) are back-to-back and carry very little momentum along $\vec{q}$, indicating that they are spectators. Experimental and theoretical evidence indicates that we have measured NN correlations in ^{3}He(e,e′pp)n by striking the third nucleon and detecting the spectator correlated pair.

To

my parents

and

my family

ACKNOWLEDGMENTS

First I would like to express my sincere gratitude to my advisor, Lawrence B. Weinstein, without whose support this work could not have been accomplished. I thank my advisor for his continuing friendship, encouragement, patience and guidance throughout my graduate school years. I have gained much insight into nuclear physics from many lengthy discussions with him.

I would like to thank my thesis committee members: John Adam, Charles Sukenik, Sebastian Kuhn and Rocco Schiavilla for giving me opportunity to learn physics, discussions and help with my research project.

I would particularly like to acknowledge the efforts of Stepan Stepanyan. His guidance, insight and valuable suggestions made essential contribution to this dissertation and my studies.

I would like to thank Andy Klein and Garry Copeland, my former graduate committees for their guidance and help. My thanks to Gail Dodge for all your support and encouragement.

Thanks to the Hall B research stuff, CLAS Collaboration members and E2 run group, Maurik Holtrop, Kim Egiyan, Bin Zhang, Dan Protopopescu, Hovhannes Baghdasaryan, Alexey Klimenko, Gagik Gavalian, Steven McLauchlan, Westley Ingram for their work that helped make the experiment a success.

I would also like to thank Misak Sargsian, Igor Strakovsky and Jean-Marc Laget for their invaluable help with my research project.

I am indebted to many other people who have made my graduate experience. My special thanks to my friend Luminita Todor, whose kind support during the years helped me keep my spirit alive.

I would like to thank my parents for their support, understanding and love. I could never have come this far without the love and support of my wife, Olga. Thank you for your endless patience and understanding that allowed me to pursue my dream.

TABLE OF CONTENTS

LIST OF TABLES

LIST OF FIGURES

CHAPTER 1

INTRODUCTION

Traditional nuclear physics describes nuclear properties in terms of protons and neutrons. In an attempt to understand the physics of the nucleus, a full theoretical explanation would need a solution to a quantum mechanical many-body problem, with not only a set of coupled equations describing the mutual interactions of the nucleons, but also the correlations of all these nucleons as they act on others. Even for a nucleus with only a few nucleons, this quickly becomes an impossibly large dimensional problem. It is therefore only feasible to adopt simplified theories, based on macroscopic phenomena and atomic shell model analogies, and adapt them to account for specific nuclear properties. The hope is then that as the model becomes more sophisticated, we can not only understand and describe these properties, but also predict trends and additional new observables. Most nuclei are well described as nucleons interacting either through empirical interactions in the shell model, or through a force derived from nucleon-nucleon scattering.

The single nucleon energy and momentum distributions in nuclei have been thoroughly measured by (e,e'p) nucleon knockout reactions [1, 2]. The shapes of these distributions, although not their magnitudes, are well described by distorted wave impulse approximation calculations. The discrepancies between the measured and calculated magnitudes indicate that nucleon-nucleon (NN) correlations are an important part of the nuclear wavefunction. The nucleon-nucleon interaction can be described by a potential that is attractive at long distances and repulsive at short distances. Strong short range interactions give rise to a correlated motion of two and possible three nucleons in a nucleus. Nuclear models including only NN potentials (e.g.: CD Bonn, Argonne v_{18}, Nijmegen-93) underbind nuclei. Three nucleon interactions (e.g.: the Tucson-Melbourne 2π-exchange and the Urbana IX) are nessesary to get the correct binding energies.

For an empirical understanding of the character of NN correlations in a nuclear medium, experimental guidance is required. The study of exclusive two-nucleon emission by electrons at intermediate energies provides a tool to investigate the role of

This Dissertation follows the form of *The Physical Review, C*

NN correlations inside atomic nuclei. In order to investigate the reaction mechanism of two nucleon emission and the relative importance of one-body and two-body hadronic currents in the cross section, measurements should be performed over a wide range of momentum-energy transfer values. In order to extract information on the relative and center-of-mass motion of the nucleon pairs, measurements covering a large angular domain and a sufficient range in kinetic energy have to be performed.

The high duty cycle new facilities which have been built in the last years, such as the Thomas Jefferson National Accelerator Facility (TJNAF) [1] have opened a new area in the study of nuclear structure: now we are passing from the study of one body dynamics, which started with extensive experimental and theoretical activities in the 60's, to the investigation of two body dynamics. Our main objects of interest are no longer average properties of single nucleons in nuclei, but the average properties of pairs of nucleons.

This thesis presents the study of NN correlations based on two proton knock-out reactions from ^{3}He measured by the CEBAF Large Acceptance Spectrometer (CLAS). The diagram of that process is shown in Figure 1. This experiment was performed at TJNAF in the spring of 1999. The results of this data analysis exhibit a strong signature for NN correlations. In this chapter, two descriptions of nuclei as well as the definitions of correlations are presented. Chapter 2 describes our experiment and the experimental apparatus that we used for our measurements. Chapter 3 contains the details of data processing and calibrations. Chapter 4 describes the data analysis and the theory models we used for comparison with the data and acceptance calculations. Chapter 5 presents our physics results and discussions.
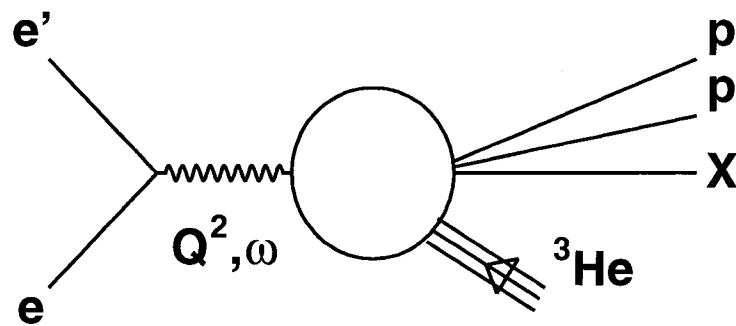
FIG. 1. Diagram of the two proton knockout in ^{3}He(e,e'pp) .

---

[1]The former name was the Continuous Electron Beam Accelerator Facility (CEBAF)
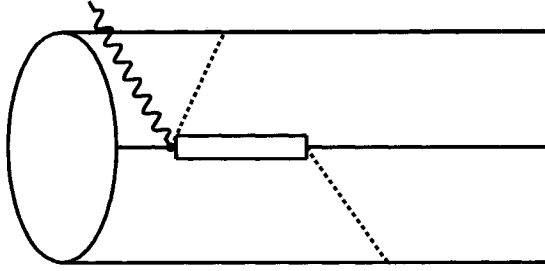
FIG. 2. Three body absorption diagram.

1.1 DESCRIPTIONS OF NUCLEI

One of the central challenges of theoretical nuclear physics is the attempt to describe the basic properties of nuclear systems in terms of a realistic NN interaction. Such an attempt typically contains two major steps. In the first step one has to consider a specific model for the NN interaction. Such models are considered as a realistic description of the NN interaction, if the adjustment of parameters within the model yields both a good fit to the NN scattering data at energies below the threshold for pion production as well as the binding energy and other observables of the deuteron. As was mentioned earlier, models developed for NN potential, like CD Bonn [3], Argonne v_{18} [4], Nijmegen-93, I and II [5], as well as the Tucson-Melbourne 2π-exchange [6] and the Urbana IX [7] models include, in addition to two body, three nucleon interactions as a necessary ingredient. In any case, however, one finds that a two-nucleon interaction alone does not lead to the empirical saturation point of nuclear matter and also fails to reproduce the binding energies and densities of finite nuclei. The calculations tend to predict binding energies which are too small and/or densities which are too large. This can be corrected by introducing empirical three-nucleon forces. Three body forces are induced by presence of virtual Δ resonances and the long range term of the three nucleon interaction involves the intermediate excitation of a Δ, with a pion exchanges involving two other nucleons. The corresponding diagram showing the intermediate excitation of a Δ with double-pion exchange is presented in Figure 2. It is not clear, however, whether such three-nucleon forces simulate sub-nucleonic degrees of freedom (Δ excitations of the nucleons) or relativistic features [8]. Further theoretical studies are needed to clarify

this point.

In a few nucleon systems, the Schrödinger equation, expressed in the form of Faddeev-Yakubovsky equations, can be solved exactly and the calculations can be performed based on the above mentioned NN interactions. The agreement between theory and data for binding energies [9, 10] and low energy spectra, as well as three-nucleon scattering observables, is in most cases quite remarkable. However, 'exact' calculations are only possible for light nuclei at low energies [11]. After the definition of the nuclear Hamiltonian, the second step entails the solution of the many-body problem of A nucleons interacting in terms of such a realistic two-body NN interaction [12].

1.1.1 Single Particle Description

The simplest approach to the many-body problem of interacting fermions is the mean field or Hartree-Fock approximation where the nuclear wave function describes the nucleus as a system of nucleons moving independently from each other in a mean field derived from the average interaction with all other nucleons. This model has no NN correlations, e.g.: $\rho(p1, p2) = \rho(p1) \cdot \rho(p2)$.

However, this wave function contains a large probability for configurations, where two nucleons are so close to each other that they are exposed to the very repulsive components of the short distance NN interaction. This means that Short Range Correlations (SRC) must be added by hand to the Hartree-Fock wave function.

The Hartree-Fock approximation procedure yields very good results for the experimentally determined nuclear ground state properties as e.g., binding energies and radii, if one employs simple phenomenological NN forces like the Skyrme forces, which are adjusted to describe such nuclear structure data [13, 14]. However, employing realistic NN interactions the Hartree-Fock approximation fails very badly: it leads to unbound nuclei [15].

The mean field model has provided a very economical description and has allowed us to understand many features of nuclei. Yet this model must fail in certain areas, given the NN correlations resulting from the repulsive core and the tensor part of the NN interaction. The experimental and theoretical work of the past decade has provided us with a much clearer picture of the consequences of these correlations. In particular, it has became clear that the main consequences are the depletion of single particle states below the Fermi energy that are fully occupied in the shell model and
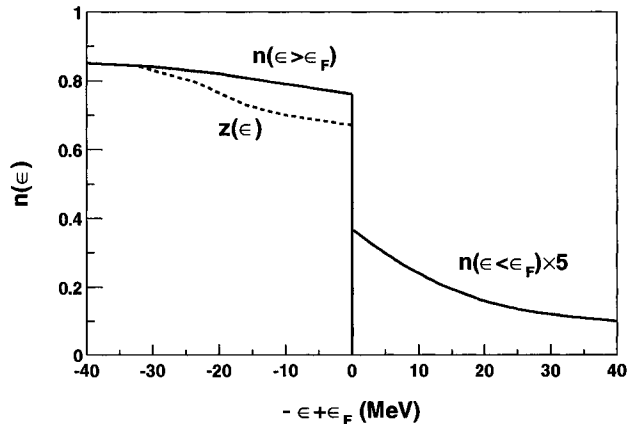
FIG. 3. Occupation of states of nuclear matter. Occupation of states is shown as a function of ϵ, with ϵ_F referring to the Fermi energy.

a spreading of this strength over an extremely wide range of excitation energies. Figure 3 shows the occupation of the states $n(k)$ as a function of ϵ, with ϵ_F referring to the Fermi energy [16]. Due to correlations, the occupation number $n(k < K_F)$ for momenta below the Fermi momentum k_F is reduced to 0.7–0.8, and the states with $k > k_F$ have small but finite occupations.

The quantitative information we have today from both theory and experiment tell us that at any time only 2/3 of the nucleons in the nucleus act as independent particles moving in the nuclear mean field. The remaining third of nucleons are correlated [12, 16]. The further discussion about (e,e'), (e,e'p) and (e,e'pp) results is presented in Section 1.3.

1.1.2 Multi-Baryon Description

Various different tools have been developed to account for NN correlation effects. These include corrections to the mean field wave function for large A and "exact" wave function calculations for small A $(A \leq 12)$. Mean field correction methods include the Brueckner hole-line expansion [17, 18, 19], and the coupled cluster or "exponential S" approach [20]. "Exact" methods include the self-consistent evaluation of Greens functions [21], variational aproaches using correlated basis functions [22, 23] and recent developments employing quantum Monte-Carlo techniques [24, 25]. The

Green Function Monte Carlo, Variational Monte Carlo and other (Fadeev) methods all include 3 body forces. Using such methods one obtains correlated many-body wave functions, which are rather sensitive to the NN interaction under consideration.

The hope is that different predictions derived from the various models of the NN interaction will allow us to understand better the details of the strong baryon baryon interaction at short distances. Characteristic differences can be observed if either a complete meson exchange model is used, which leads to a non-local NN interaction, or if a local approximation is used.

There is also a challenge for a cooperation between experimental and theoretical physics to search for observables which test the significance of the short-range NN correlations and thereby the short range structure of the underlying NN interactions.

The study of exclusive (e,e'NN) experiments seems to be an appropriate tool to explore the proton-proton and proton-neutron correlations. Unfortunately, measuring NN correlations directly is very difficult because their signals are frequently obscured by the effects of two body currents, such as meson exchange currents (MEC) and isobar configurations (IC) [26]. The effects of correlations can only be inferred from the experiment by comparing them to detailed calculations. But as was mentioned earlier, exact calculations are only possible for light nuclei at low energies [11].

1.2 CONTRIBUTING PROCESSES

The cross section for electron-induced two-nucleon knockout at intermediate electron energies is driven by several processes. The NN interaction at small inter-nucleon distances induces strong correlations between the nucleons inside the nucleus, which influences the momentum distributions of the bound nucleons and consequently the knock-out of nucleons by the absorption of a virtual photon via a one-body electromagnetic current. There are various ways the virtual photon can couple to the ^{3}He nucleus. Figure 4 a) shows the process of virtual photon γ^* absorption on one of the nucleons bound in ^{3}He, followed by emission of the other two nucleons, which were initially correlated. The absorption of a virtual photon by one nucleon of a correlated pair, which subsequently leads to the full breakup of the tri-nucleon system is shown in Figure 4 b). We also might expect a contribution from three nucleon correlations, if any.

The interaction of the virtual photon with two-body currents (sharing the transferred momentum between two nucleons), either via coupling to mesons or via intermediate Δ excitation, will also contribute to the two nucleon knockout cross section. These processes are shown in Figure 5 a) and b), respectively. Meson Exchange Currents (MEC) contributions might include the contact term (shown in Fig. 5 a) and the pion in flight (not shown). The exchanged mesons can be neutral (between a pp pair) or charged (between a pn pair). Isobar Configurations (IC) contributions include the decay of a ΔN intermediate state in an NN pair (pp or pn pair) (see Figure 5 b)). Contributions from MEC and IC strongly depend on the isospin of the NN pair. In the case of a pp pair, the contribution of MECs to the cross section will be strongly suppressed, as the virtual photon, in a non-relativistic reduction of the current operator, does not couple to such a pair [27]. Also the contribution due to isobar currents is reduced for two protons in a relative $^1S_0$ state, as the transition via the resonant M1 multipole is forbidden by angular-momentum and parity-conservation rules. Therefore Δ-excitation is only possible via the much weaker C2 and E2 multipoles [28]. These restrictions on MECs and ICs do not apply to pn pairs. Another contributing process - single nucleon knockout followed by double rescattering (FSI) is shown in Figure 6.

The photon can also couple to all three particles by a three-body mechanism. Sensitivity to these processes exists at real photon energies around 500–600 MeV and in specific regions of phase space, where the struck meson initially propagates on-shell and is subsequently reabsorbed by the remaining nucleon pair [29]. Three body absorption diagrams are shown in Figure 7.

1.3 PREVIOUS EXPERIMENTAL RESULTS

Our object of study is NN correlations in ^{3}He, i.e. the average connections between the partners of the NN pairs, while the system is in its ground state [30]. These average connections manifest themselves as the momentum or angular correlations. These average connections are due not only to their direct interaction, but also to the fact that the third nucleon may act on them via the NN interaction. We need to distinguish between Initial State Correlations (ISC) and Final State Interactions (FSI) corresponding to the system being in its ground state or excited state, respectively.

Given this definition of correlations, one needs to clarify it further, mentioning what is not generally called a correlation. When the system is viewed as an assembly
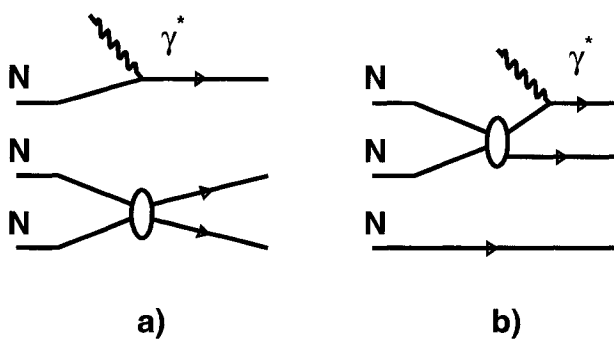
FIG. 4. Two nucleon emission diagram. Absorption of virtual photon on a) one of the nucleons with emission of other two correlated nucleons; b) one of the nucleons from correlated NN pair
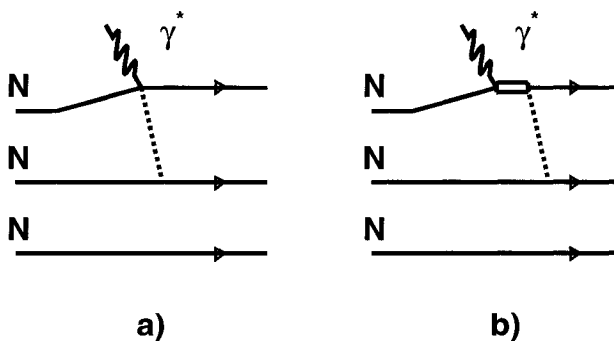
FIG. 5. Two body rescattering diagram. a) One of the contributing MEC procecess; b) One of the contributing IC processes.
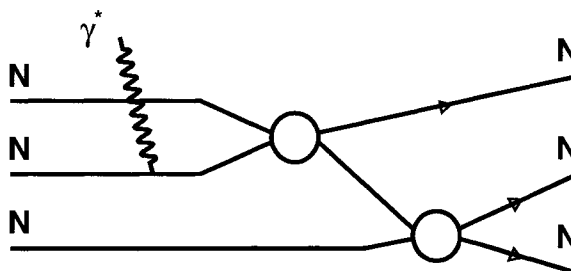
FIG. 6. Quasifree knockout and double rescattering.
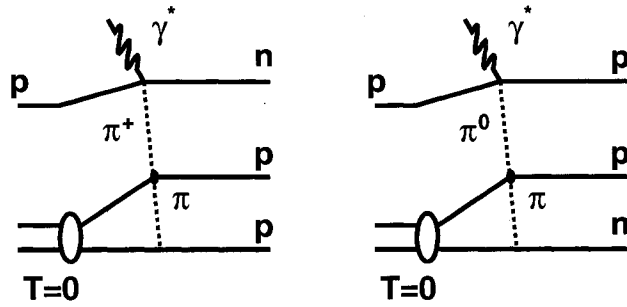
FIG. 7. Three body absorption diagrams. Virtual photon absorption on one nucleon with the resulting pion absorbed on the remaining pair.

of independent particles moving in an average potential one does not speak about correlations: if the particles move independently then they are not correlated by definition. There is another correlation that needs to be mentioned: Pauli blocking. Each independent particle feels the presence of the others due to the simple fact that it is not allowed to occupy a single particle state already occupied by another particle. This is indeed a correlation, however it has a statistical origin and therefore is not the dynamical correlation we are after.

The dynamical correlations result from different range properties of the NN potential. There are long range, intermediate range and short range correlations of dynamical origin. Long range correlations reflect the collective behavior of all particles. Intermediate range correlations are manifesting the non-central character of the correlations which are influenced by the tensor part of the potential dominating at these distances. Short range correlations (SRC) reflect the repulsive nature of the NN potential at those small distances. SRC affect the reactions where the momentum transferred from a probe to the system is high enough to resolve the dynamical properties of the particles when they are close to each other.

Recent $A(e, e')$ measurements [31] and theoretical calculations [32, 33] indicate a several times higher probability to find a nucleon pair at short distance (ie: in a correlation) in nuclei than in deuterium. These short distance nucleon pairs are primarily responsible for the high momentum components of the nuclear wave function [33]. At quasielastic kinematics, $\omega \approx Q^2/2m$, the (e,e') cross section is predominantly

due to electron scattering from single nucleons in the nucleus. Figure 8 shows (e,e') cross sections from ^{3}H and ^{3}He as a function of energy transfer [34] which mostly indicate the one body character of the (e,e') process. The two bumps in Figure 8 appear approximately at the energies corresponding to quasifree elastic scattering from nucleons and quasifree Δ-excitation. The quasifree elastic peak has a width corresponding to the ground state momentum distribution. Figure 9 shows (e, e') cross section ratios R^A_{He3} for a) C and b) Fe in respect to ^{3}He as a function of $x_B = \frac{Q^2}{2m_p\nu}$ for $1.4 < Q^2 < 2.6$ (GeV/c)^2 [31]. The cross section ratios are constant (scale) for $x_B > 1.5$ (see Figure 9). This scaling is predicted by the Short Range Correlation model [35] and indicates the dominance of scattering from correlated NN pairs. These ratios in the scaling regime are proportional to the relative probability of NN correlations in the two nuclei.
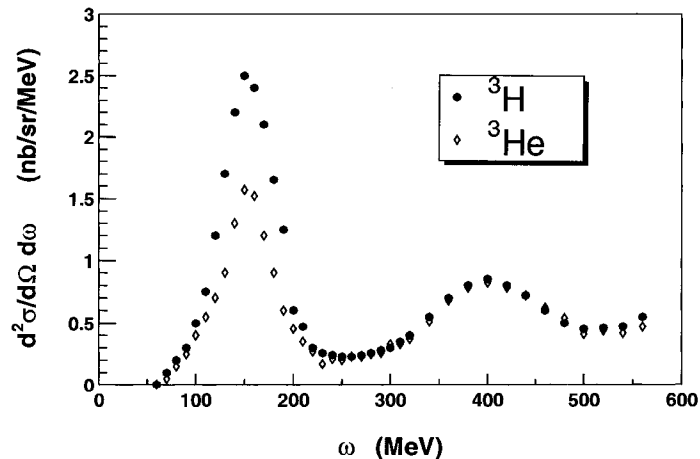
FIG. 8. (e,e') cross section from ^{3}H and ^{3}He as a function of energy transfer. Results are obtained for $E_{\text{beam}} = 651$ MeV and $\theta_e = 54°$ [34].

Explicit evidence for NN correlations was also obtained by studying A(e,e'p). Liyanage et al. [36] studied the ^{16}O$(e, e'p)$ reaction at missing energies up to $E_{\text{miss}} = 120$ MeV. They measured four missing momenta in the range 50 – 345 MeV/c. Figure 10 shows the measured cross section as a function of missing energy at $E_{\text{beam}} = 2.4$ GeV, $Q^2 = 0.8$ GeV^2 and $\omega = 445$ MeV for various proton angles, $2.5° \leq \theta_{pq} \leq 20°$. The prominent peaks at 12 MeV and 18 MeV are due to 1p-shell proton knockout and are described in [37], where it was shown that the p-shell cross sections are well described up to $P_{\text{miss}} = 340$ MeV/c by relativistic Distorted Wave Impulse
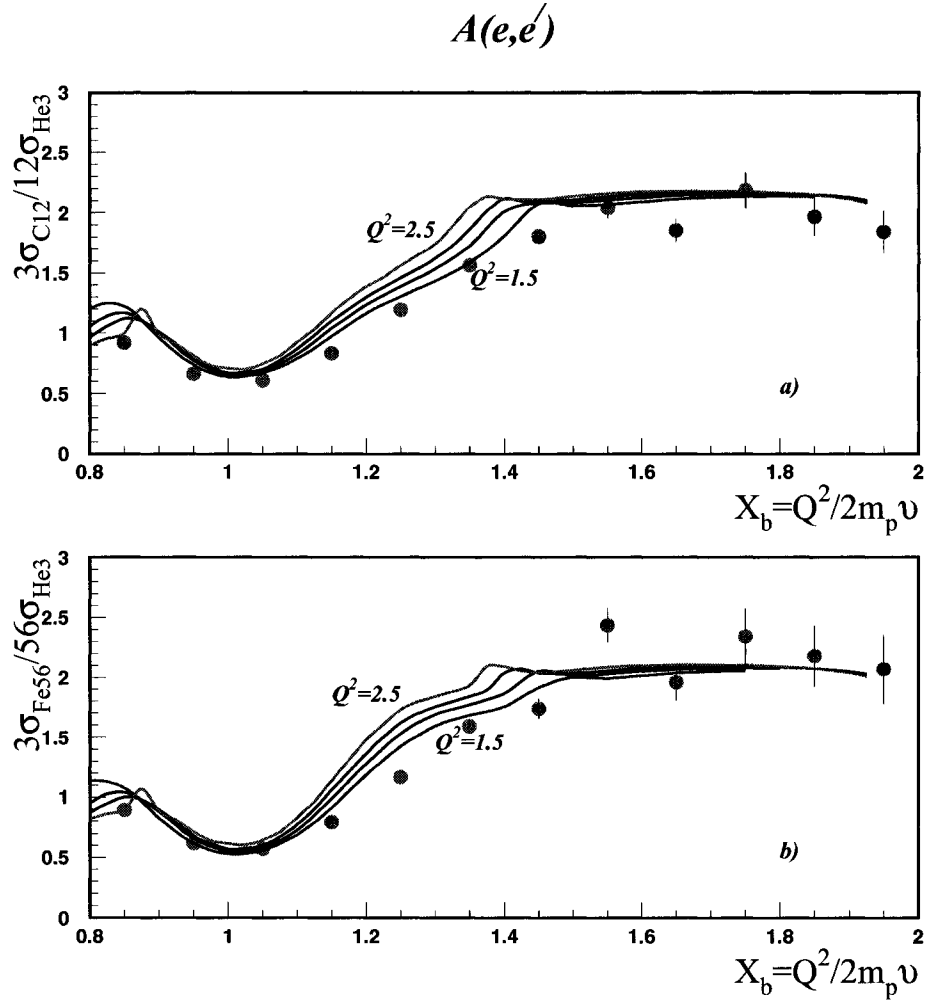
FIG. 9. A(e,e$'$) cross section ratios to ^{3}He. $R^A_{He3}(x_B)$ is shown as a function of x_B for $1.4 < Q^2 < 2.6$ (GeV/c)^2. Curves are Short Range Correlation model predictions. a) ^{12}C, b) ^{56}Fe. Shown results are preliminary [31].

Approximation (DWIA) calculations.

However the spectra for $E_{\text{miss}} > 20$ MeV exhibit a very different behavior. At the lowest missing momentum, $P_{\text{miss}} \approx 50$ MeV/c, the wide peak centered at $E_{\text{miss}} \approx 40$ MeV is due predominantly to knockout of protons from the $1s_{1/2}$-state. This peak is less prominent at $P_{\text{miss}} \approx 145$ MeV/c and has vanished beneath a flat background for $P_{\text{miss}} \geq 200$ MeV/c. At $E_{\text{miss}} > 60$ MeV or $P_{\text{miss}} > 200$ MeV/c, the cross section does not depend on E_{miss} and decreases only weakly with P_{miss}. Single proton knockout from the $1s_{1/2}$ shell can only explain the cross section for $E_{\text{miss}} < 60$ MeV or $P_{\text{miss}} < 200$ MeV/c. The flat continuum cross section must be due to two nucleon knockout processes.

Calculation by Ryckebusch [39, 40, 41, 42, 43] which included the contributions from both $(e, e'pp)$ and $(e, e'pn)$ due to pion-exchange currents, intermediate $\Delta(1232)$ creation, central short-range correlations, and tensor correlations predicted a flat cross section for $E_{\text{miss}} > 50$ MeV which is consistent with the data, but accounts for only about half the measured cross section. These measurements do not allow us to disentangle SRC from two body currents.

The study of NN correlations by means of the (e,e'pp) reaction was pioneered at NIKHEF in the ^{12}C(e,e'pp) experiments by Zondervan et $al.$ [45] and Kester et $al.$ [46]. The advance of high duty-cycle electron accelerators has made possible the three-fold coincidence experiments necessary to measure exclusive electron-induced two-nucleon knockout. The results of ^{12}C(e,e'pp) measurement in which the protons are ejected in directions close to back-to-back correlation are shown in Figure 11. The data are compared with calculations based on the direct-knockout mechanizm, which includes one- and two-body currents. This comparizon shows that there is some evidence for processes leading to multinucleon knockout.

Measurements performed by Onderwater et $al.$ [47, 48] at NIKHEF using large-solid-angle proton detectors, revealed clear signatures of short-range correlations in the ^{16}O(e,e'pp)^{14}C reaction. This reaction has been studied at a transferred four-momentum $(\omega, |\vec{q}|) = (210$ MeV, 300 MeV/c$)$. Figure 12 shows the comparison of the data from this experiment with theory results based on microscopic model calculations [49]. Similar results were obtained with a three-spectrometer setup at the Mainz Microtron MAMI [50]. Further experimental evidence for short-range correlations was obtained by Starink et $al.$ [51] from the measured energy-transfer dependence of the ^{16}O(e,e'pp)^{14}C$_{\text{g.s.}}$ reaction.
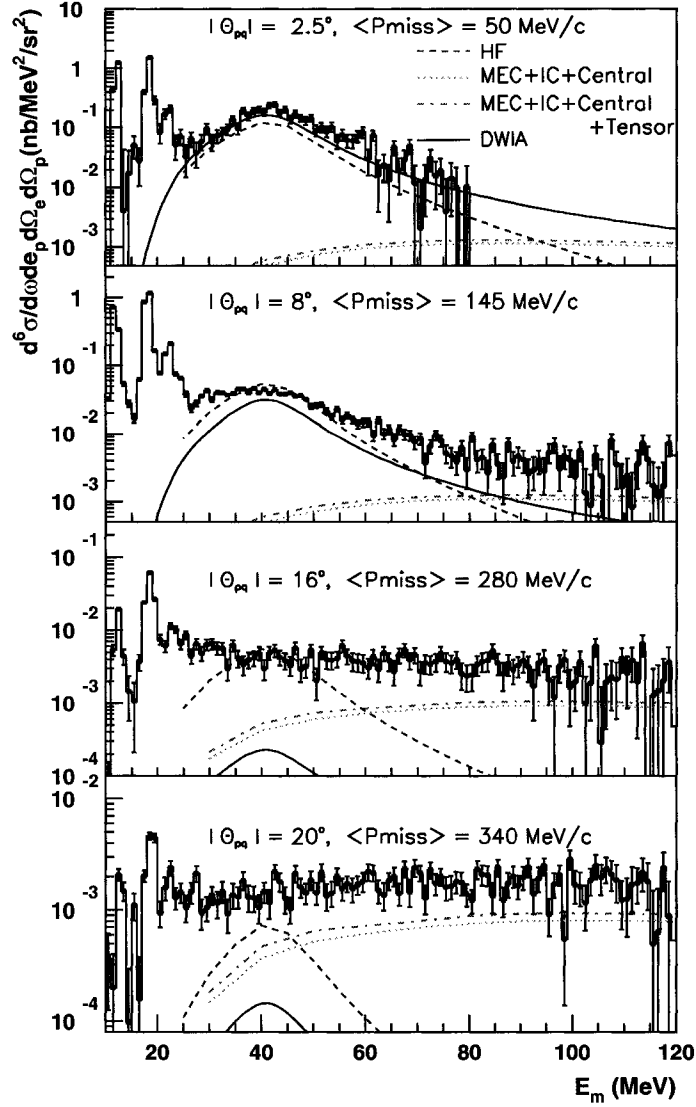
FIG. 10. Six-fold differential $^{16}O(e, e'p)$ cross section. Cross section is shown as a function of missing energy for four different average values of missing momentum. The solid (dashed) lines represent the Kelly [38] (Ryckebusch et al. [39, 40, 41, 42, 43]) single nucleon knockout calculations folded with the Lorentzian parameterization of Mahaux [44]. The dotted Ryckebusch et al. calculation shows the $(e, e'pp)$ and $(e, e'pn)$ contributions due to pion-exchange currents, intermediate $\Delta(1232)$ creation, and central short-range correlations, while the dot-dashed calculation also includes tensor correlations. The prominence of the broad peak centered at $E_{\text{miss}} \approx 40$ MeV, which is primarily due to knockout from the $1s_{1/2}$-state, decreases with increasing p_{miss}. Figure courtesy N. Liyanage [36].
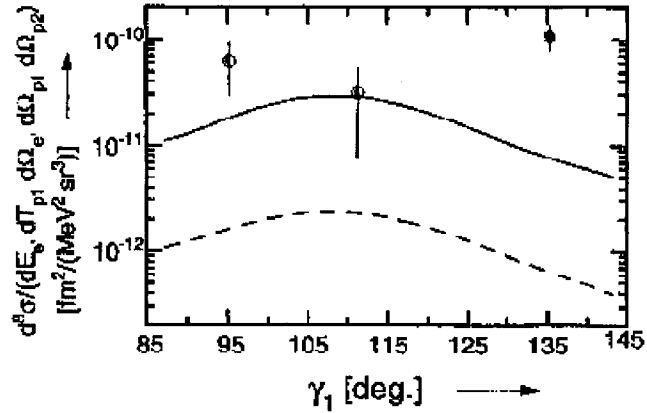
FIG. 11. Eight-fold differential ^{12}C(e,e'pp) cross section. Cross section is shown as a function of angle γ_1 between the momentum transfer and backward-emitted proton. The solid and dashed curves are the (e,e'pp) cross section for (1p)^2 knockout from a fully occupied 1p shell, calculated with the radial parameter c=0.6 and 0.4 fm, respectively. The three data points represent the measured cross section of ^{12}C(e,e'pp) reaction [45].

Measurements of the cross sections over a wide range of energy and three-momentum transfer (170 $\leq$ ω $\leq$ 290 MeV; 305 $\leq$ $|\vec{q}|$ $\leq$ 445 MeV/c) for ^{3}He(e,e'pp)n were provided by the AmPS facility at NIKHEF [52, 53]. The data were compared to results of continuum Faddeev calculations based on realistic nucleon-nucleon potential models [11]. Calculations showed that the cross section in this domain is dominated by direct two-proton emission induced by a one-body hadronic current. One of the experimental results from [53] is shown in Figure 13. Figure 13 shows the cross section for the ^{3}He(e,e'pp)n reaction as a function of momentum difference $p_{\text{diff},1} = |\vec{p}'_1 - \vec{q} - \vec{p}'_2|$ which can be identified with $(\vec{p}_1 - \vec{p}_2) \equiv 2\vec{p}_{\text{rel}}$, where $\vec{p}_1$, $\vec{p}_2$ and $\vec{p}'_1$, $\vec{p}'_2$ are the momenta of the protons in the initial state and final state, respectively and p_{rel} is the relative momentum of two nucleons in the initial state. Underestimation of the data by all four calculations with only one-body hadronic current operator was not explained in [53]. Clearly, these calculations need more than just one body current operator.

Two-proton emission from ^{3}He also has been studied using real photons produced via bremsstrahlung. The measurements were performed by Audit et al. [54, 55] in a kinematic domain selected to emphasize the production of on-shell pions on the
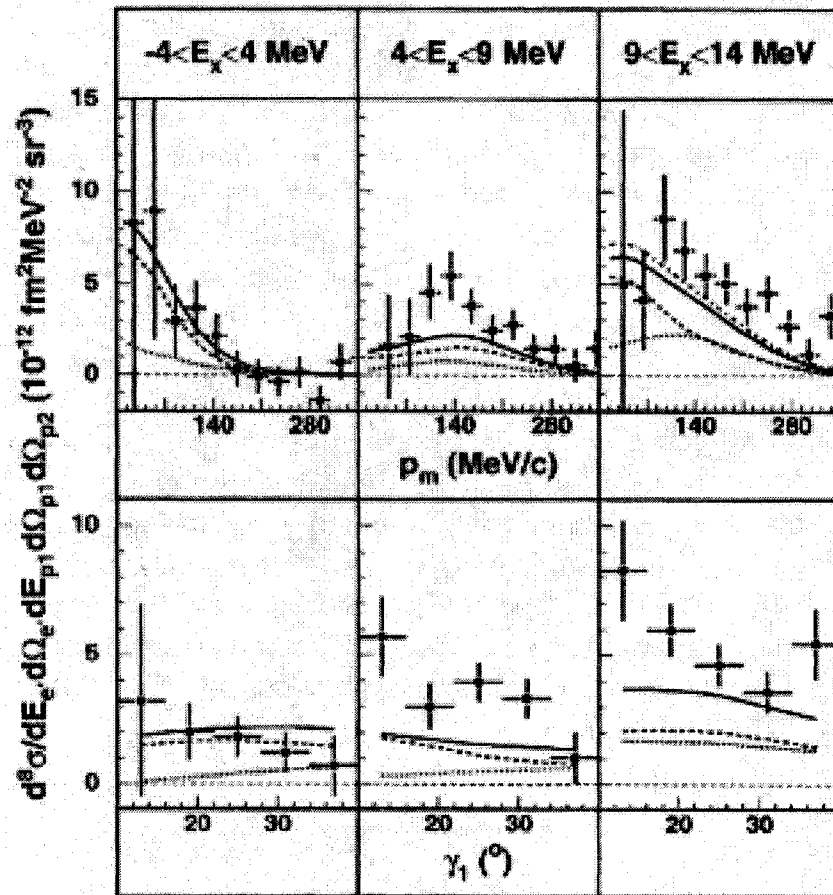
FIG. 12. Eight-fold differential ^{16}O(e,e'pp)^{14}C cross section. Cross section is integrated over the indicated excitation energy ranges. The upper panels show the cross sections as a function of p_m averaged over the γ_1 (angle between the proton emitted in forward direction and $\vec{q}$) range from 10° to 40°. The lower panels show the cross section as a function of γ_1 averaged over p_m ranges from 15, 60, and 70 to 300 MeV/c, for three consecutive bins in E_x. The curves correspond to results of a microscopic calculation. Solid curve is (e,e'pp) cross section, predominantly from the 1p shell. Dashed and dotted curves are contributions from one- and two-body nuclear currents, respectively. Dot-dashed curve corresponds to the sum of the theoretical cross section and the continuum.
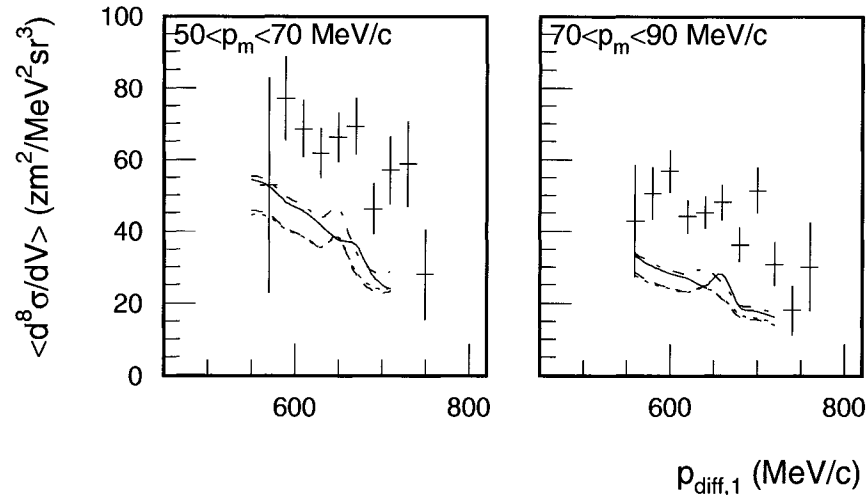
FIG. 13. Average cross section for the ^{3}He(e,e'pp)n reaction. Cross section is shown as a function of $p_{\text{diff},1}$ for two slices in p_m of 20 MeV/c wide. All curves are based on one-body currents only, but calculated using various models for the NN potential: solid curves Bonn-B, dashed curves CD-Bonn, dotted curves Argonne v_{18}, dot-dashed curves Nijmegen-93 [53].

struck nucleon that are subsequently reabsorbed on the nucleon pair. The results were evaluated in a theoretical framework based on a diagrammatic expansion of the reaction amplitude [56]. These measurements indicated an important role for processes in which three nucleons are involved, in particular, a sequential pion exchange. Such processes were also observed at lower energy transfers, in which the initial pion is assumed to propagate off-shell [57].

The use of tagged photon beams opened the possibility to perform kinematically complete measurements of the cross section for full breakup. Data obtained with the large-solid-angle detector DAPHNE [58] in the Δ resonance region, showed that the cross section for photon-induced breakup at $E_\gamma < 500$ MeV is dominated by two-step three-nucleon processes in those regions of phase space where final-state rescattering effects are minimal. No neutron momentum distribution could be extracted from this data set. The role of three-nucleon mechanisms was also observed by Kolb *et al.* [59] at lower photon energies. Neutron momentum distributions extracted from the ^{3}He(γ, pp)n [60] and ^{3}He(γ, pn)p [61] reactions by Emura *et al.* in the Δ-resonance region (E_γ=200–500 MeV and 125–425 MeV, respectively) showed that both two-nucleon and three-nucleon photo-absorption mechanisms are needed to explain the

data, but that at low neutron momentum the two-nucleon processes dominate the cross section. The choice of the kinematic domain and the transverse nature of the probe used in these experiments caused that the absorption of the photon by a two-proton pair was found to be largely driven by two-body hadronic currents.

Thus, to date, there have been only a limited number of two nucleon knockout measurements. In order to understand better the average NN properties in nuclei, more experimental data on two nucleon emission is certainly needed. This would also provide theory a test grounding to probe nuclear forces, correlated wave functions, and currents.

CHAPTER 2

EXPERIMENT

This thesis is based on the experimental data taken during the 1999 E2a run period. E2a measured electron scattering from nuclei, $A(e, e'X)$, using the Jefferson Lab CLAS (CEBAF Large Acceptance Spectrometer), a 4π magnetic spectrometer. The E2a run includes 7 experiments of the multihadron physics group, therefore the running conditions were chosen to satisfy the requirements of all the experiments. The number of triggers collected during E2a for each target and beam energy is given in Table I. The beam charge measured by the Faraday Cup while the data acquisition system was recording the data is shown in Table II. We have collected 2.2×10^9 triggers and 13 mC of beam charge in 4278 raw data files of 365 runs. Torus field settings were set to $I_t = 750$ A and $I_t = 1500$ A for 1.1 GeV runs, $I_t = 2250$ A for 2.2 GeV, and $I_t = 2250$ A and $I_t = -2250$ A for 4.4 GeV runs. The raw data from the CLAS detector were recorded on the tapes of the JLAB tape silo in BOS format files [62]. This chapter describes the main characteristic of the single detector systems as well as of the CEBAF accelerator and beam.

2.1 CONTINUOUS ELECTRON BEAM ACCELERATOR FACILITY

The experiment has been carried out using the electron beam provided by the Continuous Electron Beam Accelerator Facility (CEBAF) at Jefferson Lab. Its electron accelerator is based on 338 superconducting cavities that boost the beam with radio-frequency waves and provide a high luminosity continuous electron beam with energy up to almost 6 GeV. A schematic of the machine is shown in Fig. 14. The 45 MeV injector delivers polarized electrons from a strained GaAs photocathode source. The beam has a 1.497 GHz microbunch structure. The beam from the injector is accelerated through a unique recirculating beamline that looks like a racetrack, with two linear accelerators joined by two 180° arcs with a radius of 80 meters. Twenty cryomodules, each containing eight superconducting niobium cavities, line the two linear accelerators. Accelerating cavities are cooled to 2 Kelvin by liquid helium, produced at the Lab's Central Helium Liquefier. The two parallel linacs recirculate the beam up to five times boosting the beam energy up to 1.1 GeV for each turn. Presently, the maximum beam energy is 5.6 GeV, with a maximum current of 180

TABLE I. Number of triggers collected during E2a run period. All values shown in the table are given in millions.

Target	Beam Energy			Total triggers
	1.161 GeV	2.261 GeV	4.461 GeV	
^{3}He	141	217	186	544
^{4}He	-	333	445	778
^{12}C	62	238	310	610
^{56}Fe	-	23	30	53
CH_2	10	35	21	66
Empty Cell	19	69	33	121
Total triggers	232	915	1025	2172

TABLE II. Beam charge collected during E2a run period. Values of the accumulated beam charge shown in the table are given in mC.

Target	Beam Energy			Total charge
	1.161 GeV	2.261 GeV	4.461 GeV	
^{3}He	0.32	1.44	1.17	2.93
^{4}He	-	1.08	0.87	1.95
^{12}C	0.19	1.79	2.14	4.12
^{56}Fe	-	0.22	0.29	0.51
CH_2	0.07	0.33	0.18	0.58
Empty Cell	0.17	1.34	1.58	3.09
Total charge	0.75	6.20	6.23	13.18
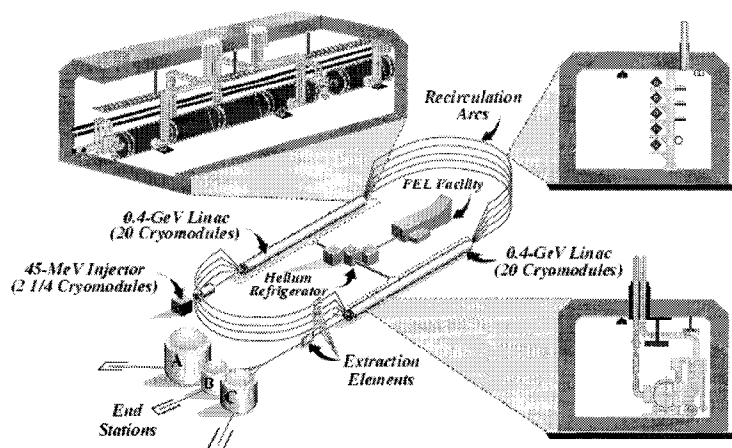
FIG. 14. A schematic view of the accelerator. One of the cryomodules is shown in the upper left corner. A vertical cross section of a cryomodule is shown in the lower right corner. A cross section of the five recirculation arcs is shown in the upper right corner.

μA. Quadrupole and dipole magnets in the tunnel steer and focus the beam as it passes through each arc. More than 2,200 magnets are necessary to keep the beam on a precise path and tightly focused. The energy spread of the beam is $\Delta E/E < 10^{-4}$. Beam is directed into each experimental hall's transport channel using magnetic or RF extraction. The RF scheme uses 499 MHz cavities, which kick every third bunch out of the machine. Beam is delivered into three experimental areas (Hall A, B and C) with one beam "bucket" every 2 ns.

2.2 CEBAF LARGE ACCEPTANCE SPECTROMETER, HALL B

2.2.1 General Description.

CLAS (CEBAF Large Acceptance Spectrometer) is located in Hall B, Jefferson Lab. The CLAS is an almost 4π spectrometer. It provides a unique facility to investigate reaction mechanisms involved in inelastic electron scattering by allowing us to detect almost all of the particles emitted following virtual photon absorption. The magnetic field in the CLAS is generated by six superconducting coils arranged around the beam line to produce a field oriented primarily in the azimuthal direction about the beam axis, with maximum magnitude of about 2 Tesla (see Fig. 15). The coils divide the detection system into six independent sectors. Each sector essentially acts as an
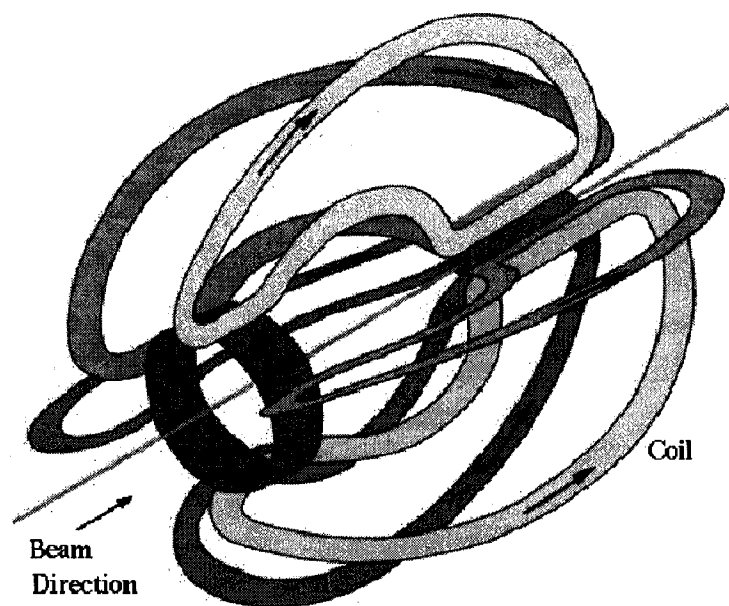
FIG. 15. Configuration of the torus coils.

independent spectrometer. The size and the shape of the coils (about 5 m long and 2.5 m wide) were chosen to optimize measurements with fixed targets. Each sector of the CLAS consists of three separate Drift Chamber (DC) assemblies to determine the trajectories and momenta of charged particles, Čerenkov Counters (CC) for electron identification, Scintillation Counters (SC) for time-of-flight (TOF) measurements, and an Electromagnetic Shower Calorimeter (EC) to identify showering particles such as electrons and photons and to detect neutrons (see Fig. 16). A Faraday cup, located at the very end of the Hall-B beam line, is used to measure the integrated beam charge passing through the target. All detectors may be used to build the trigger configuration for the reaction of interest. The EC system coverage is extended by the Large Angle Calorimeter (LAC). The polar angle coverage in CLAS varies as $8°$ to $140°$ for DC, $9°$ to $143°$ for SC, and $8°$ to $45°$ for CC and EC. LAC accepts particles from $45°$ to $75°$ in two sectors.

2.2.2 Drift Chambers.

The trajectories and momenta of the charged particles are measured by the drift chambers [64].

The drift chamber system is divided into six sectors by the six superconducting
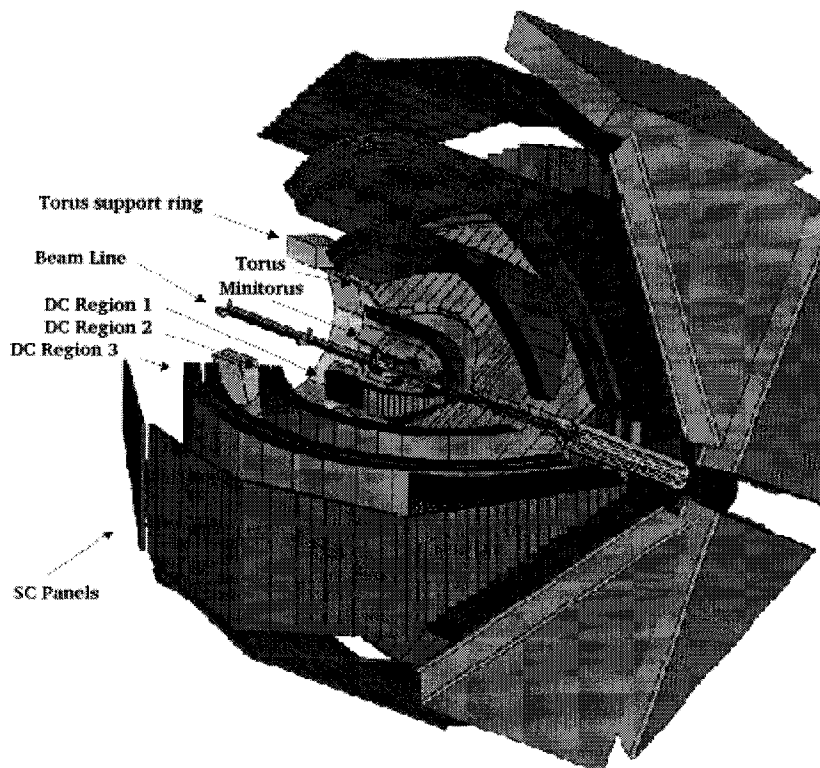
FIG. 16. Three dimensional view of CLAS.

toroidal magnets (Fig. 15). The coils create a field free region around the target and a magnetic field that is primarily transverse to the particle trajectory. Each of the six sectors of the drift chambers consists of three separate regions: Region 1 close to the target (no magnetic field), Region 2 between the coils (high magnetic field up to 2 Tesla), and Region 3 outside of the coils (see Fig. 15 and 16). The Region 2 drift chambers were built by the experimental nuclear physics group at ODU. Each region of the drift chambers consists of axial and stereo superlayers of wires.

Axial wires are strung parallel to the direction of the magnetic field (perpendicular to the beam direction) to measure scattering angles and momenta. Stereo superlayer wires are strung at an angle of 6° with respect to the axial wires. The two superlayer combination in each region allows us to determine the azimuthal angle ϕ of each particle. Each superlayer consists of six layers of sense wires, surrounded by field wires in hexagonal cells (see Fig. 17)[1]. There are 192 sense wires per layer in Region

[1] Actually, the first (stereo) superlayer in Region 1 has only 4 layers of sense wires.
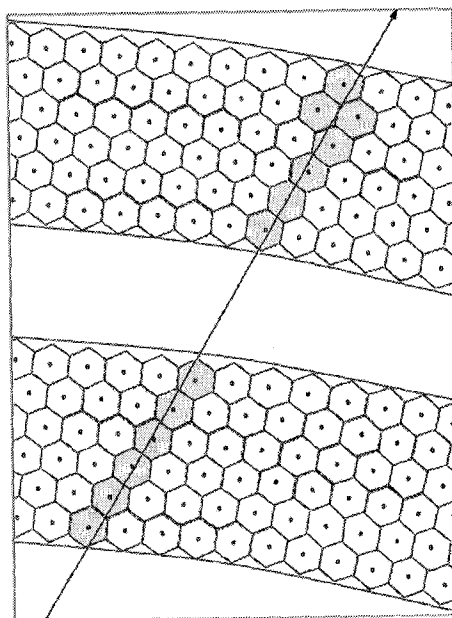
FIG. 17. Schematic of a section of drift chambers showing two superlayers. The wires are arranged into a hexagonal patterns (cells). The sense wires are located in the center and field wires are located at each corner of each cell. The arrow ahows a charged particle passing through the drift chambers and the shadowed hexagons represent the hit cells.
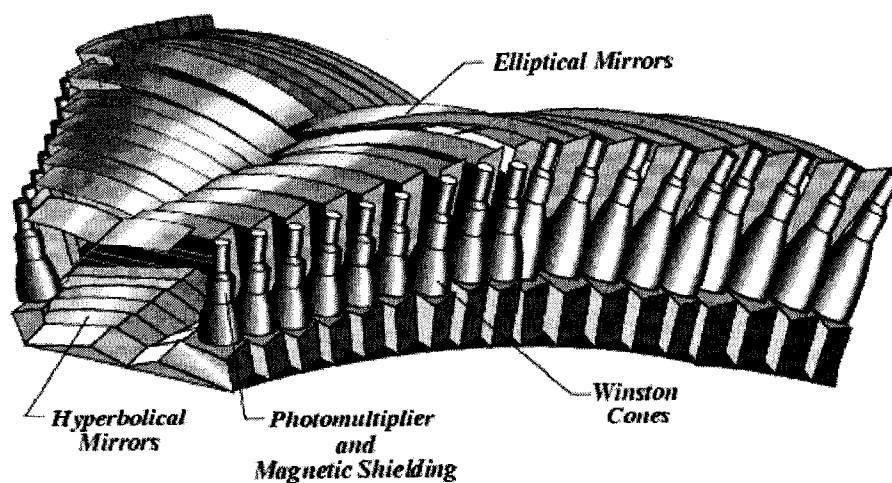
FIG. 18. Array of CC optical modules in one sector.
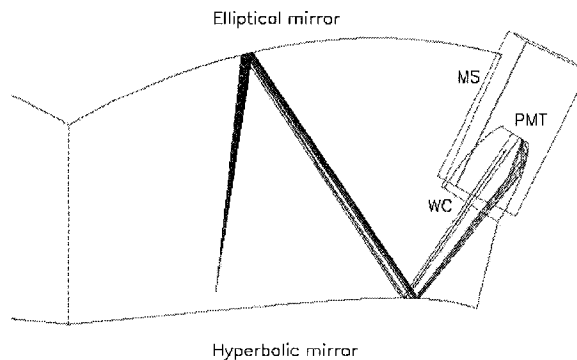
FIG. 19. One optical module of the CLAS Čerenkov Detector. Optical and light collection components are also shown. Čerenkov light from electrons reflected from the hyperbolic and and elliptical mirrors gets into the Winston Cone (WC), surrounded by a Magnetic Shield (MS) and collected by Photomultiplier Tubes (PMT).

2 and Region 3 and 128 sense wires per layer in Region 1. The total of 18 drift chambers with 35148 instrumented hexagonal drift cells can detect charged particles with momenta greater than 200 MeV/c over the polar angle range from $8°$ to $143°$. There are also guard wires surrounding each superlayer to reproduce the electric field configuration of an infinite number of cells.

Charged particles traversing the drift chamber ionize gas molecules. The gas is maintained in an electric field so that the electrons and ions created in the ionization process drift toward the cathode and anode wires, respectively. In the high field region near the cathode wires, drifting electrons collide with gas atoms and produce secondary ionization resulting in a multiplication of collected electrons and ions. Detected electric signals carry information about the particle's drift time which translates to the hit position of the original charged particle going through the detector. The electric signal passes through a preamplifier, an amplifier, a discriminator and 2:1 multiplexer and then starts a TDC. The TDCs are stopped by the event trigger. More details on that subject are given in Section 3.1.

The drift chamber system uses an Ar/CO_2 gas mixture, 90/10 by volume, which has an ionization gain of $\approx 10^4$. That mixture is non-flammable, it provides drift velocity of typically 4cm/μsec and an operational voltage plateau of several hundred volts before breakdown. The intrinsic resolution provided by this gas is ≈ 100 μm [65]. The final space resolution is ≈ 400 μm, mostly limited by the knowledge of the geometry and quality of drift velocity parameterization (see DC Calibration
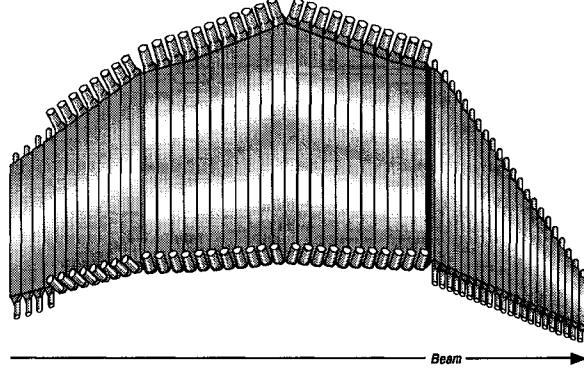
FIG. 20. The four panels of TOF scintillator counters for one of the sectors. Scintillators have different light guides and PMT's for different scattering angle coverage.

Section 3.1.2).

2.2.3 Čerenkov Counters

The threshold Čerenkov Counters (CC) are designed to discriminate between electrons and hadrons, mostly negative pions, at the trigger level [66]. Charged particles travelling through the medium with a speed exceeding the local phase velocity of light emit electromagnetic radiation. The velocity threshold for Čerenkov light emission is $\beta=1/n$ where n is the refraction index of the medium. The Čerenkov material used is perfluorobutane C_4F_{10}, which has $n=1.00153$. That corresponds to a threshold in energy of the particle:

$$E = \frac{m}{\sqrt{1 - \beta^2}} = \sqrt{\frac{n}{n-1}}m = 18.09m,$$

where m is a mass of the particle. This provides an acceptably high pion momentum threshold ($p_\pi > 2.5$ GeV/c).

The Čerenkov detector of CLAS consists of six independent identical Čerenkov detectors (one per sector) and each detector covers a scattering angle θ from 8° to 45°. Each detector consists of 36 optical modules (see Fig. 18) to cover 18 regions of θ, with two modules per θ region. Each module has three mirrors - elliptical, hyperbolic and cylindrical - to direct the light into a light collecting Winston cone (see Fig. 19). The mirrors are aligned to optimize the light collection by PMTs.

In electron scattering experiments with CLAS, the trigger is given by the detection of an electron in the final state. The Čerenkov counter is one of the detectors

that might be used in the event trigger. The CC discriminator thresholds for our experiment are given in Section 2.2.8. The electron efficiency within the fiducial acceptance from the measured photoelectron yield exceeds 99% (see [66]). Outside of the fiducial region the efficiency drops rapidly, it has very strong spatial variation and therefore the nonfiducial region is usually excluded from the data analysis. The CC fiducial region is smaller than the EC fiducial region.

2.2.4 Time of Flight System

The Time-of-Flight (TOF) system of CLAS is designed to measure the time of flight for charged particles [67]. In conjunction with the tracking information, the TOF system allows us to determine the velocity of the particle, which determines the particle's mass

$$m = \frac{p\sqrt{1 - \beta^2}}{\beta}. \tag{1}$$

That explicitly identifies the particle.

The TOF system consists of 57 scintillator strips (BC-408) in each of six sectors mounted as four panels combined together (see Fig. 20). The length of the scintillator counters varies from 30 to 450 cm, with a width of 15 or 22 cm and a thickness of 5.08 cm. Scintillator strips are located perpendicularly to the beam direction with angular coverage of 2° each. The signal readout is done by PMT's connected to light guides attached to both ends of each paddle. Signals from the PMT's are read out by TDC's and ADC's. Due to cost considerations, the last 18 scintillators in the back angles are grouped into 9 pairs each connected to a single TDC and single ADC channel. Because of that pairing, each sector comprises 48 electronic channels.

The timing resolution for scintillator counters varies with the length and width of the strip. The average time resolution is about 130–150 ps, which allows us to separate reliably pions and protons up to a momentum of 2.5 GeV/c.

2.2.5 Electromagnetic Shower Calorimeter

The Electromagnetic Calorimeter of CLAS (EC) is designed to identify electrons, neutrons, and photons. Mostly it is used for detection and triggering of electrons at energies above 0.5 GeV, detection of photons at energies above 0.2 GeV, and detection of neutrons, assuming their separation from photons based on time information [68].
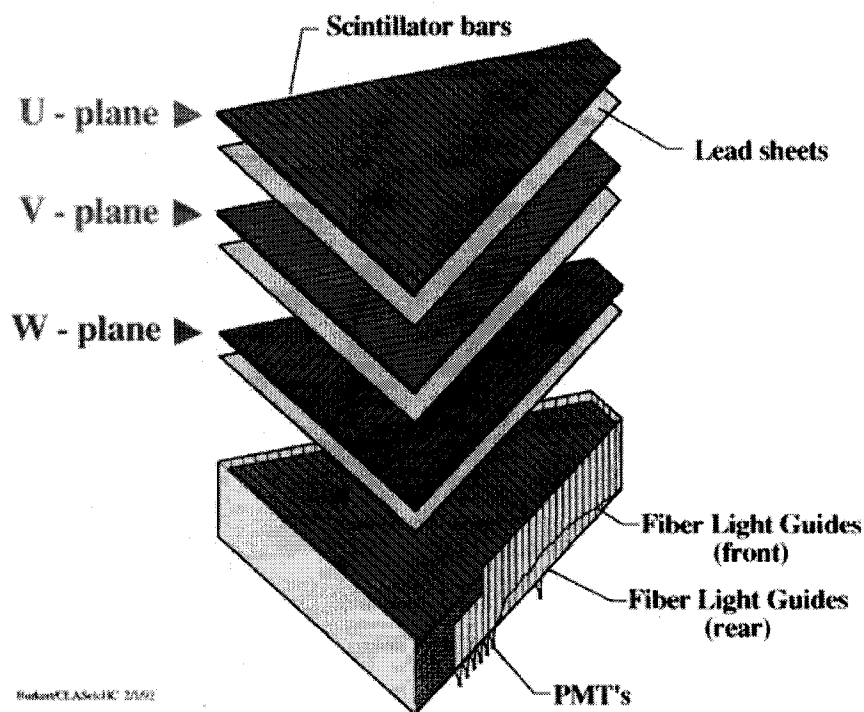
FIG. 21. View of one of the six CLAS electromagnetic calorimeter modules.

The EC system consists of alternating layers of scintillator strips and lead sheets with a total thickness of 16 radiation lengths. Electrons and photons travelling through the calorimeter produce an electromagnetic shower in the lead. The energy of the shower is converted into light by the scintillator strips, which is finally collected by PMT's. [2] A lead:scintillator thickness ratio of 0.2 was used, which requires 40 cm of scintillator material and 8 cm of lead per module. That gives approximately 1/3 of the energy of the shower to be deposited in the scintillator. In order to match the hexagonal geometry of the CLAS, the lead-scintillator sandwich is contained within a volume having a shape of an equilateral triangle (see Fig. 21). There are 39 layers in the sandwich, each consisting of a 10 mm BC-412 scintillator followed by a 2.2 mm thick lead sheet. The calorimeter utilizes a "projective" geometry, in which the area of each successive layer increases. This minimizes shower leakage at the edges of the active volume and minimizes the dispersion in arrival times of signals originating in different scintillator layers. Each scintillator layer is made of 36 strips parallel to one side of the triangle, with the orientation of the strips rotated

---

[2] Neutrons and the other hadrons make "hadronic showers".
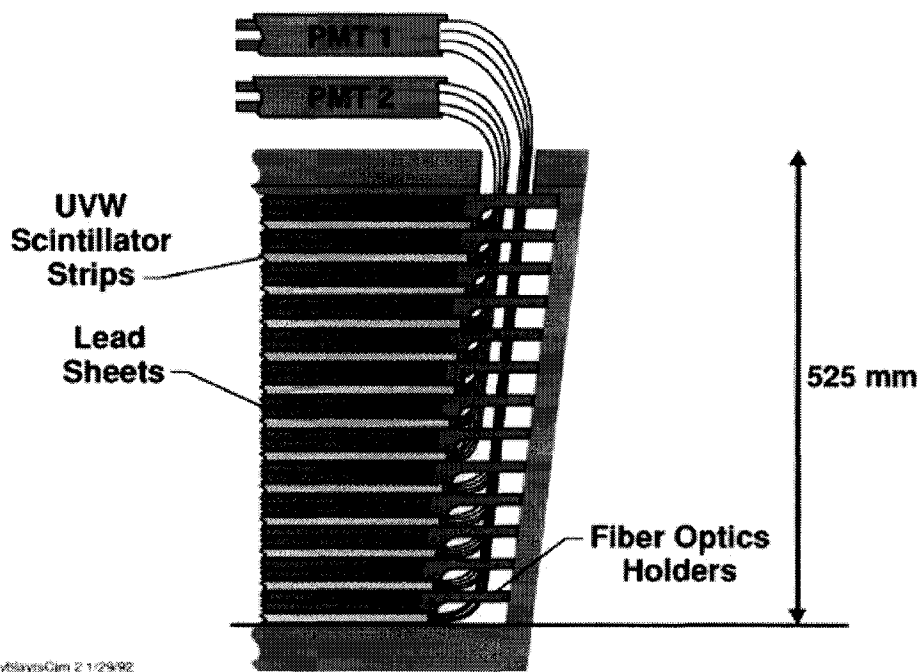
FIG. 22. Schematic side view of the fiber-optic readout unit of the calorimeter module.

by 120° in each successive layer (see Fig. 21). Thus there are three orientations or views (labeled U, V and W), each containing 13 layers, which provide stereo information on the location of energy deposition. The 13 layers of each view are combined into an inner (5 layers) and outer (8 layers) stack, to provide longitudinal sampling of the shower for improved hadron identification. Each module thus requires 36(strips)×3(views)×2(stacks) = 216 PMTs. Altogether there are 1296 PMTs and 8424 scintillator strips in the six EC modules used in CLAS.

A fiber-optic light readout system transmits the scintillator light to the PMTs. Fig. 22 displays a schematic side view of the fiber-optic readout unit of the calorimeter module. These fibers were bent in a controlled way to form semi-rigid bundles originating at the ends of the scintillator strips and terminating at a plastic mixing light-guide adapter coupled to a PMTs.

The total energy deposited in the calorimeter is available at the trigger level to reject minimum ionizing particles or to select a particular range of scattered electron energy. Pion events are largely suppressed by setting the EC total energy threshold E_{total} in the CLAS hardware trigger. The overall calorimeter position resolution is $\sigma = 2.3$ cm. The time resolution is about $\tau = 3$ ns.

TABLE III. Specifications of the cryogenic helium target.

Item	Value
Length (cm)	4.00
Diameter (cm)	2.769
Temperature (K)	3.25
Pressure (mBar)	765
Density (g/cm^3)	0.067

2.2.6 ^{3}He Target

We used a liquid helium target at an average temperature of 3.25 K. Cooling and
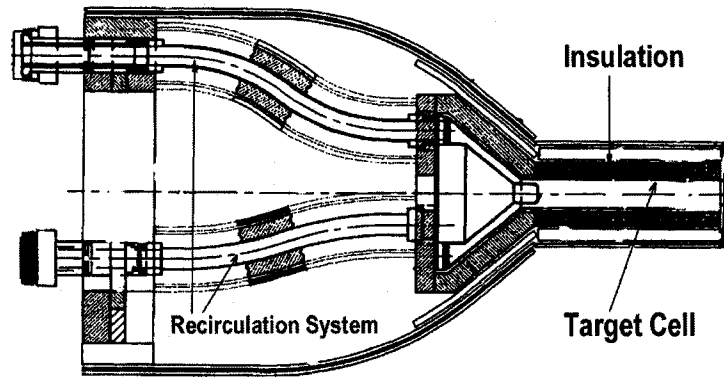
FIG. 23. Schematic view of the cryogenic target cell and recirculation system. Aluminum target cell, polystyrene insulation layers and tubes for liquid helium recirculation are shown. The target cell is the central cylindrical white area.

recirculation of ^{3}He was provided by the CLAS cryogenic system. The target cell (see Fig. 23) is made of aluminum about 4 cm long, 2.7 cm diameter with 15 μm thick 5 mm diameter input and output windows. The specifications of the ^{3}He target are shown in Table III. The target parameters, such as temperature and pressure were monitored during the run. We used density versus pressure dependance given in [69] to extract target density for our run. Target conditions were very stable, temperature and pressure were fluctuating from 3.1 to 3.4 K and from 790 to 740 mBar, respectively. That gives a 1% change in the target density, which was found to be 0.067±0.0007 g/cm^3.

2.2.7 Beam Position Measurement and Stability

The position of the beam in Hall B is measured by nanoAmp Beam Position Monitors (BPM). The nA BPMs measure the beam position and are designed specifically to work with the low beam currents used in the Hall B line. Note that these monitors do not accurately measure the beam position at currents of less than 1 nA.

We used three BPMs, installed sequentially in Hall B along the beam: 2C22, 2C24, and 2H01. These are approximately 40 m, 20 m and 8 m, respectively, from the target. 2H01 is the closest to the target so it gives more precise information about the beam position on target. The beam position readings of the 2C22, 2C24, and 2H01 BPMs for ^{4}He (beginning of the data taking) and ^{3}He (end of the data taking) runs for the E2a data period are shown in Figure 24. The measured beam positions are stable within 1 mm. Shifts in the Y coordinate for runs after run 18158 could be explained by a new tuning of the beam location needed to hit the center of a new target cell. All of the ^{3}He running was done with one target cell and stable beam position (runs 18346-18521).

2.2.8 Event Trigger and Data Acquisition

The event trigger is formed from a combination of the signals from the CLAS detector components that pass pretrigger discriminators. The configuration of the event trigger and the pretrigger discriminator thresholds are set to satisfy the requirements of each experiment.

We used an inclusive (e,e′) trigger. A coincidence signal that selects an electron in the final state is used to initiate a readout of the event by the Data Acquisition System. The Level 1 trigger used in our experiment required a hit in the same sector for both CC and EC for 2.2 GeV and for EC only for 4.4 GeV runs. In order to get more forward angle electrons we did not use the CC in the trigger at 4.4 GeV. The Level 2 trigger uses information from the drift chambers to select events with corresponding track of the particle, combined from track segments. The Level-2 trigger was not used in this experiment. The pretrigger thresholds are specified in Table IV. Equation 2 relates EC thresholds with the detected electron energy [70]

$$E_{el}{}^{EC} \text{ (in MeV)} = 214 + 2.47 \times \text{EC}_{\text{threshold}} \text{ (in mV)}. \tag{2}$$

The threshold on the total deposited energy in the calorimeter, EC_{total}, was chosen to reduce the background due to low energy electrons and photons. The threshold
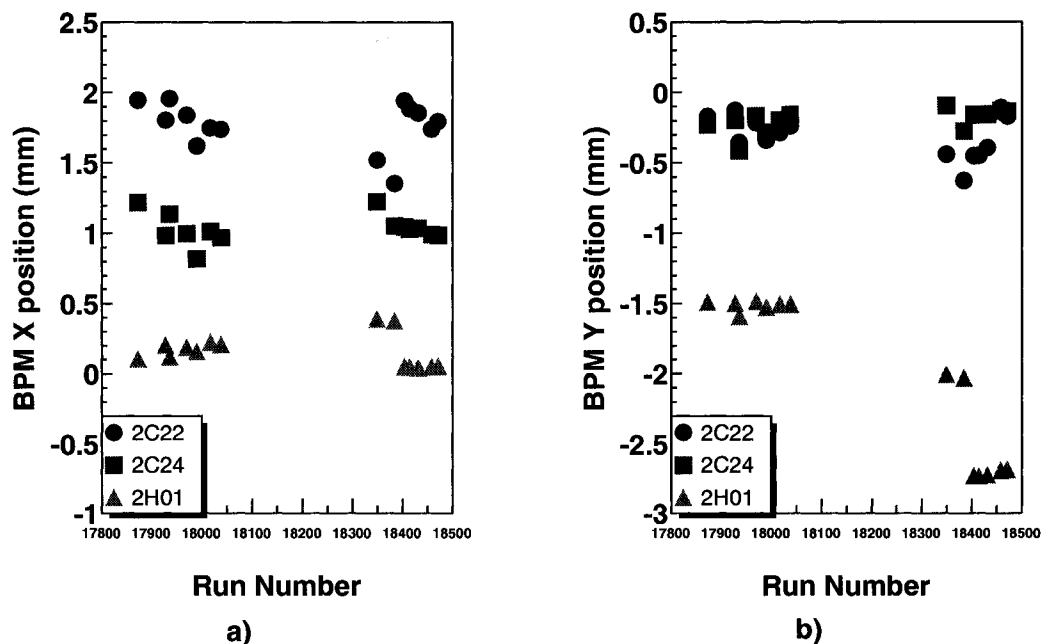
FIG. 24. Hall B BPM readings for ^{3}He runs of E2a run period. a) X positions of the beam b) Y positions of the beam from each BPM. This thesis data covers runs 18346–18521.

on EC_{inner} was set to exclude minimum ionizing particles. The CC threshold is set well below the single photoelectron peak in PMTs. About 30% and 17% out of 255 and 188 million collected raw trigger events have a reconstructed identified electron in the 2.2 and 4.4 GeV ^{3}He data, respectively.

A schematic of the Data Acquisition System is shown in Fig. 25. The signals from the CLAS detectors that form a trigger are sent to a pretrigger. If the pretrigger conditions are satisfied, the signal is submitted to the Level-1 trigger. If there is a trigger in the event then the signal is passed to the Trigger Supervisor (TS) which communicates with Read Out Controllers (ROCs). The data are then read out, digitized and transferred to the Event Builder (EB). Finally the Event Recorder (ER) receives the information from the Event Builder through the Data Distribution (DD) shared memory. The data are written to the disk and later transferred to the tape SILO for permanent storage. During the experiment, the typical rates characterizing the DAQ performance were about 1.5–2.0 kHz with a live time of about 90%. We had a luminosity of 0.5–1 · 10^{34} nucleons cm^{-2} s^{-1} for the 2.2 and 4.4 GeV runs on

TABLE IV. CC and EC Discriminator Thresholds (DT). pe = number of photoelectrons.

	2.2 GeV			4.4 GeV	
	EC_{total}	EC_{inner}	CC	EC_{total}	EC_{inner}
DT	128 mV	60 mV	20 mV	350 mV	60 mV
Physics Equivalents	0.5 GeV	0.4 GeV	0.2 pe	1.1 GeV	0.4 GeV

^{3}He . During the run, the beam conditions, live time, trigger rates, the status of the detectors and data quality plots were continuously monitored by shift personnel.

tape silo

disk

clon00(smp)

MON

dd

CED

IPC to dd

clon10(smp)

ER   DD   EB

DD to IPC

L-2 F.Clr./Busy/Trigger type

L-1

TS

L-1
true

Gate
logic

ROC

ROC
mem.

L-2
true/
false

L-2

discriminators

pretrigger

detector

L-1:	Level-1 Trigger	ER:	Event Recorder
L-2:	Level-2 Trigger	DD(dd):	Data Distribution
TS:	Trigger Supervisor	IPC:	InterProcess Control
ROC:	17 Read-Out-Controllers	MON:	Monitor and user software
EB:	Event Builder	CED:	Event Display

FIG. 25. Data Acquisition system of CLAS.

CHAPTER 3

DATA PROCESSING

This chapter presents the data processing steps. I will describe the detector calibration, tracking, processing the data through the reconstruction code, and monitoring the data quality. I will then discuss particle identification and the corrections applied to the electrons and protons in our physics analysis. Then I will focus on the cuts we applied to the data to select proper fiducial regions and target region. I will also discuss the beam charge and energy measurements as well as our (e,e'p) normalization. Finally I will describe selection of ^{3}He(e,e'pp) and ^{3}He(e,e'pp)n events and present the data statistics summary table.

3.1 DETECTOR CALIBRATION

3.1.1 Calibrated Detectors

Calibration of the detectors is crucial to achieving good detector resolution. For calibration purposes, a fraction of data ("calibration runs") was selected for each day of the running period and processed several times. Each iteration (pass) involved processing the calibration runs through the event reconstruction software and refitting the calibration constants. Final, improved parameters resulting from the calibration are written to the calibration maps and are "frozen" for the rest of the data processing. Calibration of CLAS detectors in our experiment was done by multihadron group graduate students [71], [73]. I will briefly describe the calibration of the most important CLAS components, giving more space to the drift chamber calibration which was done by me.

3.1.2 Drift Chamber Calibration

In order to optimize the overall resolution, we calibrated the drift chambers by parametrizing the drift velocity function. 36 out of 365 runs collected during the E2a run data taking were chosen for calibration purposes, at least one for each day of the run period. The calibration program dc_calib_check-2-0 written by David Lawrence was used to calibrate these calibration runs [74].

Track Reconstruction

The reconstruction of the momentum and angles of the tracks is done in two stages [64]. In the first stage, individual tracks are fit only to hit-wire positions in a procedure known as "hit-based" tracking (HBT). In that stage, data are combined into track segments within individual superlayers and these segments are then linked together to form tracks across all three regions of the drift chambers within one sector. Due to the comparatively small size of the drift cells and the large number of wire layers, the track momenta can already be reconstructed with a resolution of 3% to 5%. Additional information on these tracks, derived from the Čerenkov, time-of-flight, and electromagnetic calorimeter detectors, allows for determination of the identities and speeds of the charged particles.

In the second stage of the analysis, the "drift time" between when the charged particle crossed the cell and when the electron avalanche is detected on the sense wire is used to localize the charged particle trajectory within the cells and greatly improve the resolution. The flight-time information of the particles from the target to the outer scintillators is used to correct the measured drift times. A pre-determined table is then used to convert the corrected drift times to drift distances. These corrected track positions in each drift cell are fit in a procedure known as "time-based" tracking (TBT) in order to determine the final track parameters. The drift time is given by:

$$t_{drift} = t_{TDC} + t_0 - t_{start} - t_{flight} - t_{prop} - t_{walk}, \tag{3}$$

where t_{TDC} is the raw time measured by the TDC, t_0 is the fixed-time delay for the wire, t_{start} is the event start time, t_{flight} is the flight time of the particle from the reaction vertex to the wire, t_{prop} is the signal propagation time along the wire, and t_{walk} is a time-walk correction made for short drift times due to different ionizations for slow and fast particles. For the experiments with an electron beam, the event start time is given by the TOF counter time for the primary scattered electron corrected for the calculated flight time of this electron from the target (track path length divided by the speed of light).

Drift Chamber Nomenclature

The CLAS drift chambers can be separated in several ways. Figure 26 gives a basic idea of how the chambers are arranged.
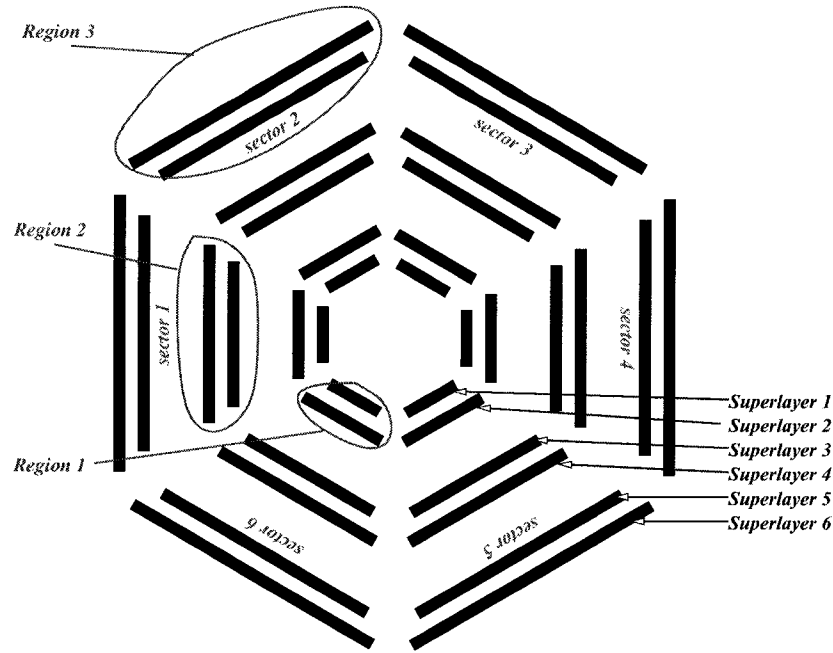
FIG. 26. Schematic of CLAS drift chambers. Schematic shows how regions and superlayers are named. This represents a slice through the drift chambers at the target position.

Each of the 6 sectors in CLAS has an identical set of drift chambers. Each set can be separated by region or by superlayer. Physically, each region is a separate physical volume containing two superlayers. Each superlayer contains 6 layers of sense wires (with the exception of superlayer 1 which has only 4 layers). Each superlayer of each sector is calibrated separately for a total of 36 sets of parameters.

When a charged particle goes through the drift chambers, each of the 34 layers is hit.[1] Each hit detected in the chamber is used to determine the particle's track via a least squares fit done inside the CLAS reconstruction program. Two terms are used to describe the distance a charged particle track is from a sense wire: *DOCA* - (Distance Of Closest Approach) The distance from the sense wire to the track as determined by time-based-tracking (TBT). The DOCA values are obtained from fits to global tracks (i.e. fits which include all layers).

DIST - The predicted distance (calculated Distance of Closest Approach) from the sense wire to the track. This is calculated from the drift time (see Fig. 27) as well

---

[1]Actually, we find an average of 30 hits per time based track (see Fig. 30 b). This is mostly due to inefficiencies or holes in the chamber.
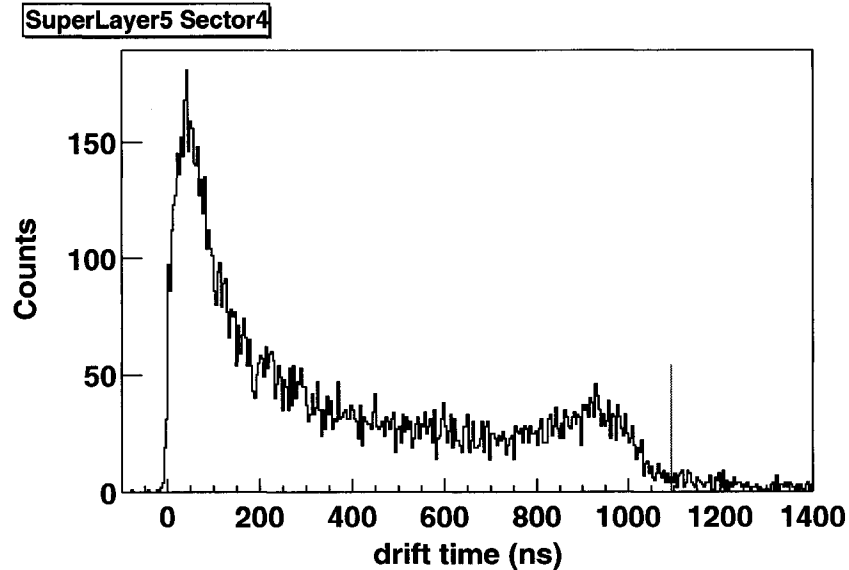
FIG. 27. Drift time distribution. Drift time for superlayer 5 sector 4 is shown. The vertical line indicates t_{max}.

as some other parameters. The drift time is determined from the wire's TDC values correcting for fixed cable delays and event dependent delays such as flight time.

Residual is the difference between the absolute values of DOCA and DIST ($R = |DOCA| - |DIST|$). This is also known as the "time residual" because its sign is determined by the sign of any systematic time shift. The residuals are the primary means of measuring the resolution of the drift chambers. We estimate standard deviations (residual sigma) of the residual distributions by Gaussian fit. Note also that DIST is positive definite, while DOCA is assigned a sign determined by whether the track passed to the right or to the left of the wire. A more detailed description of the drift chamber calibration procedure is given in [74].

Time to Distance Calibration

The drift velocity function is the relation between the calculated distance of closest approach (DIST) of a particle track and the drift time, which is the time it takes for electrons created by the particle to drift to the sense wire. The function's parameters are determined by fits to the DOCA versus time plots produced from CLAS data. Figure 28 shows a typical DOCA versus time distribution. The drift time to drift

distance (DIST) calibration was performed in two steps. First, the maximum drift time t_{max} was monitored on a run-by-run basis. Its variation is sensitive to changes in the gas mixture or pressure. Since t_{max} is explicitly used in the drift time to distance function, its reliable extraction is crucial to determine the function. Secondly, the drift velocity function is fitted separately for each superlayer and sector which allows us to determine the correlation function.

Function Parameterization

The time to distance correlation function is determined by the drift chamber geometry and operating conditions like inhomogeneous magnetic fields in the Region 2 drift chambers and the drift chamber gas mixture. An angular dependent correction is also needed due to the hexagonal geometry of drift chamber cells. The correlation function can be written:

$$x = x(t, \theta, B) \tag{4}$$

where θ is the entrance angle of a track with respect to a drift chamber cell which is between $0°$ and $30°$ and B is the magnetic field strength from the main torus for Region 2 drift chambers. The actual functional form used in drift chamber calibrations consists of a base function and several correction functions which have been parametrized once by Liming Qin and currently assumed to be the same. These correction functions are described in detail in [64, 65].

The drift time to drift distance function at a given track entrance angle is parameterized as:

For Region 1 and 2:

$$x(t) = p_1\hat{t} + p_2\hat{t}^2 + p_3\hat{t}^3 + p_4\hat{t}^4 + ((D_{max} - p_1 - p_2 - p_3)\hat{t}^5), \tag{5}$$

For Region 3:

$$x(t) = p_1 t + \left(\frac{(D_{max} - (p_1 t_{max}))}{1 - p_2} \right) \hat{t}^{p_3} - p_2\hat{t}^{p_4}, \tag{6}$$

where p_1, p_2, p_3, p_4 are the parameters, D_{max} is the effective cell size, and $\hat{t}$ is the time normalized to t_{max}. Both equations are constrained to equal D_{max} at $t = t_{max}$. The parameters p_1, p_2, p_3, p_4 have different meanings depending on which region the parameters are being used for. The values normally determined by the DC calibration program are the four mentioned above base parameters, the average local angle, the
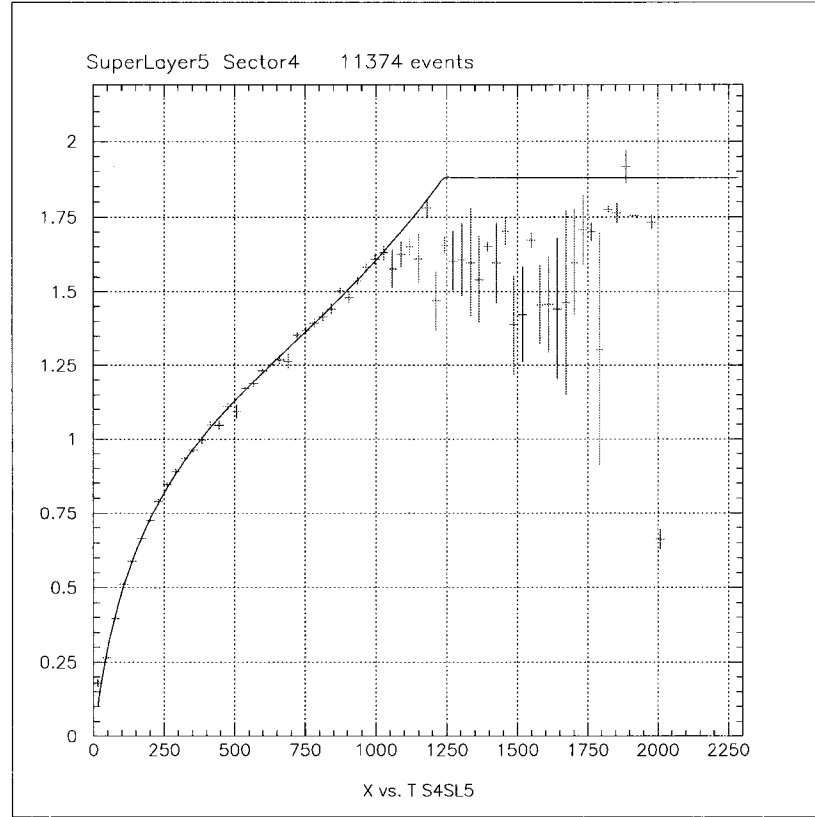
FIG. 28. Drift velocity function. Drift velocity for superlayer 5 sector 4 is shown. Vertical axis is defined by DOCA [cm], horizontal axis is defined by drift time [ns]. The t_{max} value is about 1100 ns (See Figure 27) which determines $D_{max} \approx 1.7$ cm.

average magnetic field strength, t_0 and t_{max}. The average local angle and average magnetic field strength are those of the data sample used to produce the calibration. These values are extrapolated from the reconstruction software.

Drift Chamber Calibration Quality

We check the quality of the calibration by examining several quantities, such as drift chamber resolution (time residual sigmas), TBT hits per track, and χ^2 values obtained for all 36 fits[2].

Figure 29 shows drift chamber resolution as a function of calibration run number

---

[2]6 sectors times 6 superlayers
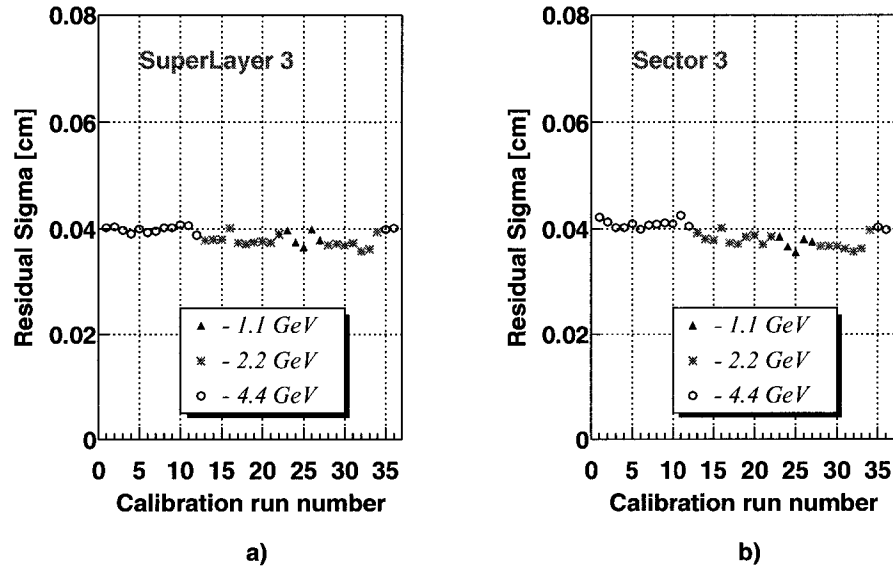
FIG. 29. Resolution versus calibration run number. *a*) Superlayer 3 averaged for 6 sectors *b*) Sector 3 averaged for 6 superlayers. Different markers correspond to different beam energies of the runs. Calibration run number corresponds to the time of data taking (covers each day of the running period).
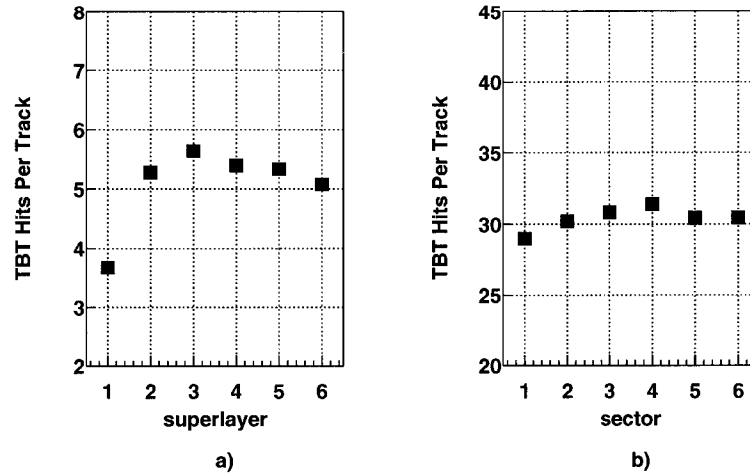
FIG. 30. Hits per track. Hits per track are shown versus *a*) superlayer averaged over 6 sectors *b*) sector averaged over 6 superlayers; both *a*) and *b*) are averaged over 36 calibration runs.
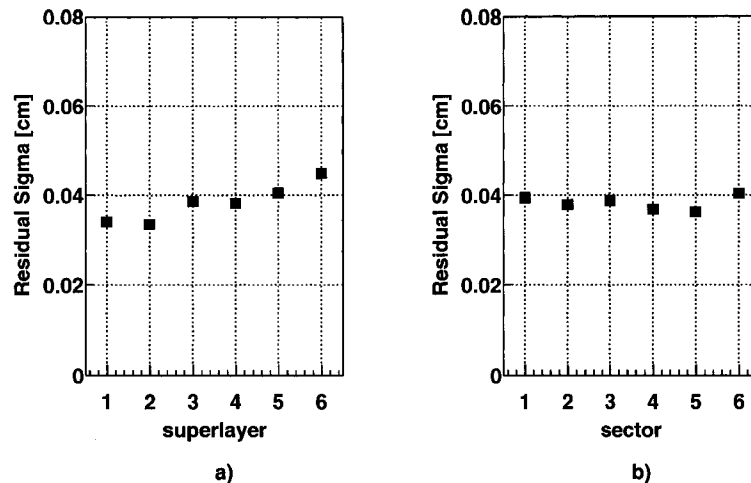
FIG. 31. Drift chamber resolution. Resolution is shown versus a) superlayer averaged over 6 sectors b) sector averaged over 6 superlayers; both a) and b) are averaged over 36 calibration runs.

for Superlayer 3 averaged for 6 sectors and for Sector 3 averaged for 6 superlayers. Different symbols on the plots correspond to different beam energies of the calibration runs. There is a slight dependence of the resolution on the beam energy. Figure 30 shows the TBT hits per track as a function of superlayer number and sector number averaged over all calibration runs. Superlayer 1 has fewer hits per track because it has only 4 layers. Figure 31 shows the drift chamber resolution as a function of superlayer number and sector number averaged over all calibration runs.

3.1.3 Time of Flight Calibration

The ability of the CLAS to distinguish between different types of the charged particles is based on the information derived from tracking and scintillator counters. That information is crucial for studying multihadron final states. Therefore, TOF system calibration is very important for particle recognition. The procedure of TOF calibration consists of 10 steps as shown in Table V. The calibration steps are shortly described below:

1) The ADC thresholds are called pedestals and were measured by taking data with a dedicated DAQ configuration. The data were analyzed online and the resulting constants were saved into the calibration database.

TABLE V. The TOF calibration procedure steps.

CALIBRATION STEP	REQUIRES
1 Pedestals	dedicated data
2 TDC calibration	dedicated data
3 Time-walk correction	laser data
4 Left-right alignment	raw data
5 Energy loss	L-R time alignment at SC BOS-bank level
6 Attenuation length	L-R time alignment at SC BOS-bank level
7 Effective velocity	all of the above and good TBT
8 RF parameters	all of the above
9 Paddle-to-paddle delays	all of the above
10 RF offsets	all of the above

2) All TDC channels were pulsed and the response of the TDC for different delays between the START and STOP signals were analyzed. Calibration parameters were obtained by fitting channel versus time distribution with a quadratic function.

3) Time-walk is an instrumental shift in the time measured using a leading-edge discriminator that is due to the finite time-rise in the analog pulse. Time-walk corrections as a function of pulse height were obtained for each PMT separately using laser calibration data.

4) Establishing the left-right signal time offsets is crucial for hit position identification in the scintillator paddle. The left-right alignment is the correction for different time delays of the signals from left and right ends of the scintillators.

5) 6) In order to be able to separate pions from protons without relying on timing information we calibrate the energy deposited in the scintillator material and the attenuation length for each scintillator counter.

7) Effective velocity and time offset corrections are applied in order to match the hit position along the length of the scintillator determined by tracking with the timing information from the left and right tubes of the scintillator paddle.

8) 9) 10) The RF signal from the accelerator is generated for every electron bunch with frequency of $\nu_{acc} = 1.497$ GHz at the CEBAF injector (see Section 2.1) and sent to the three experimental halls with a prescale factor of 40. Each CLAS trigger is caused by an electron from one of these bunches (each beam bucket is ≈ 2 ps wide and
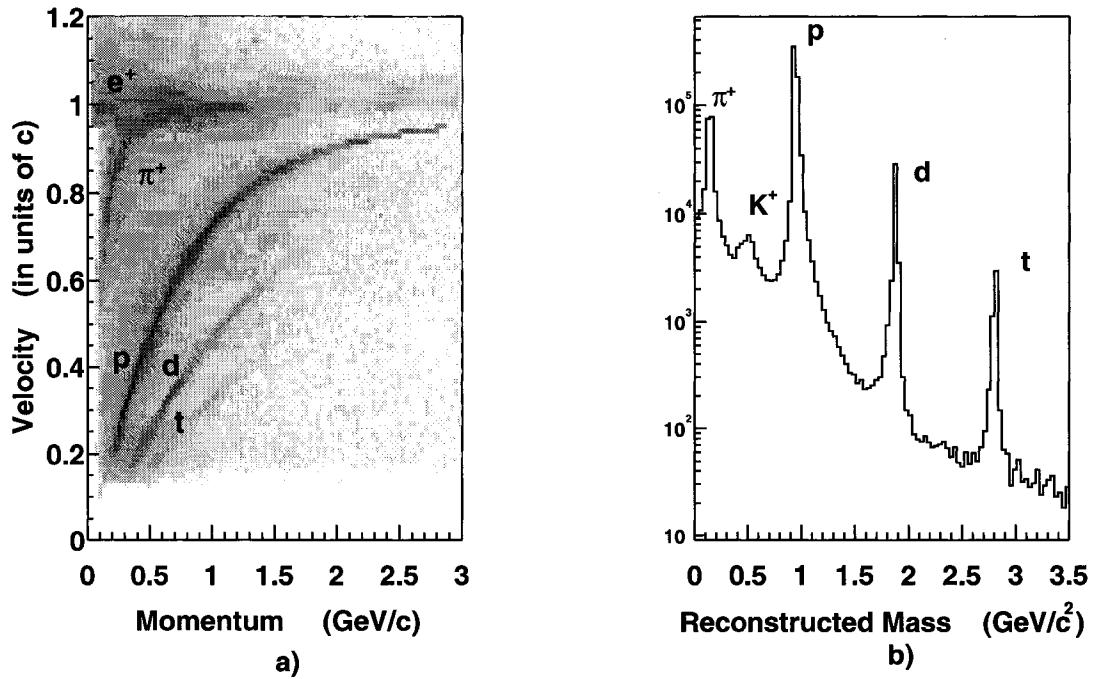
FIG. 32. Particle identification quality check for Al(e,e′X) events. a) Plot of reconstructed velocity versus momentum for positive tracks. b) Reconstructed mass spectrum for positive tracks. The proton and pion bands are reliably separated.

spaced every 2 ns). In order to align the time measured by the scintillator counter with the corresponding RF signal, RF parameters, paddle-to-paddle corrections and RF offsets are determined during the calibration. More details on this subject can be found in [71] and [72].

The purpose of TOF calibration procedures is to allow the CLAS offline analysis software to distinguish between different types of hadrons and select different multi-particle final states by using missing mass techniques. The timing resolution determined by the TOF calibration directly affects the level of non-physical background of the selected final states. The quality of the TOF calibration can be seen from the dependence of the velocity of the particle on its momentum and reconstructed particle's mass distribution (see Eq. 1) from empty target runs measured at 2.2 GeV electron beam energy (see Fig. 32). The electrons are scattered by the aluminum walls of the target cell on these plots. As seen from Figure 32 a) the pion and proton bands are reliably separated. In addition to the proton and pion peaks

one can see peaks due to deuterons and tritons as well.

3.1.4 Electromagnetic Calorimeter Energy Calibration

The EC energy calibration was done by Cole Smith using the cosmic rays. See [75] for details.

3.1.5 Electromagnetic Calorimeter Time Calibration

The Electromagnetic Calorimeter (EC) time calibration is crucial for detection of neutral particles (photons and neutrons). Good EC timing is important because it allows us to discriminate between photons and neutrons, and to calculate the neutron kinetic energy.

We use electron time measured by TOF counters to calibrate the EC time measurements [73]. EC time is given by:

$$t_{EC} = t_{TOF} + \frac{d_{SCEC}/\cos\alpha}{c}, \tag{7}$$

where t_{TOF} is the arrival time of the electron measured by the TOF, t_{SCEC} is the distance between TOF and EC layers,[3] c is the electron velocity which is close to the speed of light, and α is the impact angle to the EC plane (see Fig. 33 a)).

The value t_{EC} is assigned to the EC scintillation bar with the largest ADC pulse height for each of the three views, exactly the same way as it is done in the reconstruction code. The time dependence is fitted with the function:

$$t_{EC} = p_0 + p_1 \cdot tdc + \frac{p_2}{\sqrt{adc}} + p_3 \cdot l^2 + p_4 \cdot l^3 - \frac{l}{v_{eff}}, \tag{8}$$

where p_i are five fit parameters, tdc and adc are the TDC and ADC values, l is the length from the hit point to the readout edge, and v_{eff} is the speed of light in the scintillator. The first two terms are the simple linear TDC response, the third term is the time-walk correction, the fourth and fifth term are small corrections for the fact that signals arrive at the readout edge at slightly different times for scintillation bars connected to the same PMT, and the last term compensates for the time for scintillation light to travel to the readout edge.

The difference between the reconstructed EC time and the TOF time which defines our time resolution for electrons is shown in Figure 33 b). The overall resolution

---

[3]electron track is straight since there is no magnetic field between the TOF and EC detectors
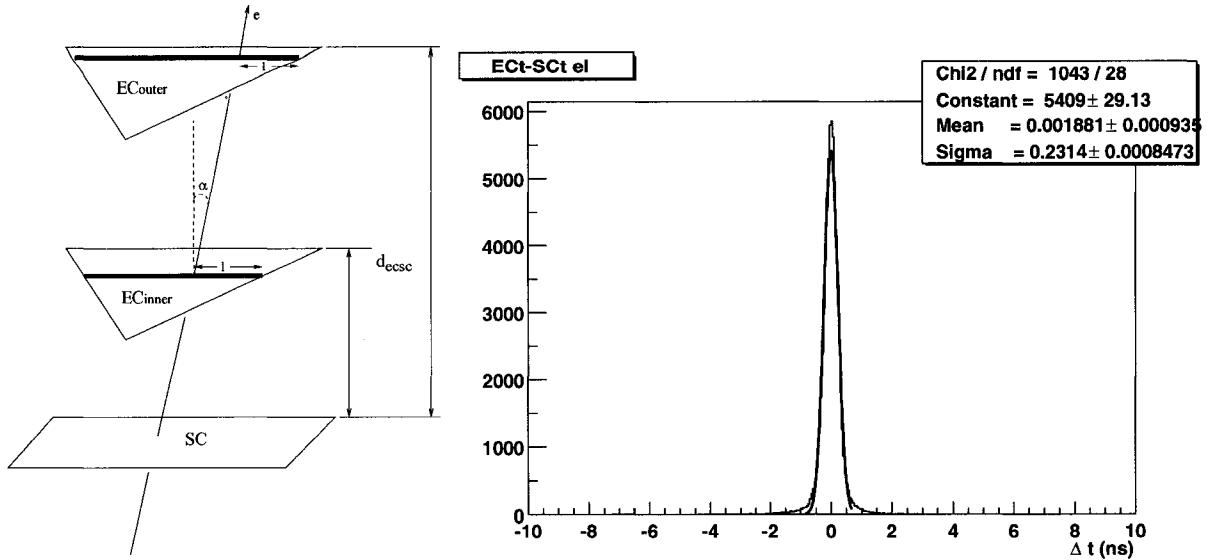
FIG. 33. EC time extrapolation and EC time resolution. a) EC time extrapolation from the TOF time. Only the scintillation bar with the largest ADC value in one view for each EC layer is shown. b) EC time resolution for electrons in sector 1 [73].

(including TOF resolution) is $\sigma \approx 250$ ps. Assuming the TOF time resolution to be $\sigma_{TOF} \approx 150$ ps, we may determine the EC time resolution $\sigma_{EC} = \sqrt{\sigma^2 - \sigma_{SC}^2} \approx 200$ ps. More details on that subject can be found in [73].

3.2 PASS 1 PROCESSING

After we finished calibrated all the subsystems, we performed the final step: "pass 1" processing. This is a production analysis pass through the data with final calibrations. This analysis includes the determination of the particle trajectories and preliminary particle identification. All runs which might have good data from the list of the raw data files were processed during this step with no selection criteria. A master Perl script was used to perform the production processing and construct an off-line MySQL database. For each raw data file a single job was launched on the JLAB batch farm. In each job a raw data file was analyzed by RECSIS (release-1-28), the CLAS reconstruction software, and output files were produced. We had three output file formats: CLAS standard BOS ("cooked files"), and condensed PAW Ntuple and Root Tree Structure formats. The structure of the Root Tree Classes used in E2a is shown in Appendix A.
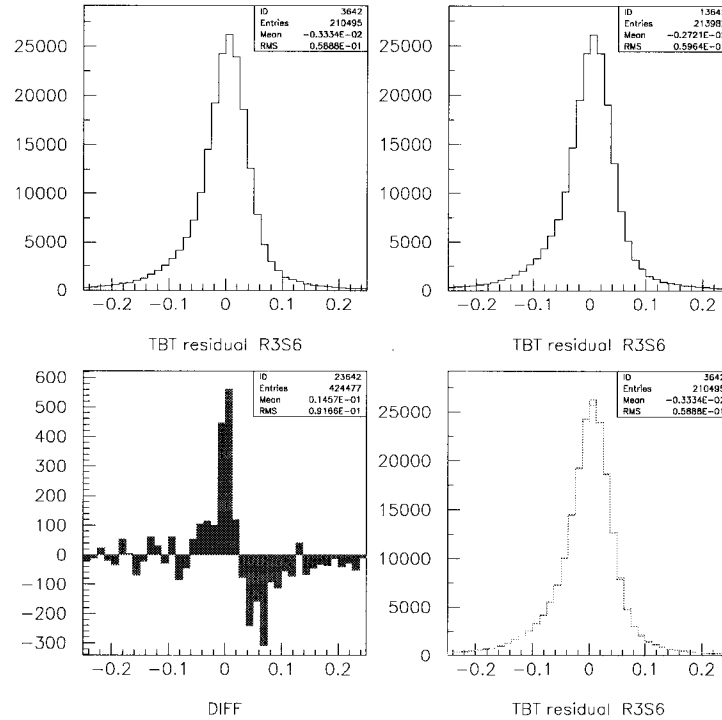
FIG. 34. Data quality monitoring plots. Example of the comparison of two good files. Upper plots are TBT residual distribution in Region 3 Sector 6 for two different production files. Left bottom plot is a normalized difference and the right bottom plot is the normalized overlay of the two histograms.

3.2.1 Selecting Good Runs

The selection of runs suitable for physics analysis ("Good runs") was based on run summary records and the logbook with the records made during the data taking. Some of the raw data files were eliminated due to bad run conditions (DC trips or mulfunctioning of the high voltage system of the EC which causing the drop of the trigger rate) or low number of events (fewer than 50000 events).

3.2.2 Data Quality Monitoring

Data quality monitoring was performed during the "pass 1" processing. The monitoring included checking run stability by looking at quantities such as single particle yields, hits per track, ratio of HBT to TBT, etc and comparing these to the selected monitoring histograms. For detailed comparison of the histograms we used the program "TESTER", written by Andi Klein. This program allows us to compare a large number of histograms in an automatic way and to flag all histograms which are different from the nominal value. Some of the runs that "TESTER" flagged were fixed later. For example, the electron z-vertex distribution for ^{3}He runs 18405, 18460 and 18520 was shifted from the observed average value due to the 0 mini torus current setting during the cooking procedure. We determined and applied shifts to z-vertex for these runs in our analysis. About 400 distributions for each file were monitored, reflecting the stability of histograms that involve particle identification (SEB), tracking of the electrons and protons, response from drift chambers, scintillator counters and electromagnetic calorimeter. One of the monitored quantities - TBT residual for the Drift Chamber Region 3 Sector 6 and comparison with another production file is shown in Figure 34. Totally about 10% of the data were eliminated due to mulfunctioning of the detectors, low number of events, and reconstruction or monitoring failure.

3.3 PARTICLE IDENTIFICATION

3.3.1 Electron ID

Electron identification is one of the key issues in electron scattering experiments with the CLAS, where the electron is the trigger particle and proper electron ID based on precise time information is required for proper event reconstruction. The pion contamination appears to be a main source of the electron misidentification.

CLAS electron identification at the trigger level is done by requiring a minimum amount of energy in the EC in coincidence with a signal in the CC (used for runs at 2.2 GeV only). In the off-line analysis some additional requirements were used to select events with a good electron. Electron ID has two steps:

1) Preliminary ID by RECSIS/SEB (Simple Event Builder in the framework of the

TABLE VI. Cuts for the geometrical matching of detector elements to identify electron tracks. TRK – track information.

Matching	Tolerance
TRK × EC	30 cm
TRK × CC	5°
EC × CC	5°

CLAS reconstruction code). Preliminary ID determination is based on the comparison of the velocity measured by DC and velocity, determined from TOF measurements [77, 78].

2) Further ID in TE2AnaTool (E2 run analysis software)

1) The initial requirement for selecting electrons is a negative track matched to a showering hit in the EC. Electrons, unlike hadrons, will shower electromagnetically and deposit all of their energy in the EC. SEB requires that the EC and SC hits are geometrically matched with a track reconstructed in the drift chambers. The values of the geometrical cuts in SEB are given in Table VI [78]. Note that SEB assignes ID=11 and ID=0 to electron candidates that pass and fail, respectively the cuts. We analize both ID=11 and ID=0 particles.

2) We cut on the energy deposited in the EC by the trigger particle to further identify electrons. The sampling fraction cut on EC was applied to make sure that the matched hits are caused by an electron, and are not due to accidental background. The sampling fraction is the fraction of electromagnetic shower energy deposited in the EC that is detected as scintillation light. This depends on the details of the lead/scintillator sandwich and is mostly constant (≈ 0.27 for CLAS) above 0.2 GeV, but drops sharply below this energy. The total energy deposited in the calorimeter can be calculated either considering the entire EC as a single module and calculating the total energy or adding the deposited energies in the inner and outer layers to obtain the total energy. Both methods give approximately the same result. In our experiment we compare both results and we use the larger value as the total energy deposited in the EC. The distribution of the total energy deposited in the calorimeter for identified electrons at 2.2 GeV versus their momentum is shown in Figure 35 a). We apply a 3σ cut derived from that distribution to eliminate pion contamination.

1
0.9
0.8
0.7
E{tot} (GeV) 0.6
0.5
0.4
0.3
0.2
0.1
0
0   0.5   1   1.5   2   2.5
Momentum (GeV/c)
a)

1
0.9
0.8
0.7
E{tot} (GeV) 0.6
0.5
0.4
0.3
0.2
0.1
0
0   0.5   1   1.5   2   2.5
Momentum (GeV/c)
b)
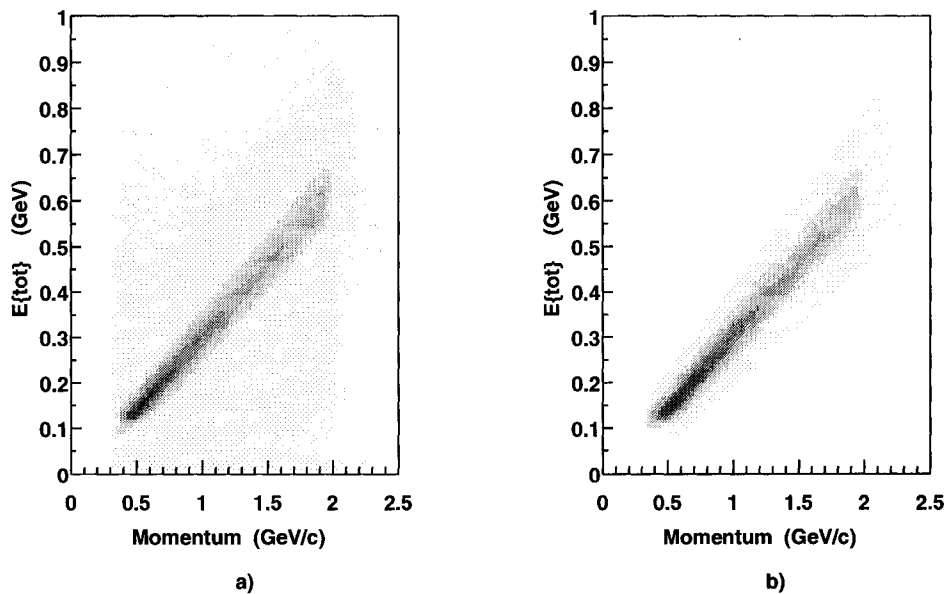
FIG. 35. Total energy deposited to calorimeter. Total energy deposited to calorimeter versus momentum of the electron is shown for ^{3}He data at 2.2 GeV. a) Before 3σ cut was applied b) After 3σ cut was applied.

The cut is determined by the fit of the electron band:

$$E_{tot}^{lower}(p_e) < E_{tot}(p_e) < E_{tot}^{higher}(p_e) \tag{9}$$

where p_e is the electron momentum and $E_{tot}^{lower}(p_e)$ and $E_{tot}^{higher}(p_e)$ are lower and higher limits of the cut at reconstructed momentum p_e. These quantities are parametrized as $a^i + b^i \cdot p_e$ with four fit constants. The distribution of the total energy deposited to the calorimeter versus the momentum of the reconstructed electron with the applied 3σ cut is shown in Fig. 35 b).

To eliminate the non-showering minimum ionizing particles (pions), we also require a 55 MeV threshold on the energy deposited in the inner layer of the calorimeter. For 4.4 GeV runs, we also required $E_{tot} > 0.33$ GeV and electron momentum $p_e > 1.1$ GeV due to the higher calorimeter threshold (see Figure 36). Note that we do not apply software cuts on Čerenkov Counters assuming that applying hardware cuts on CC would be enough for electron identification.
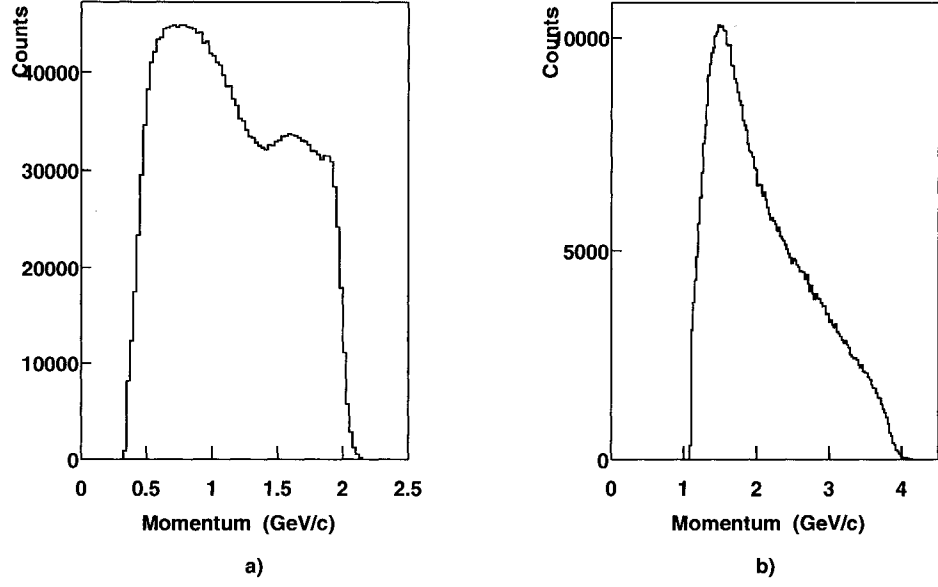
FIG. 36. Momentum of the electrons. a) 2.2 GeV data b) 4.4 GeV data. Note the higher calorimeter threshold at 4.4 GeV.

3.3.2 Proton ID

Hadron identification in CLAS uses the particle's momentum and time of flight to reconstruct its mass (see Eq. 1).[4] The reconstructed velocity versus momentum and the reconstructed mass distributions for positive tracks were shown in Figure 32. We are selecting the mass that gives us the velocity calculated from proton's momentum $\beta_{calculated} = p/\sqrt{(p^2 + m^2)}$ to be close to the velocity measured by the TOF system $\beta_{measured}$. To identify protons and eliminate background we apply a 3σ cut requiring:

$$|\beta_{measured} - \beta_{calculated}| < 3\sigma \tag{10}$$

where σ is the proton band deviation around its mean value at each momentum. The distribution of the velocity of the protons versus their momentum for 2.2 GeV is shown in Figure 37.
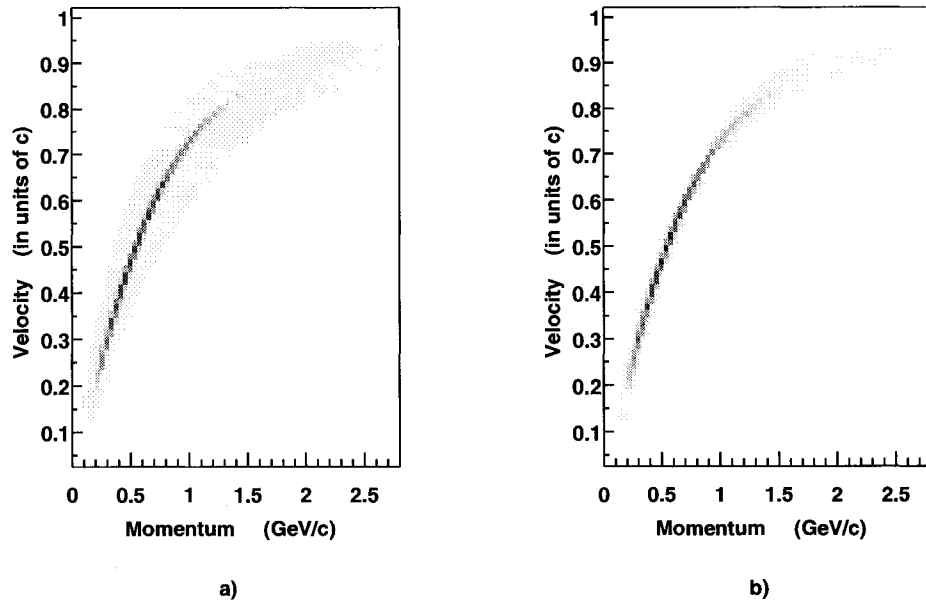
FIG. 37. Velocity measured by the TOF system versus momentum of the protons measured by drift chambers. The data shown is ^{3}He at 2.2 GeV. a) Before 3σ cut was applied b) After 3σ cut was applied.

3.4 ELECTRON MOMENTUM CORRECTIONS

The calculation of the momentum of the particles is based on the drift chamber tracking measurements and the torus magnetic field. Due to the limitation of our knowledge about the precise drift chamber location and the precise torus magnetic field we expect some small deviations of the physics quantities. The existing CLAS data show a systematic shift of the reconstructed electron momentum relative to the expected one in the case of kinematically complete events from H(e,e'p). For elastic kinematics the fixed value of missing mass $W = 0.938$ GeV allows us to correct the momentum of the electron, assuming that electron scattering angles are measured precisely. The main assumption is that the wrong W position of the elastic peak is due to the wrong electron momentum, while the electron angles, θ_e and ϕ_e, are correct. Based on this assumption, the expected momentum for the electrons in the elastic region is calculated starting from the measured theta angle and assuming

---

[4]Note that the momentum of the particle is measured by drift chambers and the time-of-flight is measured by the TOF system.
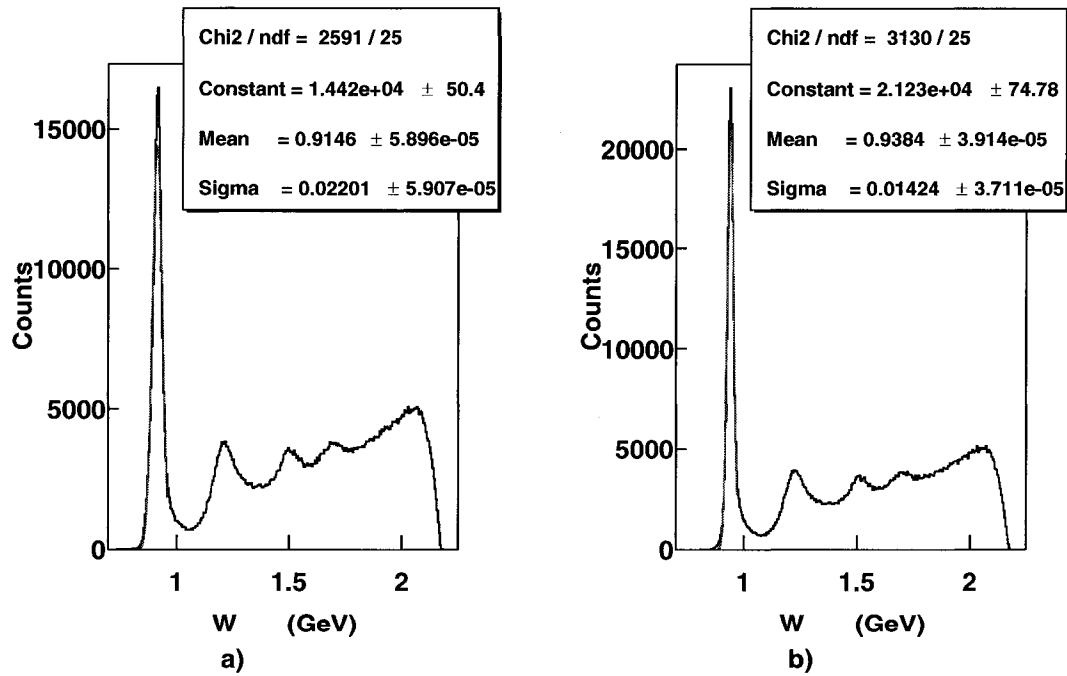
FIG. 38. W distribution from E1b hydrogen data. W distribution, corresponding to hydrogen data, measured at 2.567 GeV beam energy, 2250 A torus current during E1 data taking. a) Without electron momentum corrections b) With electron momentum corrections.
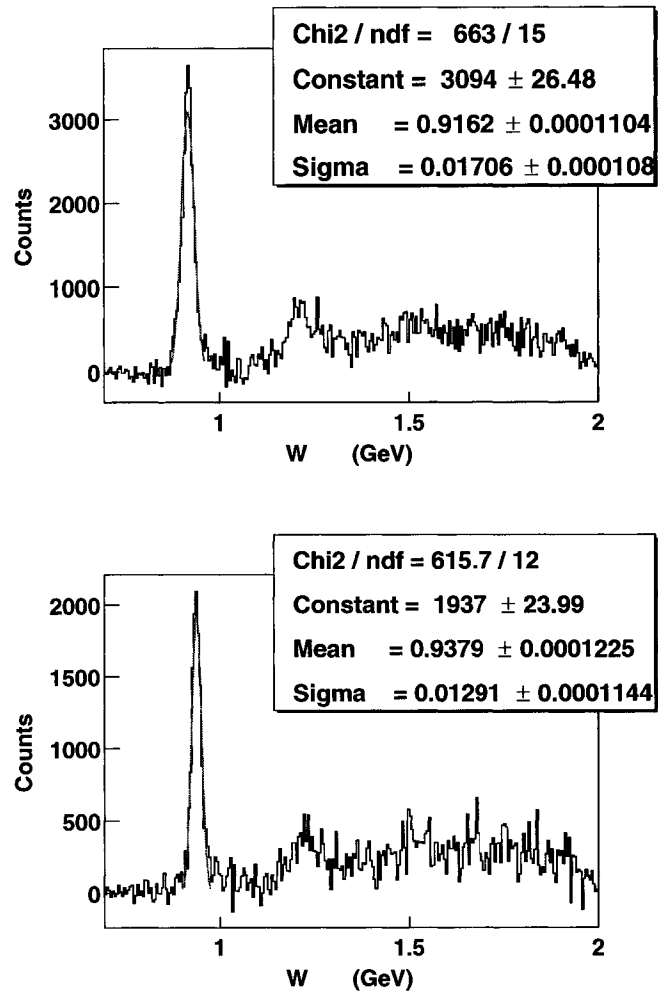
FIG. 39. W distribution for H(e,e'p) from E2a data. Beam energy is 2.2 GeV, torus current is 2250 A. Top plot is the difference between CH_2 and ^{12}C(e,e'p) with no corrections applied. Bottom plot is the difference between CH_2 and ^{12}C with electron momentum corrections. Note the final improvement of the peak position and width (mean = 0.938 GeV, $\sigma = 13$ MeV). Both plots are arbitrarily normalized.

that the correction can be factorized in a θ_e and ϕ_e dependent function. The ratio between the calculated momentum and the measured one is then evaluated and the corresponding correction extracted. The uncorrected data are shifted by about 23 MeV (see Fig. 38 a). For electron momentum corrections we used elastic events from hydrogen data, measured by the E1 group about a month before we started the E2 run. The electron momentum correction method and results for 2.2 GeV and 4.4 Gev data are described in detail in [73] and [79], respectively. An empirical expression was used to fit the data. The average size of the correction factor is about 1.001. The corrected hydrogen data distribution is shown in Figure 38 b). As a result, the elastic peak was shifted to the expected position and the width of the peak significantly improved from 22 MeV to 14 MeV, which is the energy resolution of CLAS. We also checked the electron momentum correction function using H(e,e'p) extracted from the difference of CH_2(e,e'p) and ^{12}C(e,e'p) data measured in E2. The results are shown in Figure 39.

Another test was done to check how electron momentum corrections derived from elastic data would work at lower momenta. We looked at the missing mass distribution from H(e,e'π^+) where we expect to see a peak at the neutron mass (see Fig. 40). The corrections shift the peak to the right position and improve the width of the peak. Note that we do not correct the momentum of the protons because proton momenta are lower compared to electron momenta and we do not expect that could improve much our resolution.

3.5 PROTON ENERGY LOSS CORRECTIONS

Proton momenta need to be corrected for the energy losses of the protons in the target material. We used the CLAS GEANT Monte Carlo simulation (GSIM) [76] to simulate the proton energy loss in CLAS which allowed us to extract the correction function. We generated (e,e'p) events with $\omega = 1.25$ GeV, $\theta_e = 30°$, $\phi_e = 0°$ in each sector and distributed uniformly in p_p and Ω_p. Protons were generated within the fiducial volume of the detector.

Then we ran these events through GSIM to simulate the CLAS environment [5] and produce a set of files analogous to our raw data. We used the GSIM post processor (GPP) routine to remove the dead wire and photo-tube channels corresponding to our real data. We also used GPP to smear the simulated events to better simulate

---

[5]Natasha Dashyan implemented E2a targets in GSIM
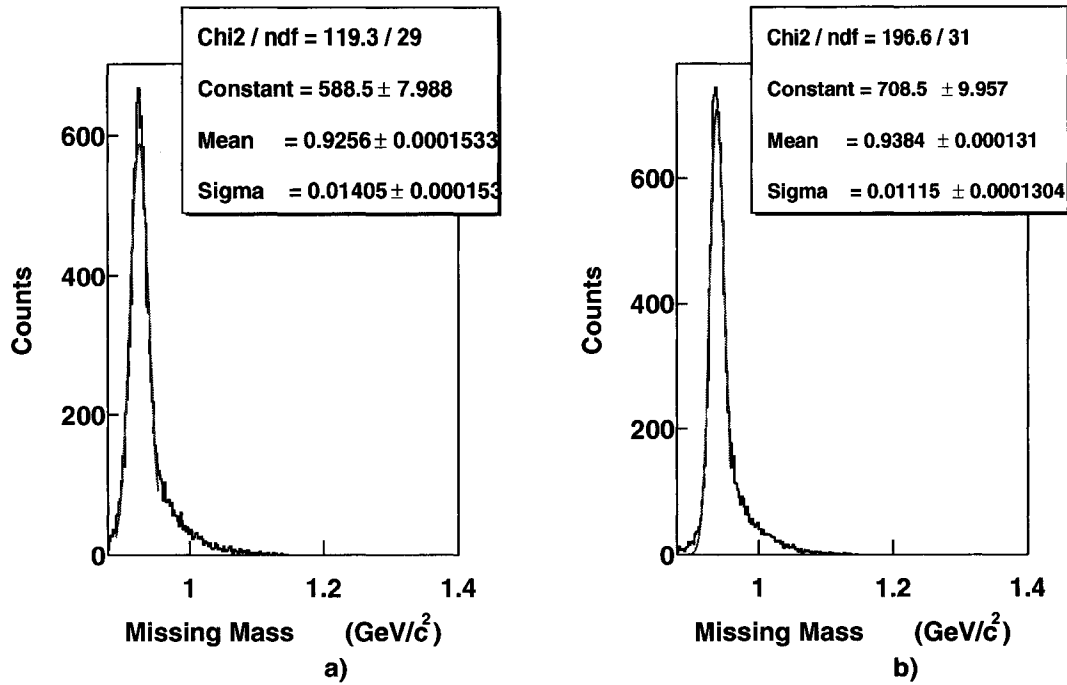
FIG. 40. H(e,e'π^+) missing mass distribution. a) Before electron momentum correction was applied a) After electron momentum correction was applied.

the detector resolution. Next the files were processed by the same reconstruction software and analyzed the same way as we treated the data. The comparison between generated and reconstructed protons gives information about the energy loss of the protons in the target. Figure 41 shows a) the difference between the generated and reconstructed momenta, $P_{gen} - P_{rec}$, versus reconstructed momentum and c) the ratio of $P_{gen} - P_{rec}$ to the reconstructed momentum for the ^{3}He target at 2.2 GeV beam energy and 2250 A torus current. The distribution in Figure 41 a) was fitted by a polynomial to derive the correction function. As one can see from the plot mostly low momentum protons need to be corrected. The same distribution with applied corrections is shown in Fig. 41 b). Figure 41 d) shows the improvement of the corrections. There are 50 MeV/c corrections at lowest proton momentum. This correction function also improved the missing mass distribution for ^{3}He(e,e'pp) using the Plane Wave Impulse Approximation (PWIA) model generator (see Section 5.4.2). Figure 42 shows the effect of corrections applied to the proton that shifts the missing
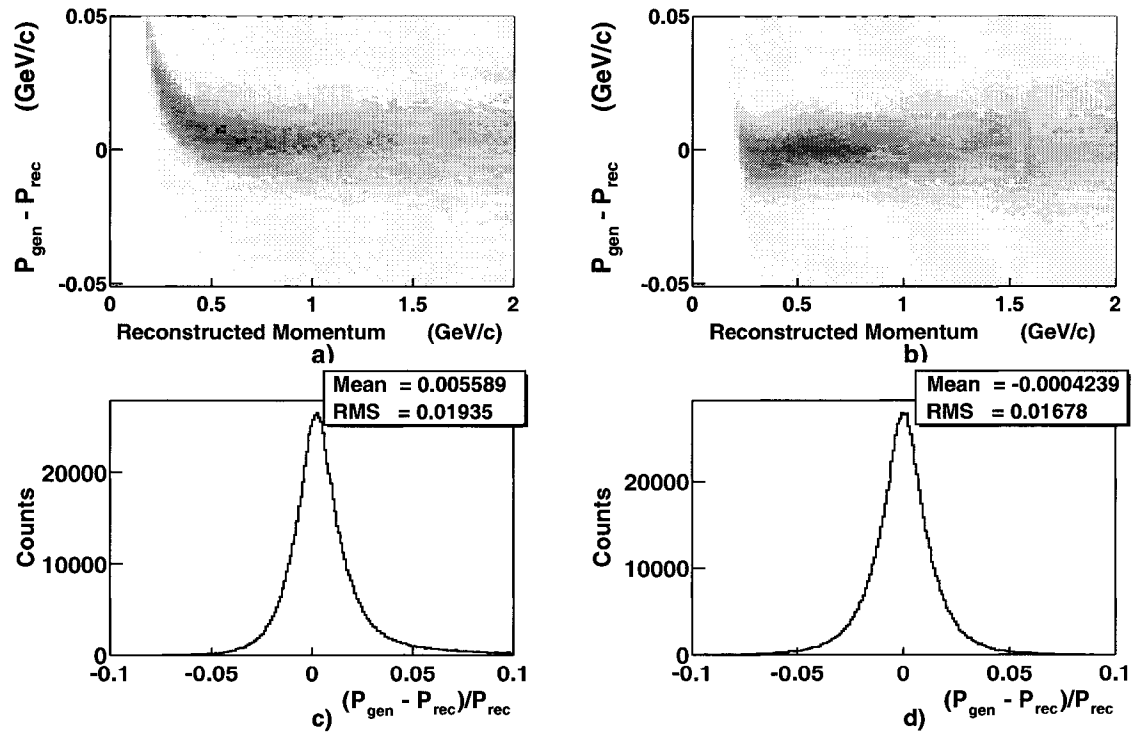
FIG. 41. The proton energy loss correction distributions. a) The uncorrected momentum difference of the generated and reconstructed protons versus reconstructed momentum for ^{3}He at 2.2 GeV. c) The ratio of uncorrected momentum difference to the reconstructed momentum. b) and d) are the same as a) and c), but with proton energy loss correction applied.

mass peak to the right position. Figure 43 shows the ^{3}He(e,e'pp) missing mass distribution from data at 2.2 GeV. The peak with applied proton energy loss corrections Figure 43 b) is about 2.5 MeV/c^2 off from the expected value which is about 6 times less than the CLAS resolution.
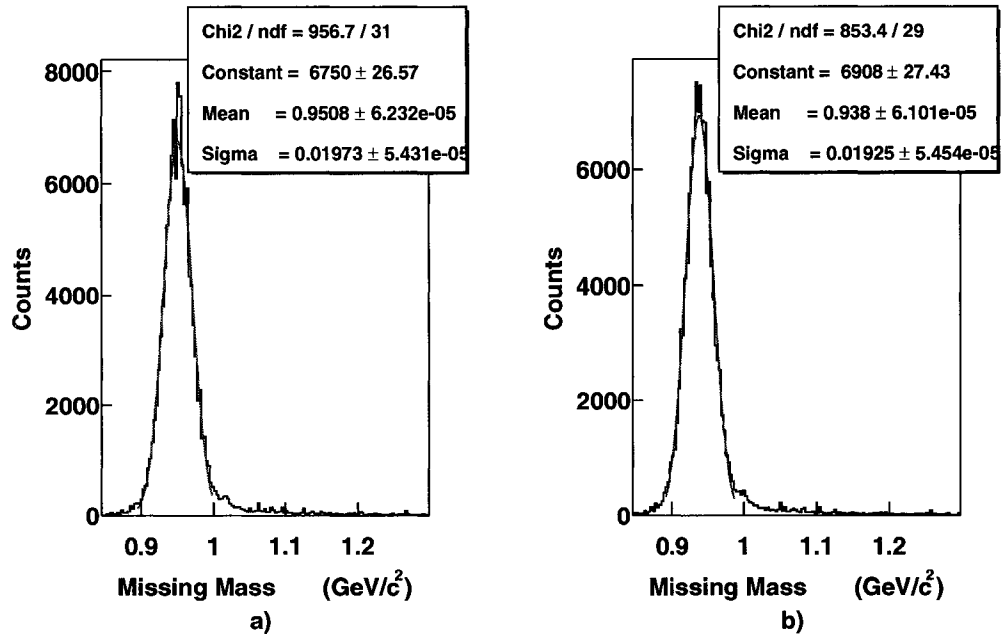
FIG. 42. Missing mass of two reconstructed protons from simulation. Missing mass is obtained from ^{3}He(e,e'pp)n GSIM Monte Carlo simulation at 2.2 GeV a) Before proton energy loss corrections b) After proton energy loss corrections.

3.6 FIDUCIAL CUTS

The purpose of the geometrical fiducial cuts is to select the regions of the detector where the acceptance is flat. Due to the complicated structure of the CC and EC, the particle detection efficiency varies rapidly near the edges of the detectors and is not well understood there. In order to determine the regions with uniform detection efficiencies in (θ,ϕ,p) space the fiducial cuts were developed.

3.6.1 Electron Fiducial Cuts

The calorimeter efficiency decreases near the edges due to shower leakage and geometrical effects. Therefore we cut on the edges of the EC. Electromagnetic calorimeter
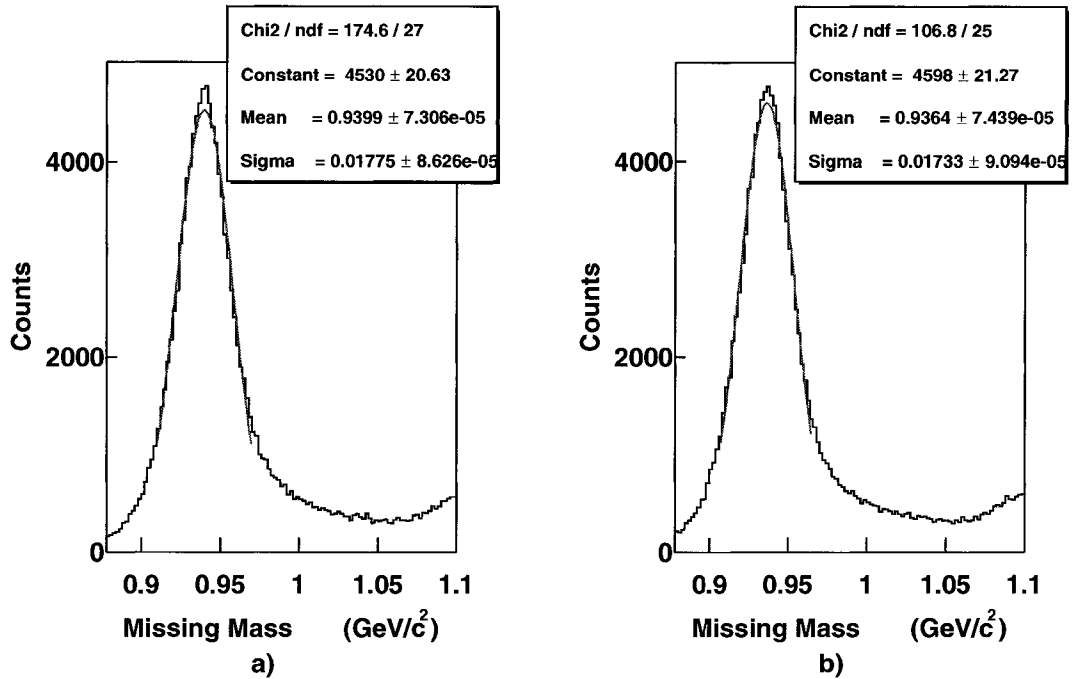
FIG. 43. Missing mass of two reconstructed protons from ^{3}He(e,e'pp) data at 2.2 GeV a) Before proton energy loss corrections b) After proton energy loss corrections.

U, V and W coordinates of the electrons detected by EC in sector 6 and EC edge cuts are shown in Figure 44, where the electrons were selected according to Section 3.3.1.

The fiducial cuts for electrons were determined for different bins in electron momentum. For 2.2 GeV, we plotted θ versus ϕ angular distributions for each sector and each 50 MeV/c momentum bin. Angular distributions in sector 6 for two different momentum bins (1.050 and 1.675 GeV/c) are shown in Figure 45 a) and c). These distributions were sliced in θ to make a number of ϕ distributions at fixed momentum and θ (Fig. 46). As one can see from Fig. 45 a), c) and Fig. 46, efficiency still drops on the edges. The ϕ distribution for each θ and momentum bin and each sector was fitted with a trapezoid function to determine the flat acceptance regions of CLAS. That information was parameterized and a smooth function which selects the fiducial regions was developed. Figure 45 b) and d) show the effect of the fiducial cuts applied to the data. Electron fiducial cuts at 2.2 GeV are discussed in detail in [73]. The functional form of the fiducial cuts is given in Appendix B.0.1.

Note that fiducial cuts include the cuts eliminating bad scintillator paddles. These
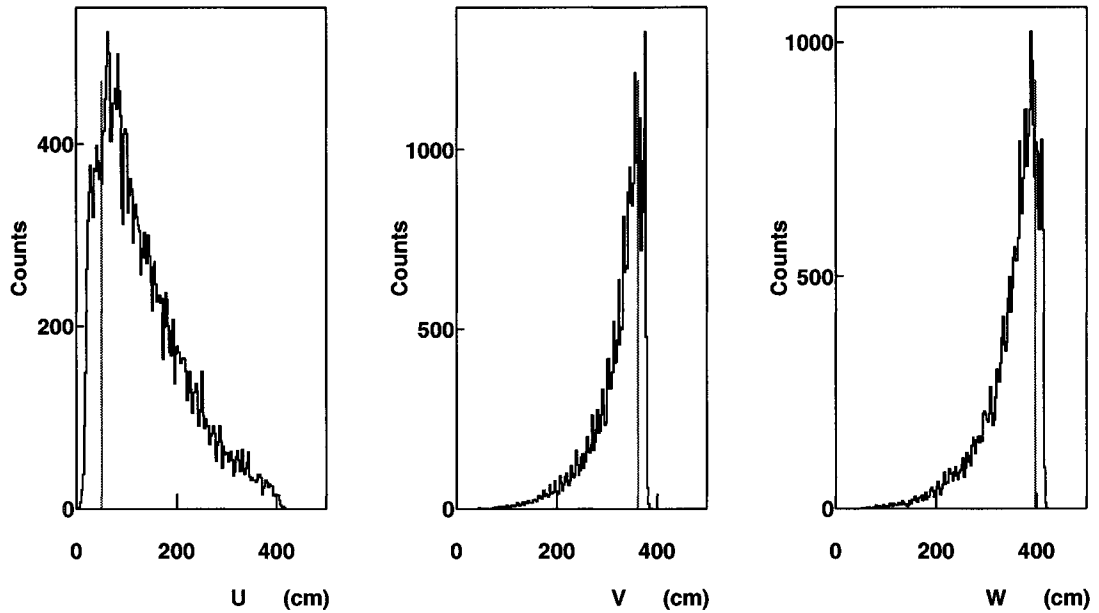
FIG. 44. Range of the calorimeter U, V and W coordinates. Only sector 6 is shown. The line in each plot shows the position of the EC edge cut.

are the scintillation counters that were mulfunctioning during the data taking. For the purpose of phase space calculation, we had to cut off the entire theta range covered by the single bad scintillation counter. We determined the theta cuts that eliminate bad paddles by fitting the lower and upper position of the gaps as a function of electron momentum. Figure 47 a) shows the θ versus ϕ distribution for the electrons in Sector 5 at $P_{el} = 1.050$ GeV/c without bad scintillation counters knockout. Figure 47 b) shows the same as a), but with bad scintillation counters knockout.

Electron fiducial cuts for 4.4 GeV runs are done similarly as for 2.2 GeV and described in [80]. The parameters and functions of these cuts are given in Appendix B.0.2.

3.6.2 Proton Fiducial Cuts

Geometrical fiducial cuts for protons were defined the same way as for electrons. The detailed procedure of deriving the fiducial cut function for 2.2 GeV and 4.4 GeV data and results are given in [81] and [82], respectively. See Appendix C for a description
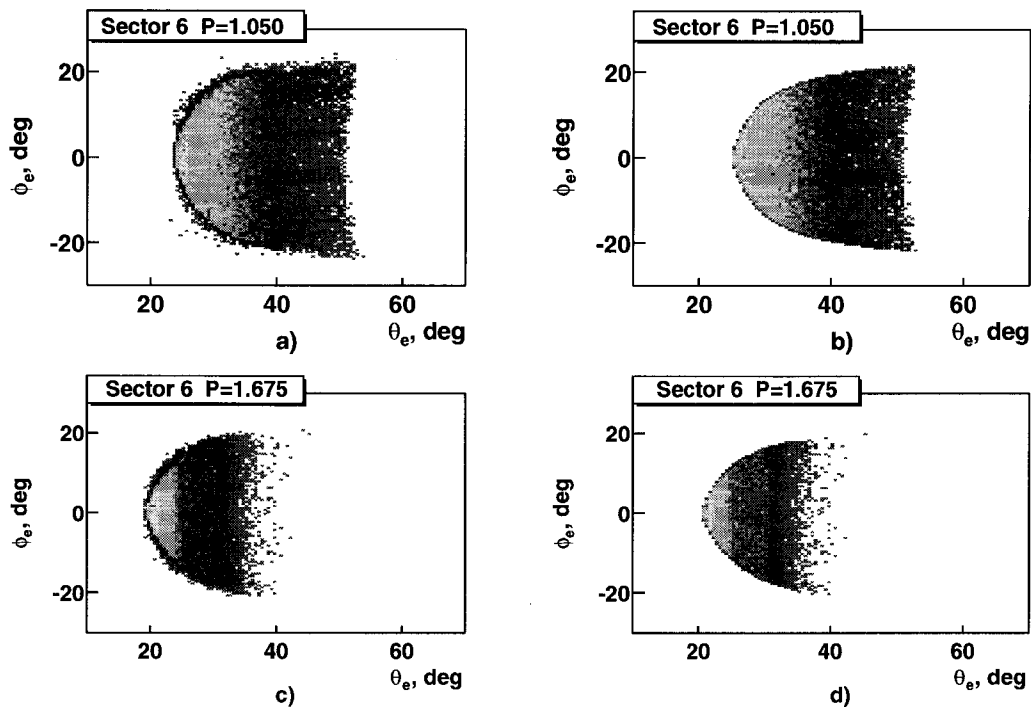
FIG. 45. θ_e versus ϕ_e angular distribution. Only Sector 6 for two electron momentim bins measured at $E_{beam} = 2.2$ GeV is shown. a) and c) are angular distributions with no fiducial cut; b) and d) with fiducial cut. a), b) are at $p_e = 1.050$ GeV/c and c), d) are at $p_e = 1.675$ GeV/c.

of the method used in [82]. The parameters and functions of the proton fiducial cuts are given in Appendix B.0.3 and B.0.4 for 2.2 and 4.4 GeV data, respectively.

3.7 VERTEX CUTS

The purpose of the vertex cut is to select the reactions that occur within the target cell. During the E2 run, vertex coordinates were determined from the multiparticle fit of the beam position which is a least squared fit of the vertex location to minimize the distance to each track. The X and Y coordinates of the beam were determined on run by run basis. After that, vertex coordinates were fitted to the beam line. Z vertex is the Z coordinate of the reaction vertex. The electron Z vertex distributions from the data and Monte Carlo simulation (using the PWIA event generator) and cuts for the ^{3}He target at 2.2 GeV and 4.4 GeV are shown in Figure 48. Z vertex cut values $(-3.3, 0)$ cm defined from these distributions are the same for both beam
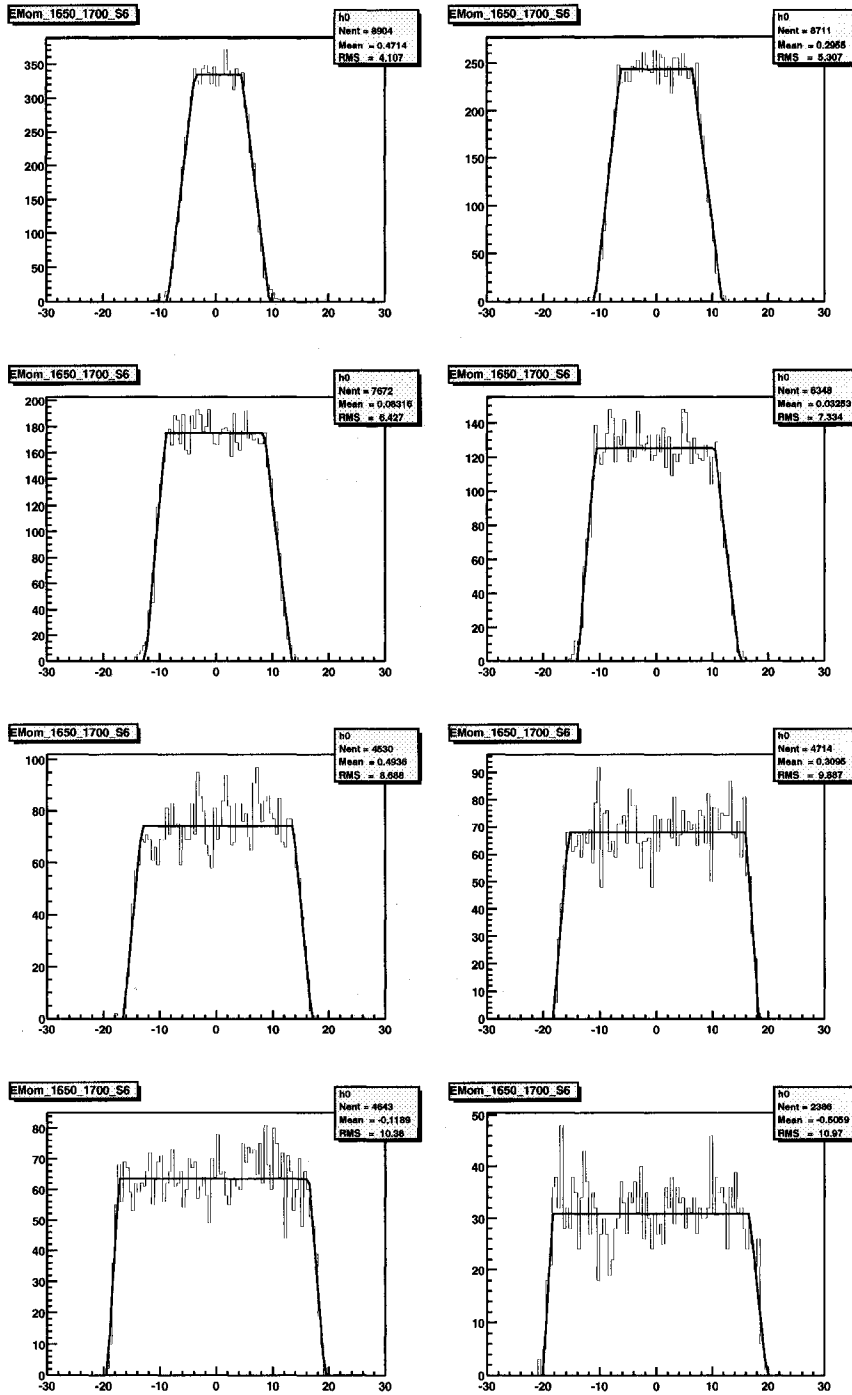
FIG. 46. ϕ distribution of the electrons and trapezoid function fits. 8 different θ bins in sector 6 at momentum 1.675 GeV/c for 2 GeV data are shown. The top defines our "flat" region.
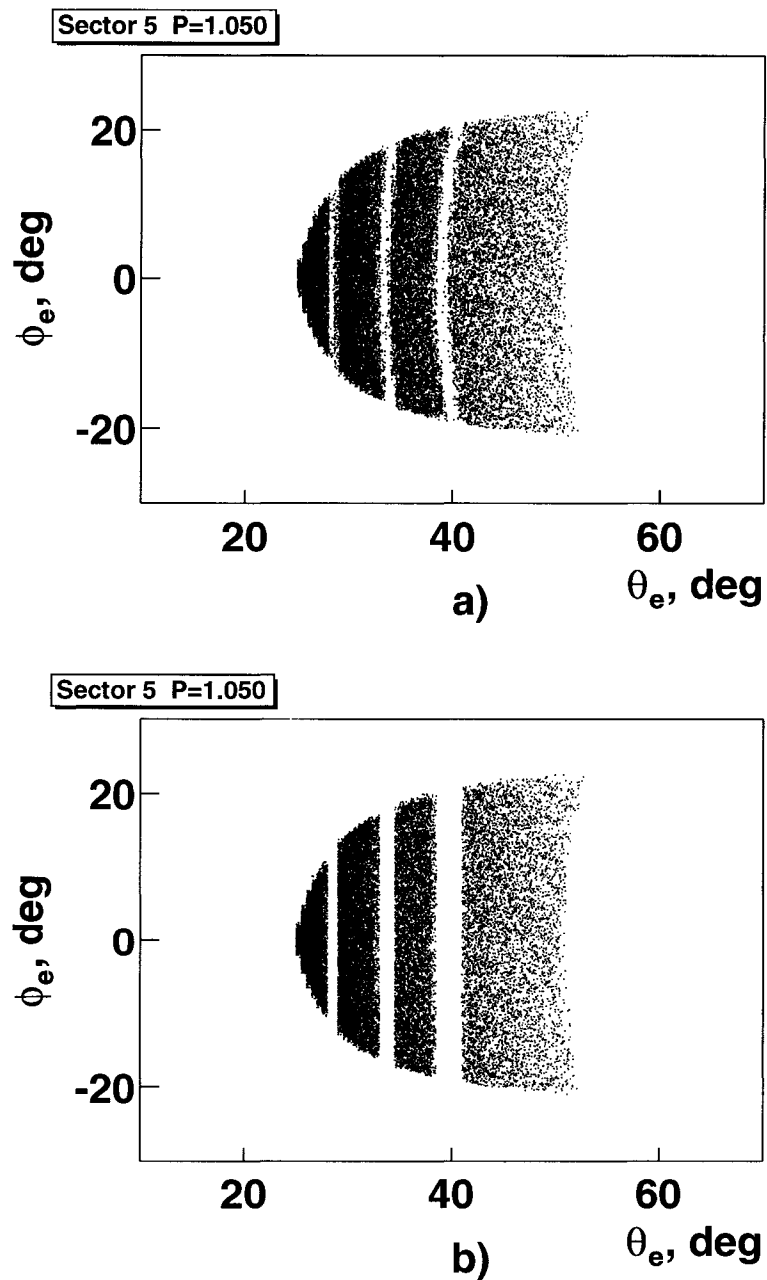
FIG. 47. θ_e versus ϕ_e distribution with bad scintillation counters cutoff. a) Fiducial cuts without bad scintillation counters knockout. b) Fiducial cuts with bad scintillation counters knockout. These are measured in Sector 5 at $E_{beam} = 2.2$ GeV and $P_{el} = 1.050$ GeV/c.
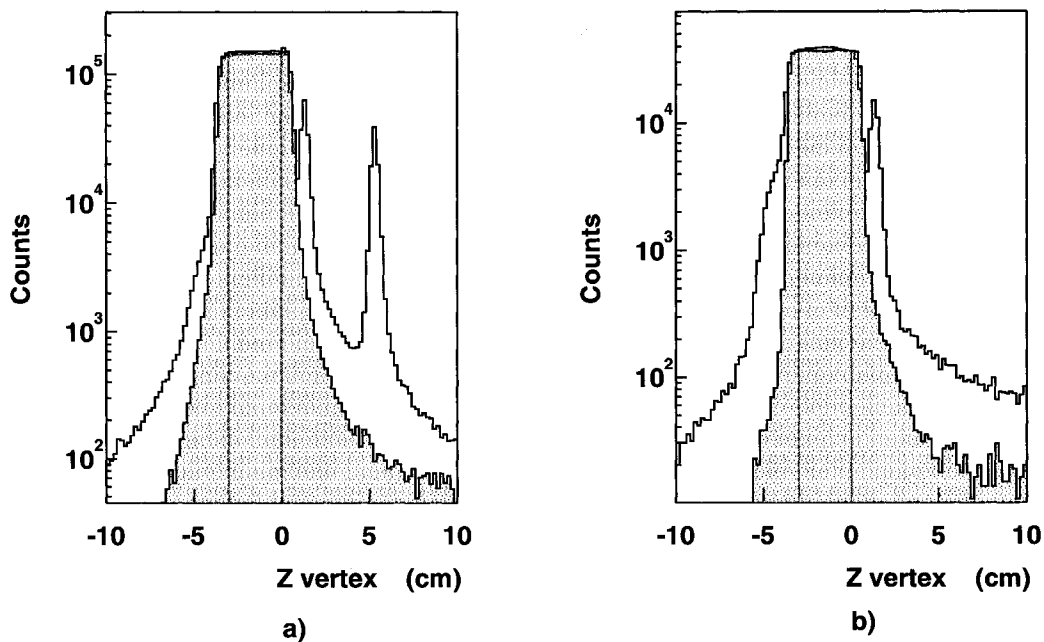
FIG. 48. Z vertex coordinate of the electrons along the beam line for ^{3}He target. a) 2.2 GeV run. Flat area is the target material. Two peaks to the right are the heat insulation and the reference foil. b) The same for 4.4 GeV. No reference foil was presented at this beam energy. The shaded histogram shows the Monte Carlo simulation with a PWIA event generator. The vertical lines indicate the cuts applied to the data and simulation events.

energies.

3.8 BEAM CHARGE MEASUREMENT

The beam charge in CLAS is measured by the Faraday Cup. The Faraday Cup collects the electron beam in the beam dump, precisely measuring the total beam charge incident on the target during a run. The charge measurements are livetime-gated which involves measurements only when the data acquisition system is running. Beam charge integration is recorded by scalers which are read out every 10 seconds. Each scaler bit represents $10^{-4} \mu C$ of charge. We eliminated scaler events associated with the physics events which we excluded from the data analysis. These are the events from the damaged or corrupted files or files we skipped due to some other reasons. The values of the total integrated charge for ^{3}He data at 2.2 GeV and 4.4

TABLE VII. Accumulated beam charge for ^{3}He target runs.

Beam Energy	2.2 GeV	4.4 GeV
Beam Charge (μC)	1190	994

GeV are given in Table VII.

3.9 BEAM ENERGY MEASUREMENT

We used the beam energies measured in Hall A and Hall C during the E2 run period to determine the beam energy in Hall B. The Hall A arc measurement was 0.15% below the beam energy and Hall C arc measurement was 0.15% above. The beam energies in Hall A [84] and Hall C [85] were determined from

$$E_b^A = 1.0015 \times E_{Arc}^A \tag{11}$$

$$E_b^C = 0.9985 \times E_{Arc}^C \tag{12}$$

The Linac energy is given by

$$E_{Linac}^i = \frac{E_b^i}{n + 0.05625} \tag{13}$$

where i=A or C, n is the number of beam passes.

If E_{Linac}^i is known from Hall A and Hall C measurements the beam energy in Hall B can be determined as

$$E_b^B = (n + 0.05625) \times E_{Linac}^i \tag{14}$$

The measured and calculated beam energy values for Hall A, C, and B are given in Table VIII.

The beam energy determined from Hall A and Hall C (see Table VIII) are close to the nominal value of 2261 MeV used in our data analysis. The uncertainty of the beam energy measurement is $\approx 0.1\%$.

TABLE VIII. Quantities used for Hall B beam energy calculations. All values except n are given in MeV. The values in brackets are errors.

	Hall A	**Hall C**
n	3	4
E_{Arc}	3355.2 (0.7)	4471.1 (2.0)
E_b	3360.2 (0.7)	4464.3 (2.0)
E_{Linac}	1099.5 (0.2)	1100.6 (0.5)
E_b^B	2260.8 (0.5)	2263 (1)

TABLE IX. ^{3}He(e,e'p) normalization cut limits.

ω cut (GeV)	$(0.799, 0.875)$
θ_e cut (degree)	$(16.26, 19.37)$
P_{prot} cut (GeV/c)	$(1.44, 1.56)$
Missing Mass cut (GeV/c^2)	< 1.96

3.10 DATA NORMALIZATIONS

In order to check the normalization of our data we compared our ^{3}He(e,e'p) cross section with Hall A preliminary results [86]. Experiment e89044, performed at Jefferson Lab in Hall A in January 2000 measured ^{3}He(e,e'p)d in perpendicular kinematics. They used $E_{beam} = 4.803$ GeV, $|\vec{q}| = 1.5$ GeV/c, $\omega = 837$ MeV and $\theta_e = 16.4$ degrees. The large CLAS kinematic coverage allowed us to match the Hall A energy and momentum transfer at $E_{beam} = 4.461$ GeV and $\theta_e = 17.8°$. We match our kinematics to Hall A by applying the cuts shown in Table IX. Figure 49 shows the missing mass of our ^{3}He data, where $M_{miss} = E_{miss} + m_d$. We do not have enough resolution to separate two-body breakup from three-body breakup channels. The cut of $M_{miss} < 1.96$ GeV/c^2 corresponds to $E_{miss} < 0.085$ GeV. Since we cannot separate two and three body breakup we use Salme's model [87] to estimate their relative contribution so we can subtract the three-body strength from our data. This model agrees well with Hall A data for both channels [88]. Figure 50 shows the ratio of three body strength to the total cross section as a function of missing momentum
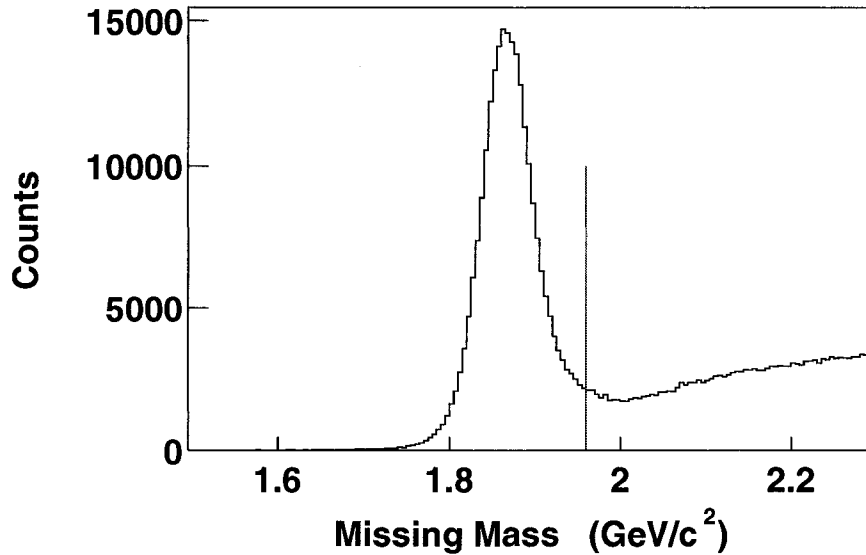
FIG. 49. Missing mass of ^{3}He(e,e'p). Vertical line indicates the cut selecting events below the pion threshold.

in this model. We estimate the uncertainty for that ratio to be about 15%. We use (1−ratio) as a correction factor.

The differential (e,e'p) cross section is

$$\frac{d^5\sigma}{d\omega d\Omega_{e'} d\Omega_p} = R\frac{E_p p_p}{(2\pi)^3}\sigma_{Mott}\left(V_L R_L + V_T R_T + V_{LT} R_{LT}\cos\phi_{pq} + V_{TT} R_{TT}\cos2\phi_{pq}\right)$$

(15)

We integrated the CLAS cross sections over all ϕ_{pq}. This eliminated the R_{LT} and R_{TT} contributions. To compare with the Hall A measurements we averaged the Hall A cross sections $d\sigma = \frac{1}{2}(d\sigma(\phi = 0°) + d\sigma(\phi = 180°))$ to eliminate the R_{LT} contribution. The R_{TT} contribution to Hall A is estimated by Laget [89] to be less than 2% at these kinematics. V_L's for both measurements are the same and V_T's are almost the same (difference is less than 1% due to the difference in θ_e).

The calculation of the cross section is based on the following steps:

1. Calculation of the luminosity $\mathcal{L} = N_t \cdot N_e$, where N_t is the number of target nuclei, and N_e is the number of electrons hitting the target.

$$N_t = \frac{N_A \rho L_T}{A}$$

(16)
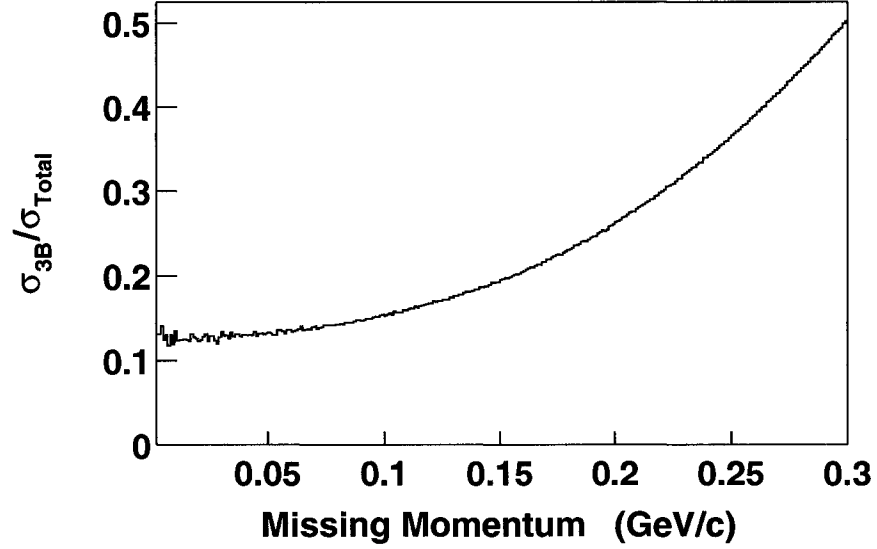
FIG. 50. Relative contribution from three body breakup channel. Ratio of three body with respect to the total cross section as a function of missing momentum.

$$N_e = \frac{Q_{FCup}}{e} \qquad (17)$$

where N_A is Avogadro's number, $\rho = 0.067$ g/cm^3 is the target density, $L_T = 3.3$ cm is the target length, $A = 3$ is the ^{3}He atomic number, $Q_{FCup} = 0.994$ mC is the integrated beam charge and e is the electron charge. Finally for the luminosity we get: $\mathcal{L} = 2.757 \cdot 10^{38}$ cm^{-2}.

2. Missing momentum binning with 20 MeV/c bin size.

3. Calculation of the phase space factors (see Table IX): $\Delta\omega = 0.076$ GeV is the energy transfer bin; $\Delta\Omega_e = \Delta\theta_e \Delta\phi_e \sin(\theta_e)$ is the electron solid angle, where $\Delta\theta_e = 3.11°$; $\Delta\phi_e = 113.3°$; $\theta_e = 17.8°$. $\Delta\phi_e$ was obtained from the electron fiducial cut distribution including all six sectors at $\omega = 0.837$ GeV and $\theta_e = 17.8°$.

For each missing momentum bin we calculate $\theta_{pq} = \arccos\left(\frac{q^2 + p^2 - p_{miss}^2}{2 \cdot p \cdot q}\right)$ is the proton angle with respect to $\vec{q}$; $\Delta\Omega_p^i = \Delta\theta_{pq}\Delta\phi_{pq}\sin(\theta_{pq})$ is the proton solid angle for bin i, where $\Delta\theta_{pq} = |\theta_{pq}^{min} - \theta_{pq}^{max}|$; θ_{pq}^{min} and θ_{pq}^{max} correspond to p_{miss}^{min} and p_{miss}^{max}, respectively, for that bin, averaged over the electron acceptance; $\Delta\phi_{pq} = 2\pi$.

4. Calculation of the cross section in each p_{miss} bin i.

$$\frac{d\sigma}{d\omega dE' d\Omega_e d\Omega_p} = \frac{N_i}{\mathcal{L}\Delta\omega\Delta\Omega_e\Delta\Omega_p^i},$$

(18)

where N_i is the number of events in the bin.

5. Calculation of the missing momentum bin centroids:

We fit our data with the exponential function $F(p) = Ae^{-Bp}$ to determine the average momentum for each missing momentum bin by using

$$<p> = \frac{\int_{p^{min}}^{p^{max}} p \cdot Ae^{-Bp}dp}{\int_{p^{min}}^{p^{max}} Ae^{-Bp}dp},$$

(19)

where p^{min} and p^{max} are the minimal and maximal values of the missing momentum bin, respectively. The difference between the central value of the bin and $<p>$ is 1.2 MeV/c. We apply that shift to set a new bin centroids.

6. Averaging Hall A cross section.

As mentioned earlier, we averaged the Hall A cross sections to eliminate the R_{LT} contribution. Before doing this we averaged Hall A data points from different kinematical sets. That was done only for the data set with higher cross sections that corresponds to $d\sigma(\phi = 180°)$. These are cross sections measured at missing momentum $p_{miss} = 0.104$, 0.114, 0.224, 0.233, 0.243, 0.253, 0.263, 0.273, 0.283, and 0.293 GeV/c.

7. Fitting the exponential to Hall A data to facilitate making the ratio.

We fit the Hall A data with the same exponential function as for our data within the missing momentum range from 0.1 to 0.22 GeV/c. We compared the Hall B data points to that function. We added the rms scatter of the Hall A data around the fit function (2.4%) to the systematic error.

8. We apply radiative corrections to our data (see Section 5.2).

9. We "correct" our data for σ_{Mott} using the factor $\sigma_{Mott}^{HallA}/\sigma_{Mott}^{HallB} = 1.2$.
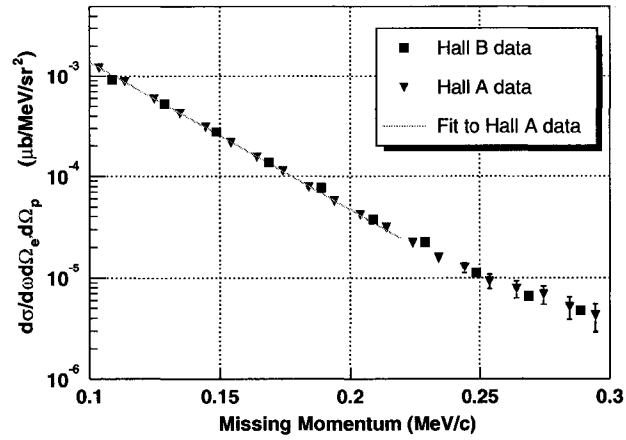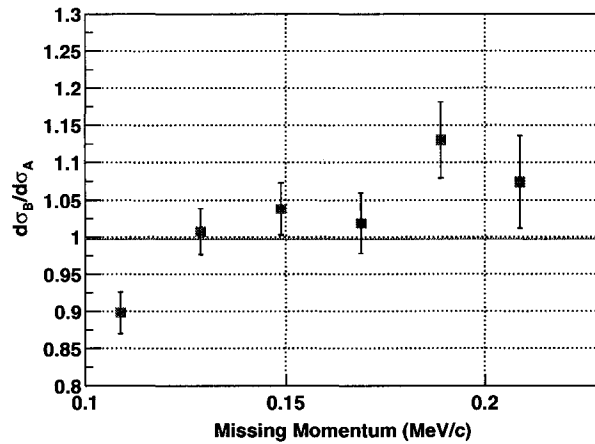
FIG. 51. The comparison of $d\sigma$ for ^{3}He(e,e'p)d with Hall A preliminary data. a) Boxes are our data, triangles are Hall A data and solid line is a fit to Hall A data. b) Ratio of our data to Hall A data. The horizontal line indicates the average ratio for all data points.

TABLE X. Cuts applied to data selecting ^{3}He(e,e′pp) final states.

Particle	Cuts	Description
Electron	Good detector status	Good TBT tracking
	Fiducial cut	See section 3.6.1
	EC cut	See section 3.3.1
	Z Vertex cut	See section 3.7
Proton	(e,e′pp) cut	SEB cuts, selecting two or more protons
	Proton PID cut	See section 3.3.2
	$Z_{vertex}^{electron}$-Z_{vertex}^{proton} cut	See section 3.11

Figure 51 a) shows the comparison of the Hall A and B cross sections. Figure 51 b) shows the ratio of our data to Hall A result. The horizontal line indicates the average ratio that includes all points in the missing momentum range from 0.1 to 0.22 GeV/c weighted by their statistical uncertanties. The rms scatter is 7%. The final systematic uncertainty that also includes kinematical uncertanties of the measurements is 15% (see Appendix D). Note that this does not include the CLAS particle detection efficiencies, but as far as uncertainties from electron and proton detection efficiency are small (about 3%) we may ignore them. The ratio of ^{3}He(e,e′p) measured in Hall B to the same measured in Hall A is 1.00 ± 0.15.

3.11 (E,E′PP) EVENT SELECTION

The purpose of this work is to study nucleon-nucleon correlations in ^{3}He at 2.2 and 4.4 GeV. In order to reduce the data sample to a manageable size and save our time while studying particle identification and applied data cuts, the ^{3}He data were filtered by selecting ^{3}He(e,e′pp) final states. Selected events were required to have an electron that was registered by the CC, SC and EC at 2.2 GeV and by the SC and EC at 4.4 GeV and to have at least two protons as determined by SEB. These filtered data were then analyzed and more cuts were applied. The list of the applied cuts is given in Table X.

To improve our Z vertex position estimation we apply a cut on the difference in vertices for the electron and protons. The vertex difference distributions for data and PWIA model simulation (see Section 5.4.2) for ^{3}He(e,e′pp) at 2.2 and 4.4 GeV
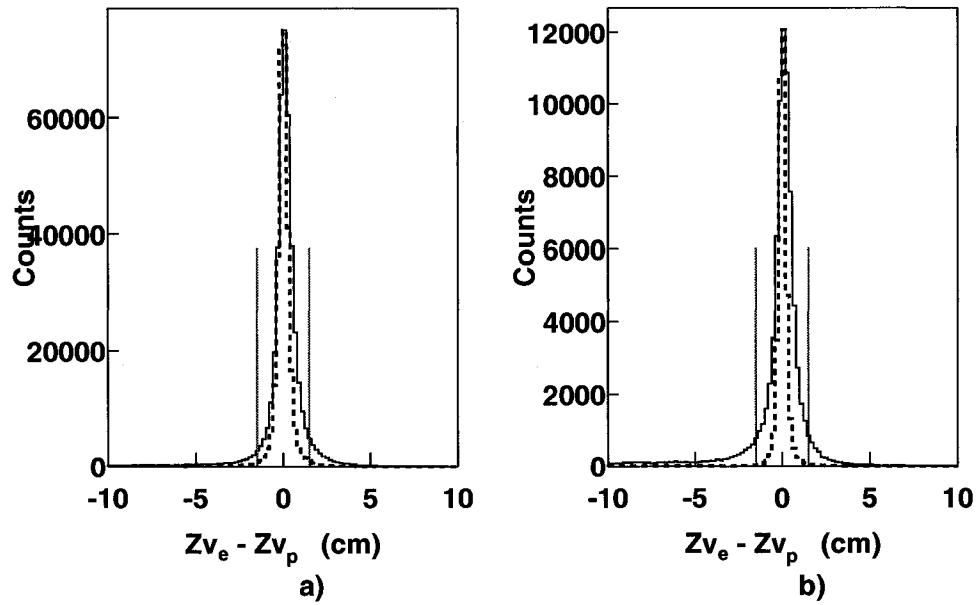
FIG. 52. Electron-proton vertex difference for ^{3}He(e,e'pp) events at a) 2.2 GeV b) 4.4 GeV beam energy. Solid line distribution is data. Dash line distribution is simulation based on PWIA model. The vertical lines indicate the cuts applied to the data and simulation events. Only one of two protons is shown.

are shown in Figure 52. The values of the cuts are given in Table XI.

3.12 (E,E'PP)N EVENT SELECTION

In order to select ^{3}He(e,e'pp)n events, we identify neutrons from the missing mass of ^{3}He(e,e'pp) :

$$M_x = \sqrt{(^3He_\mu + q_\mu - p_\mu^1 - p_\mu^2)^2}. \tag{20}$$

Missing mass distributions for data and PWIA model simulation for ^{3}He(e,e'pp) at 2.2 and 4.4 GeV are shown in Figure 53. The proton energy loss corrections were applied to both data and simulation. The width of the simulated peak was adjusted by GPP smearing to correspond data distribution. We see a fair agreement for data and PWIA at 2.2 GeV, and a little higher missing mass for PWIA than for data at 4.4 GeV. We did not study the difference between data and PWIA at 4.4 GeV because for the purpose of our analysis statistical precision of 4.4 GeV data is less worth than 2.2 GeV data. The values of the cuts are given in Table XII. As one can

TABLE XI. Electron-proton vertex difference cut limits.

Beam Energy	2.2 GeV	4.4 GeV
Vertex difference cut (cm)	$(-1.5, 1.5)$	$(-1.5, 1.5)$

TABLE XII. Missing mass cut limits.

Beam Energy	2.2 GeV	4.4 GeV
Missing mass cut (GeV/c^2)	$(0.88, 1.02)$	$(0.78, 1.02)$

see, the 4.4 GeV cut is wider because the resolution is worse at this energy and there is little background at lower M_x.

3.13 DATA STATISTICS SUMMARY

Data analysis cuts and statistics summary for reconstructed electrons and reconstructed two proton events at 2.2 GeV are given in Tables XIII and XIV, respectively. The tables consist of TRUE and FALSE columns that define the number of events that passed and failed the cuts, respectively. Also these numbers are given in percent with respect to the total number (column Total) of events before the cut. Tables XV and XVI are the same for 4.4 GeV data.

TABLE XIII. Cuts applied to reconstructed electrons at 2.2 GeV. TBT – Time Based Tracking.

Cuts	True	True %	False	False %	Total
Good TBT	6876110	91.00	679758	9.00	7555868
Fiducial cut	3533213	51.38	3342897	48.62	6876110
EC cut	3343291	94.62	189922	5.38	3533213
Z Vertex cut	2366588	70.79	976703	29.21	3343291
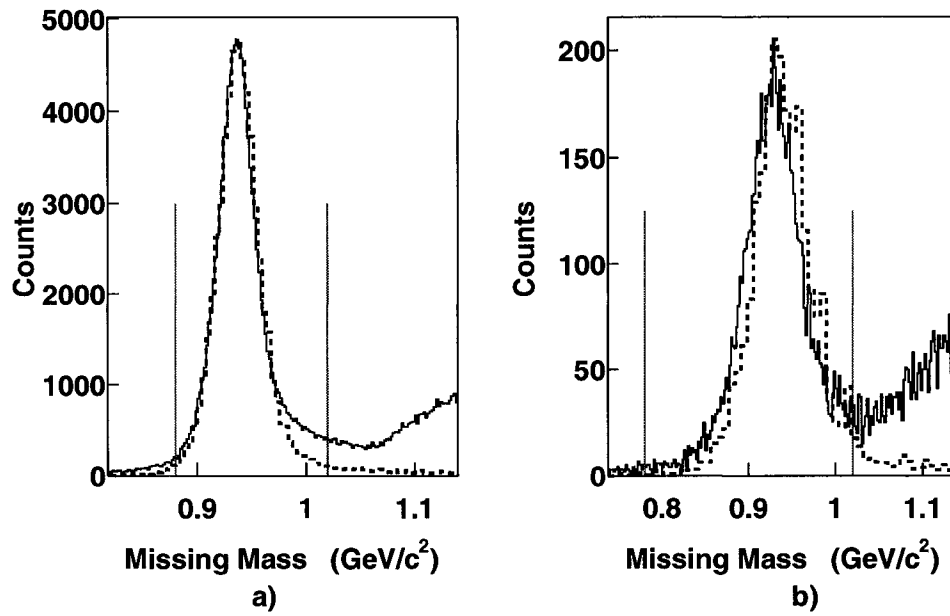
FIG. 53. Missing mass for ^{3}He(e,e′pp) events at a) 2.2 GeV b) 4.4 GeV beam energy. Solid line distribution is data. Dash line distribution is simulation based on PWIA model. The PWIA distribution is arbitrarily normalized. The vertical lines indicate the neutron missing mass cuts applied to the data and simulation events.

TABLE XIV. Cuts applied to reconstructed two proton events at 2.2 GeV.

Cuts	True	True %	False	False %	Total
^{3}He(e,e′pp)	661629	27.96	1704959	72.04	2366588
Fiducial cut	504911	76.31	156718	23.69	661629
Proton PID	433352	85.83	71559	14.17	504911
$Z^{electron}_{vertex}$-Z^{proton}_{vertex}	339450	78.33	93902	21.67	433352
^{3}He(e,e′pp)n	104558	30.80	234892	69.20	339450

TABLE XV. Cuts applied to reconstructed electrons at 4.4 GeV.

Cuts	True	True %	False	False %	Total
Good TBT	3346336	84.75	602314	15.25	3948650
Fiducial cut	1202906	35.95	2143430	64.05	3346336
EC cut	875144	72.75	327762	27.25	1202906
Z Vertex cut	635769	72.65	239375	27.35	875144

TABLE XVI. Cuts applied to reconstructed two proton events at 4.4 GeV.

Cuts	True	True %	False	False %	Total
^{3}He(e,e'pp)	141706	22.29	494063	77.71	635769
Fiducial cut	100196	70.71	41510	29.29	141706
Proton PID	82130	81.97	18066	18.03	100196
$Z^{electron}_{vertex}$-Z^{proton}_{vertex}	58171	70.83	23959	29.17	82130
^{3}He(e,e'pp)n	6825	11.73	51346	88.27	58171

CHAPTER 4

PHYSICS ANALYSIS

Because this is the first time that ^{3}He(e,e$'$pp)n has been measured using an almost 4π detector, our data analysis philosophy is to follow and understand the dominant features of the data. Section 4.1 shows a detailed look at all the data. Section 4.1.3 is a selective overview of the evidence for correlations.

4.1 DATA ANALYSIS

First we looked at the electron acceptance Q^2 versus ω data distribution for ^{3}He(e,e$'$pp)n events ($Q^2 = -q_\mu q^\mu = \vec{q}^{\,2} - \omega^2$ is the square of the four-momentum transfer, ω is the energy transfer and $\vec{q}$ is the three-momentum transfer). Q^2 versus ω distributions for ^{3}He(e,e$'$pp)n events at 2.2 and 4.4 GeV are shown in Figure 54. There is a gap can be seen for 2 GeV data which is due to the bad scintillation counters (see Section 3.6.1). As one can see, ^{3}He(e,e$'$pp)n events are measured over a wide kinematic range and concentrated between 0.5 and 1 (GeV/c)^2 at 2.2 GeV and between 1 and 2 (GeV/c)^2 at 4.4 GeV beam energy. The energy transfer for these events is peaked around quasielastic kinematics.

In order to understand the energy sharing in the reaction, we plotted the kinetic energy of the first proton divided by the energy transfer (T_{p1}/ω) versus that of the second proton (T_{p2}/ω) for each event. (Note that the assignment of protons 1 and 2 is arbitrary.) Due to the fact that CLAS accepts protons with momentum $p_p > 0.2$ GeV/c and reconstruction of low momentum protons is not very good (see proton efficiency graph in Fig. 91) we put a tighter cut at $p_p > 0.25$ GeV/c. T_{p1}/ω vs T_{p2}/ω Dalitz distributions in the Lab frame at 2.2 and 4.4 GeV are shown in Figure 55 a), c), e) and b), d), f), respectively. Figure 55 a) and b) show kinetic energy sharing for all events. As one can see from these distributions the dominant feature is a ridge running from the upper left corner (proton 1 has all the energy) to the lower right corner (proton 2 has all the energy) corresponding to events where the two protons share the energy transfer and the neutron is a spectator. We want to separate spectator neutrons by putting a cut $p_n < 0.25$ GeV/c on neutron momentum. The kinetic energy sharing distributions with spectator neutrons is shown in Figure 55 c) and d).
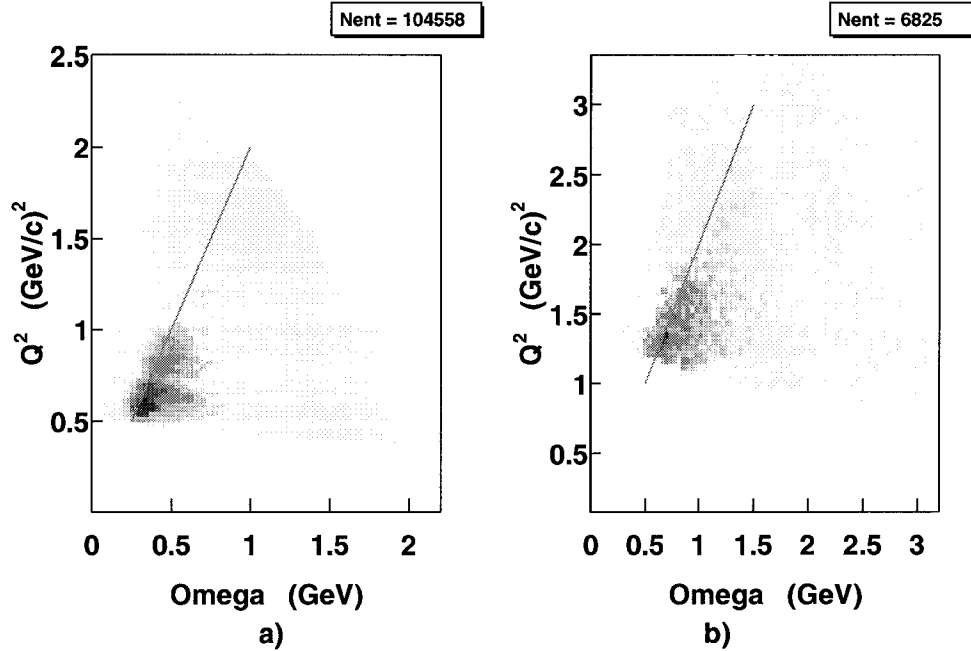
FIG. 54. Q^2 vs ω for ^{3}He(e,e'pp)n events. These are measured at a) 2.2 GeV; b) 4.4 GeV beam energy. The line shows the quasielastic condition $\omega = Q^2/2m$. Note the huge kinematic acceptance.

Figure 55 e) and f) show the same distributions for $p_n \geq 0.25$ GeV/c, corresponding to events where all three nucleons have momentum greater than 250 MeV/c. In this case we see three peaks at the three corners of the plot, corresponding to events where two nucleons each have less than 20% of the energy transfer and the third 'leading' nucleon has the remainder. We call the two nucleons 'fast' because $p \geq 250$ MeV/c $\gg p_{fermi}$. These peaks are much more pronounced at $E_{beam} = 4.4$ GeV. We cut on these peaks, as indicated by the lines in Figure 55 e) and f). The solid lines indicate the leading n, fast pp pair cut and the dashed lines indicate the leading p, fast pn pair cut.

Nucleon kinetic energy distributions in the Center of Mass (CM) frame with the same cuts as in Figure 55 are shown in Figure 56. Note the equal energy sharing (1/3 of ω) at the center of distibutions in Figure 56 e) and f) and the difference between 2.2 and 4.4 GeV plots, which is not seen in the Lab frame. Figure 57 shows a triangular CM Dalitz plot $T_n/(T_{p1} + T_{p2} + T_n)$ versus $(T_{p2} - T_{p1})/\sqrt{3}(T_{p1} + T_{p2} + T_n)$ with the same cuts applied as in Figure 55. The three additional axes on the plot correspond to T_{p1}, T_{p2}, and T_n normalized to the total CM energy. This plot shows the same
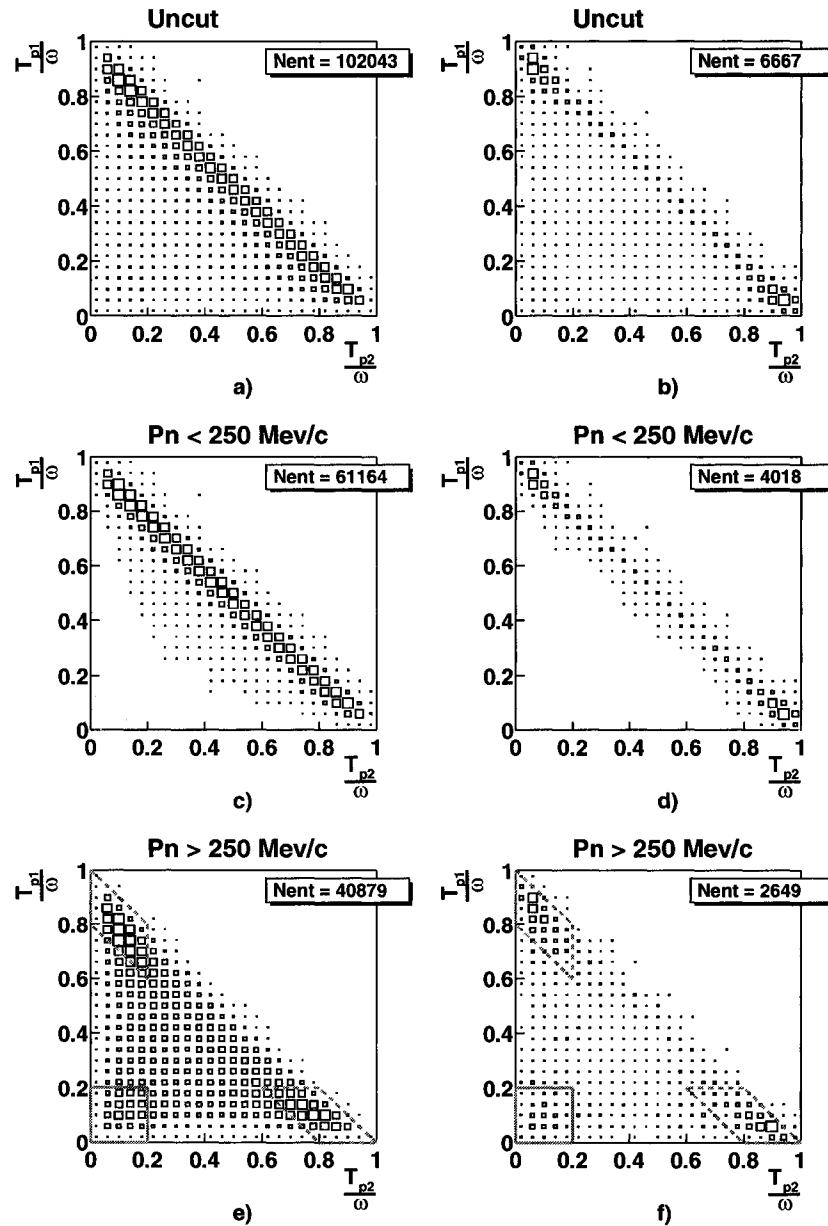
FIG. 55. ^{3}He(e,e'pp)n lab frame Dalitz plot. T_{p1}, the kinetic energy of proton 1, divided by ω plotted against T_{p2}/ω. a), c), e) 2.2 GeV; b), d), f) 4.4 GeV. a),b) are distributions for all events; c),d) for events with $p_n < 0.25$ GeV/c; e),f) for events with $p_n > 0.25$ GeV/c. The assignment of p_1 and p_2 is arbitrary and each proton has momentum $p_p > 0.25$ GeV/c. Solid and dashed lines indicate the leading n, fast pp pair and the leading p, fast pn pair cuts, respectively.
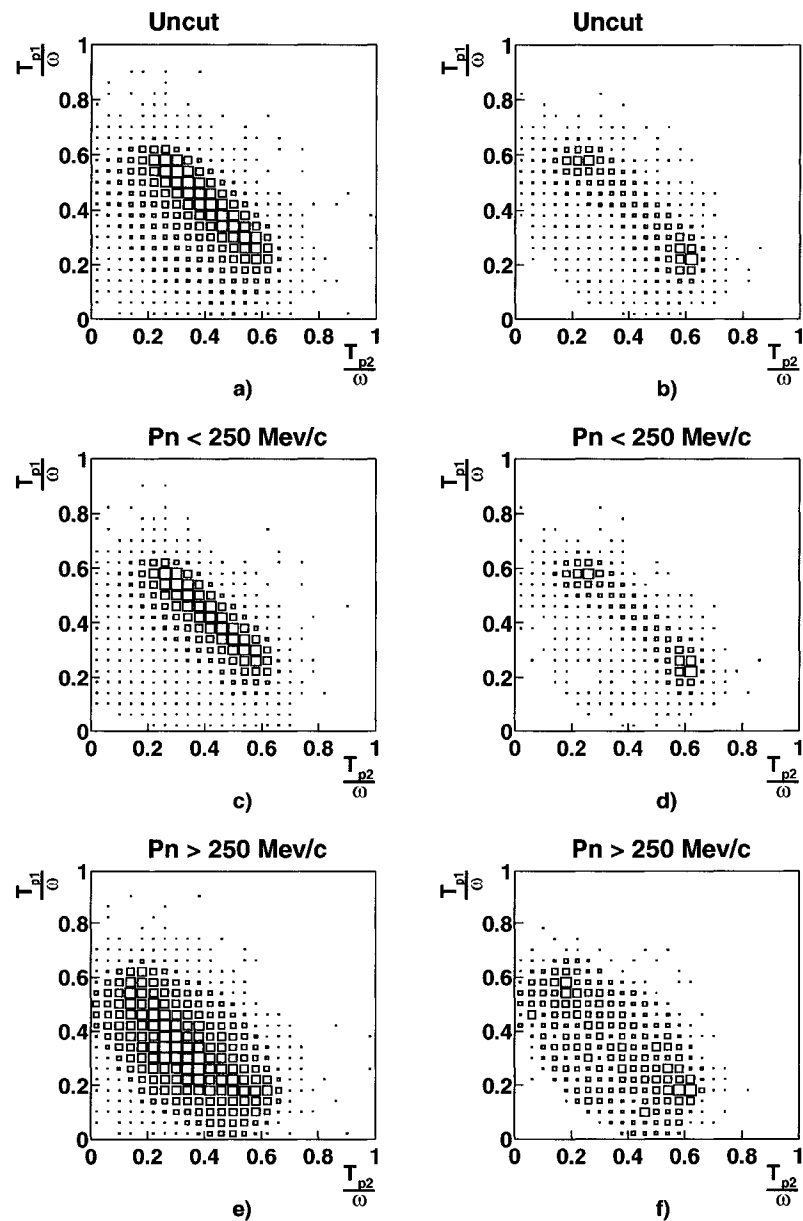
FIG. 56. ^{3}He(e,e'pp)n CM frame Dalitz plot. a), c), e) T_{p1}, the kinetic energy of proton 1, divided by ω is plotted against T_{p2}/ω. a), c), e) 2.2 GeV; b), d), f) 4.4 GeV. The plots correspond to the same cuts as in Fig. 55.
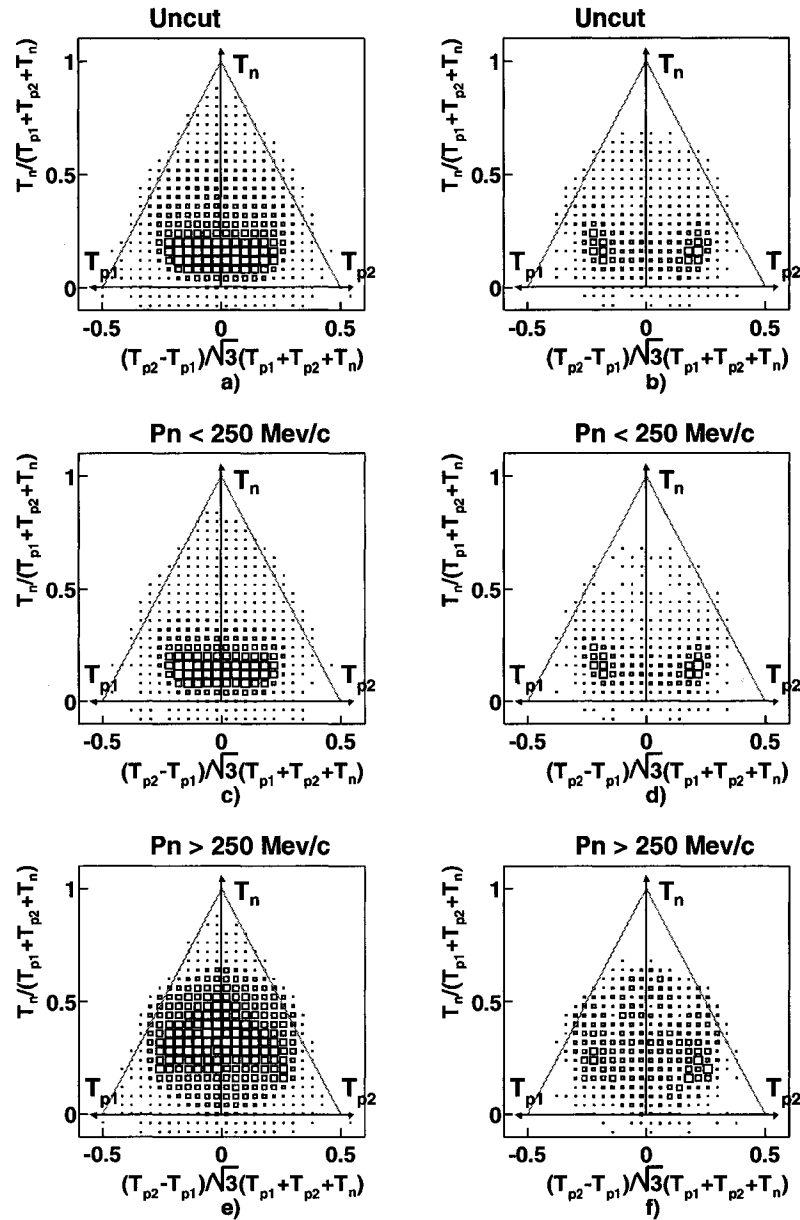
FIG. 57. Triangular ^{3}He(e,e'pp)n CM frame Dalitz plot. The three axes are the CM kinetic energies of proton 1, proton 2, and neutron, normalized to the total CM energy. a), c), e) 2.2 GeV; b), d), f) 4.4 GeV. The plots correspond to the same cuts as in Fig. 55.

features as seen in Figure 55 and Figure 56. We clearly see a dominance of the final state rescattering in Figure 57 a), b) by comparing it to c), d) plots, respectively. One can see from Figure 57 e), f) that the 2.2 and 4.4 GeV distributions are very different, which is also seen in Figure 56, but not in the Lab frame (see Fig. 55). Note that detector resolution causes negative values of T_n on the plots due to the fact that the neutron was reconstructed by missing mass. The CM frame Dalitz plots are more useful for events where the virtual photon is absorbed on two or more nucleons. We choose instead to investigate the peaks in the Lab frame Dalitz plots (see Fig. 55 e) and f)).

Now we want to study the angular dependences of the nucleons. In order to understand distinctions among the nucleons in ^{3}He(e,e'pp)n events we reassign the protons: the faster and slower protons in event are assigned as proton 1 and proton 2, respectively. The cosine of the pp, p_1n and p_2n opening angle distributions for ^{3}He(e,e'pp)n events at 2.2 GeV are shown in Figure 58 a), c) and e), respectively. The same distributions at 4.4 GeV are shown in Figure 58 b), d) and f). As one can see, the opening angle of the two protons has a large peak at 90° (see Fig. 58 a) and b)), which is more pronounced if we select only "spectator" neutrons $p_n < 0.25$ GeV/c (see Fig. 59 a) and b)). That indicates the dominance of hard final state rescattering (ie: virtual photon absorption on one proton followed by billiard ball rescattering on the second proton). We do not see that large peak for the p_1n and p_2n opening angles since they are dominated by events where $p_n < 0.25$ GeV/c (i.e. spectator neutrons) (see Fig. 58 c), d), e), f)). As we would expect with spectator neutrons, the p_1n and p_2n opening angle distributions with $p_n < 0.25$ GeV/c are isotropic (see Fig. 59 c), d), e), f)). Since we are not interested in final state rescattering, we eliminated those events and focussed on events where all three nucleons have momentum greater than 250 MeV/c (see Fig. 55 e), f)).

4.1.1 Studying NN opening angles of events with three active nucleons

Now we look at events in the peaks at the corners of the Dalitz plot. The NN opening angles for events with a leading n and fast pp pair are shown in Figure 60 and for events with a leading p and fast pn pair in Figure 61. Note that the angle between the leading nucleon and one of the two fast nucleons has a broad peak just backward of $90°$ (see Fig 60 c), d), e), f) and Fig 61 a), b), c), d)).

Now we want to look at the opening angle of the two fast nucleons. Figure 60 a)
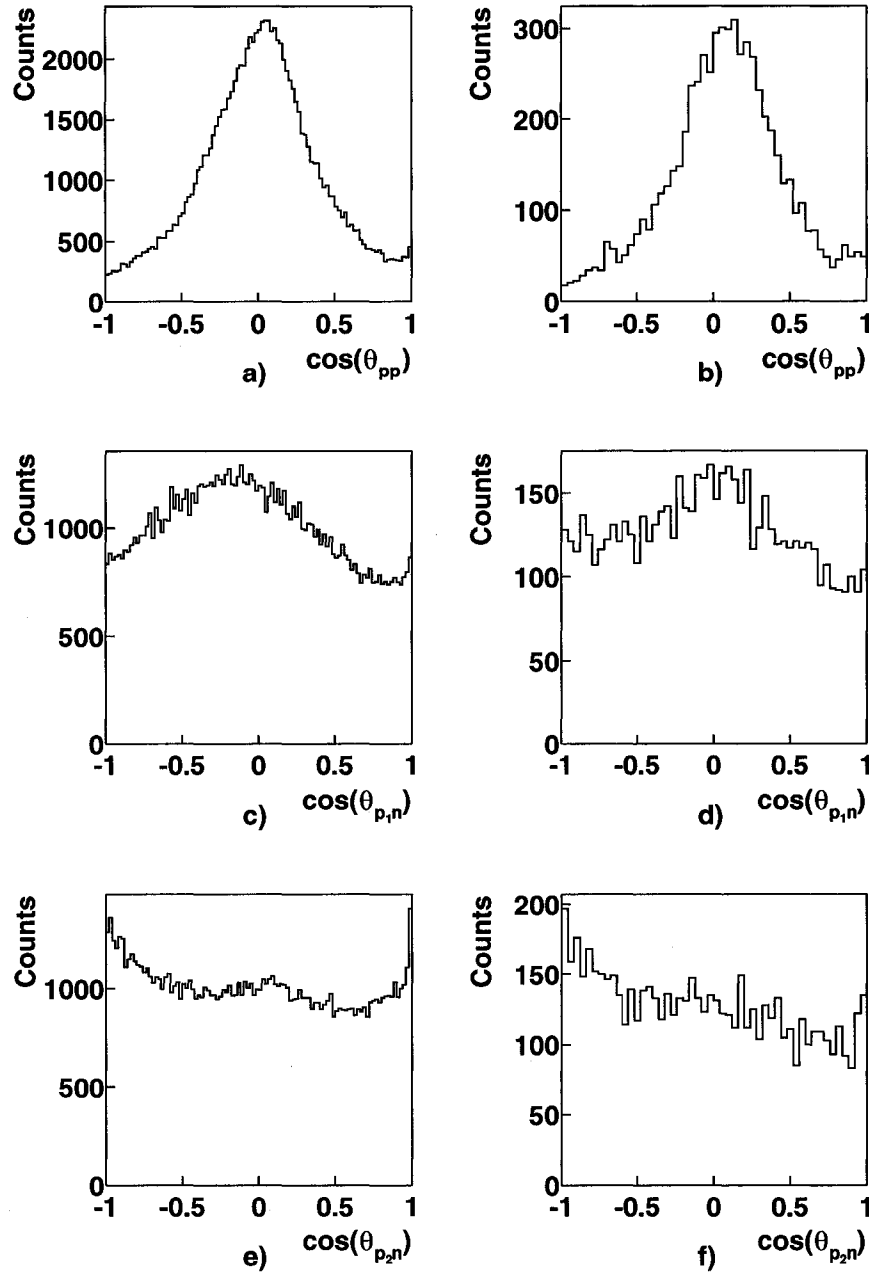
FIG. 58. All ^{3}He(e,e'pp)n events: a), c), e) The cosine of the pp, $p_1 n$, and $p_2 n$ opening angles, respectively, for all events at 2.2 GeV; b), d), f) the same for 4.4 GeV. Note each proton has momentum $p_p \geq 0.25$ GeV/c and $p_{p1} > p_{p2}$.

and b) shows the pp opening angle for fast pp pairs with a leading neutron at 2.2 and 4.4 GeV, respectively. The pn opening angle distribution of fast pn pairs for events with a leading proton at 2.2 and 4.4 GeV is shown in Figure 61 e) and f). Note the large peak at 180 degrees ($\cos\theta_{NN} \approx -1$). This peak is the first indication of NN correlated events. Our further analysis steps will concern this very interesting strong signal.

The angular distributions of the p_1 and p_2 in respect to the direction of leading neutron at 2.2 and 4.4 GeV are shown in Figure 60 c), d) and e), f), respectively. The same distributions in respect to leading proton are shown in Figure 61 c), d) and e), f). No evident features are seen in these distributions, except that they are similar, although we might see the effect of the CLAS acceptance for backward going neutrons in Figure 61 c), d) compared to backward going protons in Figure 60 c), d), e), f) and Figure 61 a), b) (which is based on the assumption that p_1 goes in direction of $\vec{q}$). The enhancement at the backward angles of the $p_1 n$ opening angle distribution in Figure 61 c), d) is due to fact that the neutrons are reconstructed whereas the proton detection in the backward direction is limited because of the hole in the back of the CLAS.

The Q^2 versus ω distributions for selected NN pairs at 2.2 and 4.4 GeV are shown in Figure 62.

To see if the observed 180 degrees peak for fast pp pairs with a leading neutron and fast pn pairs with a leading proton is due to the cuts, we compared the distributions to a fire ball phase space simulation assuming three body absorption of the virtual photon followed by phase space decay. We used the virtual photon from data, generated random angles, isotropic in $\cos(\theta_1)$ and in ϕ_1 for the first nucleon, as well as in ϕ_{12} between the first and second nucleons. All the other variables were determined from the corresponding kinematical relations described in [90]. We then applied electron and proton fiducial cuts to model the effects of the CLAS acceptance. The shaded histogram in Fig.63) shows the results of the simulation with arbitrary normalization. Note that the fire ball phase space distribution does not show the peak at 180° and therefore this peak is not due to the purely kinematical correlations in three nucleon system.

The observed back-to-back peak is also not due to the CLAS acceptance since we see it for both fast pp and fast pn pairs. This back-to-back peak is a very strong indication of correlated NN pairs.
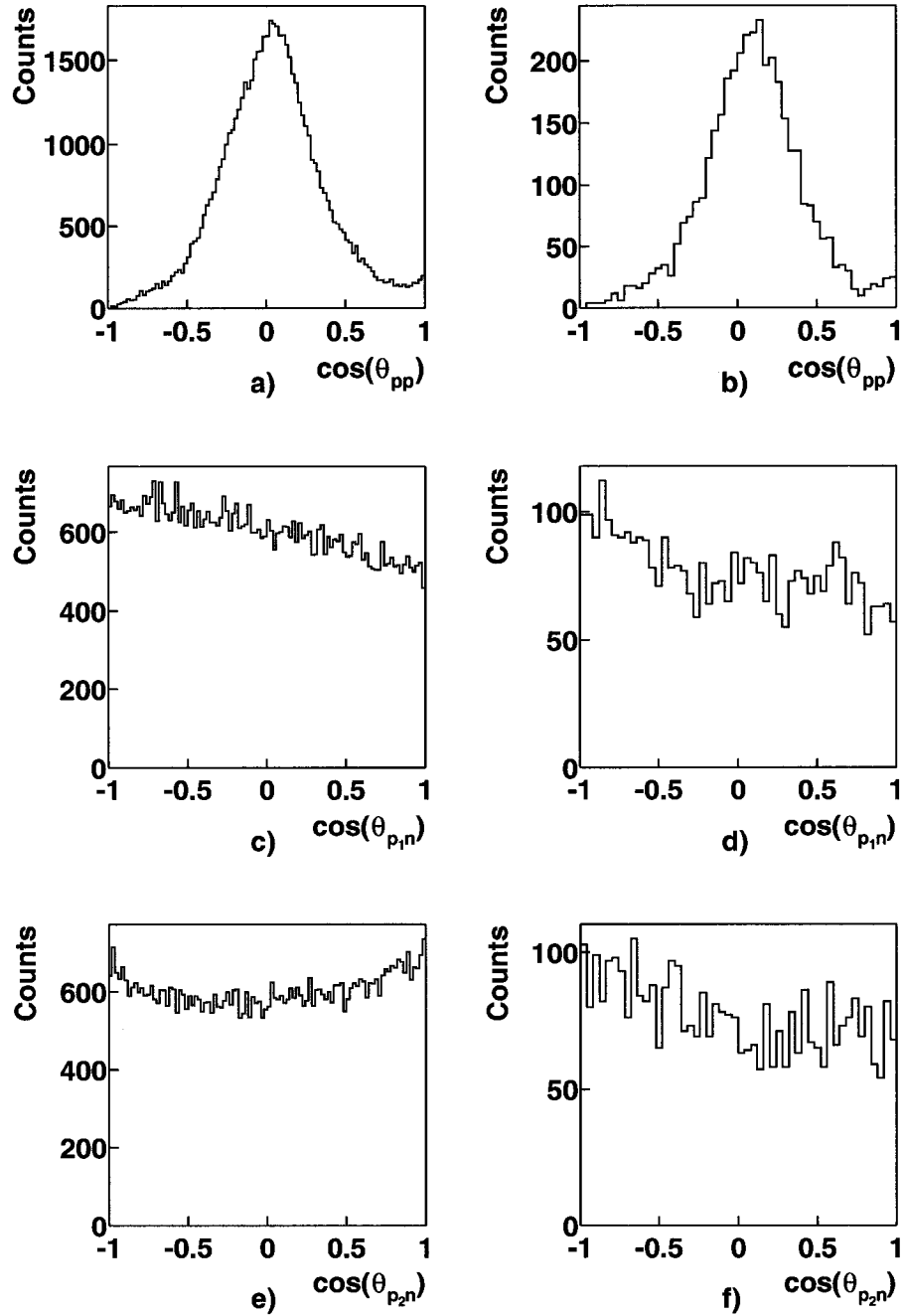
FIG. 59. ^{3}He(e,e'pp)n events with $p_n < 0.25$ GeV/c: a), c), e) The cosine of the pp, $p_1 n$, and $p_2 n$ opening angles, respectively, for 2.2 GeV; b), d), f) the same for 4.4 GeV. Note that $p_{p_1} > p_{p_2}$; $p_{p_2} \geq 0.25$ GeV/c.
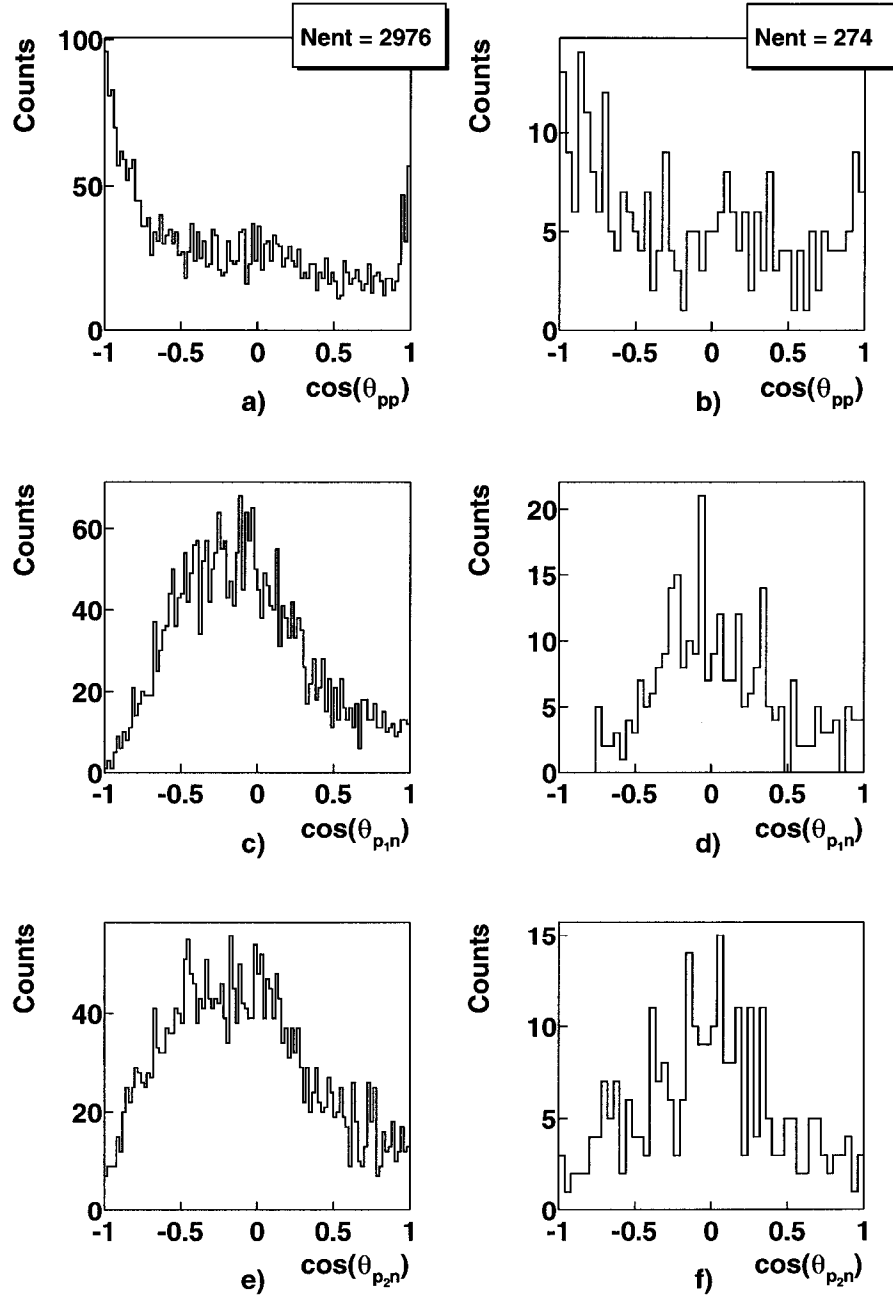
FIG. 60. ^{3}He(e,e'pp)n events with $p_n \geq 0.25$ GeV/c, fast pp pairs $(T_{p1}, T_{p2} \leq 0.2\omega)$: a), c), e) The cosine of the pp, $p_1 n$, and $p_2 n$ opening angles, respectively, with cut on fast pp pairs (leading neutron) at 2.2 GeV; b), d), f) the same for 4.4 GeV. Note that $p_{p_1} > p_{p_2}$; $p_{p_2} \geq 0.25$ GeV/c.
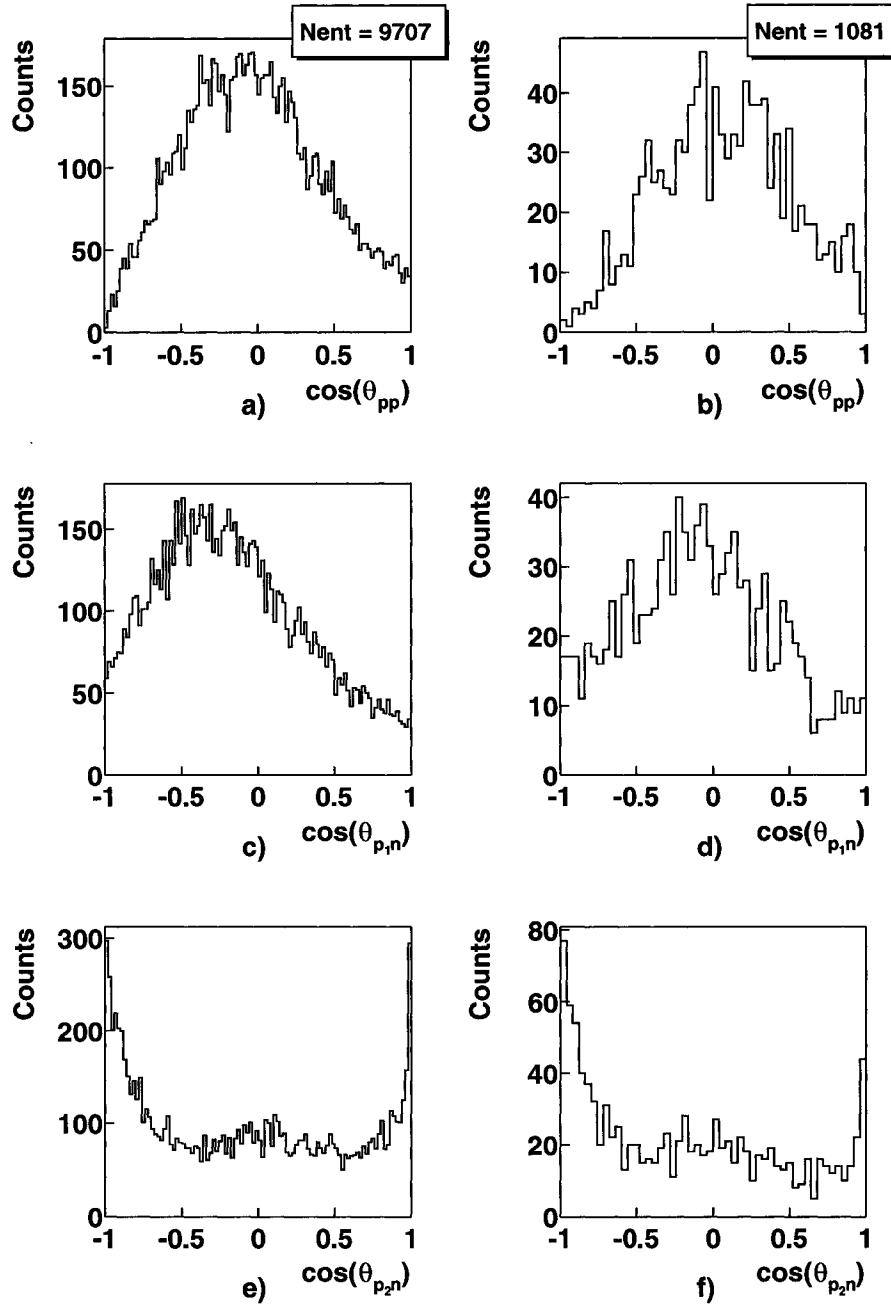
FIG. 61. ^{3}He(e,e'pp)n events with $p_n \geq 0.25$ GeV/c, fast pn pairs $(T_{p2}, T_n \leq 0.2\omega)$: a), c), e) The cosine of the pp, $p_1 n$, and $p_2 n$ opening angles, respectively, with cut on fast pn pairs (leading proton) at 2.2 GeV; b), d), f) the same for 4.4 GeV. Note that $p_{p_1} > p_{p_2}$; $p_{p_2} \geq 0.25$ GeV/c.
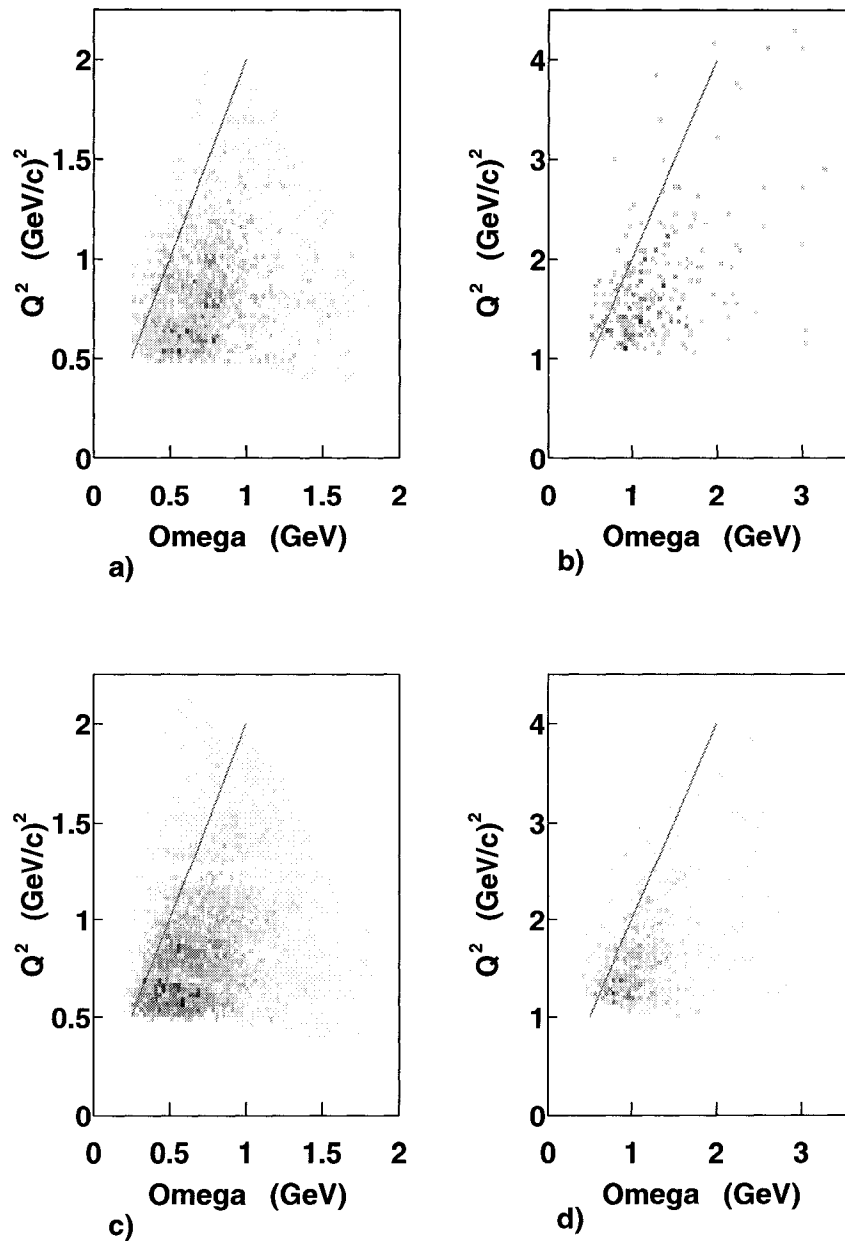
FIG. 62. Q^2 vs ω distribution with kinetic energy cuts. a), c) are fast pp, pn pairs at $E_{beam} = 2.2$ GeV. b), d) are the same for 4.4 GeV. The cuts on nucleon kinetic energies were applied. The line shows the quasielastic condition $\omega = Q^2/2m$.
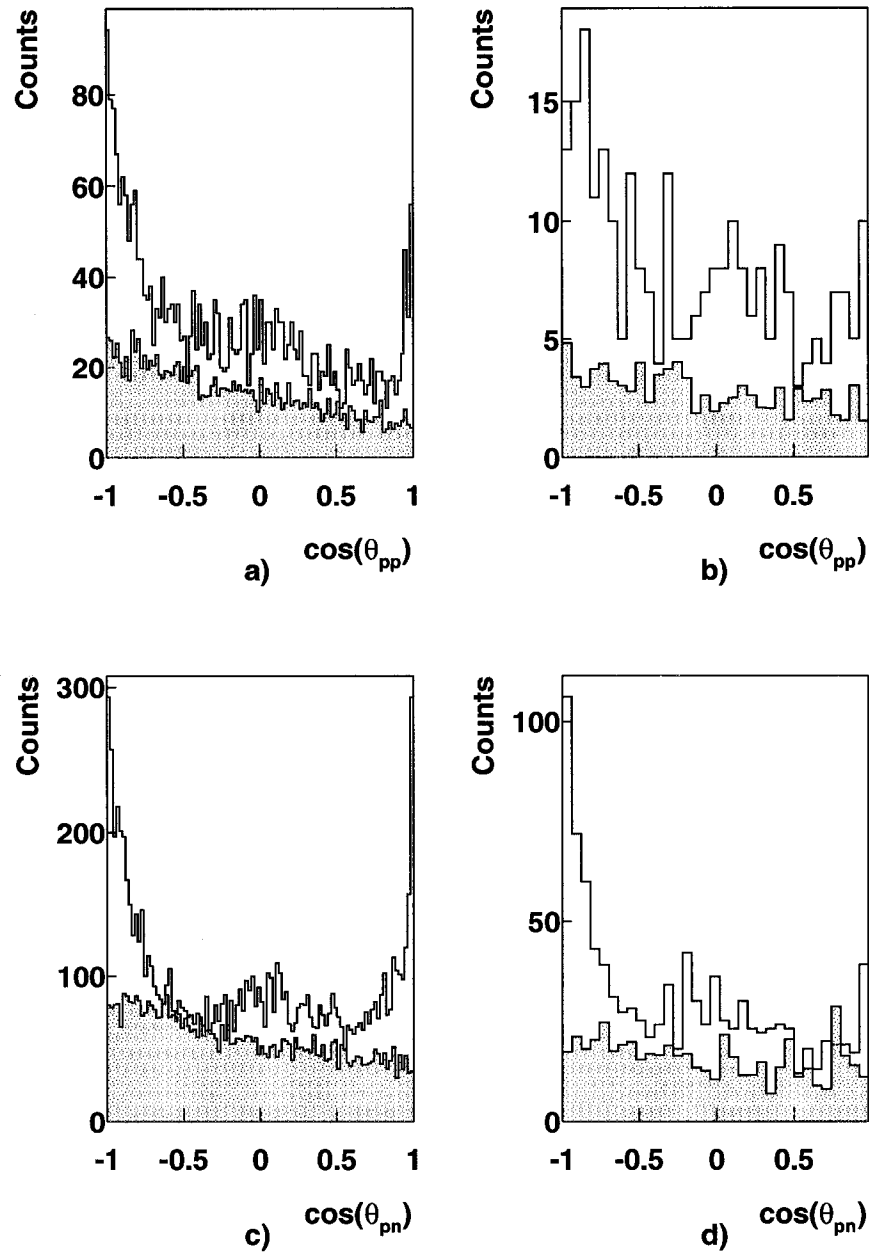
FIG. 63. Comparison with fireball phase space simulation. a), c) The cosine of the fast pp and pn opening angle, respectively, for events with $p_n \geq 0.25$ GeV/c at 2.2 GeV; b), d) the same for 4.4 GeV. The shaded distribution shows the fireball phase space simulation (with arbitrary normalization).

4.1.2 Studying correlated pairs

Now that we have identified correlated pairs, we want to study them. In order to reduce the effects of final state rescattering, we cut on the perpendicular component of the leading nucleon's momentum, $p^\perp \leq 0.3$ GeV/c. This value was a compromise between the number of events remaining and the quasifree nature of those events. The distributions of the perpendicular component of the leading nucleon's momentum versus the cosine of the fast pp and pn opening angle at 2.2 GeV are shown in Figure 64 a), c), respectively. Note that the events of interest are mostly concentrated at the lower left corner of the plot. The same distributions at 4.4 GeV are shown in Figure 64 b), d). The same plots, but only for the perpendicular component of the leading nucleon's momentum are shown in Figure 65.

The resulting fast NN pair opening angle distribution is almost entirely back-to-back. Figure 66 shows the cosine of the fast pp and pn opening angle at 2.2 and 4.4 GeV after we selected quasifree knockout events by applying a cut $p^\perp \leq 0.3$ GeV/c. The shaded histogram in Figure 66 is due to the three body fireball phase space model. It does not look like the data distribution.

These fast nucleons are distributed almost isotropically with respect to $\vec{q}$. Figure 67 a), c) and e) show the cosine of the neutron, p_1 and p_2 angle in respect to $\vec{q}$, respectively for fast pp pairs (events with a leading neutron) at 2.2 GeV. One can see a very sharp peak in the direction of $\vec{q}$ for leading neutrons. Both protons from these events exhibit a drop in yield at 180° due to the CLAS acceptance, discussed earlier. Figure 67 b), d) and f) show the same distributions at 4.4 GeV. We see the same behavior for fast pn pairs (events with a leading proton). Figure 68 a), c) and e) show the cosine of the $p1$, $p2$ and neutron angles with respect to $\vec{q}$, respectively, for fast pn pairs at 2.2 GeV. Note that the acceptance does not affect $\cos\theta_{nq}$ in Figure 68 c) due to the fact that the neutron was not detected, but reconstructed from missing mass.

Another piece of evidence that the fast pairs are spectators is that the mean value of pair total momentum parallel to $\vec{q}$ (Figure 69) is much smaller than q. These distributions for pp, pn pairs at 2.2 and 4.4 GeV are shown in Figure 69 a), c) and b), d). Note that these distributions are not corrected for the CLAS acceptance yet; acceptance corrections and results are disscussed later in Section 4.2.3

Both observations 1) fast nucleons are distributed almost isotropically with respect to $\vec{q}$ and 2) the pair total momentum parallel to $\vec{q}$ is small, indicate that the

fast pairs are predominantly spectators (i.e. they do not interact with the virtual photon).

Pair total momentum $\vec{p}_{tot}$ distributions for pp and pn pairs at 2.2 GeV are shown in Figure 70 a) and c). The same distributions at 4.4 GeV are shown in Figure 70 b) and d). The total momentum distribution rises rapidly from zero, peaks at about 0.25 GeV/c, and falls rapidly. This distribution goes up to 600 MeV/c. Pair relative momentum $\vec{p}_{rel}$ distributions for pp, pn pairs at 2.2 and 4.4 GeV are shown in Figure 71 a), c) and b), d). Pair total and relative momentum are defined as follows:

$$\vec{p}_{tot} = |\vec{p}_1 + \vec{p}_2| \tag{21}$$

$$\vec{p}_{rel} = (\vec{p}_1 - \vec{p}_2)/2 \tag{22}$$

The relative momentum distribution rises rapidly starting at about 0.25 GeV/c (limited by the minimum nucleon momenta of 0.25 GeV/c), peaks at about 0.35 GeV/c and has a tail extending to about 0.7 GeV/c.

Note that the distributions in Figures 69, 70, 71 are very similar for both pp and pn pairs and for 2.2 and 4.4 GeV data. A little Q^2 dependence can be seen comparing 2.2 with 4.4 GeV distributions. Figure 72 a) and b) shows the pn pair relative momentum versus total momentum at 2.2 and 4.4 GeV, respectively. One can see a hole in the lower left corner of the plot which is due to the cut on proton's momentum $p_p \geq 0.25$ GeV/c.

4.1.3 Analysis Summary

This section summarizes the analysis path described in too much detail in Section 4.1. Figure 73 shows this graphically for the 2.2 GeV pn pairs. Top plots are the data distributions from Figures 55 e) and 61 e), middle from Figures 64 c) and 66 c), and bottom from Figures 69 c) and 68 e). When we select ^{3}He(e,e'pp)n events with one leading and two fast nucleons with momentum $p_{fast} \geq 250$ MeV/c and kinetic energy $T_{fast} \leq 0.2\omega$ we see that the two fast nucleons are emitted preferentially back-to-back (see top distributions in Figure 73). We select a quasifree leading nucleon (or reduce Final State Interactions) with a cut $P_\perp \leq 300$ MeV/c (see middle distributions in
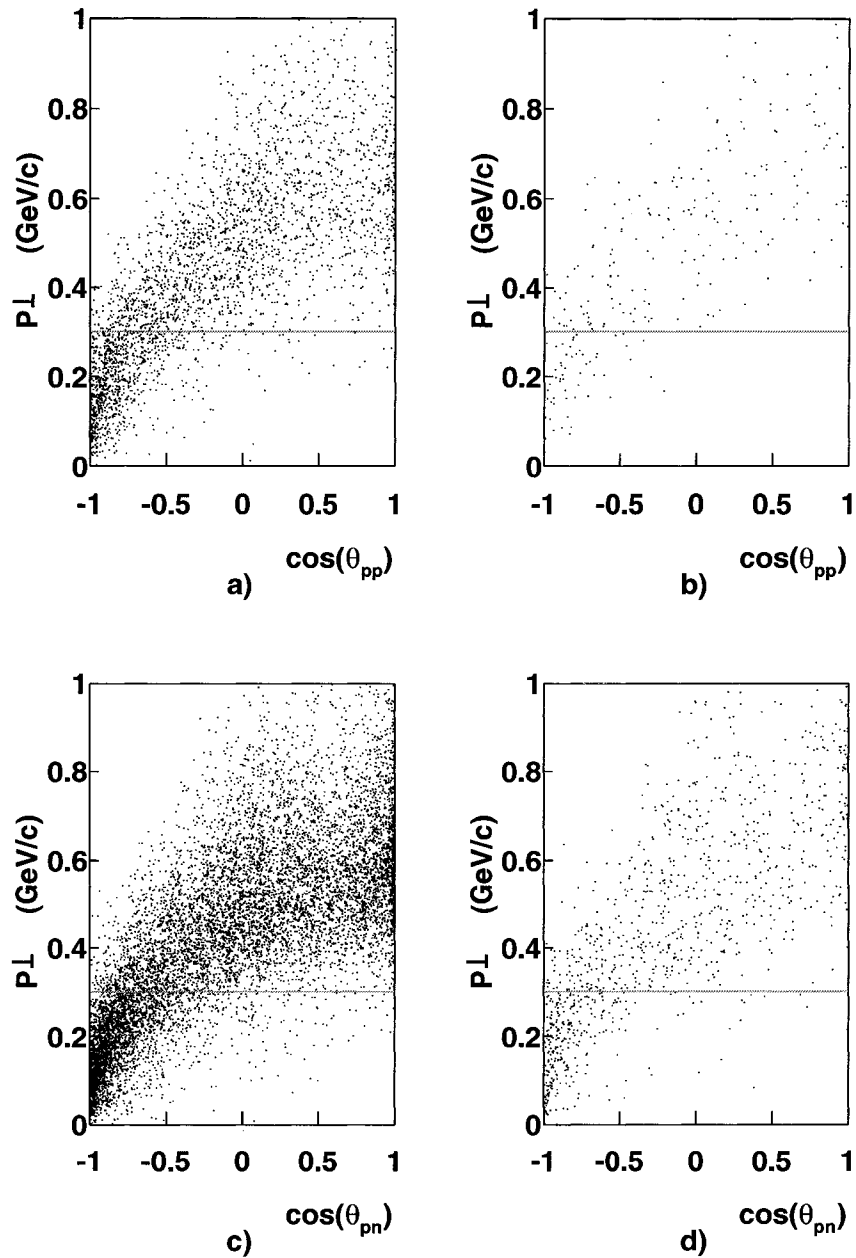
FIG. 64. $p^\perp$ versus the cosine of the opening angle of the fast NN pair. a), c) The perpendicular component of the leading nucleon's momentum $p^\perp$ versus the cosine of the fast pp and pn opening angle, respectively, for events at 2.2 GeV; b), d) the same for 4.4 GeV. The horizontal lines indicate the cut $p^\perp \leq 0.3$ GeV/c.
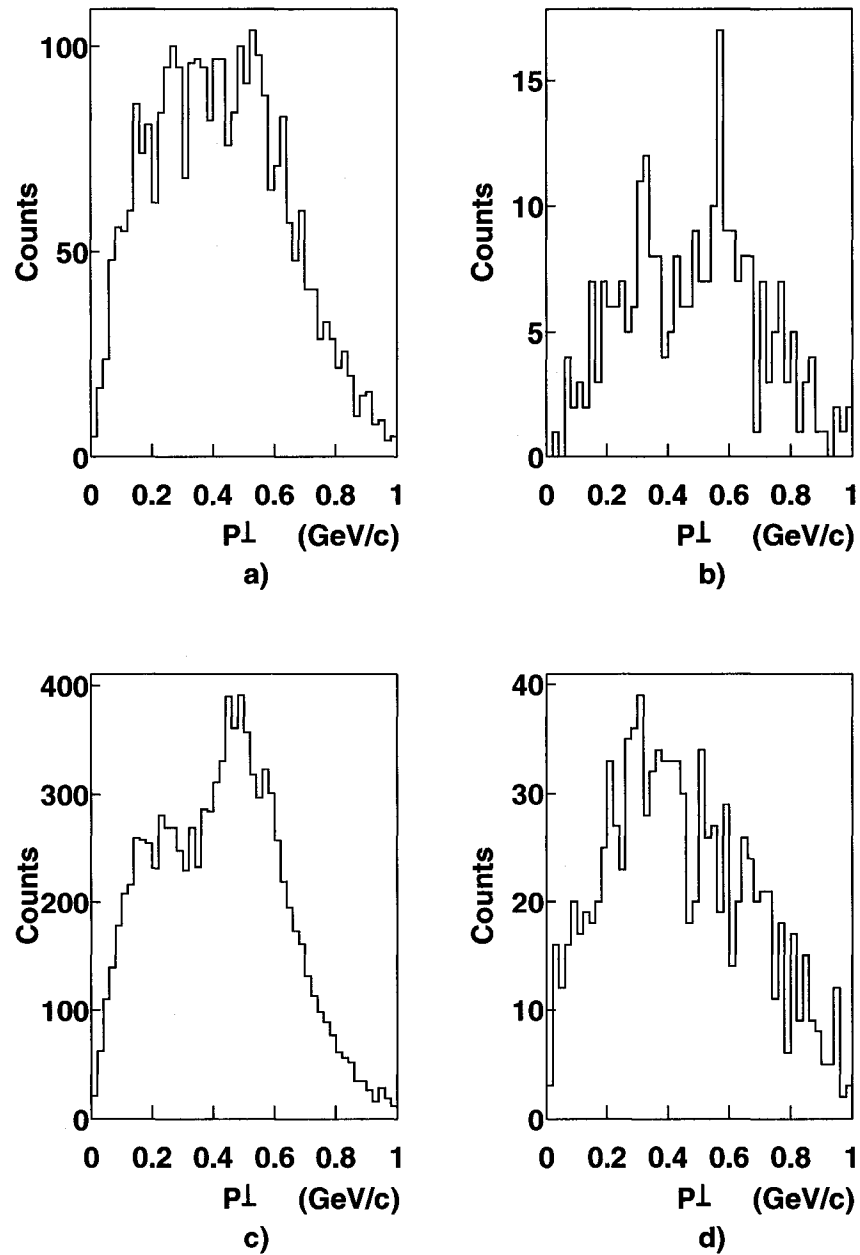
FIG. 65. $p^\perp$ distribution for fast NN pair. a), c) The perpendicular component of the leading nucleon's momentum $p^\perp$ for the fast pp and pn pairs, respectively, for events at 2.2 GeV; b), d) the same for 4.4 GeV.
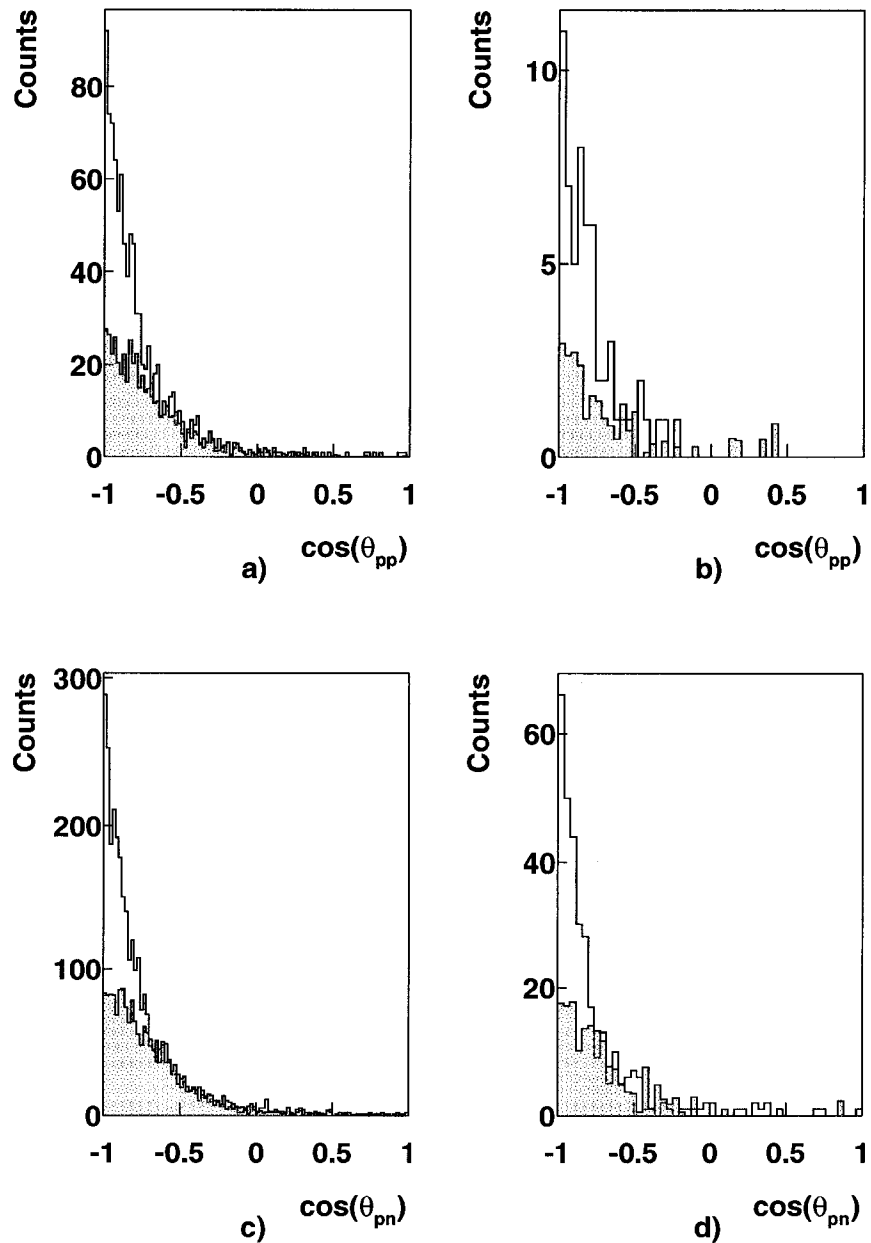
FIG. 66. The cosine of the fast NN pair opening angle with cut on $p^\perp$. a), c) The cosine of the fast pp and pn opening angle, respectively, for events with cut on $p^\perp \leq 0.3$ GeV/c at 2.2 GeV; b), d) the same for 4.4 GeV. The shaded distribution shows the fireball phase space simulation (with arbitrary normalization).
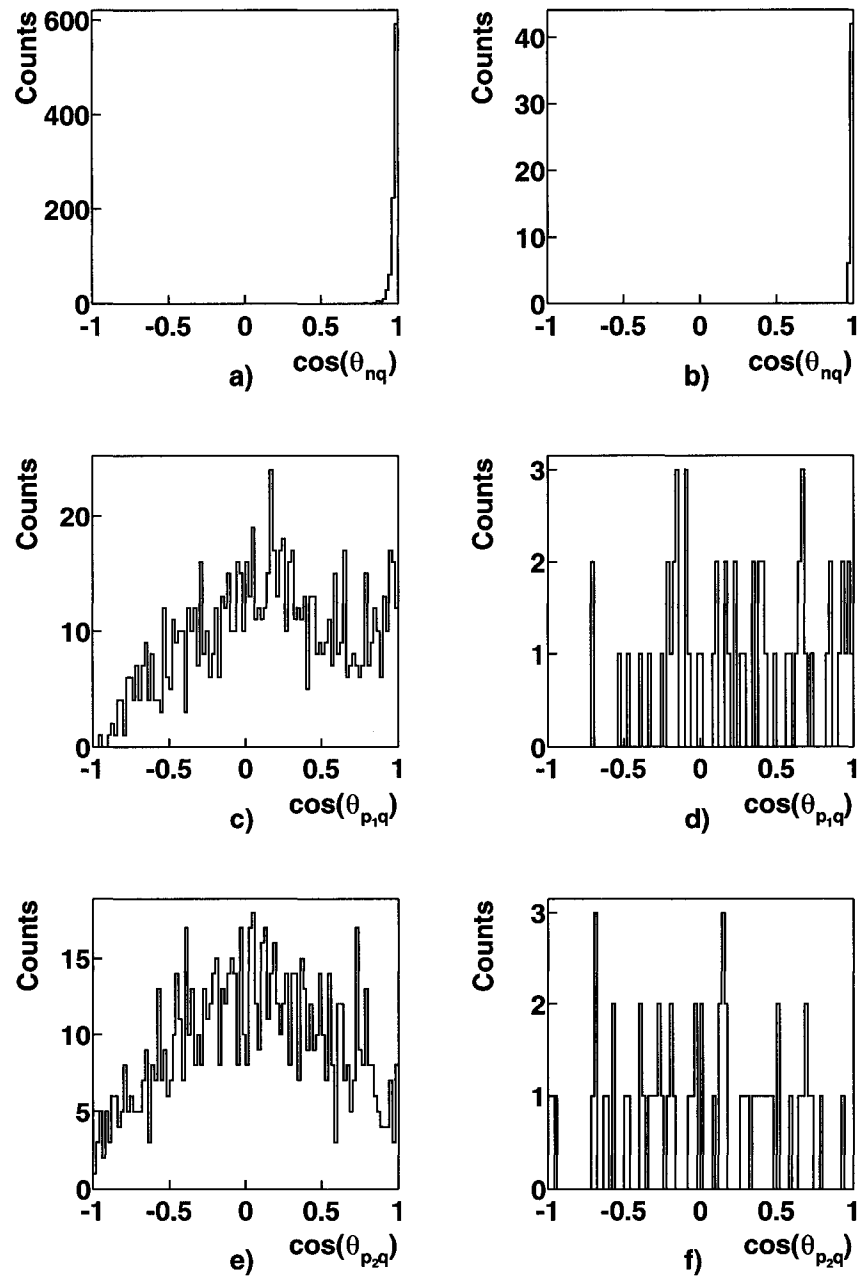
FIG. 67. a), c), e) The cosine of the nucleon's angle in respect to $\vec{q}$ direction for $^3\mathrm{He}(\mathrm{e,e'pp})\mathrm{n}$ events with leading neutron at 2.2 GeV; b), d), f) the same for 4.4 GeV. All three nucleons are shown. Note that $p_{p1} > p_{p2}$. Note the hole in the back of CLAS in c), d), e) and f). Events are selected with cut $p^{\perp} \leq 0.3$ GeV/c.
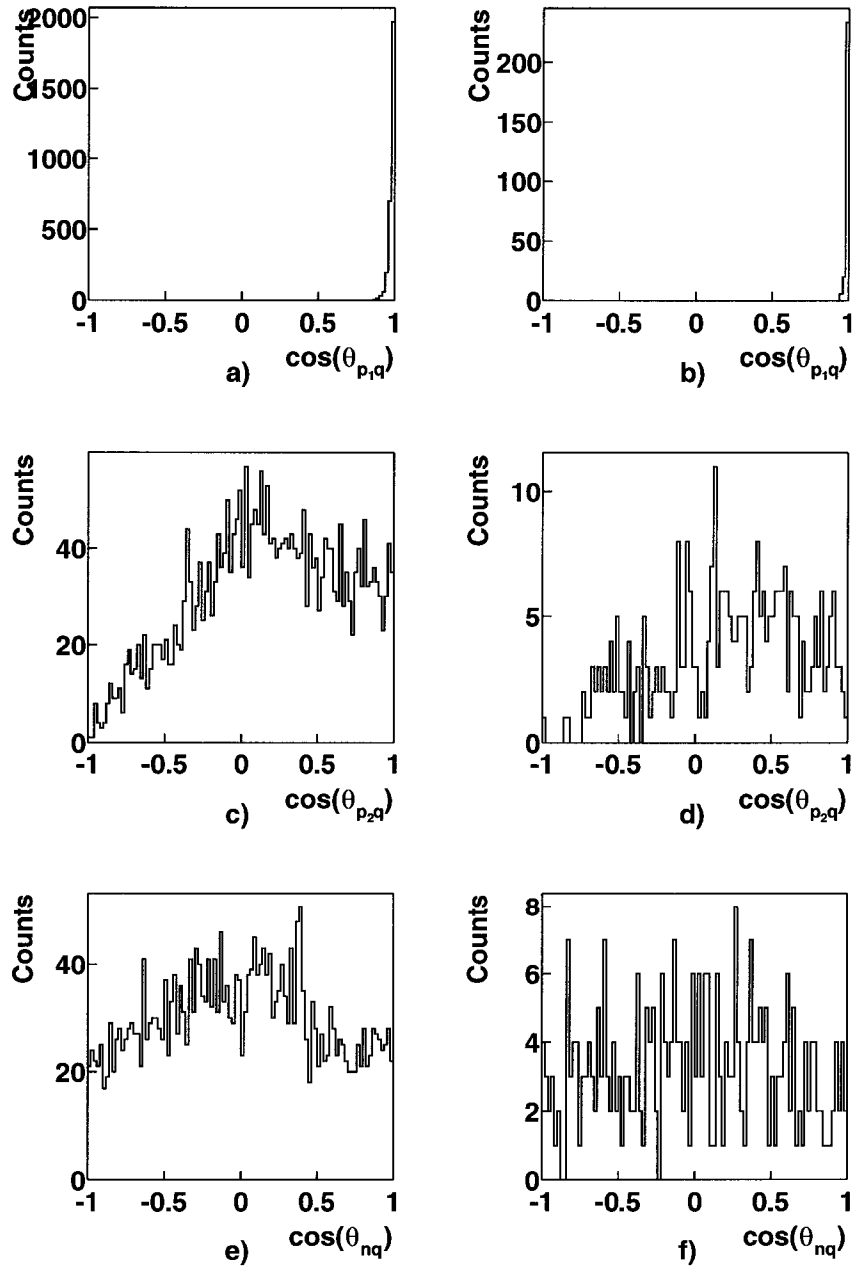
FIG. 68. a), c), e) The cosine of the nucleon's angle in respect to $\vec{q}$ direction for ^{3}He(e,e'pp)n events with leading proton at 2.2 GeV; b), d), f) the same for 4.4 GeV. All three nucleons are shown. Note that $p_{p1} > p_{p2}$. Note the hole in the back of CLAS in c) and d). Events are selected with cut $p^{\perp} \leq 0.3$ GeV/c.
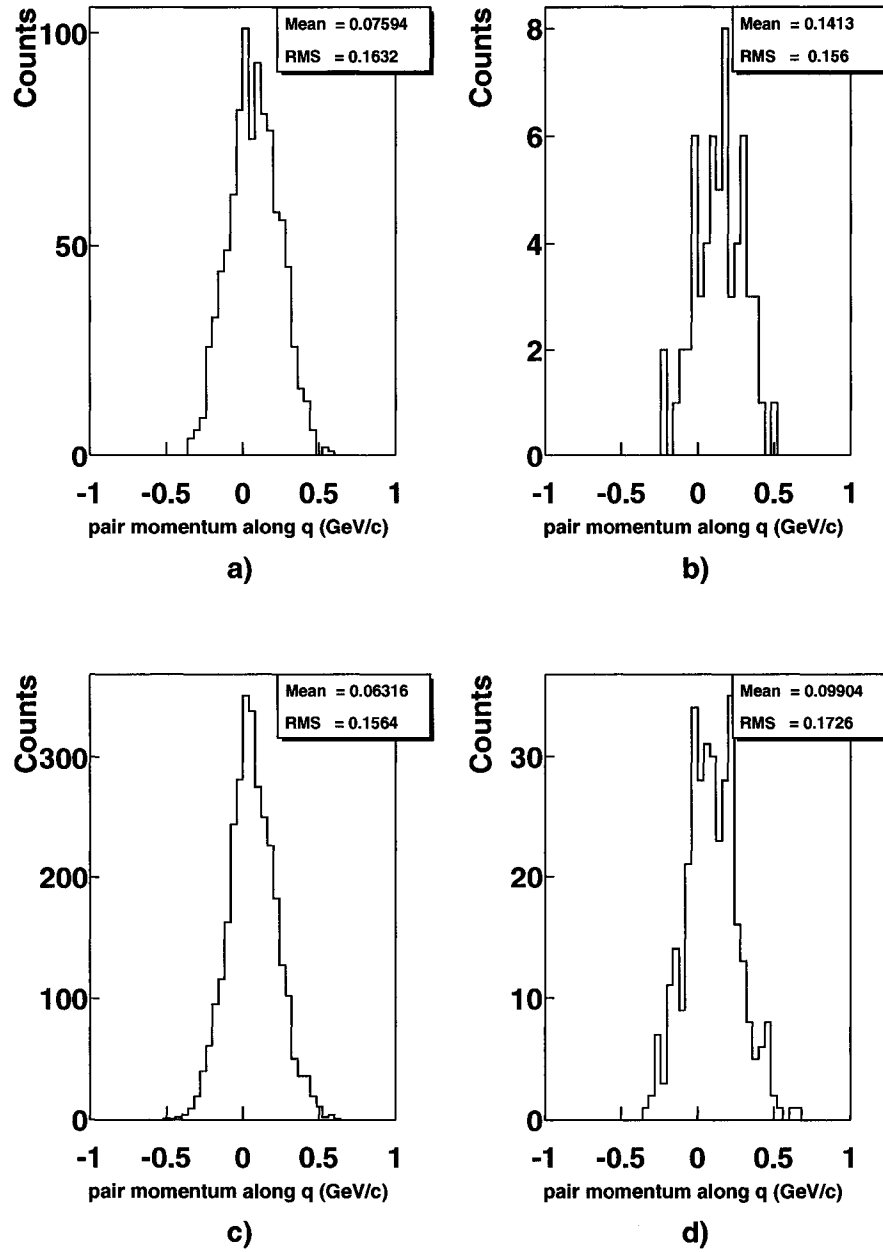
FIG. 69. Pair total momentum parallel to $\vec{q}$. a) 2.2 GeV pp pair b) 4.4 GeV pp pair c) 2.2 GeV pn pair d) 4.4 GeV pn pair. Cut $p^{\perp} \leq 0.3$ GeV/c was applied.
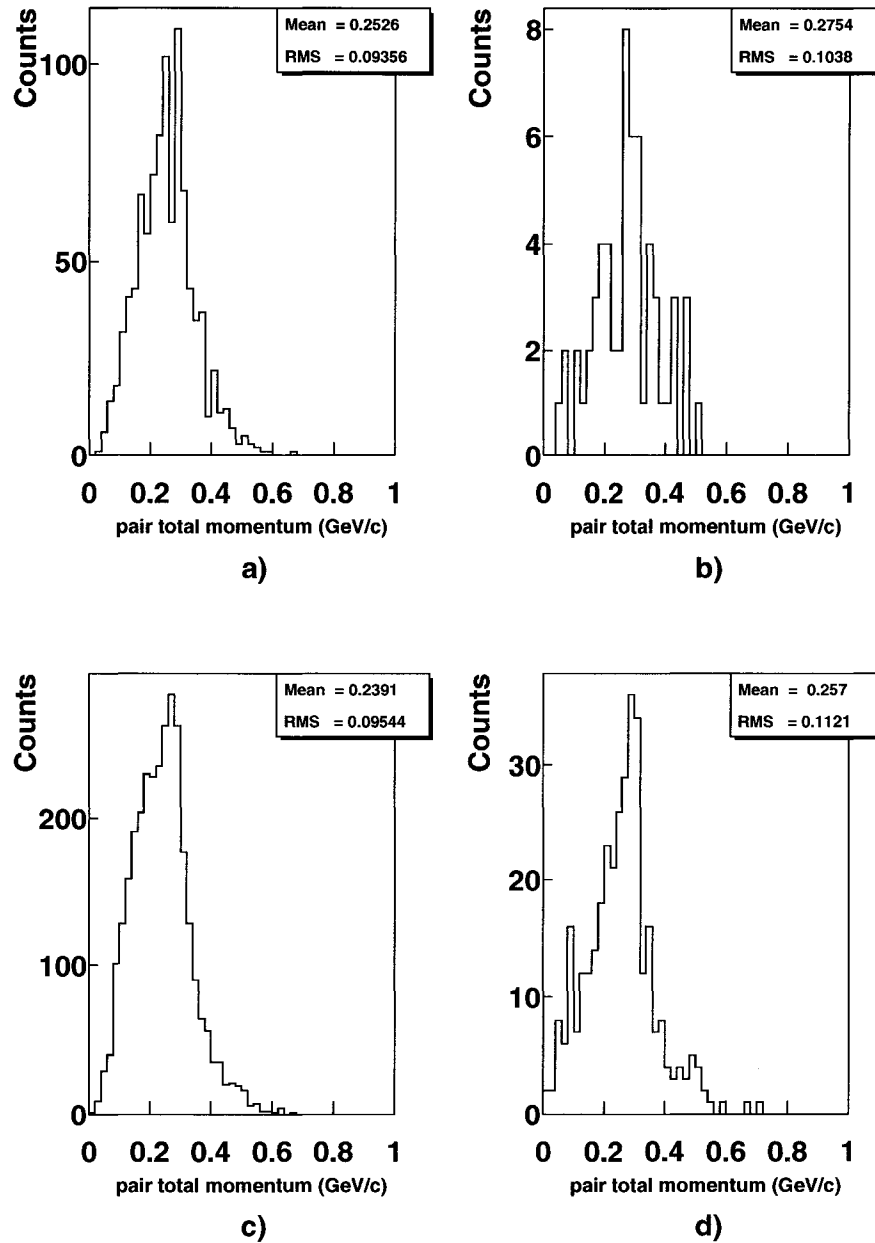
FIG. 70. Pair total momentum. a) 2.2 GeV pp pair b) 4.4 GeV pp pair c) 2.2 GeV pn pair d) 4.4 GeV pn pair. Cut $p^\perp \leq 0.3$ GeV/c was applied.
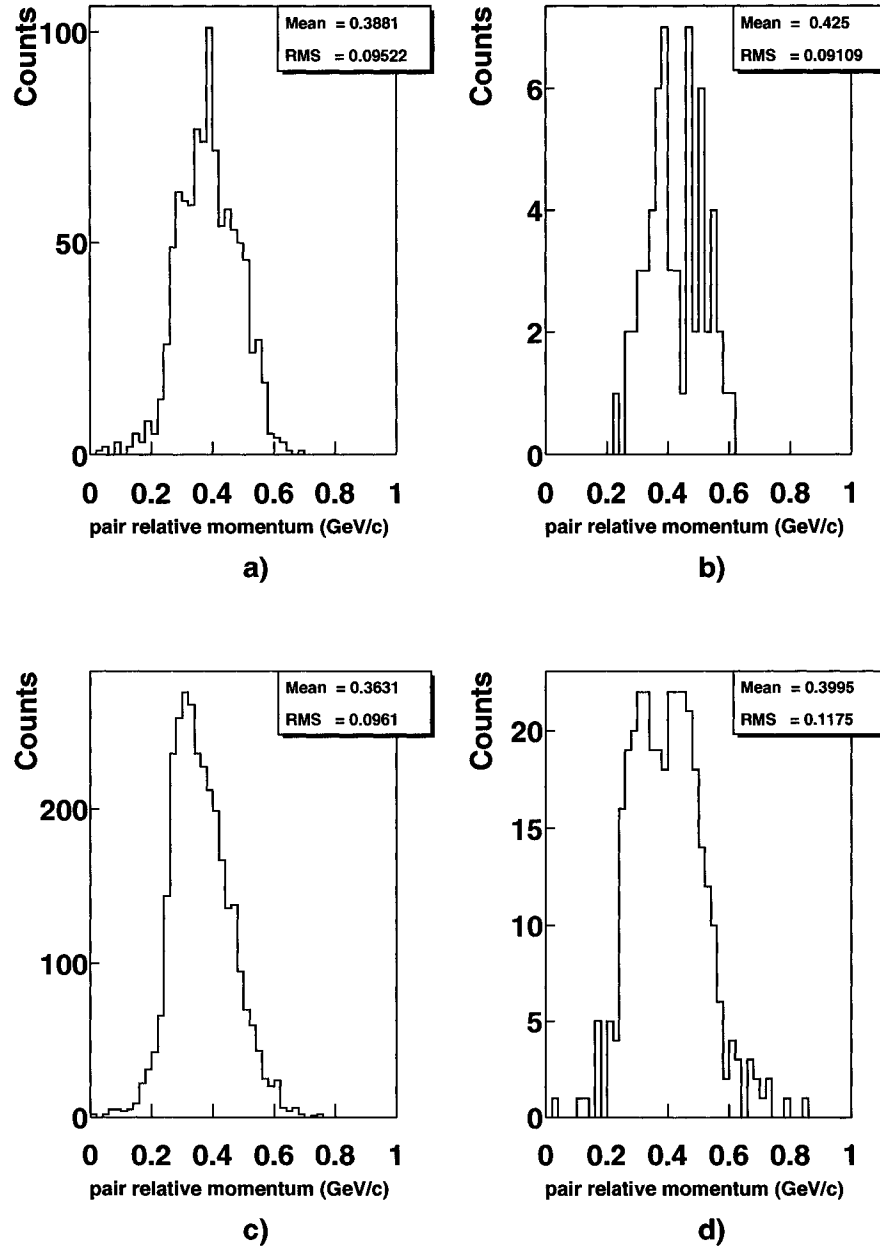
FIG. 71. Pair relative momentum. a) 2.2 GeV pp pair b) 4.4 GeV pp pair c) 2.2 GeV pn pair d) 4.4 GeV pn pair. Cut $p^\perp \leq 0.3$ GeV/c was applied.
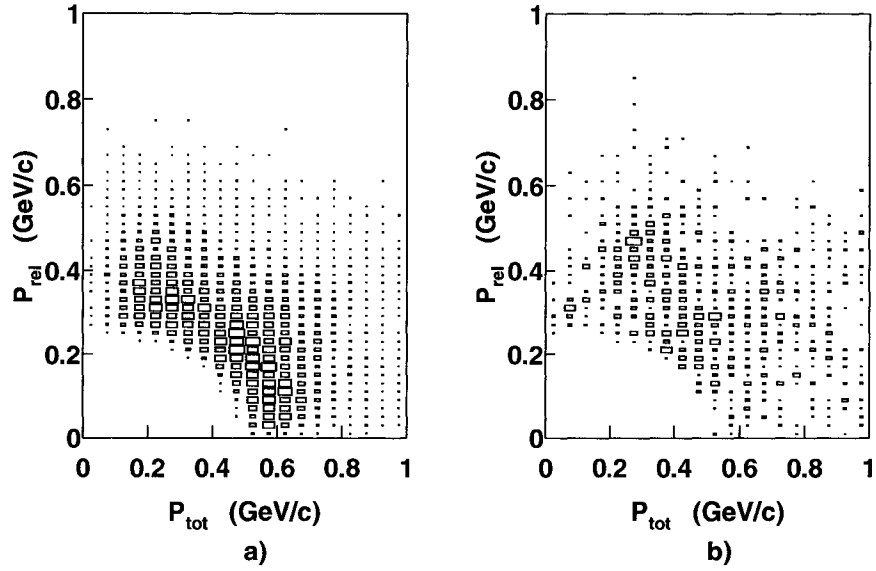
FIG. 72. The pn pair relative momentum versus total momentum. a) 2.2 GeV data; b) 4.4 GeV data. Cut $p^{\perp} \leq 0.3$ GeV/c was not applied. Note the hole in the lower left corner which is due to the $p_p \geq 0.25$ GeV/c cut.

Figure 73). Selected fast NN pairs have small momentum parallel $\vec{q}$ ($P^{\parallel}_{pair} \approx 5\%$ of $|\vec{q}|$) and are almost isotropic with respect to $\vec{q}$ (see bottom distributions in Figure 73). Figure 74 shows the p_{tot} and p_{rel} distributions at 2.2 and 4.4 GeV from Figures 70 and 71.

The correlated pair distributions are shown in Figure 74. The 2.2 GeV plots are corrected for the CLAS proton acceptance. The 4.4 GeV plots are not. The fast pn and pp pair distributions are overlaid for comparison. There is clearly little differemce in shape between them. The 4.4 GeV distributions are also quite similar to the 2.2 GeV distributions.

Now if we collect all the observations made until now which are:

1) Fast NN pairs are back-to-back;

2) Fast NN pairs are almost isotropic;

3) Fast NN pairs have small average momentum along direction of $\vec{q}$;

4) We see similar total and relative momentum distributions for pp and pn pairs;

5) We see similar total and relative momentum distributions for two different Q^2 bins ($0.5 < Q^2 < 1$ and $1 < Q^2 < 2$ (GeV/c)^2); we conclude that we have measured
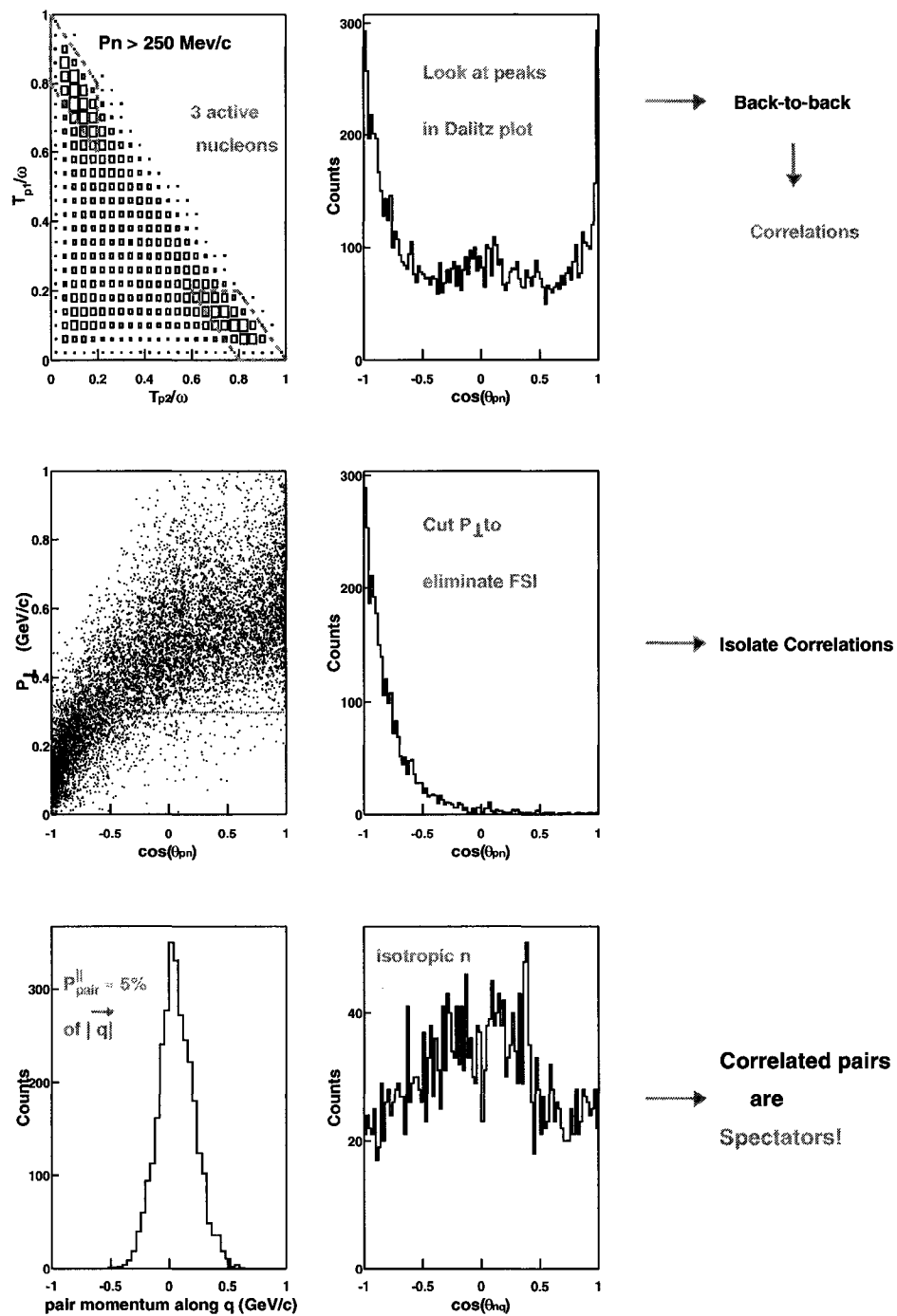
FIG. 73. Summary of the analysis path.
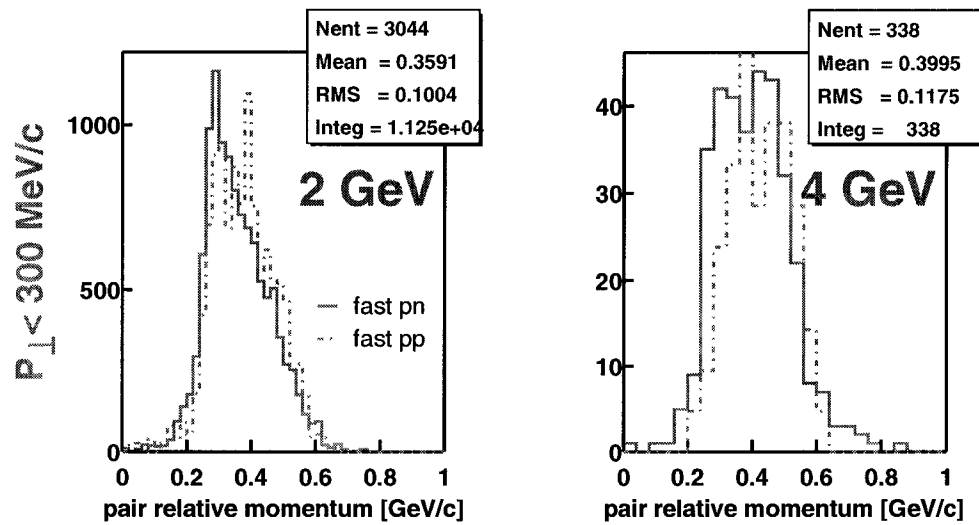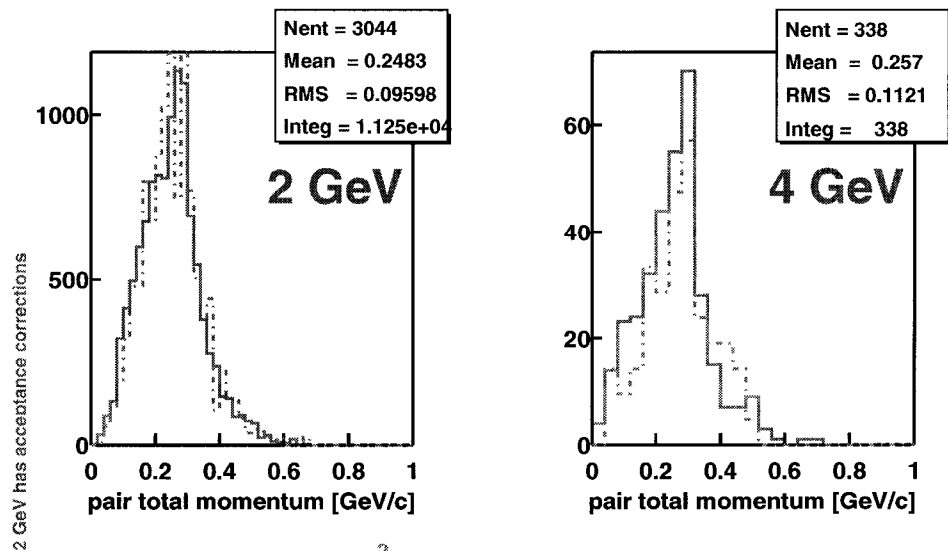
FIG. 74. Summary of the correlated NN pair distributions. The statistics box refer to the pn distributions. The pp distributions have been rescaled to have the same integral as the pn distributions. The number of entries does not match the vertical scale at 2.2 GeV due to the acceptance corrections.
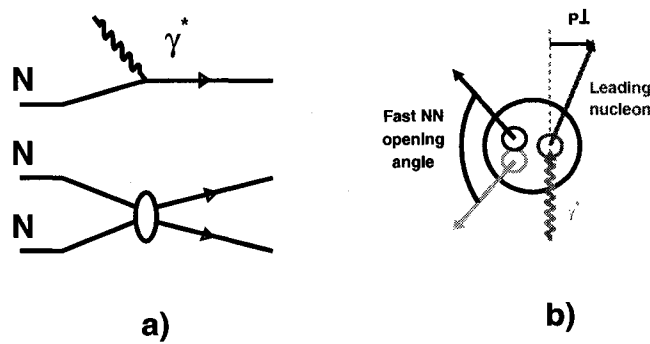
FIG. 75. Process of emission of the two correlated nucleons by hitting the third nucleon. a) Diagram of the process (the same as in Figure 4 a)); b) Cartoon of the process showing the absorption of the virtual photon on the leading nucleon and emission of the other two correlated spectator nucleons. The perpendicular component of the leading nucleon's momentum $P^\perp$ is also shown.

spectator correlated NN pairs by hitting the third nucleon. The diagram of the process (the same as in Figure 4 a)) and the cartoon showing the absorption of the virtual photon on one of the nucleons and emission of the other two correlated spectator nucleons are shown in Figure 75 a) and b), respectively.

This conclusion requires theoretical corroboration by comparing the data to various models. This part will be discussed in Section 5.4.

4.2 MONTE CARLO PROCESSING

4.2.1 Overview of the Monte Carlo Process

The Monte Carlo process is described by following steps:

1. We generate event

2. We apply loose fiducial cut

3. We calculate the cross section

4. Events are passed through GSIM

5. Events are passed through GPP

6. Events are reconstructed by RECSIS

7. Events are converted to Root format

8. We analyze events with *E2AnaTool* and all standard E2 cuts

9. We apply cross sections as weights and histogram the events

These steps are shown in Figure 76 and discussed in Section 4.2.2.

4.2.2 Event Generator

We developed an event generator for the PWIA model (see Section 5.4.2) which could be also useful for all models that give a cross section differential in $\{E_e, \Omega_e, p_1, \Omega_{p_1}, \Omega_{p_2}\}$.

We generate randomly events isotropically in 8 variables: $E_e, \phi_e, \cos(\theta_e)$ – energy, azimuthal angle and cosine of the polar angle of the outgoing electron, $P_1, \phi_1, \cos(\theta_1)$ – momentum, azimuthal angle and the cosine of the polar angle of the first outgoing nucleon, $\phi_2, \cos(\theta_2)$ – azimuthal angle and cosine of the polar angle of the second outgoing nucleon (all in the lab frame). The range of values for each variable is shown in Table XVII. (1,2,3) can stand for any permutation of (p_1, p_2, n). We assume for calculational purposes that the first nucleon absorbed the virtual photon $q_\mu = (\vec{q}, \omega)$. The missing momentum and missing energy for this process are:

$$\vec{P}_{miss} = \vec{q} - \vec{p}_1, \tag{23}$$

$$E_{miss} = M_{He3} + \omega - \sqrt{p_1{}^2 + m_1{}^2}, \tag{24}$$

where M_{He3} is the mass of ^{3}He ; p_1, m_1 are the momentum and mass of the ejected nucleon.

The minimal recoil energy of the remaining pair is:

$$E_r = \sqrt{p_{miss}{}^2 + (m_2 + m_3)^2}, \tag{25}$$

where m_2, m_3 are masses of the second and the third nucleons.

Our requirement is that the missing energy must be greater than the minimum possible recoil energy:

$$E_{miss} \geq E_r, \tag{26}$$
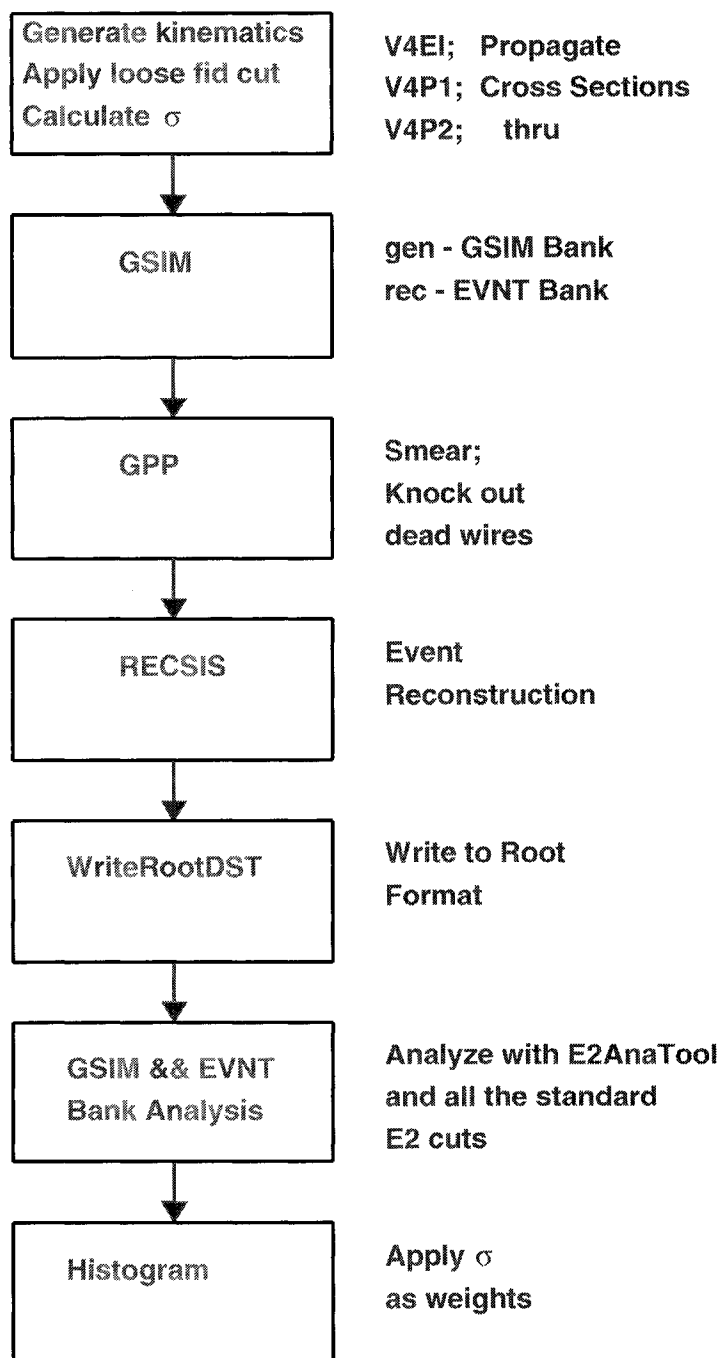
FIG. 76. The Monte Carlo process flowchar.

which allows us to keep only physical solutions. The subroutine *GenEvent* that generates the scattered electron and the three nucleons in the final state is presented in Appendix E.

In order to save simulation time, after generating the event we applied loose fiducial cuts to eliminate events where CLAS could not detect all of the charged particles. In this case, the ϕ range was about 10% larger than the actual fiducial region. We applied the same cuts as for data to select NN correlated pairs, except loose kinetic energy cuts $T_1, T_2 < 0.23\omega$.

Finally, we generated 9 and 6 million events (total) at 2.2 and 4.4 GeV, respectively, for all three index combinations of nucleons: (1,2,3)=(ppn), (pnp), and (npp), where indices 1, 2 and 3 refer to the struck, recoil and spectator nucleons, respectively. Actually, we generated a lot more events than that, these 9 and 6 million events refer to events passing all the cuts.

The PWIA cross section for each event was calculated by calling the external subroutine *eheppn* written by Misak Sargsian. The cross section is calculated differently for each index combination. Energies and momenta of the generated electron and two protons as well as the cross section for each event were saved to an output file in BOS format. See Section 5.4.2 for PWIA details.

Next, the generated events were processed by GSIM, GPP and RECSIS. GSIM and GPP were earlier discussed in Section 3.5. The output reconstructed and generated events are saved in the EVNT and GSIM banks, respectively [1]. This output file of RECSIS was converted to root format (see Appendix A) by using the *WriteRootDST* program written by Gagik Gavalian. These files were analyzed by analysis routines implemented in the *E2AnaTool* code.

4.2.3 Proton Acceptance Corrections

In order to relate the experimental yields to the cross sections we need to calculate the acceptance and the efficiency of the detector. Due to the very high complexity of the CLAS, the geometrical acceptance, the detector efficiency calculations, and the detector resolution are hard to separate. This can be solved by introducing a combined correction factor that includes both the geometry of the detector, and the inefficiencies and resolutions of detection and reconstruction. Therefore this combined correction factor will be referred to as "acceptance corrections".

---

[1] The structure of these banks is determined by the TGSIMClass in Appendix A

TABLE XVII. Kinematic variables for ^{3}He(e,e'pp)n simulation. $E_{threshold} = 0.35$ GeV for 2.2 GeV and $E_{threshold} = 0.8$ GeV for 4.4 GeV

Variable	Range
E_e	$[E_{threshold}, E_{beam}]$
ϕ_e	$[0, 2\pi]$
$\cos(\theta_e)$	$[\cos 15°, \cos 45°]$
P_1	$[0, E_{beam}]$
ϕ_1	$[0, 2\pi]$
$\cos(\theta_1)$	$[-1, 1]$
ϕ_2	$[0, 2\pi]$
$\cos(\theta_2)$	$[-1, 1]$

The PWIA distributions are similar to the data and therefore can be used for acceptance corrections (see the results of the comparison PWIA to data in Sections 5.4.2 and 5.1).

To determine the acceptance correction factor, we generated events, within a model, and passed them through the CLAS Monte Carlo and reconstruction software. The ratio of reconstructed to generated events weghted with model cross sections for a particular kinematic bin is the acceptance correction factor for that bin. This procedure is clearly model dependent. However, this model dependence vanishes in the limit that the kinematic bin size is tiny if we neglect the effects of the CLAS resolution. Therefore we also studied the dependence of these correction factors on the bin size. We determined that the model dependence was insignificant when further changing the bin size did not significantly change the corrected spectra.

The ^{3}He(e,e'pp)n reaction at fixed beam energy can be defined by 8 independent kinematical variables to uniquely determine all other kinematical quantities. To generate events for the PWIA model, we used the variables that the cross section is differential in: E_e, Ω_e, p_1, Ω_{p_1}, and Ω_{p_2}. For acceptance calculations we bin the data in other, more physics related, variables: Q^2, ω, ϕ_e, p_{rel}, $p_m^{\parallel}$, $p_m^{\perp}$, $\cos(\theta_{p_{tot}p_{rel}})$ and ϕ_{pm}, where Q^2, ω are the square of the four-momentum and the energy transfer; ϕ_e is the azimuthal angle of the scattered electron; p_{rel} is the pair relative momentum; $p_m^{\parallel}$, $p_m^{\perp}$ are the parallel and perpendicular components of the leading nucleon missing momentum $(\vec{p}_m = \vec{q} - \vec{P}_{leading} = -\vec{p}_{tot})$; $\cos(\theta_{p_{tot}p_{rel}})$ is the cosine of the angle between

the directions of the pair total and relative momentum vectors (see Equation 21 and 22); and ϕ_{pm} is the azimuthal angle of the leading nucleon's missing momentum relative to $\vec{q}$.

The cross section is uniform in ϕ_e and should be mostly uniform in ϕ_{pm}, therefore averaging over 2π will not introduce any uncertainty and will increase the statistics in the bins. The binning in the remaining 6 variables is done by the following procedure:

1. For each of the 6 variables, we choose an appropriate number of bins

2. We divide the range of that variable so that there are an equal number of data events in each bin (see Figure 77)

3. We generate a tremendous number of events ($\approx 5 \times 10^9$ events), using the PWIA event generator with the PWIA cross sections as a weight

4. We apply loose electron fiducial cut, loose T_{p_1} vs T_{p_2} cut ($T_p \leq 0.23\omega$) and $p_m^\perp \leq 300$ MeV/c cut

5. We pass these events through GSIM (the CLAS GEANT Monte Carlo Simulation), GPP (to eliminate bad detector channels) and RECSIS (to reconstruct the events)

6. We apply the following cuts to generated events:
   a) electron cuts on the reconstructed electron as follows from Table XIX
   b) fast pair cuts ($p_p \geq 250$ MeV/c; $T_p \leq 0.2\omega$) and leading nucleon cut ($p_m^\perp \leq$ 300 MeV/c) on the generated nucleons

7. We apply all standard cuts to the reconstructed events
   a) electron cuts as follows from Table XIX
   b) proton cuts as follows from Table XX
   c) fast pair cuts ($p_p \geq 250$ MeV/c; $T_p \leq 0.2\omega$) and leading nucleon cut ($p_m^\perp \leq$ 300 MeV/c)

8. We integrate the total cross section for all generated events (after cuts) that lie in each (p_{rel}, $p_m^\parallel$, ω, Q^2, $p_m^\perp$, $\cos(\theta_{p_{tot}p_{rel}})$) bin

9. We integrate the total cross section for all reconstructed events (after cuts) that lie in each (p_{rel}, $p_m^\parallel$, ω, Q^2, $p_m^\perp$, $\cos(\theta_{p_{tot}p_{rel}})$) bin

TABLE XVIII. Bin configurations

Configuration	Number of bins per variable						Total bins
	p_{rel}	$p_m^{\parallel}$	ω	Q^2	$p_m^{\perp}$	$\cos(\theta_{p_{tot}p_{rel}})$	
1	1	1	1	1	1	1	1
2	4	4	3	3	4	3	1728
3	8	4	3	3	4	3	3456
4	4	8	3	3	4	3	3456
5	4	4	6	3	4	3	3456
6	4	4	3	6	4	3	3456
7	4	4	3	3	8	3	3456
8	4	4	3	3	4	6	3456
9	8	8	3	3	4	3	6912
10	8	8	6	6	4	3	27648

10. For each bin, we use the ratio of generated cross sections to reconstructed cross section as the acceptance correction factor for that bin

11. We determine the statistical uncertainty of this factor using the weighted binomial distribution

12. We apply these correction factors to the data, event by event, to get the acceptance corrected histograms

Kinematic variables and binning

We arbitrarily arrange the 6 kinematical variables in the following order: p_{rel}, $p_m^{\parallel}$, ω, Q^2, $p_m^{\perp}$, $\cos(\theta_{p_{tot}p_{rel}})$. We studied the effects of bin size on the correction factors using 10 different bin configurations. For example, the 111111 configuration is defined by 1 bin in each variable (averaging), the 443343 configuration by 4 bins in p_{rel}, 4 bins in $p_m^{\parallel}$, 3 bins in ω, 3 bins in Q^2, 4 bins in $p_m^{\perp}$, and 3 bins in $\cos(\theta_{p_{tot}p_{rel}})$, and so on. The size of the bin for each variable depends on the shape of the distribution and is determined by requiring equal number of events in each one dimensional bin. The selected bin configurations are presented in Table XVIII. The 6 kinematical data distributions used in acceptance calculations as well as the uniformly distributed ϕ_e and ϕ_{pm} distributions are shown in Figure 77.
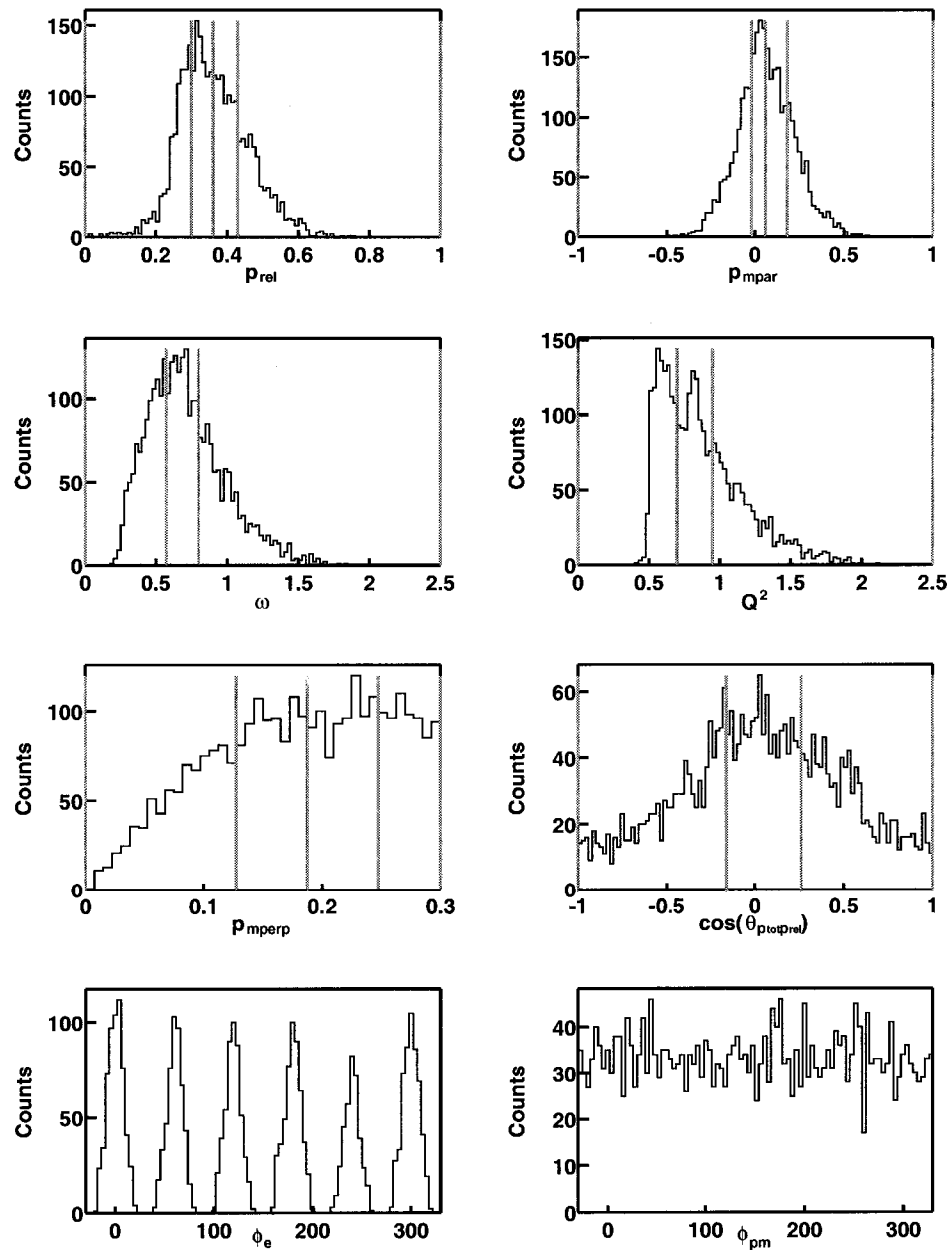
FIG. 77. Kinematical variables distributions for fast pn pairs at 2.2 GeV. Only 6 top distributions were used for binning. Vertical lines indicate the bins for each variable. Selected number of bins per distribution corresponds to configuration 443343.

TABLE XIX. Cuts applied to both reconstructed and generated electrons for fast
pn pairs at 2.2 GeV. The number of electrons selected by these cuts are shown for
simulated fast pn pairs at 2.2 GeV.

Cuts	True	True %	False	False %	Total
Good TBT	2815206	93.84	184791	6.16	2999997
Fiducial cut	2127458	75.57	687748	24.43	2815206
EC cut	1815547	85.34	311911	14.66	2127458
Z Vertex cut	1426960	78.60	388587	21.40	1815547

Analysis of the reconstructed and generated events

As was mentioned earlier, we analyze reconstructed and generated events separately.
We apply the same electron cuts for both reconstructed and generated events, ana-
lyzing only events with a "good" reconstructed electron in both EVNT and GSIM
banks. The information about reconstructed and generated events were written to
EVNT and GSIM banks, respectively, during GSIM–RECSIS event processing. The
structure of these banks is given in Appendix A. Table XIX shows the number of
processed electron events surviving various cuts for simulated fast pn pairs at 2.2
GeV. The table consists of TRUE and FALSE columns that show the number of
electrons that passed and failed the cuts, respectively. These numbers are also given
in percent with respect to the total number of electrons before the cut. Table XX
shows the number of processed two proton events from the EVNT bank with cuts
applied to each proton for simulated fast pn pairs at 2.2 GeV. The cuts are the same
as for data. The structure of this table is the same as for Table XIX. The simu-
lation of fast np and pp pairs are done separately and similarly and the respective
statistics tables are similar. Note that we consider simulated fast pn and np events
undistinguishable, so we average the results from these events.

Next we apply the same cuts as for data ($T_{fast} \leq 0.2\omega$, $p_N \geq 250$ MeV/c, $P_\perp \leq$
300 MeV/c) to select events with fast pp and pn pairs. We weight each event with
the PWIA corresponding cross section. We binned both generated and reconstructed
events in the same way as the data.

The acceptance for each bin and each configuration is extracted as the ratio of
the sum of the weights of simulated reconstructed events in that bin to the sum

TABLE XX. Cuts applied to reconstructed two proton events in fast pn pair simulation at 2.2 GeV.

Cuts	True	True %	False	False %	Total
^{3}He(e,e'pp)	804341	56.37	622619	43.63	1426960
Good TBT	700986	87.15	103355	12.85	804341
Fiducial cut	445896	63.61	255090	36.39	700986
Proton PID	395896	88.79	50000	11.21	445896
$Z^{electron}_{vertex}$-Z^{proton}_{vertex}	355269	89.74	40627	10.26	395896
^{3}He(e,e'pp)n	334023	94.02	21246	5.98	355269

TABLE XXI. Average acceptance for fast NN pairs at 2.2 and 4.4 GeV. Statistical error calculations are based on weighed binomial distribution errors derrivied in Appendix F.

	2.2 GeV		4.4 GeV	
	fast pp	fast pn	fast pp	fast pn
Average acceptance	0.231	0.260	0.266	0.323
Statistical error	0.0009	0.0008	0.0023	0.0018

of the weights of simulated generated events for the same bin. We extracted the average CLAS acceptance from the 111111 configuration. The average acceptance and statistical error for fast pp and pn pairs at 2.2 GeV and 4.4 GeV are given in Table XXI.

In the case of bins where there were zero generated events, we used the average CLAS acceptance (the "111111" acceptance) factor for those bins. This became more of a problem as we increased the number of bins. We also see some cases when the acceptance is larger than unity $(A > 1)$ due to bin migration (events generated in one bin misreconstructed into another). We set a large statistical error $(\sigma_A = 0.99)$ for these acceptances. The statistics for average acceptance replacements and bin migration cases are shown in Table XXII. The distribution of acceptance factors for fast pn pairs from the 443343 configuration is shown in Figure 78.

The acceptance corrections were applied event-by-event. Each data event was weighted by the acceptance correction factor corresponding to the $(p_{rel}, p^{\parallel}_m, \omega, Q^2,$

TABLE XXII. Average acceptance replacements and bin migration statistics. These are shown for fast NN pairs at 2.2 and 4.4 GeV for differents bin configurations. The number of bins corresponding to each configuration are shown in Table XVIII.

	2.2 GeV		4.4 GeV	
	fast pp	fast pn	fast pp	fast pn
111111 Acceptance replacement	0	0	0	0
Bin migration	0	0	0	0
443343 Acceptance replacement	441	406	779	993
Bin migration	17	35	22	17
843343 Acceptance replacement	1125	1052	1843	2089
Bin migration	41	78	40	50
483343 Acceptance replacement	1120	1095	1885	2146
Bin migration	35	75	36	45
446343 Acceptance replacement	1298	1217	1964	2195
Bin migration	39	87	46	44
443643 Acceptance replacement	1120	1086	1895	2123
Bin migration	42	93	33	50
443383 Acceptance replacement	1019	970	1778	2048
Bin migration	33	76	41	60
443346 Acceptance replacement	1071	999	1797	2105
Bin migration	35	75	46	55
883343 Acceptance replacement	2810	2701	4335	4719
Bin migration	84	147	67	85
886643 Acceptance replacement	17595	17354	22579	23181
Bin migration	308	641	177	233
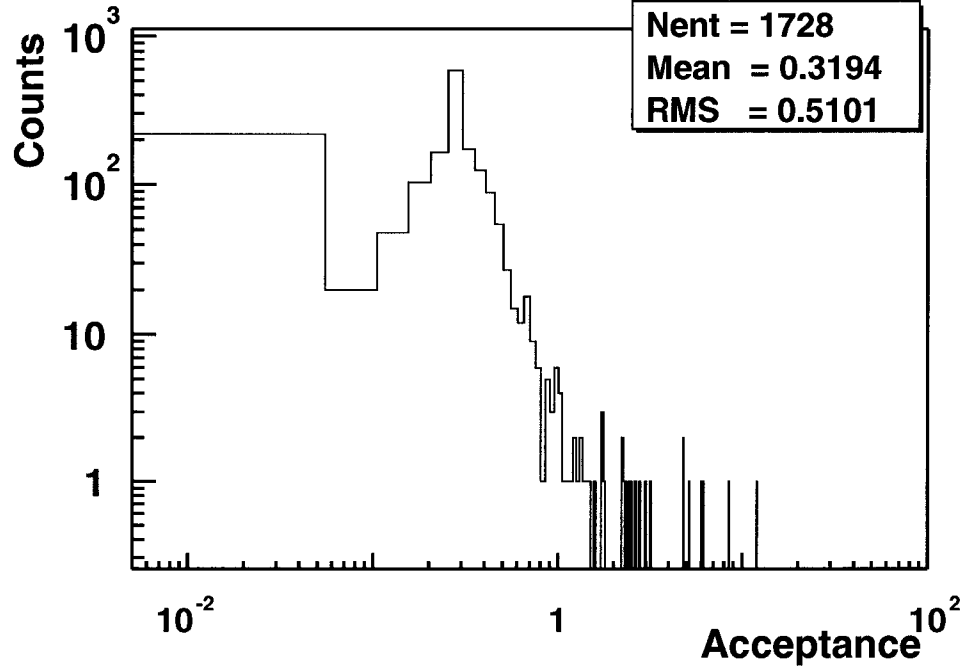
FIG. 78. Typical acceptance distribution. Acceptance for fast pn pairs at 2.2 GeV from 443343 configuration.

$p_m^{\perp}$, $\cos(\theta_{p_{tot}p_{rel}})$) bin that the event is in (see Table XVIII).

Both the number of data events in each bin and the acceptance correction factor have statistical errors. Our calculation of the statistical errors for the acceptance factor in each bin is based on the binomial error calculations for events with nonuniform weights derived in Appendix F. In each bin the integrated cross section is calculated as:

$$\sigma = \sum_{events} \frac{N_{events}}{A} \tag{27}$$

We calculate the combined data plus acceptance correction statistical error for the integrated cross section for each bin:

$$\delta\sigma^2 = \sum_{events} \left(\frac{\delta A^2}{A^4} + \frac{1}{A^2} \right) \tag{28}$$

where A and δA are the acceptance factor and acceptance factor error for the bin associated with the analyzed event. In the limiting case of $A = 1$ and $\delta A = 0$, this reduces to the poisson error $\delta\sigma^2 = N_{events}$.

The results of the acceptance corrected data with fast pn pairs at 2.2 GeV for

different bin configurations are shown in Figure 79 and Figure 80. We see the biggest change in magnitude from uncorrected data to corrected by average acceptance (configuration 111111). There is a small change in shape from 111111 to 443343 and negligible changes for the other bin configurations. The statistical errors and the change in integrated cross section $\Delta \int d\sigma$ for different bin configurations are given in Table XXIII. We used the 443343 configuration as a benchmark. The $\Delta \int d\sigma$ values for all other configurations are defined with respect to configuration 443343. Our systematic uncertainties due to model dependence are based on the variation of the integrated cross sections as we increase the number of bins compared to 443343. We might expect that the $\Delta \int d\sigma$ values in Table XXIII should increase with increasing number of bins, but unfortunately that is not the case. Due to setting an average acceptance for bins where our knowledge of acceptance is limited and due to the fact that the number of such bins is increasing with larger number of bins, we are biasing results of acceptance correction toward the 111111 configuration. Acceptance calculation appears to have converged at 2.2 GeV for both pp and pn pairs since increasing the number of bins beyond 443343 does not change the cross sections significantly. Looking at the $\Delta \int d\sigma$ values in the Table XXIII one can see that these changes in integrated cross section are not converged for fast pp and partially converged for fast pn pairs at 4.4 GeV.
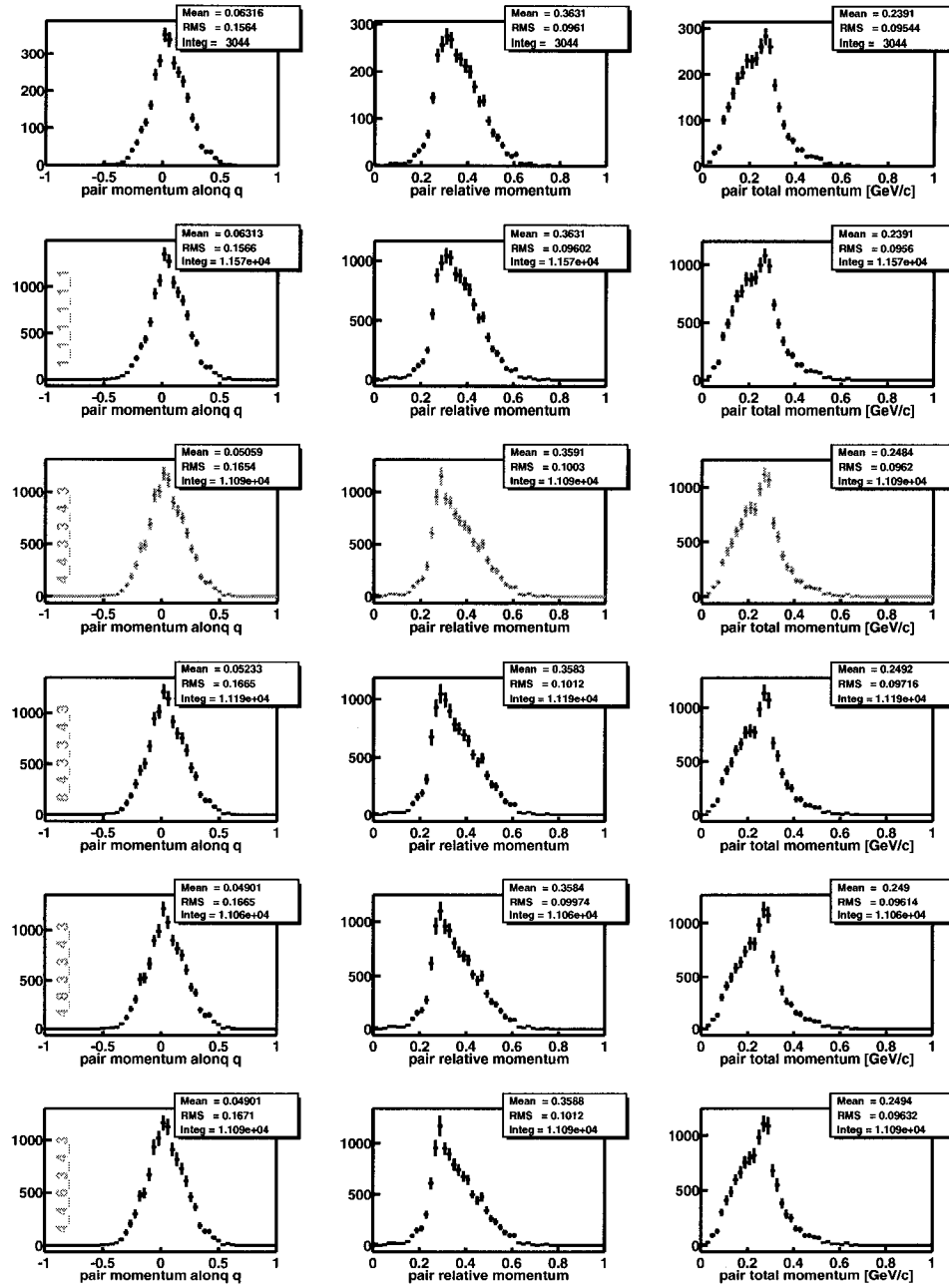
FIG. 79. Pair total momentum parallel to $\vec{q}$, pair relative momentum and pair total momentum distributions with acceptance corrections from the first five bin configurations. Note that the top plots are uncorrected data. Only fast pn pairs at 2.2 GeV are shown.
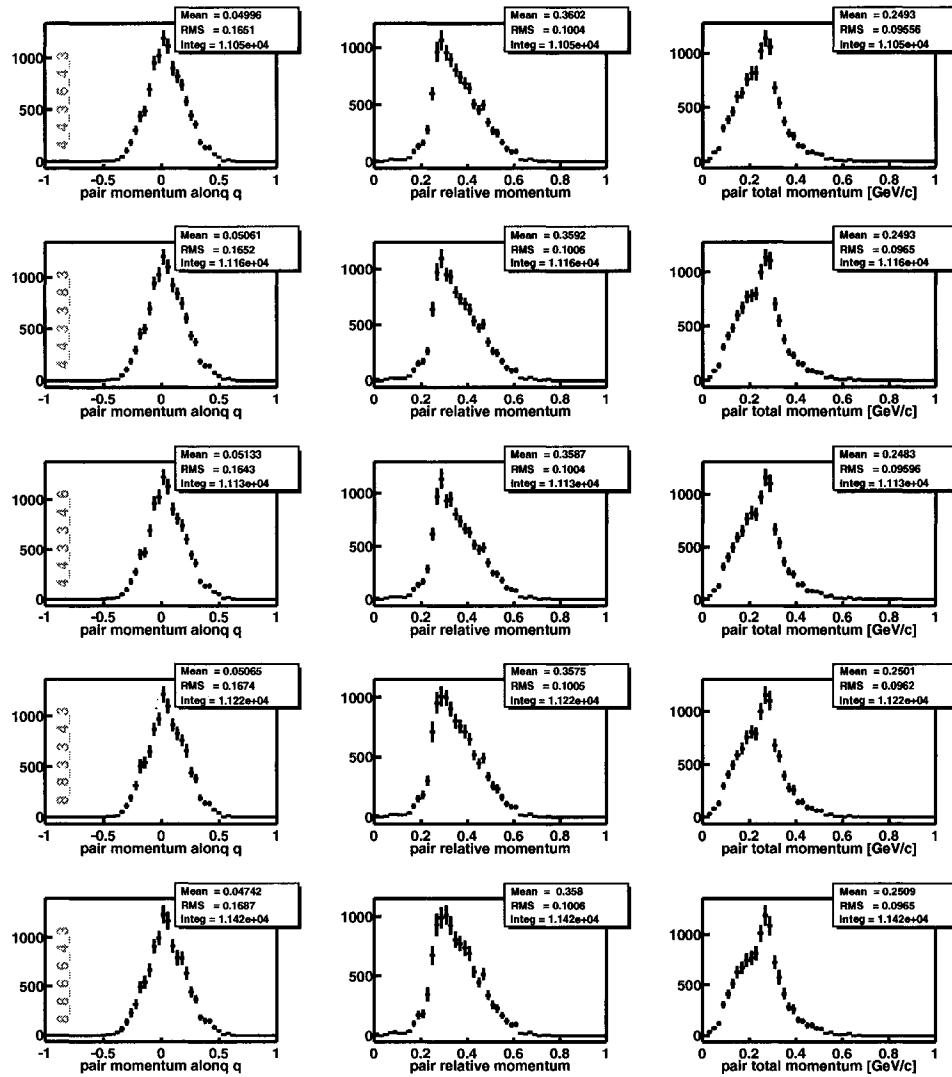
FIG. 80. Pair total momentum parallel to $\vec{q}$, pair relative momentum and pair total momentum distributions with acceptance corrections from the last five bin configurations. Only fast pn pairs at 2.2 GeV are shown.

TABLE XXIII. Percent change in integrated cross section $\Delta \int d\sigma$, and statistical errors in the integrated cross section. These are shown for fast NN pairs at 2.2 and 4.4 GeV for different bin configurations. The numbers are given in percent. The $\Delta \int d\sigma$ values are the change with respect to configuration 443343.

	2.2 GeV		4.4 GeV	
	fast pp	fast pn	fast pp	fast pn
111111 $\Delta \int d\sigma(\%)$	-1.9	4.3	8.8	1.0
Statistical error	**3.3**	**1.8**	**13.0**	**5.6**
443343 $\Delta \int d\sigma(\%)$	—	—	—	—
Statistical error	**3.6**	**2.0**	**18.7**	**8.0**
843343 $\Delta \int d\sigma(\%)$	0.1	0.8	-21.1	-1.4
Statistical error	**3.9**	**2.1**	**19.8**	**8.1**
483343 $\Delta \int d\sigma(\%)$	1.0	-0.3	-21.4	-2.0
Statistical error	**3.9**	**2.0**	**16.8**	**7.6**
446343 $\Delta \int d\sigma(\%)$	-0.6	0.0	-10.1	-8.4
Statistical error	**3.8**	**2.1**	**24.0**	**7.3**
443643 $\Delta \int d\sigma(\%)$	0.1	-0.4	-20.2	-4.9
Statistical error	**3.8**	**2.1**	**18.0**	**7.3**
443383 $\Delta \int d\sigma(\%)$	0.9	0.6	-7.0	-4.7
Statistical error	**3.8**	**2.1**	**30.0**	**7.5**
443346 $\Delta \int d\sigma(\%)$	0.4	0.3	-3.5	-4.6
Statistical error	**3.8**	**2.1**	**20.4**	**8.5**
883343 $\Delta \int d\sigma(\%)$	0.0	1.1	-19.1	-2.9
Statistical error	**4.1**	**2.2**	**15.7**	**7.8**
886643 $\Delta \int d\sigma(\%)$	-2.7	2.8	-14.2	1.7
Statistical error	**4.6**	**2.4**	**16.0**	**12.6**

CHAPTER 5

RESULTS AND DISCUSSIONS

This chapter describes our results and discussions. Section 5.1 presents the cross section calculations for both the data and the PWIA model. Section 5.2 describes the radiative corrections applied to the data. Section 5.3 describes the systematic uncertainties for our measurements. Comparison of the data with available theory models is presented in Section 5.4. The results are discussed and summarized in Section 5.5.

5.1 CROSS SECTION CALCULATIONS

5.1.1 Data Cross Section

The cross section for a bin ΔK in kinematic variable K is

$$\left(\frac{d\sigma}{dK}\right)_{data} = \frac{N_{dK}}{N_e N_t \Delta K} \tag{29}$$

where N_{dK} is the number of events in the bin, N_e is the number of electrons hitting the target, N_t is the number of target nuclei, and ΔK is the bin size. N_e and N_t are determined as

$$N_e = \frac{Q_{FCup}}{e} \tag{30}$$

$$N_t = \frac{N_A \rho L_T}{A} \tag{31}$$

where Q_{FCup} is the integrated beam charge (see Table VII), e is the electron charge, N_A is Avogadro's number, ρ is the target density, L_T is the target length (see Table III), and A is the ^{3}He atomic number. The number of events needs to be corrected for various experimental effects, including detection efficiency, detector geometry, cut efficiency, etc. Most of these are included in the acceptance correction factors determined in Section 4.2.3.

For 2.2 GeV data:

$$N_e = 1.190 \times 10^{-3}/1.6 \times 10^{-19} = 7.44 \times 10^{15}; \tag{32}$$

$$N_t = \frac{6.02 \times 10^{23}}{3} \cdot 0.067 \cdot 3.3 = 4.436 \times 10^{-17} \, [nuclei/fb] \tag{33}$$

The scale factor for the data distributions at 2.2 GeV with 20 MeV bins is:

$$\frac{1}{N_e N_t \Delta K} = \frac{1}{7.44 \times 10^{15} \cdot 4.436 \times 10^{-17} \cdot 20} = 0.15\,[fb/MeV] \qquad (34)$$

For 4.4 GeV data:

$$N_e = 0.994 \times 10^{-3}/1.6 \times 10^{-19} = 6.21 \times 10^{15}; \qquad (35)$$

$$N_t = \frac{6.02 \times 10^{23}}{3} \cdot 0.067 \cdot 3.3 = 4.436 \times 10^{-17}\,[nuclei/fb] \qquad (36)$$

The scale factor for the data distributions at 4.4 GeV with 40 MeV bins is:

$$\frac{1}{N_e N_t \Delta K} = \frac{1}{6.21 \times 10^{15} \cdot 4.436 \times 10^{-17} \cdot 40} = 0.09\,[fb/MeV] \qquad (37)$$

5.1.2 PWIA Cross Section

The cross section for the bin ΔK from the PWIA model is

$$\left(\frac{d\sigma}{dK}\right)_{PWIA} = \frac{(\sum_{events} \frac{d^8\sigma}{d\omega d\Omega_e dp_1 \Omega_{p_1} \Omega_{p_2}}) \Delta\omega \Delta\Omega_e \Delta p_1 \Delta\Omega_{p_1} \Delta\Omega_{p_2}}{N_{thrown} \Delta K} \qquad (38)$$

where $\sum_{events} \frac{d^8\sigma}{d\omega d\Omega_e dp_1 \Omega_{p_1} \Omega_{p_2}}$ is the integrated cross section (given in $nb/(GeV^2 sr^3)$) of the reconstructed events calculated by PWIA for events in bin ΔK; $\Delta\omega$, $\Delta\Omega_e$, Δp_1, $\Delta\Omega_{p_1}$, $\Delta\Omega_{p_2}$ are the phase space factors from Table XVII, N_{thrown} is the number of initially generated events, and ΔK is the bin size.

For 2.2 GeV: The phase space factor $\Delta\Gamma = \Delta\omega \Delta\Omega_e \Delta p_1 \Delta\Omega_{p_1} \Delta\Omega_{p_2}$

$$\Delta\Gamma = (E_{beam} - E_{thr}) \cdot 2\pi \cdot [cos(15°) - cos(45°)] \cdot 2.261 \cdot 2 \cdot 2\pi \cdot 2 \cdot 2\pi = 1109.58\,GeV^2 sr^3 \qquad (39)$$

where $E_{thr} = 0.35$ GeV ($E_{thr} = 0.8$ GeV at 4.4 GeV) is the electron energy threshold (see Apendix E). We used only a fraction of generated events for the PWIA cross section calculation (all events were used for extraction of the CLAS acceptance): $N_{thrown}^{pp} = 5 \times 10^8$ and $N_{thrown}^{pn} = 1 \times 10^9$. The scale factors for the fast pp and pn PWIA distributions with 20 MeV bins are:

$$\left(\frac{\Delta\Gamma}{N_{thrown}^{pp} \cdot 20}\right)_{pp} = 1.1 \times 10^{-7}\,GeV^2 sr^3/MeV \qquad (40)$$

$$\left(\frac{\Delta\Gamma}{N_{thrown}^{pn} \cdot 20}\right)_{pn} = 5.5 \times 10^{-8}\,GeV^2 sr^3/MeV \qquad (41)$$

For 4.4 GeV:

$$\Delta\Gamma = 4193.99\, GeV^2 sr^3 \tag{42}$$

We used $N^{pp}_{thrown} = 1.4 \times 10^9$ and $N^{pn}_{thrown} = 2.8 \times 10^9$. The scale factors for the fast pp and pn PWIA distributions with 40 MeV bins are:

$$\left(\frac{\Delta\Gamma}{N^{pp}_{thrown} \cdot 40}\right)_{pp} = 7.6 \times 10^{-8}\, GeV^2 sr^3/MeV \tag{43}$$

$$\left(\frac{\Delta\Gamma}{N^{pn}_{thrown} \cdot 40}\right)_{pn} = 3.8 \times 10^{-8}\, GeV^2 sr^3/MeV \tag{44}$$

5.2 RADIATIVE CORRECTIONS

After the cross section is extracted from the data a final correction needs to be applied: radiative unfolding. The electrons radiate in the presence of the electromagnetic fields which leads to the change of the cross section. Electrons can radiate real or virtual photons either in the electromagnetic (Coulomb) field of the nucleus involved in the reaction (internal bremsstrahlung) or in the electromagnetic field of the other nuclei (external bremsstrahlung). Also the electron-target interaction followed by the ionization of the target atoms results in electron energy losses (Landau straggling).

Internal bremsstrahlung, which was first calculated by Schwinger [99] and later improved by Mo and Tsai [100], [101], has the largest overall contribution to the radiative correction. These processes are shown in Figure 81. We apply corrections to our data accounting for the internal bremsstrahlung only, neglecting the other corrections. External bremsstrahlung correction to the cross section is $\approx 1.5\%$ and Landau straggling correction is less than 0.001% (see Section 5.2.1).

The corrections were applied by multiplying the observed cross section by the Schwinger factor [100], [102]

$$f_{Schw} = \frac{e^{\delta(\Delta E)}}{1 + \delta'} \tag{45}$$

$$\delta(\Delta E) = \frac{\alpha}{\pi} \ln\left(\frac{E_i E_f b}{\eta^2 (\Delta E)^2}\right)\left(\ln\frac{Q^2}{m_e^2} - 1\right) \tag{46}$$

with

$$b = 1 + \frac{2\omega}{M_{He3}}\sin^2(\frac{\theta_e}{2}) \tag{47}$$
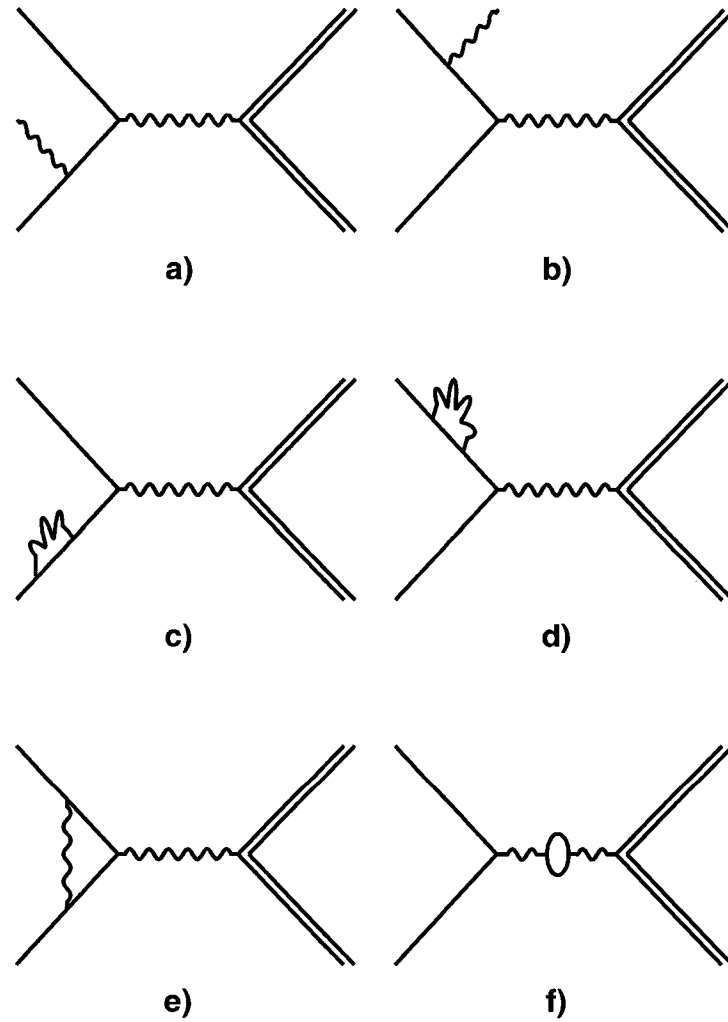
FIG. 81. Feynman diagrams for internal bremsstrahlung. a) and b) correspond to the emission of a real photon from the electron before and after the interaction, respectively. c) and d) result in renormalization of the electron mass. e) corresponds to an overall renormalization of the vertex. f) results in the renormalization of the virtual photon due to the vacuum polarization.

$$\eta = 1 + \frac{2E_i}{M_{He3}} \sin^2(\frac{\theta_e}{2}) \tag{48}$$

$$\delta' = \frac{\alpha}{\pi} \left(\frac{13}{6} \left[\ln \frac{Q^2}{2} - 1 \right] - \frac{17}{18} - \frac{\pi^2}{6} - \frac{1}{2} \ln^2(\frac{E_i}{E_f}) + \Phi(cos^2\frac{\theta_e}{2}) \right) \tag{49}$$

where ΔE is a cutoff energy that was determined as a half of the ^{3}He(e,e′p) missing mass bin (experimental resolution). $\Delta E = 70$ and 120 MeV for 2.2 and 4.4 GeV runs, respectively. α is the fine structure constant, m_e and M_{He3} are, respectively, the electron and ^{3}He masses, E_i and E_f are the energies of incoming and outgoing electrons, and θ_e is the electron scattering angle. The Spence function $\Phi(x)$ is defined by

$$\Phi(x) = \int_0^x \frac{-\ln(1-y)}{y} dy \tag{50}$$

The relative and total momentum of the fast pn pair with and without radiative corrections at 2.2 and 4.4 GeV is shown in Figure 82. The cross sections in Figure 82 were calculated using Equation 29.

The cross sections with radiative corrections for fast pn and pp pairs at 2.2 GeV are shown in Figure 83. The same cross sections at 4.4 GeV are shown in Figure 84. The same cross sections with applied radiative corrections and acceptance corrections (443343 configuration) at 2.2 and 4.4 GeV are shown in Figures 85 and 86, respectively. As one can see there is a factor of 3–4 difference between uncorrected and acceptance corrected data. Figures 87 and 88 are the same as Figures 85 and 86, respectively, but showing the statistical uncertanties extracted in Chapter 4.2.3.

5.2.1 Other Radiative Effects

We also want to estimate the contribution from the other radiative processes: external bremsstrahlung and Landau straggling. Both processes, since they are caused by external nuclei and atoms, have an effect on the cross sections proportional to the target thickness. The correction formulae for these effects are taken from [103]. The correction factor for cross section loss due to external bremsstrahlung is e^{δ_B}, where

$$\delta_B = \frac{t}{x_0 \ln 2} \ln \left(\frac{\Delta E}{E_i} \right) \tag{51}$$

where t is the target thickness, E_i is the energy of the incident electrons and x_0 is the radiation length of the target nuclei. This equation holds for $\frac{t}{x_0 \ln 2} \ll 1$. $t = 0.22$ g/cm^2 for 3.3 cm long ^{3}He target (see also target specifications in Table III).
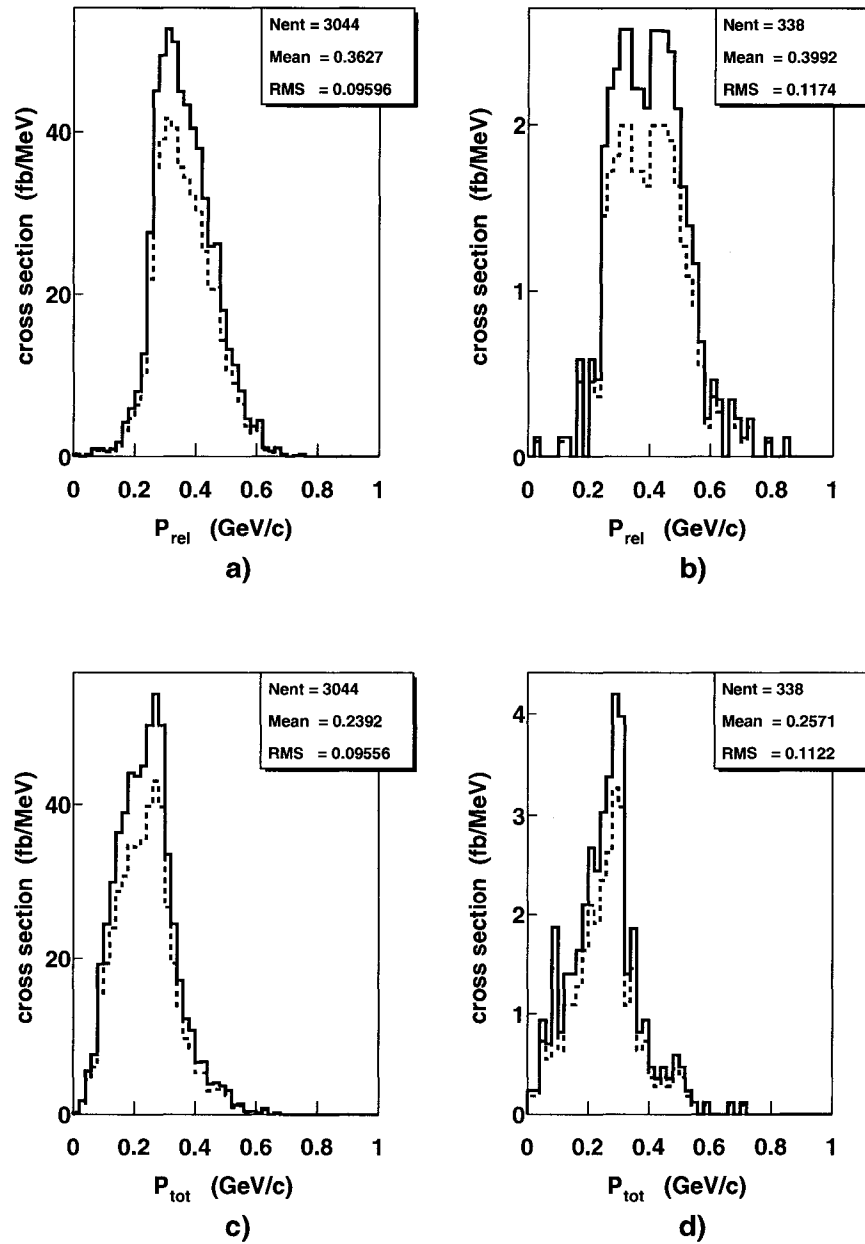
FIG. 82. Comparison of the cross sections with and without radiative corrections. a), b) Cross section vs relative momentum of the fast pn pair at 2.2 and 4.4 GeV, respectively. Dash lines correspond to data with no radiative corrections applied. Histograms are the data with applied radiative corrections. c), d) the same for the total momentum. No acceptance corrections applied.
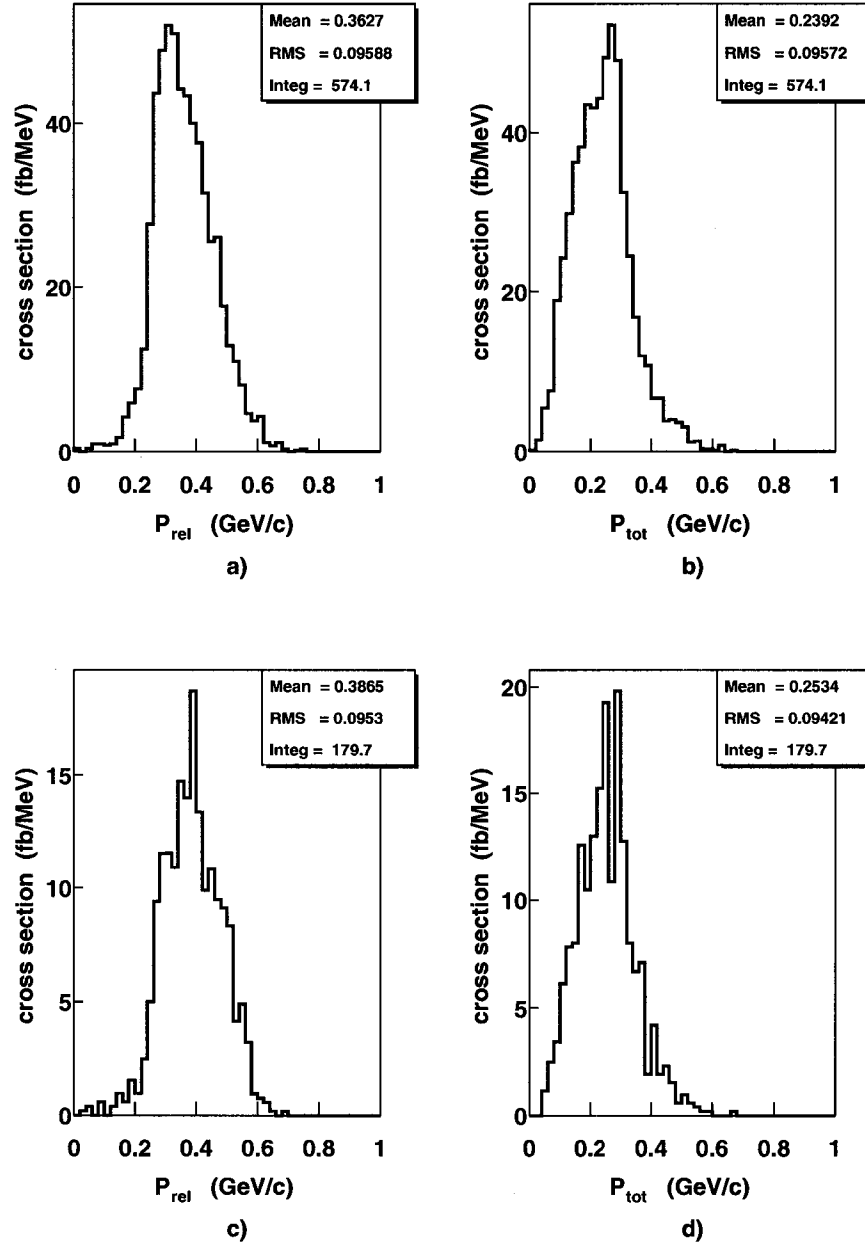
FIG. 83. Cross section vs relative momentum and total momentum at 2.2 GeV with applied radiative corrections. a) Cross section vs relative momentum of the fast pn pair. b) the same for the total momentum; c) and d) the same for fast pp pairs. No acceptance corrections applied.
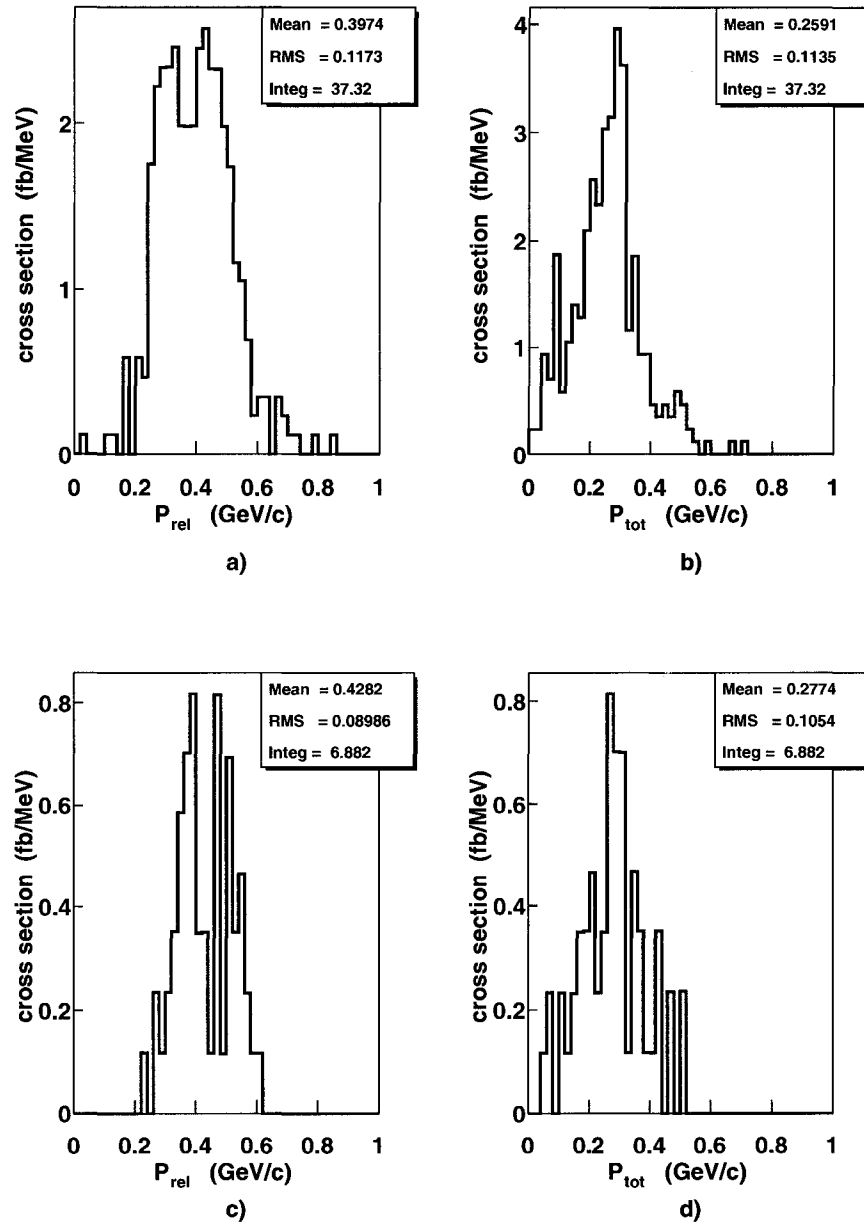
FIG. 84. Cross section vs relative momentum and total momentum at 4.4 GeV with applied radiative corrections. a) Cross section vs relative momentum of the fast pn pair b) the same for the total momentum; c) and d) the same for fast pp pairs. No acceptance corrections applied.
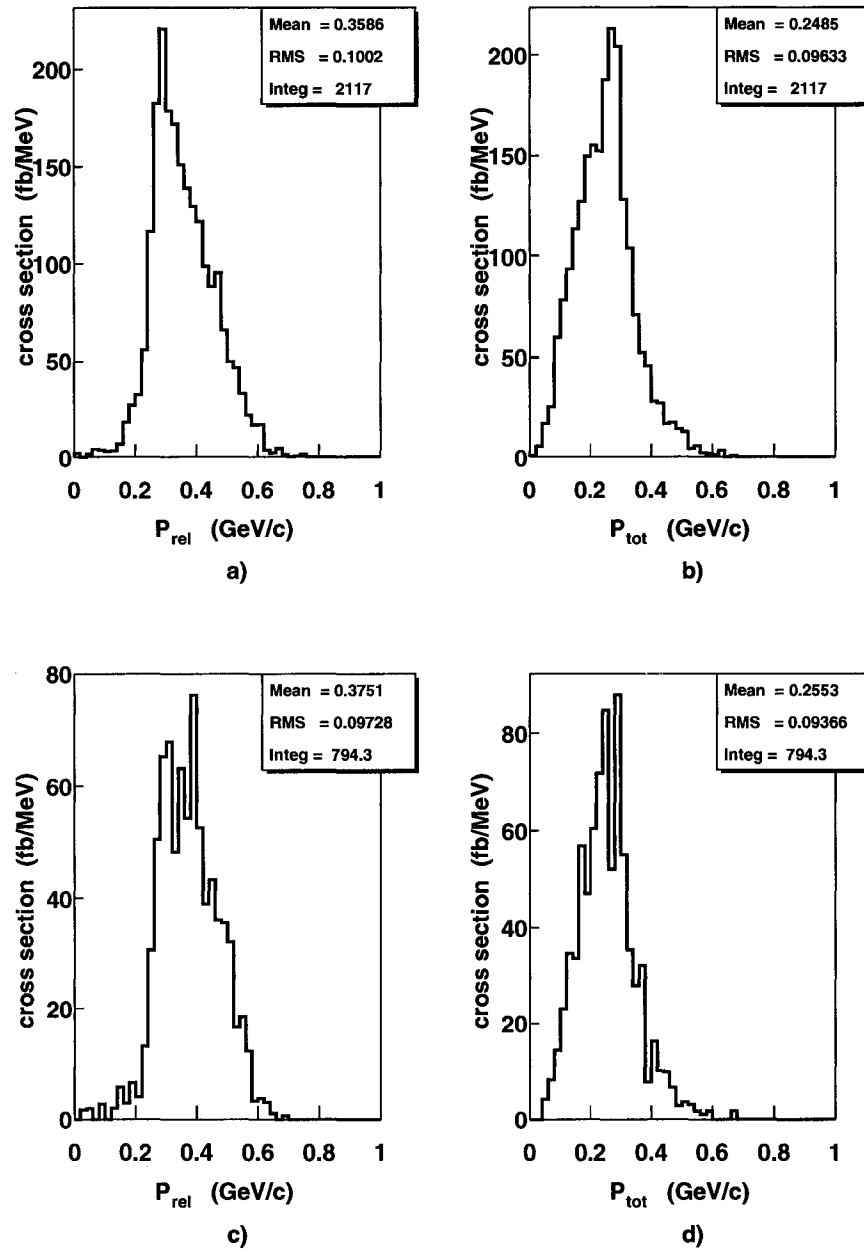
FIG. 85. Cross section vs relative momentum and total momentum at 2.2 GeV with applied radiative and proton acceptance corrections. a) Cross section vs relative momentum of the fast pn pair b) the same for the total momentum; c) and d) the same for fast pp pairs.
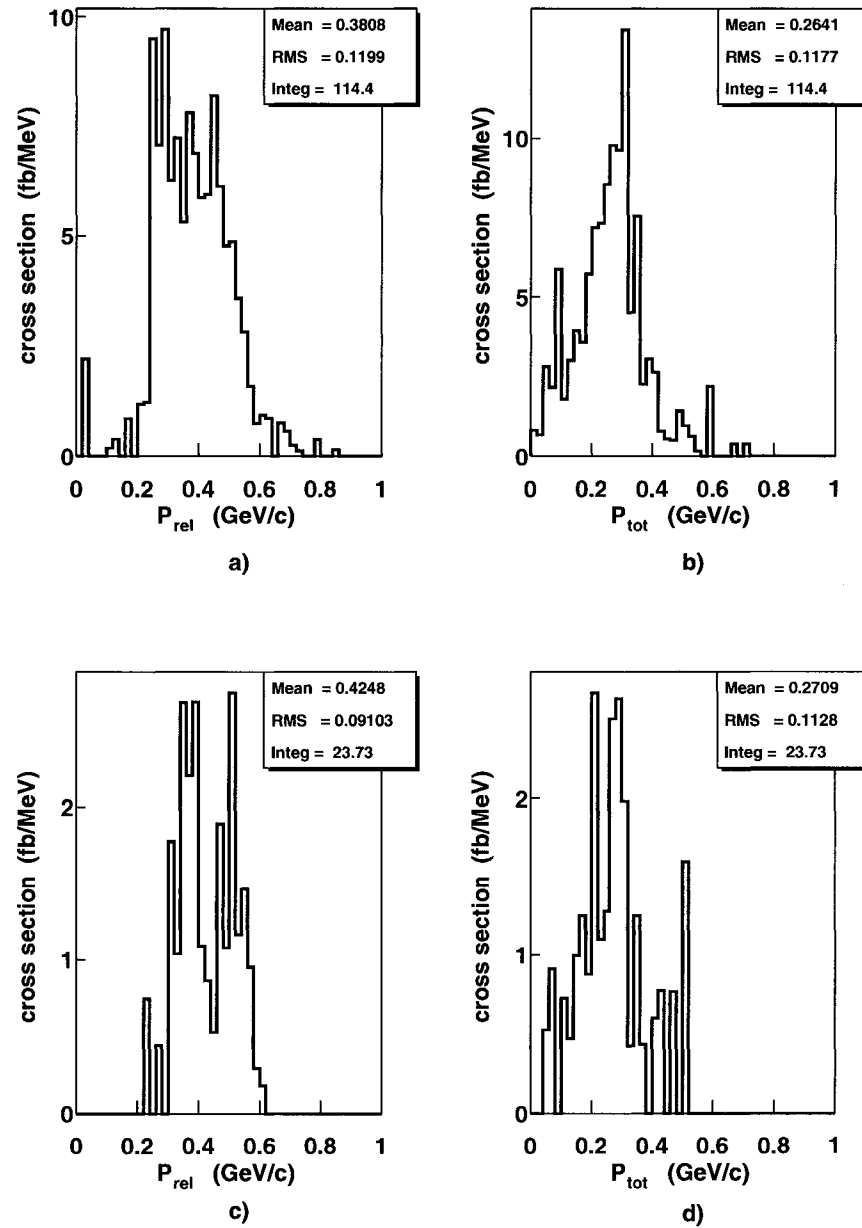
FIG. 86. Cross section vs relative momentum and total momentum at 4.4 GeV with applied radiative and proton acceptance corrections. a) Cross section vs relative momentum of the fast pn pair b) the same for the total momentum; c) and d) the same for fast pp pairs.
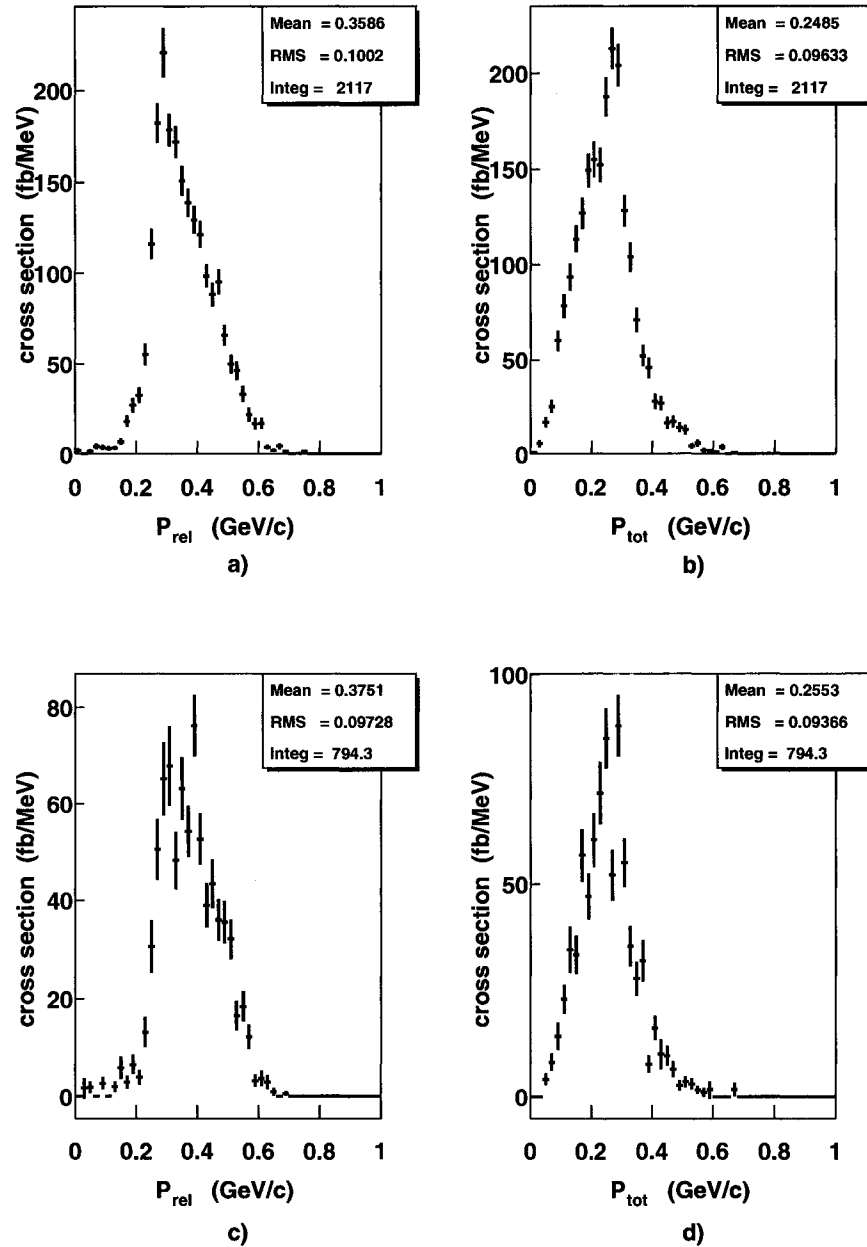
FIG. 87. Cross section vs relative momentum and total momentum at 2.2 GeV with applied radiative and proton acceptance corrections with statistical errors. a) Cross section vs relative momentum of the fast pn pair b) the same for the total momentum; c) and d) the same for fast pp pairs.
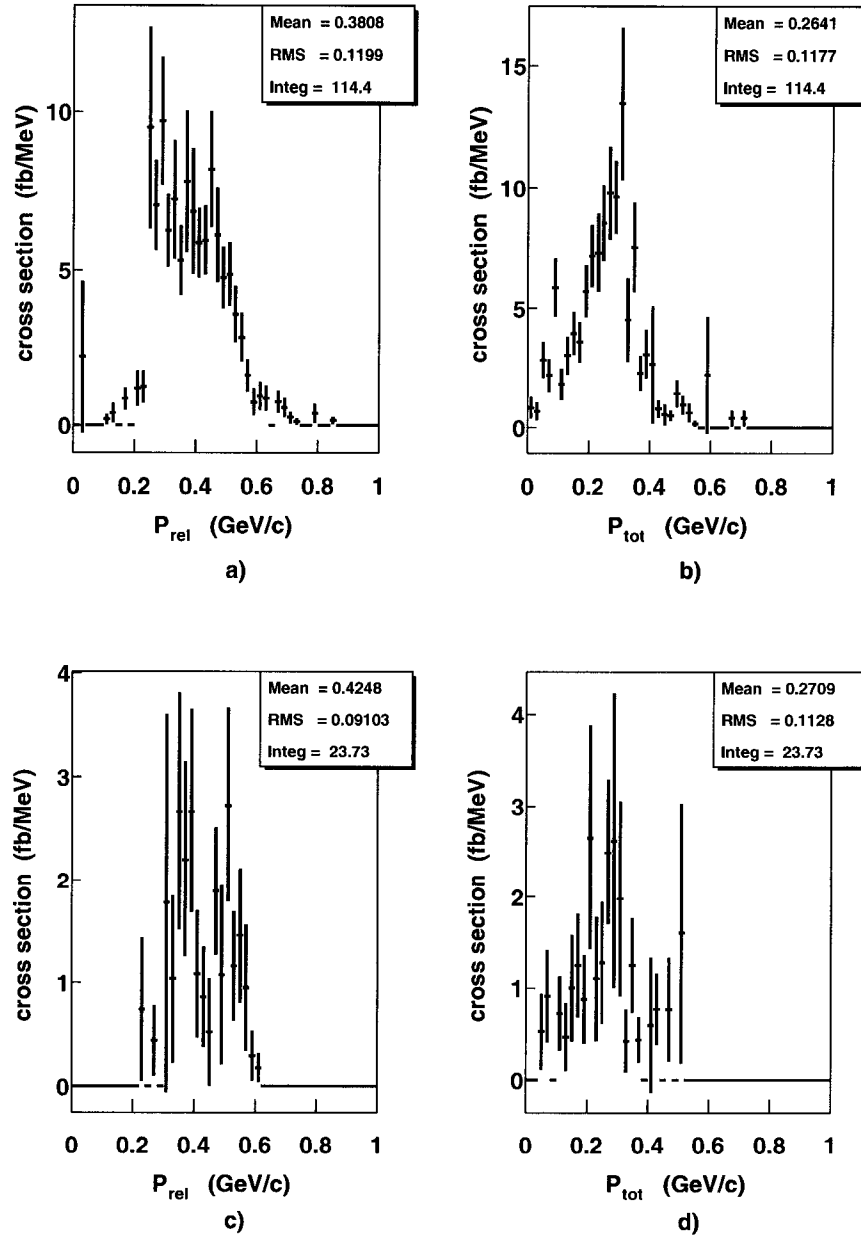
FIG. 88. Cross section vs relative momentum and total momentum at 4.4 GeV with applied radiative and proton acceptance corrections with statistical errors. a) Cross section vs relative momentum of the fast pn pair b) the same for the total momentum; c) and d) the same for fast pp pairs.

TABLE XXIV. External bremsstrahlung and Landau straggling corrections.

Beam Energy	ΔE	e_B^δ	$1 - \delta_I$
$E_i = 2.261$ GeV	70 MeV	0.9849	0.99996
$E_i = 4.461$ GeV	120 MeV	0.9841	0.99996

$$x_0 = \frac{A}{4\alpha N_A Z(Z+1)r_e^2 \ln(183Z^{-1/3})} \tag{52}$$

where Z and A are the charge and the atomic number of the nuclei respectively, $N_A = 6.02 \times 10^{23}$ and electron radius $r_e = 2.818 \times 10^{-13}$ cm. Using Equation 52 for ^{3}He we get $x_0 = 71.95$ g/cm^2. The correction factors due to external bremsstrahlung for 2.2 and 4.4 GeV incident electron energies are given in Table XXIV.

The correction factor for cross section loss due to Landau straggling is 1-δ_I, where

$$\delta_I = \frac{\lambda}{\lambda(\lambda + \ln \lambda + C)} \tag{53}$$

where $C = 0.577$ is the Euler-Macheroni constant,

$$\lambda = \frac{\Delta E - e_0}{\xi}, \tag{54}$$

$$\xi[MeV] = 0.0154 \times t[g/cm^2], \tag{55}$$

$$e_0 = \xi \left(\ln \frac{\xi}{e'} + 1 - C \right) \tag{56}$$

is the most probable energy loss,

$$e' = 2.718 \frac{(1 - \beta^2)I^2}{2m_e}, \tag{57}$$

and

$$I = 13.5 \times 10^{-6} Z[MeV] \tag{58}$$

is the average ionization potential. These corrections are given in Table XXIV.

5.3 SYSTEMATIC ERROR EVALUATION

This section is dedicated to the discussion of effects that may introduce systematic errors in determining the cross section. It is convenient to categorize these systematic

errors as being due to reconstruction and acceptance corrections. Reconstruction systematic errors come from the procedures, algorithms and calibrations that are used to reconstruct the raw data from the detector into identified particles and momenta. Also the systematic errors may be introduced due to the models and assumptions used in making the acceptance corrections. The systematic error analysis is discussed below.

5.3.1 ^{3}He(e,e′p) Systematic Errors

We already discussed the systematic uncertainties from ^{3}He(e,e′p) in Section 3.10. The resulting systematic error of 15% includes contributions from uncertainties in electron detection, uncertainties in determining our target thickness, beam charge and uncertainties in determination of the solid angle of the leading proton for ^{3}He(e,e′pp)n .
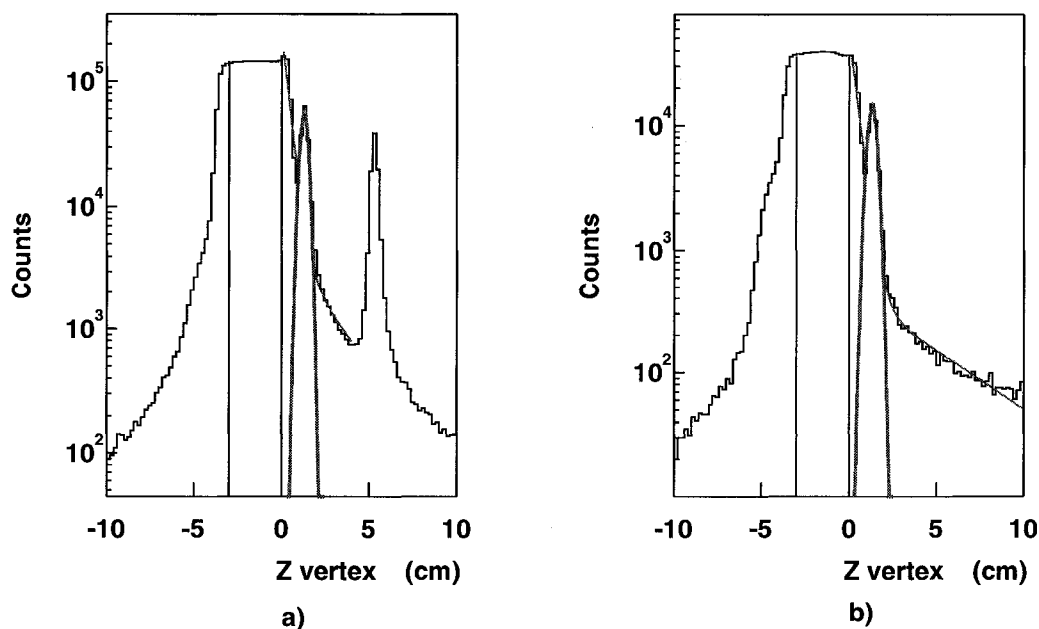
FIG. 89. Systematic error evaluation due to z-vertex cut. Z component of electron vertex along the beam line for ^{3}He target for a) 2.2 GeV run. Flat area is the target material. The Gaussian fit of the peak shows no contamination from the heat insulation. Exponential fit of the edge tail shows a little background contamination. b) The same for 4.4 GeV. The vertical lines indicate applied z vertex cuts.

5.3.2 Systematic Errors due to Z Vertex Cut

Z-vertex cuts for our data were discussed earlier in Section 3.7. Z vertex contamination due to the background was estimated by fitting the edge tail and the heat insulation peak with exponential function and Gaussian (see Fig. 89). One can see that there is no contamination presented due to the heat insulation. Figure 90 shows the comparison of the same Z vertex distribution for a ^{3}He cell with "empty" target at 2.2 GeV, normalized by corresponding beam charge. During the run the "empty" target contained some amount of cold gas. The contamination from the walls of the target cell is estimated as 0.4%.

5.3.3 Systematic Errors due to Missing Mass Cut

Missing mass cuts were discussed earlier in Section 3.12. We can estimate our systematic uncertainties due to the missing mass cut by using simulated events from the PWIA model described in Section 5.4.2. We are cutting out about 6% of the simulated events with the missing mass cut which is shown in Table XX. To check how well these 6% are determined we smear the resolution of Region 2 and 3 drift chambers in GPP, processing 100000 GSIM events at 2.2 GeV through GPP and RECSIS. The smearing factors for Region 2 and 3 drift chambers and corresponding number of events cut by SEB to identify two protons in event and by good proton TBT (^{3}He(e,e′pp) + Good TBT from Table XX) as well as the number of events cut by missing mass in percent are shown in Table XXV. We compare values from ^{3}He(e,e′pp) + Good TBT column with the corresponding value of 72% from data shown in Table XIV. The value of 77% in the 4-th row of the table gives us the conservative systematic uncertainty of 1.6% due to missing mass cut (1.6% = 28% of 6%).

5.3.4 Systematic Errors due to Fast Proton Detection

In order to evaluate systematic errors due to fast proton detection we used the same simulation events as described in Section 3.5. Protons were initially generated within the fiducial volume of the detector described in Section 3.6. Events were proccessed with GSIM, GPP and RECSIS software. Figure 91 shows the ratio of number of reconstructed to generated protons as a function of reconstructed proton momentum. This ratio defines our efficiency for proton detection at different proton momenta.
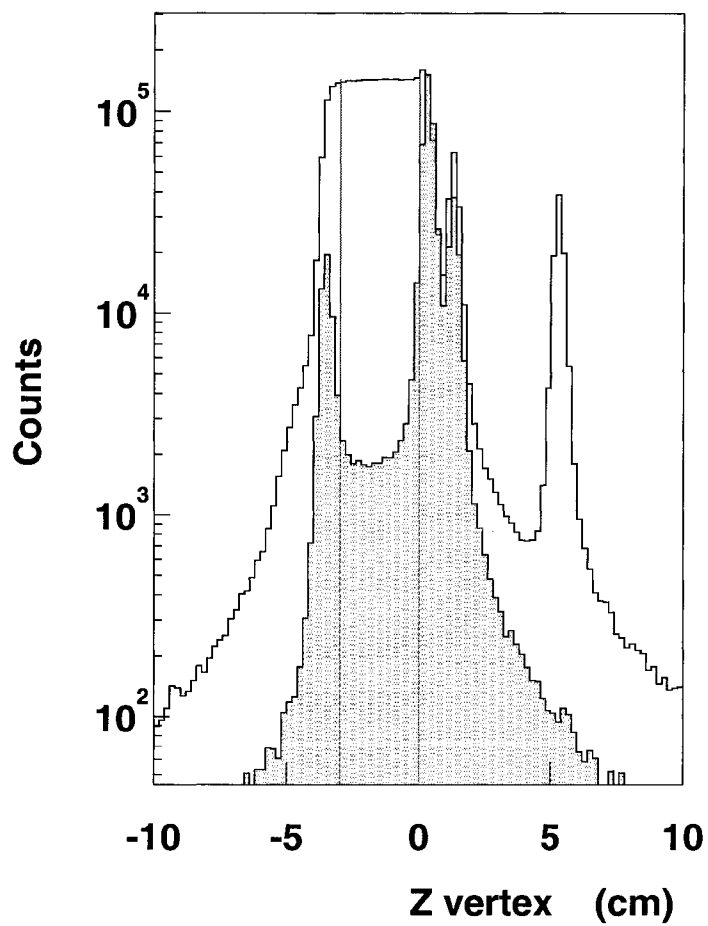
FIG. 90. Comparison of Z vertex coordinate for the full and empty targets. The histogram represents data with a full ³He target. The shaded histogram represents data with "empty" target. The vertical lines indicate the location of cuts. The beam energy was 2.2 GeV.

TABLE XXV. Region 2 and 3 drift chamber smearing factors. The number of events cut by (^{3}He(e,e'pp) + Good proton TBT) and by missing mass are also shown.

Region 2	Region 3	^{3}He(e,e'pp) + Good proton TBT	Missing Mass
2.5	3.0	56%	6.3%
3.0	3.0	62%	6.7%
3.0	3.5	70%	7.3%
3.5	3.5	77%	7.9%
3.5	4.0	86%	8.1%
4.0	4.0	95%	9.1%

The average momentum of the fast protons is $\approx$ 350 MeV/c. The conservative systematic uncertainty for detection of 300 MeV/c protons is estimated as 5%.

5.3.5 Systematic Errors due to Radiative Corrections

Radiative corrections were discussed in Section 5.2. The contributions from external bremsstrahlung and Landau straggling processes were neglected in our analysis, so we must include them to the list of systematic uncertainties in our measurements. These are estimated as 1.5% (see Section 5.2.1).

5.3.6 Systematic Errors of Acceptance

Acceptance corrections were studied in Section 4.2.3. We use 443343 (see Table XXIII) as the final bin configuration that defines our acceptance corrections. Due to the large number of average acceptance replacements (see Table XXII) we completely exlude 883343 and 886643 bin configurations from consideration. Based on all other results we estimate the systematic uncertainties of acceptance: 1.5% for both fast pp and pn at 2.2 GeV; 30% and 15% for fast pp and pn pairs, respectively, at 4.4 GeV. The systematic errors at 4.4 GeV are very conservative and based on the fact that while increasing the number of bins, we did not succeed and only partially succeed in converging the values of the integrated cross sections of pp and pn pairs, respectivly. Finally Table XXVI summarizes each of the systematic errors.
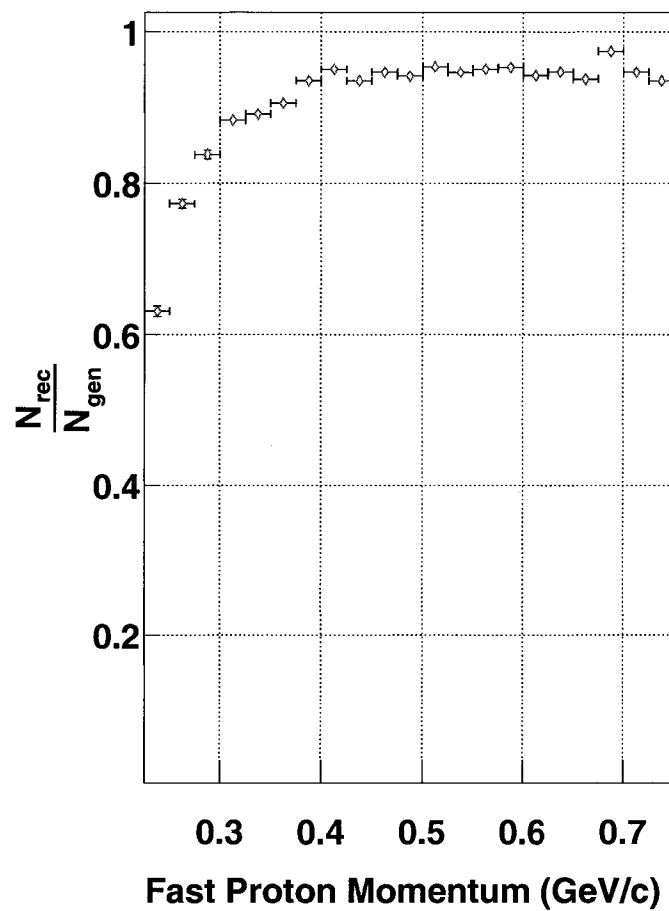
FIG. 91. Efficiency of the fast proton detection. Note that proton was initially generated within fiducial volume of the detector.

TABLE XXVI. Summary of the systematic errors. Note that (e,e′p) normalization includes the effects of electron detection, target thickness, beam charge and Ω_p determination. The systematic errors are given in percent.

Uncertainty source	2.2 GeV		4.4 GeV	
	pp	pn	pp	pn
^{3}He(e,e′p) normalization	15	15	15	15
Z Vertex Cut	0.4	0.4	0.4	0.4
Missing mass cut	1.6	1.6	1.6	1.6
Fast proton detection	5	5	5	5
Radiative corrections	1.5	1.5	1.5	1.5
Acceptance corrections	1.5	1.5	30	15
Total	16	16	34	22

5.4 DATA TO THEORY COMPARISON

In order to understand the reaction mechanism, i.e. the contribution of the various processes to the data, we need to compare our experimental cross sections with theory calculations. This section presents a Pion Production and Reabsorption model, a Plane Wave Impulse Approximation calculation as well as an exact calculation at much lower energies. The results of the calculations are compared to data and discussed. Unfortunately, no other complete calculation results are available for us at present time.

5.4.1 Pion Production and Reabsorption

One of the possible contributing processes leading to the emission of three energetic nucleons in ^{3}He(e,e′pp)n can be the production of a pion off the struck nucleon followed by reabsorption of the pion by the remaining NN pair. Our goal was to check whether the signals we see in the data can be explained by these processes. We developed a home-made model to simulate such a contribution. The diagrams included in the model are shown in Figure 92. This model includes the production of a pion (π^+ or π^0) on a proton followed by pion absorption on the residual deuteron followed by phase space decay of two nucleons. The entire calculation was done classically,
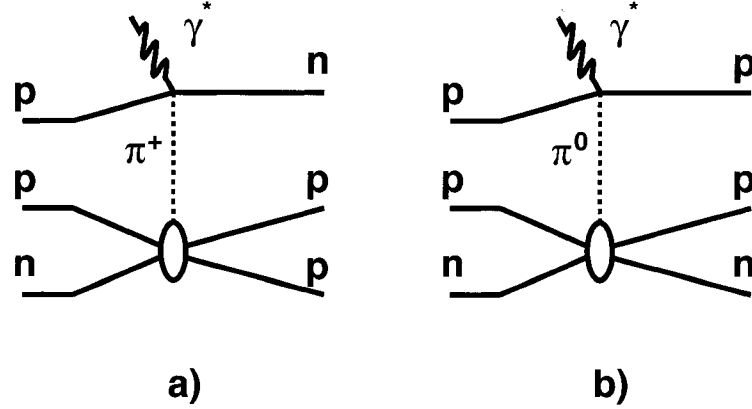
FIG. 92. Pion production and reabsorption diagrams. a) π^+; b) π^0 production and reabsorption.

on the cross section level.

We used proton initial momentum distributions for the p-d breakup channel in ^{3}He from Saclay (e,e'p) measurements [92] (see Fig. 93). We interpolated between a given set of data points with the *dcspln* subroutine which allowed us to compute a (vector-valued) cubic spline function. This spline function was used to generate 1 M points which were normalized to unity and converted to a table of probability density as a function of proton momentum. We used that table to randomly generate the initial momentum of the struck proton in ^{3}He.

The cross sections for pion electroproduction $\gamma^* p \to N\pi$ were calculated with MAID-2000 [93] and applied to the γ^*-π vertex. The cross sections for pion absorption on deuterium, $\pi^+ d \to pp$, were calculated with the SAID-1998 parameterization code [94] and applied to the π-d vertex. We estimated that the cross section for $\pi^0 d \to pn$ was half of the cross section for $\pi^+ d \to pp$ [95, 96]. We neglected π production on a neutron and subsequent absorption on a T=1 NN pair since that is estimated to be ten times smaller than π absorption on a T=0 pair [97]. We generated events with this model and applied the same geometric and momentum cuts as with the actual data. We did not use GSIM to simulate the CLAS resolution and multiple scattering. Since we do not know the number of quasideuterons in ^{3}He, we could not normalize this model absolutely, so all the distributions were arbitrarily
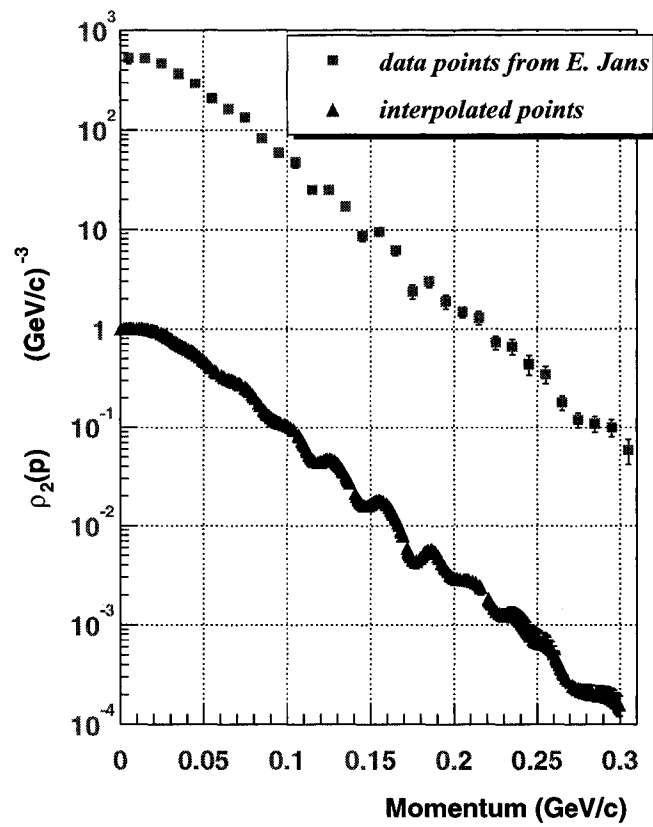
FIG. 93. Proton momentum density distribution in ^{3}He for two-body breakup. Boxes are the data points from [92]. Triangles are the interpolated points generated with a cubic spline function and normalized to unity.

normalized (although with the same scale factor).

Kinetic energy balance distributions for simulated events at 2.2 and 4.4 GeV are shown in Figure 94. We see similar peaks as in data distributions with peaks in the corners. Due to the requirement $p_{p1} > p_{p2}$ we see only one instead of two peaks for pn pair distributions (see Fig. 94 c) and d)). We cut on those peaks as indicated in Figure 94, selecting events with the corresponding leading nucleon and fast NN pair. The Q^2 versus ω distributions for selected NN pair events at 2.2 and 4.4 GeV are shown in Figure 95. One can see that the average energy transfer for simulated events are much larger than the data, which are shown in Figure 54. Pion production is clearly dominated by nucleon resonances.

After applying a cut on the perpendicular component of the leading nucleon's momentum $p^{\perp} < 0.3$ GeV/c we compared the simulation with data. The W distribution comparison with all cuts applied for pp and pn pairs at 2.2 GeV is shown in Figure 96 a) and c). The W (proton–virtual photon invariant mass) is defined as:

$$W = \sqrt{(m_p + \omega)^2 - \vec{q}'^2} = \sqrt{m_p^2 + 2m_p\omega - Q^2} \tag{59}$$

Due to poor data statistics at 4.4 GeV we do not include data distributions in Figure 96 b) and d). One can see that the simulated distribution starts at $W = 1.1$ GeV, which corresponds to the pion production threshold. The cut at $W \leq 2$ GeV in the simulation is due to the MAID-2000 limitation. This comparison shows that pion production and reabsorption processes are much more energetic than the data.

Figures 97 – 100 show the fast pair opening angle, pair total momentum parallel to $\vec{q}$, pair total momentum, and pair relative momentum for both the simulation and the data. The fast pairs from pion production and reabsorption are similar to the data in opening angle and pair total momenta. However the simulated events have too large relative momentum. This discrepancy is consistent with the much larger W distribution of the simulated events. Since simulated processes must have relative energy $E_{rel} \geq m_\pi$, that gives larger values for the relative momentum of the simulated pairs.

The only way for the relative momentum distribution to be described by a pion production and reabsorption process is for the pions to be far offshell. Production and reabsorption of far off-shell pions would be a three body mechanism, which is also a very interesting topic.

We also compared the number of events with pp and pn pairs at 2.2 and 4.4 GeV for the simulation and the data. Table XXVII shows the relative number of pairs for
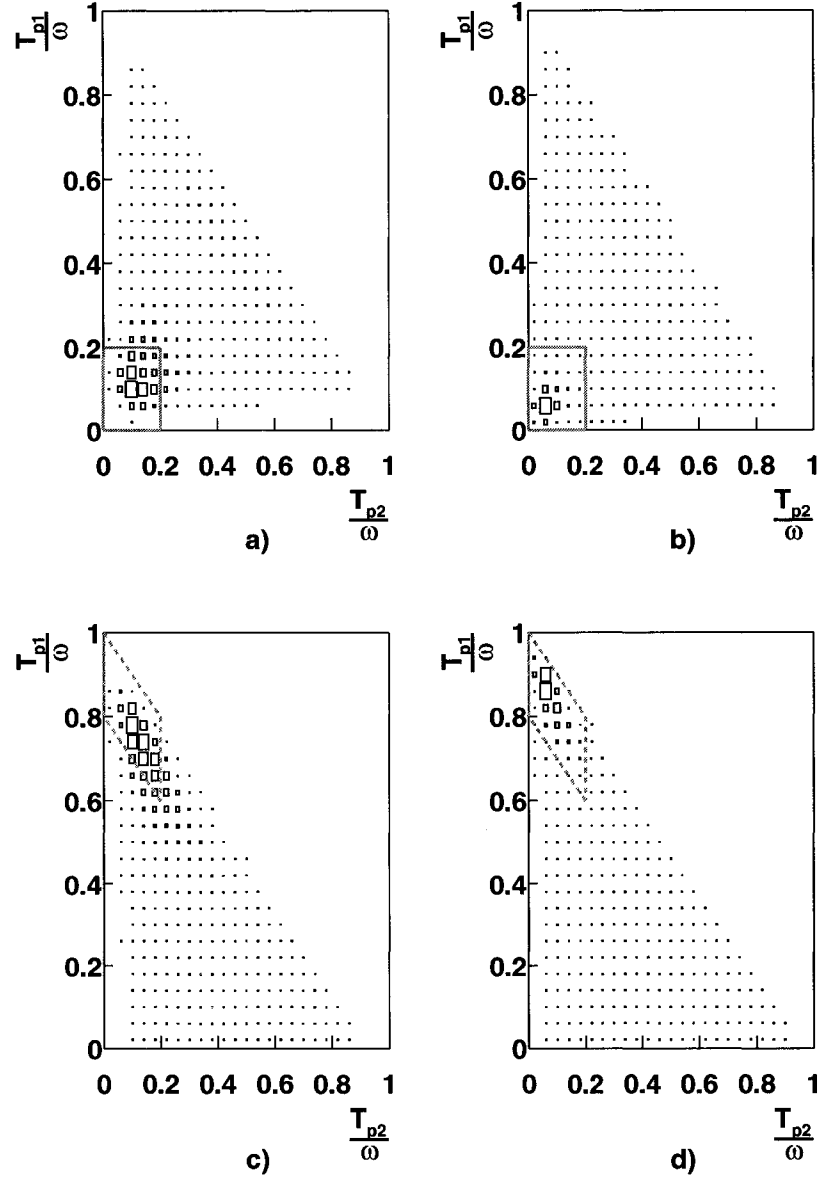
FIG. 94. Kinetic energy sharing distribution from the pion production and reabsorption simulation. a), c) are $\pi^+ d \to pp$, $\pi^0 d \to pn$ channels simulated at $E_{beam} = 2.2$ GeV. b), d) are the same for 4.4 GeV. We required the condition $p_{p1} > p_{p2}$. Solid and dashed lines indicate the 'leading n, fast pp pair' and the the 'leading p, fast pn pair' cuts, respectively. These are cut on p_{p1}, p_{p2} and $p_n > 0.25$ GeV/c.
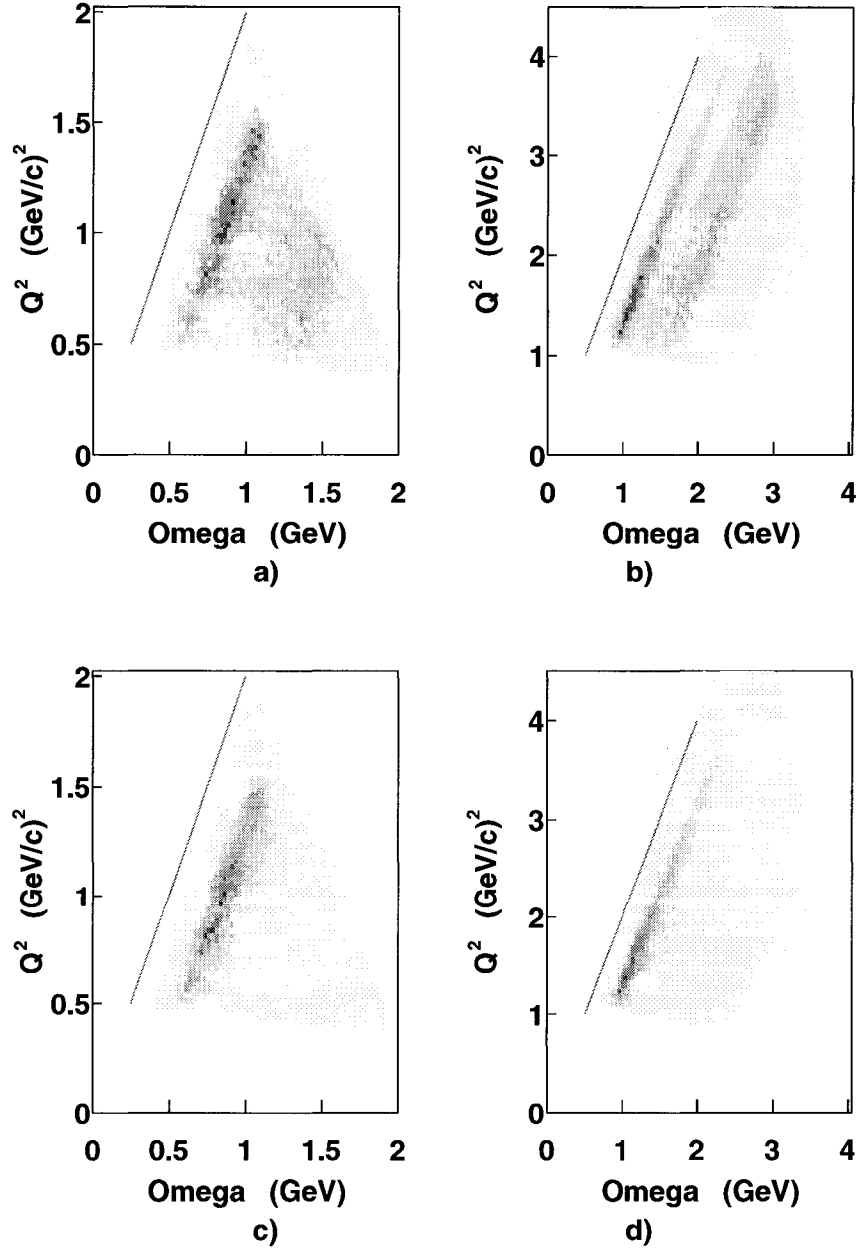
FIG. 95. Q^2 vs ω from the pion production and reabsorption simulation. a), c) are $\pi^+ d$, $\pi^0 d$ channels simulated at $E_{beam} = 2.2$ GeV. b), d) are the same for 4.4 GeV. The cuts on nucleon kinetic energies were applied. The line shows the quasielastic condition $\omega = Q^2/2m$. Note that the average energy transfer is much larger than the data (see Fig. 54).
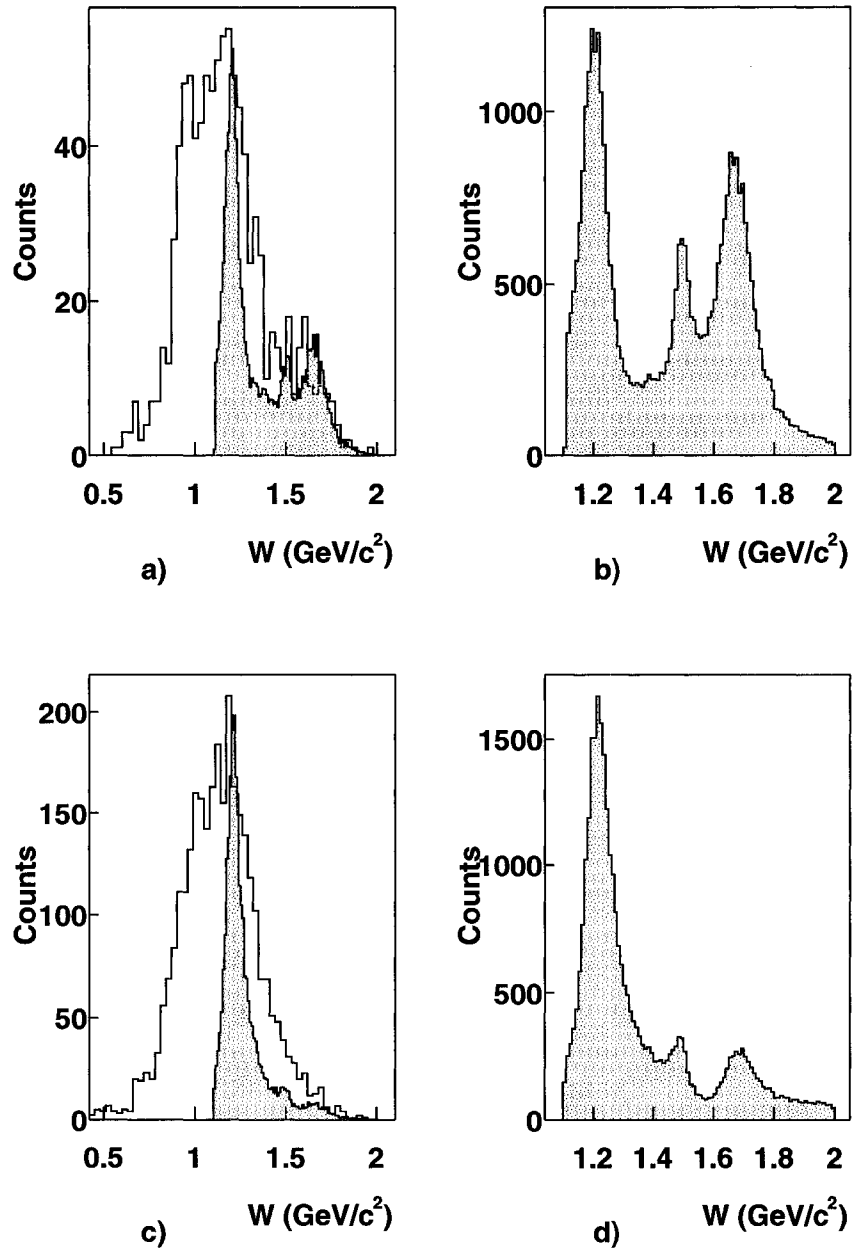
FIG. 96. W distribution from the pion production and reabsorption simulation. a), c) pp and pn pairs, respectively, for events with cut on $p^{\perp} < 0.3$ GeV/c at 2.2 GeV; b), d) the same for 4.4 GeV. Solid line is data distribution shown only for 2.2 GeV. The shaded distribution shows pion production and reabsorption simulation (with arbitrary normalization).
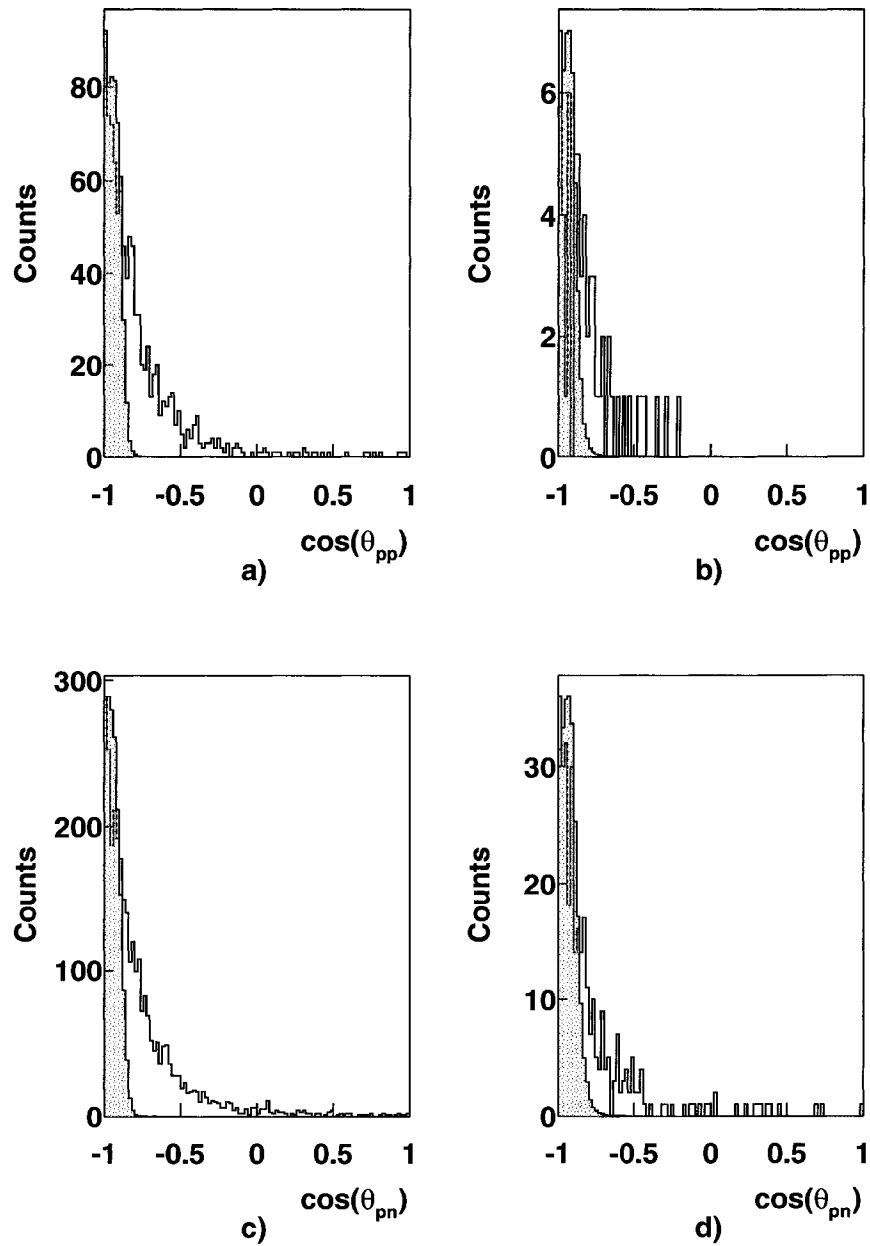
FIG. 97. The cosine of the fast pp and pn opening angle from the pion production and reabsorption simulation. a), c) The cosine of the fast pp and pn opening angle, respectively, for events with cut on $p^{\perp} < 0.3$ GeV/c at 2.2 GeV; b), d) the same for 4.4 GeV. Solid line is data distribution. The shaded distribution shows pion production and reabsorption simulation (with arbitrary normalization).
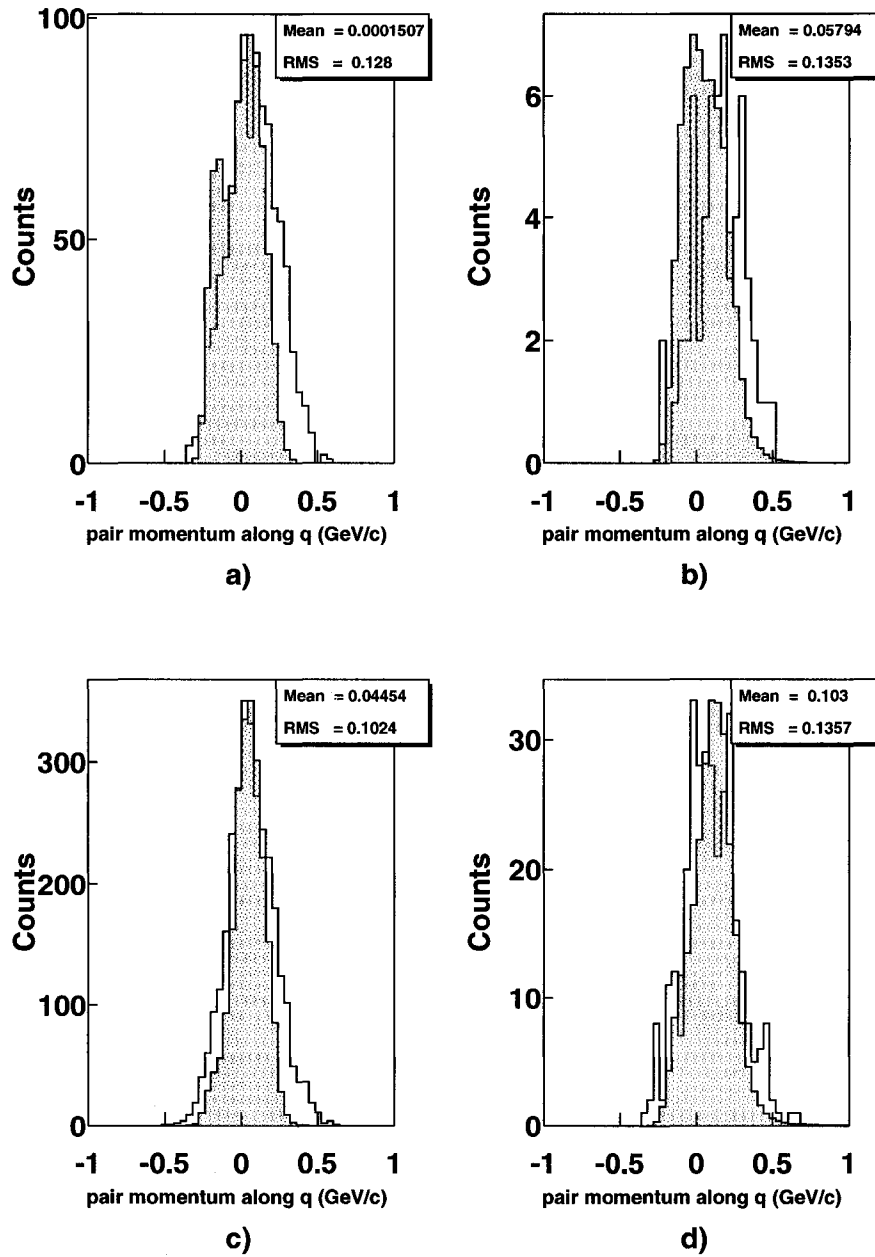
FIG. 98. Pair total momentum parallel to $\vec{q}$ from the pion production and reabsorption simulation. a), c) pp and pn pairs, respectively, for events with cut on $p^{\perp} < 0.3$ GeV/c at 2.2 GeV; b), d) the same for 4.4 GeV. Solid line is data distribution. The shaded distribution shows pion production and reabsorption simulation (with arbitrary normalization).
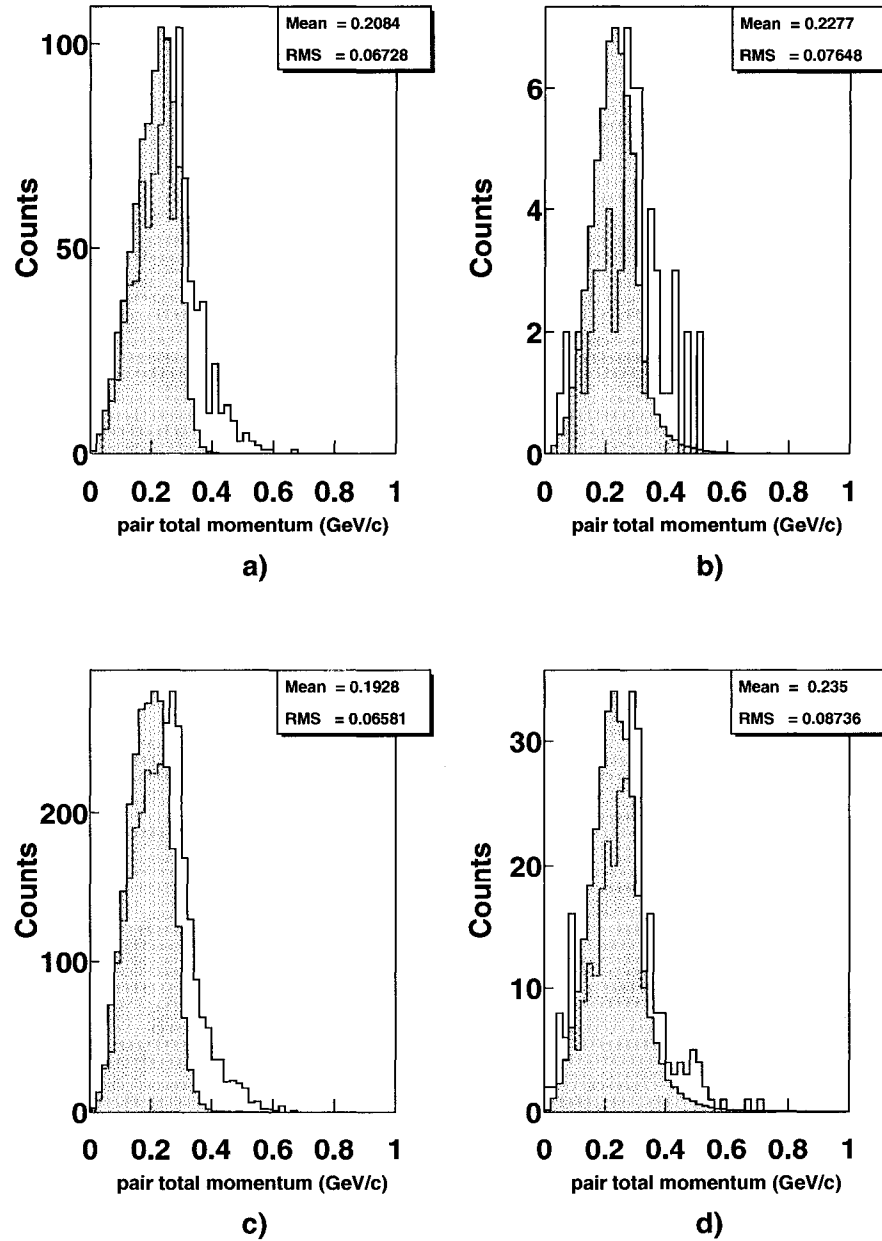
FIG. 99. Pair total momentum from the pion production and reabsorption simulation. a), c) pp and pn pairs, respectively, for events with cut on $p^\perp < 0.3$ GeV/c at 2.2 GeV; b), d) the same for 4.4 GeV. Solid line is data distribution. The shaded distribution shows pion production and reabsorption simulation (with arbitrary normalization).
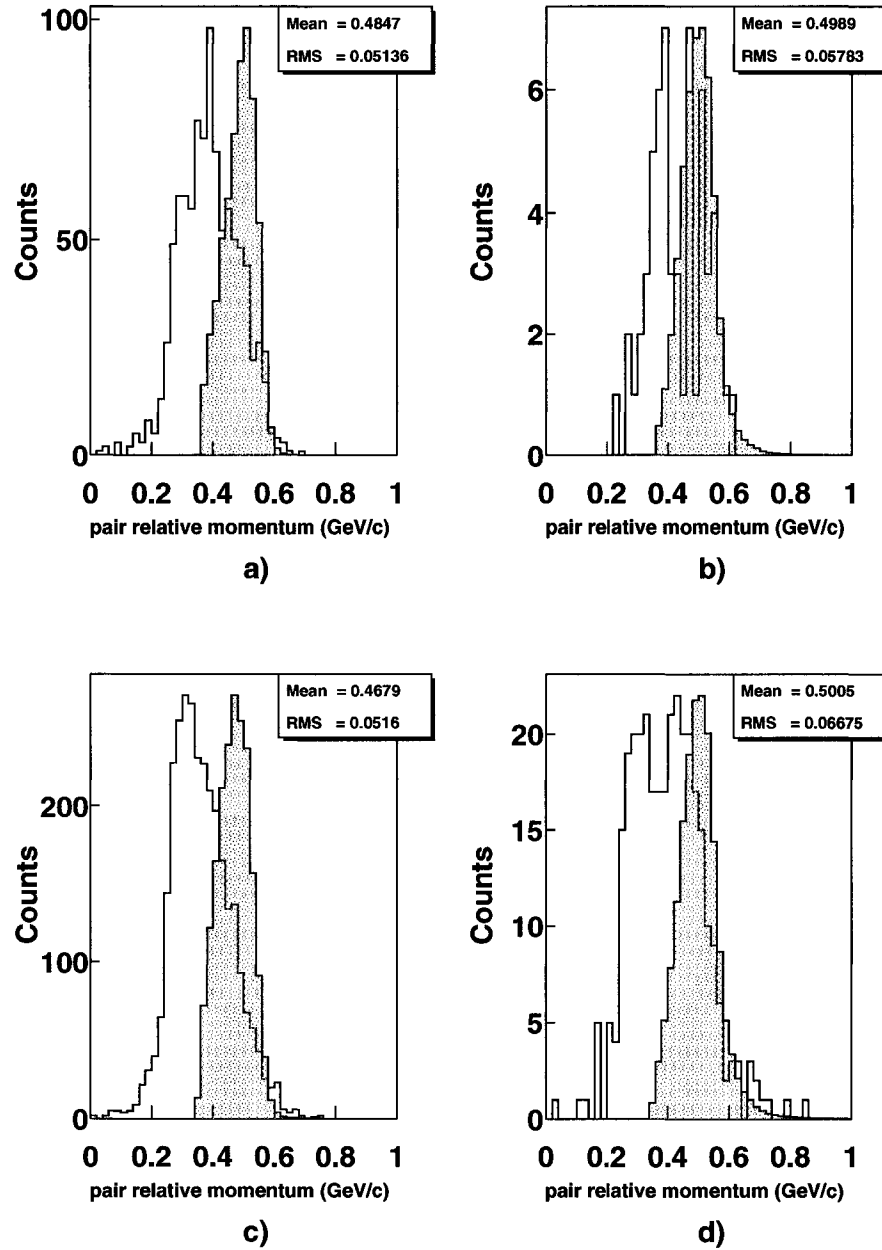
FIG. 100. Pair relative momentum from the pion production and reabsorption simulation. a), c) pp and pn pairs, respectively, for events with cut on $p^\perp < 0.3$ GeV/c at 2.2 GeV; b), d) the same for 4.4 GeV. Solid line is data distribution. The shaded distribution shows pion production and reabsorption simulation (with arbitrary normalization).

TABLE XXVII. Number of pn and pp pair events for the pion production and re-absorption and for data. These are shown for 2.2 and 4.4 GeV normalized to the corresponding number of pn pairs at 2.2 GeV. Entries in the simulation are weighted by cross section.

	2.2 GeV	4.4 GeV
Simulation pn	1	0.52
Simulation pp	0.83	0.61
Data pn	1	0.11
Data pp	0.31	0.02

simulation and data, each normalized to the corresponding number of pn pairs at 2.2 GeV.

There are 3 to 5 times more pn than pp pairs in the data, but they are about equal for π production. Similarly, the data drops by a factor of 10 from 2.2 GeV to 4.4 GeV, but the π production and reabsorption model drops much more slowly.

Based on the comparison of the simulation with data we see that the simulation failed to describe the data. While it produced events with one leading nucleon and two fast back-to-back nucleons, the electron reaction mechanism was clearly incorrect. The energy transfer was too large; it peaked in the delta region rather than in the quasielastic. The relative momentum distribution was also too large since the minimum p_{rel} is determined by the pion mass. The cross section ratio of fast pp pairs to fast pn pairs was also incorrect.

5.4.2 Plane Wave Impulse Approximation

In the Plane Wave Impulse Approximation (PWIA), the virtual photon is totally absorbed by one of the nucleons, while this nucleon comes out without further interaction with the residual nucleus and is detected in the experiment. In this case the wave function of the knocked out nucleon is just a plane wave. Figure 101 shows the diagram of this process.

We used PWIA calculations by Misak Sargsian [91] which uses an exact Faddeev ^{3}He wave function from the Bochum group and the de Forest 'cc1' single nucleon current. No FSI were included in the model. The eight-fold cross section calculated by this model for each event is differential in $\{E_e, \Omega_e, p_1, \Omega_{p_1}, \Omega_{p_2}\}$, where E_e, Ω_e
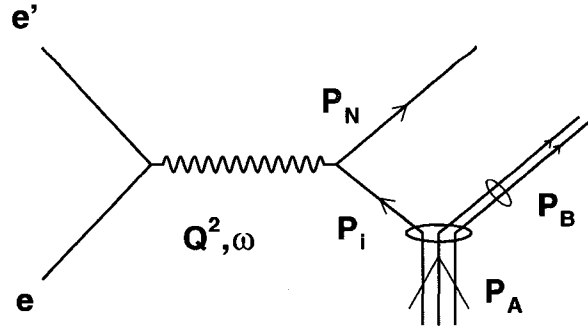
FIG. 101. Plane Wave Impulse Approximation diagram.

are the energy and solid angle of the outgoing electron, p_1, Ω_{p_1} are the momentum and solid angle of the first outgoing nucleon, and Ω_{p_2} is the solid angle of the second outgoing nucleon. From these 8 variables we can calculate the remaining kinematical quantities.

Kinetic energy balance distributions for the PWIA events at 2.2 and 4.4 GeV are shown in Figure 102. We see similar peaks as in data distributions with peaks in the corners. Similarly, as for the pion production and reabsorption model we require $p_{p1} > p_{p2}$. We see only one instead of two peaks for pn pair distributions (see Fig. 102 c) and d)). We cut on those peaks as indicated in Figure 102, selecting events with the corresponding leading nucleon and fast NN pair. The Q^2 versus ω distributions for selected NN pair events at 2.2 and 4.4 GeV are shown in Figure 103. These distributions are consistent with the data (see Figure 62). The W distribution with $p^\perp < 0.3$ GeV/c for the PWIA at 2.2 and 4.4 GeV are shown in Figure 104. One can see that the PWIA and the data are consistent (see Figure 104 a) and c)). Figures 105 and 106 show the fast pair opening angle and pair total momentum parallel to $\vec{q}$ distributions for both the PWIA and the data. From this comparison one can see that the PWIA back-to-back peak is much sharper and the average pair momentum parallel to $\vec{q}$ is much smaller than the data. But, still the PWIA and the data distributions are reasonably close. All PWIA distributions shown in comparison with the data were arbitrarily normalized. The calculation of the cross sections for both the PWIA and the data were discussed in Section 5.1. Cross section versus P_{rel} and P_{tot} distributions for the PWIA and the data are shown in Figures 109 and 110.

Note that the PWIA model cross sections were also used for acceptance corrections (see Section 4.2.3).
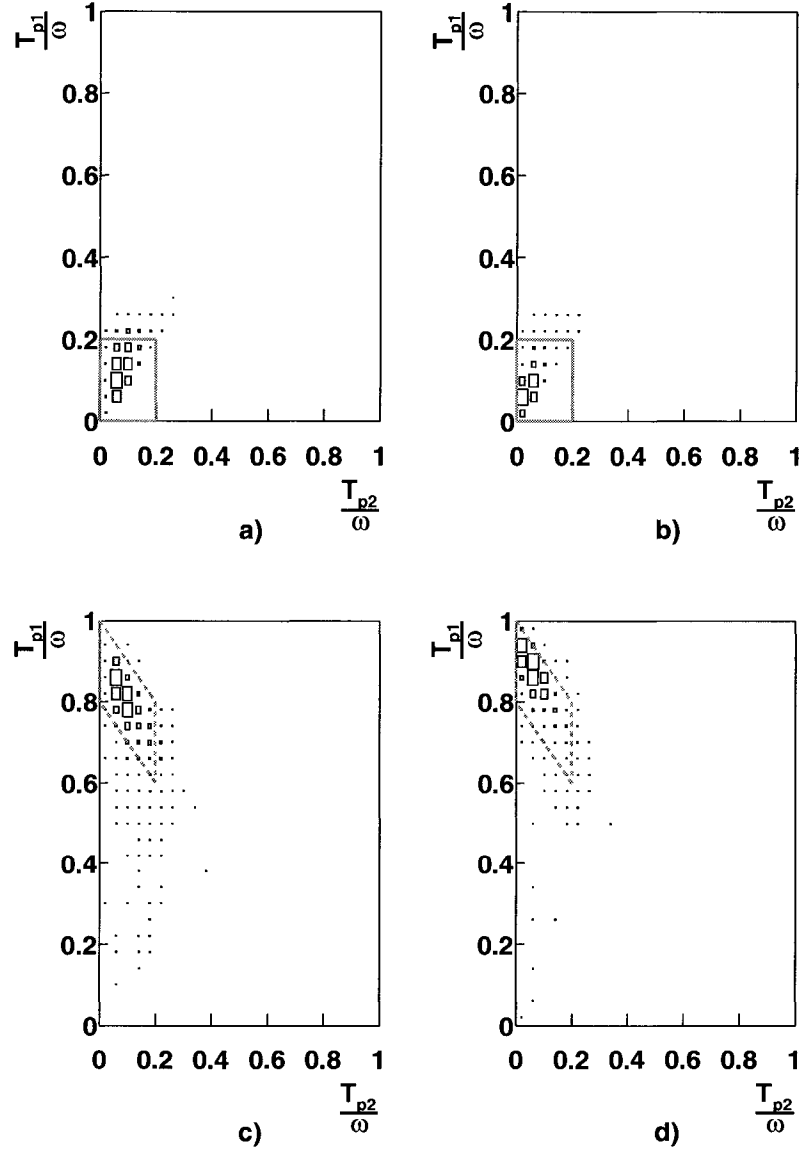
FIG. 102. Kinetic energy sharing distribution from the PWIA model. a), c) are fast pp, pn pairs at $E_{beam} = 2.2$ GeV. b), d) are the same for 4.4 GeV. We required the condition $p_{p1} > p_{p2}$. Solid and dashed lines indicate the 'leading n, fast pp pair' and the the 'leading p, fast pn pair' cuts, respectively. These are cut on p_{p1},p_{p2} and $p_n > 0.25$ GeV/c.
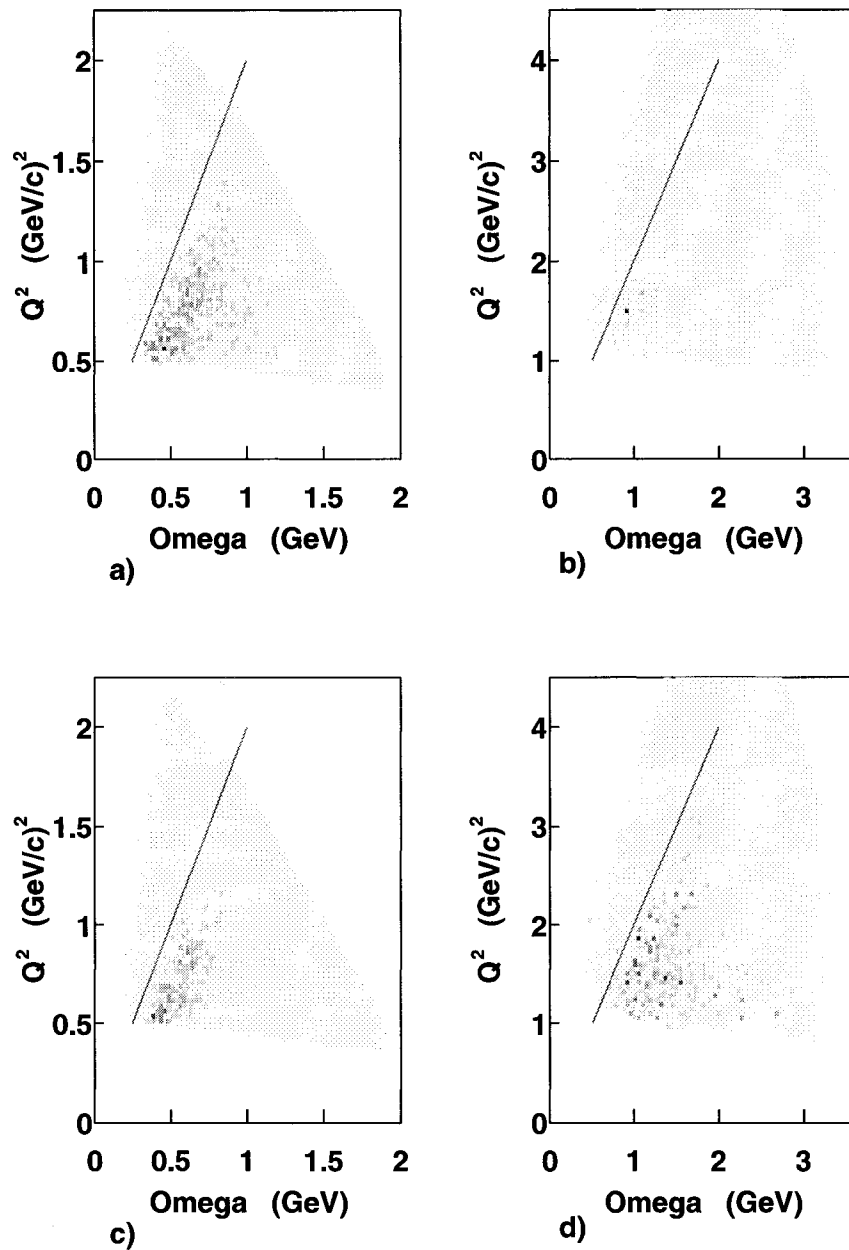
FIG. 103. Q^2 vs ω from the PWIA model. a), c) are fast pp, pn pairs at $E_{beam} = 2.2$ GeV. b), d) are the same for 4.4 GeV. The cuts on nucleon kinetic energies were applied. The line shows the quasielastic condition $\omega = Q^2/2m$. See corresponding data distribution in Figure 62 for comparison.
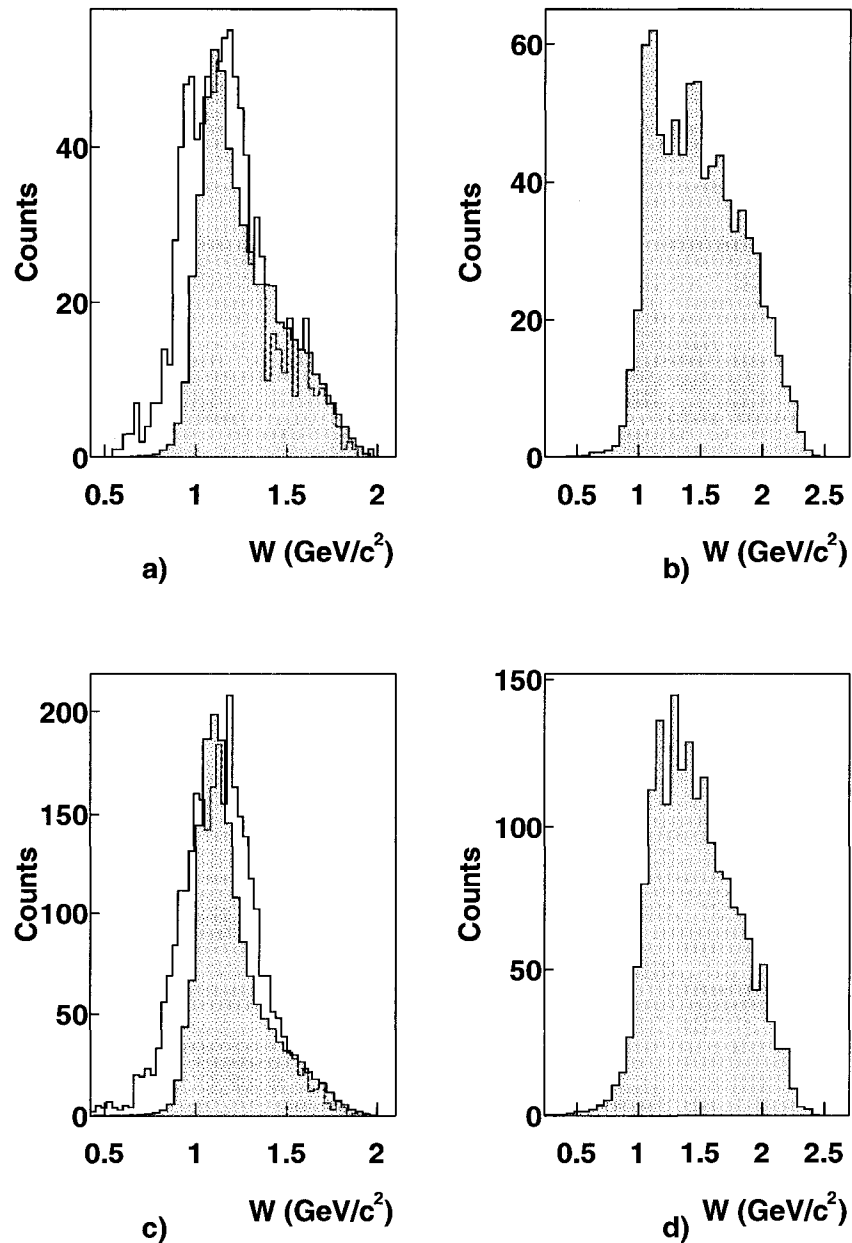
FIG. 104. W distribution from the PWIA model. a), c) pp and pn pairs, respectively, for events with cut on $p^{\perp} < 0.3$ GeV/c at 2.2 GeV; b), d) the same for 4.4 GeV. Solid line is data distribution shown only for 2.2 GeV. The shaded distribution shows PWIA (with arbitrary normalization).
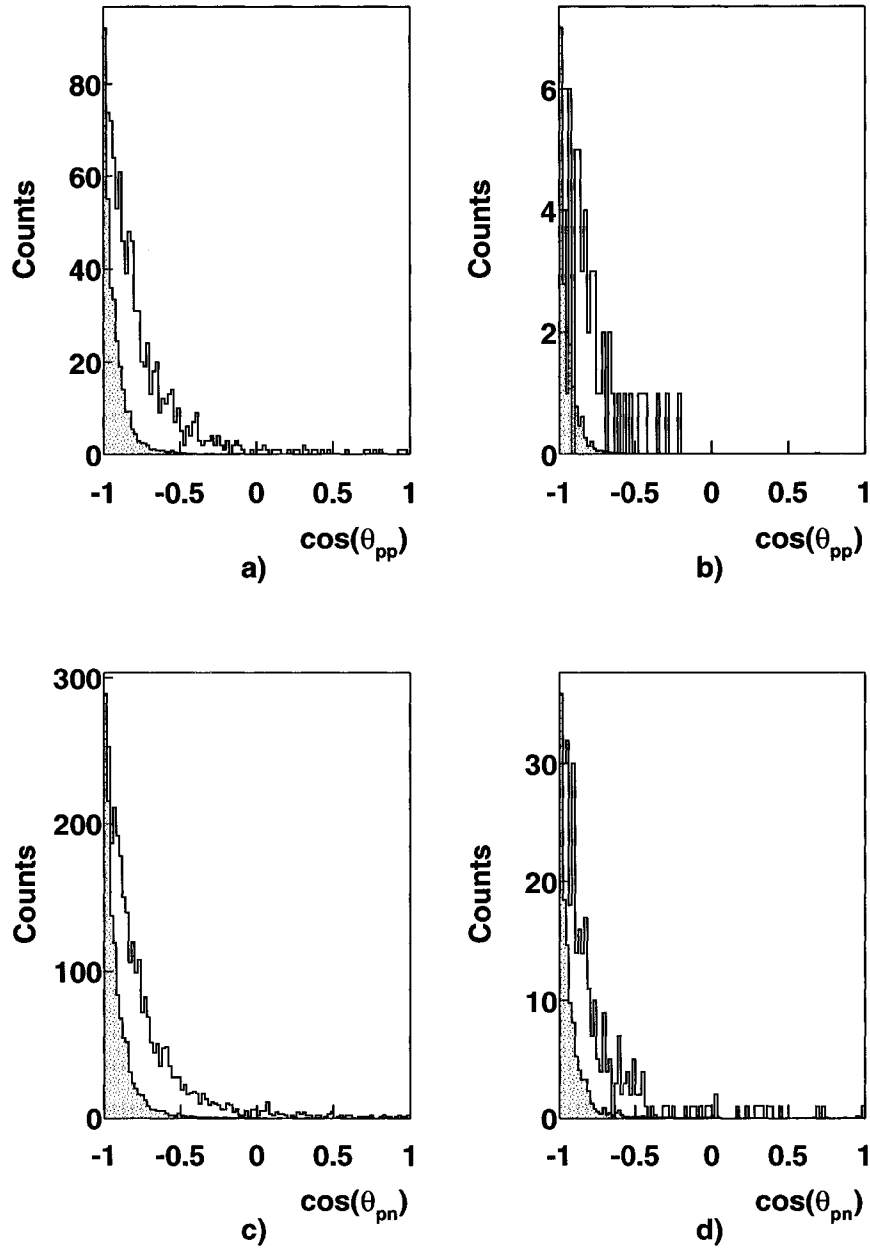
FIG. 105. The cosine of the fast pp and pn opening angle from the PWIA model. a), c) The cosine of the fast pp and pn opening angle, respectively, for events with cut on $p^\perp < 0.3$ GeV/c at 2.2 GeV; b), d) the same for 4.4 GeV. Solid line is data distribution. The shaded distribution shows PWIA (with arbitrary normalization).
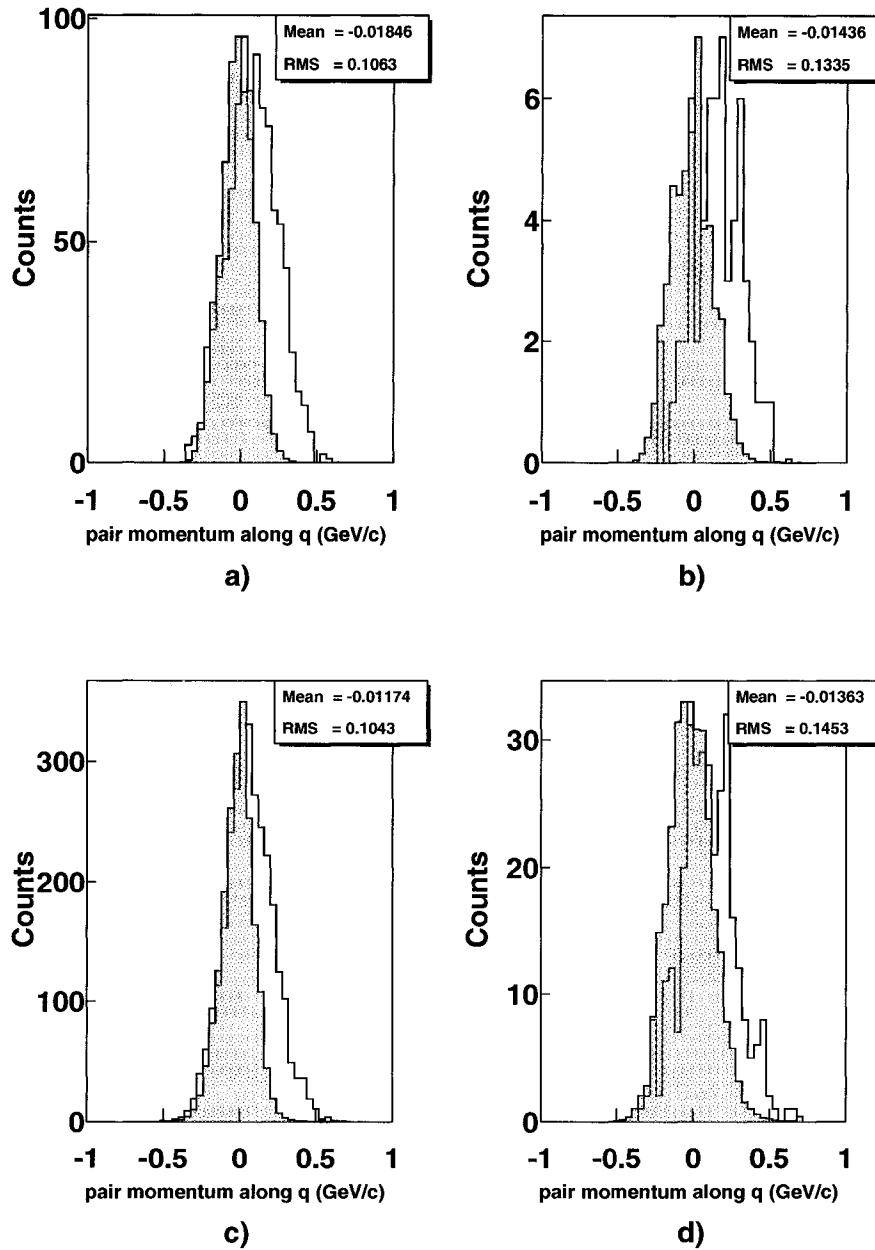
FIG. 106. Pair total momentum parallel to $\vec{q}$ from the PWIA model. a), c) pp and pn pairs, respectively, for events with cut on $p^{\perp} < 0.3$ GeV/c at 2.2 GeV; b), d) the same for 4.4 GeV. Solid line is data distribution. The shaded distribution shows PWIA (with arbitrary normalization).

5.4.3 Exact Calculations

Exact calculations of ^{3}He(e,e'pp)n including exact treatment of both the bound and continuum states can only be done below π production threshold. These calculations have been done by W. Glöckle *et al.* [10]. They use NN and three body potentials fit to NN scattering data and nuclear binding energies. They solve for the three nucleon bound and continuum wave functions using the Faddeev equation. They use a one body current operator to couple the virtual photon to a single nucleon.

Glöckle calculated the cross section for ^{3}He(e,e'pp)n where the leading nucleon has momentum $\vec{p}_N = \vec{q}$ and the other two nucleons have total momentum $p_{total} = 0$, for various values of the momentum transfer, $400 \leq |\vec{q}| \leq 600$ MeV/c, and relative momentum $0 < P_{rel} < 250$ MeV/c. The scaled transverse response function $2m_N^2 R_T/(G_M^p Q)^2$, versus the relative momentum of the fast pn pair at $|\vec{q}| = 600$ MeV/c for various treatments of the final 3N state is shown in Figure 107, where m_N is the mass of nucleon, R_T is the transverse response function, G_M^p is the magnetic form factor of the proton, and Q^2 is the square magnitude of the four-momentum transfer. The shown different treatments of the final state are explained by the diagrams shown in Figure 108.

Glöckle's calculations at these lower energy kinematics bring the following conclusions:

1. MEC did not contribute,

2. rescattering of the leading nucleon did not contribute, and

3. the continuum state interaction of the outgoing NN pair decreased the cross section by a factor of approximately 10 relative to the PWIA result.

Thus, these calculations show that this reaction is a very clean way, at least at low energies, to measure the overlap integral between the NN continuum state and the same two nucleons in the bound state. Based on these conclusions, we proceeded to compare our data to a PWIA calculation integrated over the CLAS acceptance and including CLAS resolutions and efficiencies.

5.4.4 Discussions

We compared our data cross sections to the PWIA calculation (Section 5.1). The resulting relative and total momentum distributions of the fast NN pairs at 2.2 and
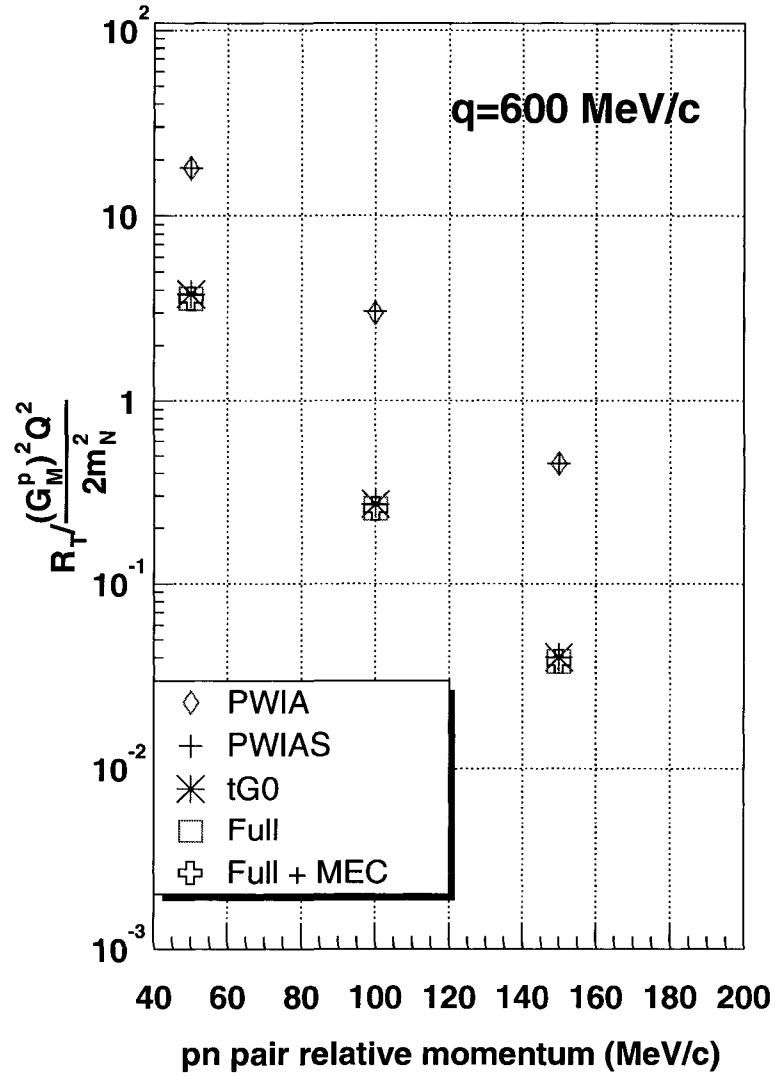
FIG. 107. $\frac{2m_N^2 R_T}{(G_M^p Q)^2}$ versus the pn pair relative momentum. Various treatments of the final 3N state at momentum transfer $|\vec{q}| = 600$ MeV/c are shown. MEC effects are negligible as shown. This corresponds to struck p, fast pn pair configuration.
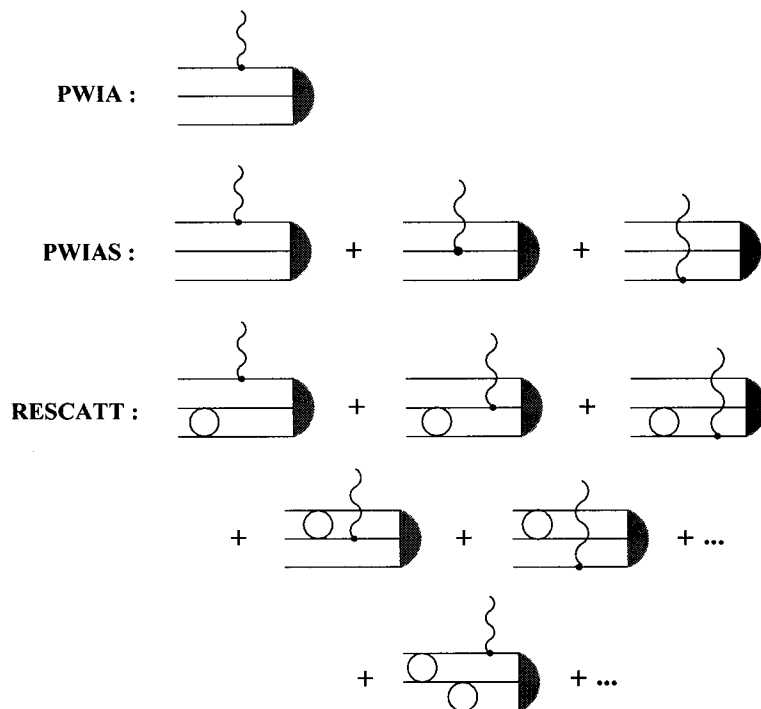
FIG. 108. The diagrams contributing to different treatments of the final state in Glöckle calculations. Diagrams for PWIA (no FSI) and PWIAS (symmetrized PWIA) are shown in the top and middle groups, respectively. The first diagram in the group RESCATT is "tG0" (pair distortion only). Complete FSI (all diagrams from RESCAT group) are referred as "Full".

TABLE XXVIII. Integrated cross sections. The statistical errors are shown. The systematic errors for our data were determined as 15% of the measured cross sections. See Section 5.3 for details.

	2.2 GeV		4.4 GeV	
	pp	*pn*	*pp*	*pn*
Data cross section (fb)	180±5.8	574±10.4	6.9±0.9	37±2.0
PWIA cross section (fb)	1188±4.0	3201±8.0	63.6±0.2	142±0.3
PWIA / Data	6.6±0.2	5.6±0.1	9.2±1.2	3.8±0.2

4.4 GeV are shown in Figures 109 and 110, respectively. The cross sections were integrated over the experimental acceptance. Radiative corrections were applied. No acceptance corrections were applied. Since the PWIA events were passed through the CLAS Monte Carlo and reconstruction software, the PWIA cross section already includes all effects of CLAS resolution, efficiency and geometry. The PWIA results are reasonably close to the data except for a scale factor.

Table XXVIII shows the integrated cross sections. The PWIA cross section is about six and four times larger than the data at 2.2 and 4.4 GeV, respectively, but both PWIA and data have about the same isospin and Q^2 dependence. The cross section ratio of pp and pn pairs is correct at 2.2 GeV. The 4.4 GeV pp/pn ratio is incorrect, but the statistics are much poorer there. Both data and PWIA drop by a factor of about 20 from $0.5 < Q^2 < 1$ GeV^2 (at 2.2 GeV) to $1 < Q^2 < 2$ GeV^2 (at 4.4 GeV). This similarity between the data and a PWIA calculation using a fully correlated ^{3}He wave function indicates that we have measured NN correlations by striking the third nucleon and observing the spectator correlated pair.

Calculations by W. Glöckle [10] (see also Section 5.4.3) strengthen this conclusion where the ratio of the PWIA cross section to the continuum state interaction of the outgoing NN pair result is ≈ 10.

5.5 SUMMARY

We have measured the ^{3}He(e,e'pp)n reaction at 2.2 and 4.4 GeV over a wide kinematic range. The kinetic energy distribution for 'fast' nucleons ($p > 250$ MeV/c) peaks where two nucleons each have 20% or less and the third or 'leading' nucleon carries
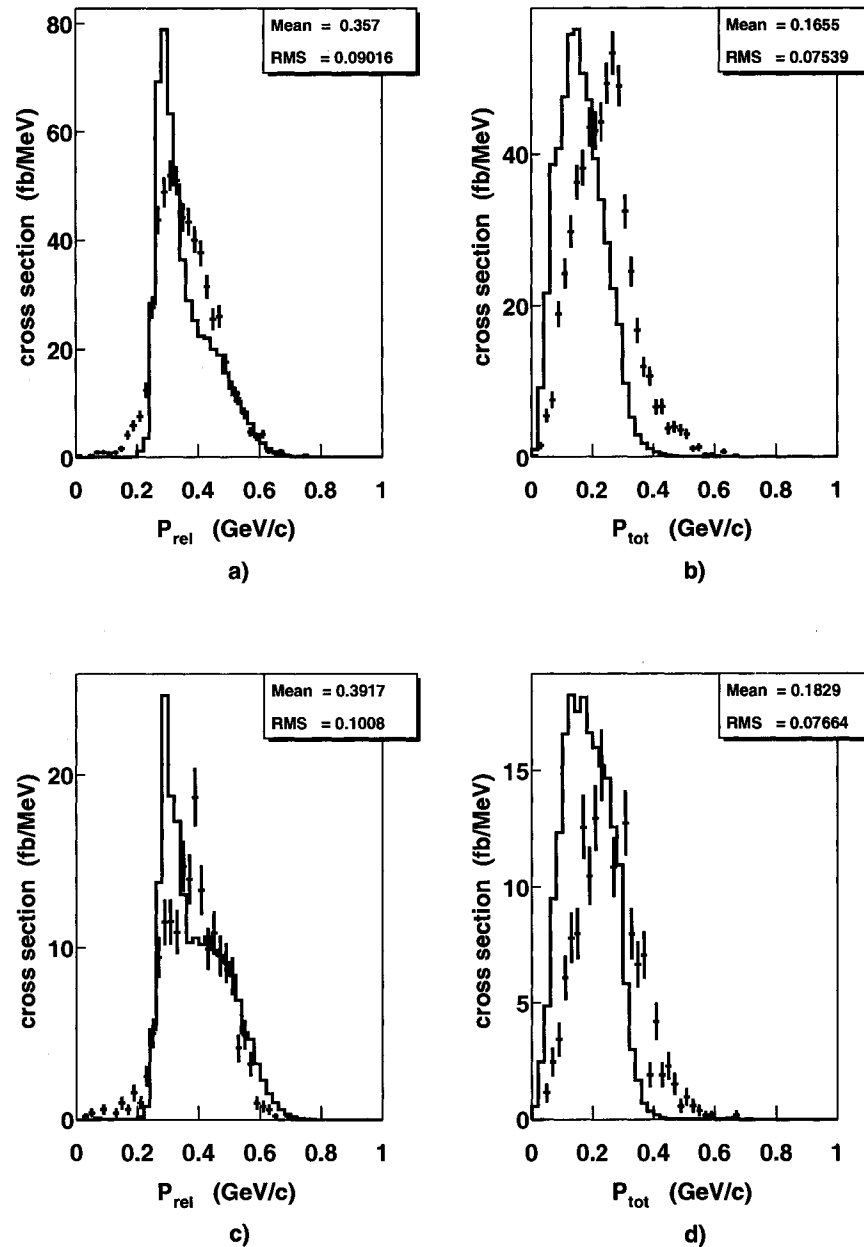
FIG. 109. Comparison of the data to PWIA at 2.2 GeV. a) Cross section vs relative momentum of the fast pn pair. Points == data, histogram shows the PWIA calculation reduced by a factor of 6; b) the same for the total momentum; c) and d) the same for fast pp pairs. Data does not have proton acceptance corrections.
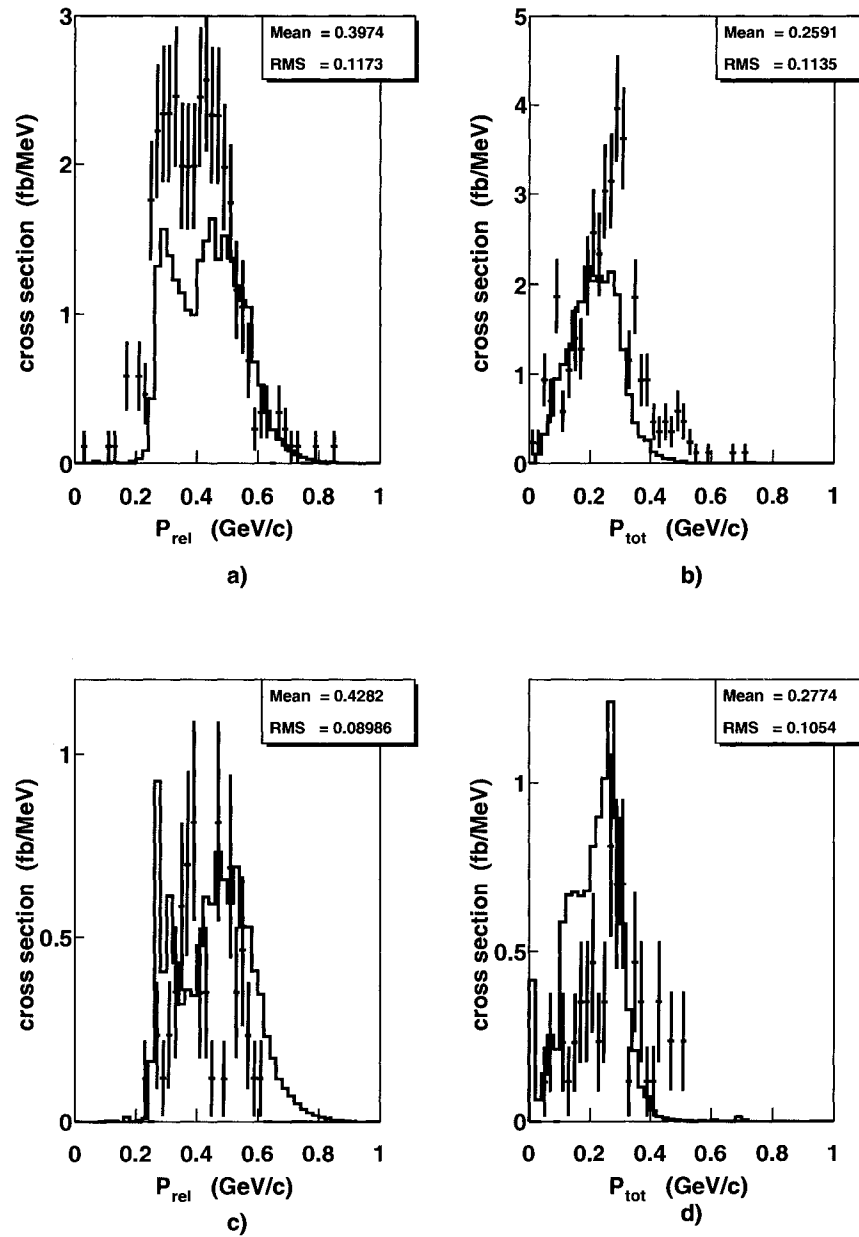
FIG. 110. Comparison of the data to PWIA at 4.4 GeV. a) Cross section vs relative momentum of the fast pn pair. Points == data, histogram shows the PWIA calculation reduced by a factor of 4; b) the same for the total momentum; c) and d) the same for fast pp pairs. Data does not have proton acceptance corrections.

most of the transferred energy. These fast nucleon pairs (both pp and pn) are back-to-back, isotropic, and carry very little momentum along $\vec{q}$, indicating that they are spectators.

We present the average cross sections within the CLAS phase space volume as a function of the pair relative and total momentum. Our results show that the relative momentum of the NN pair extends up to 700 MeV/c which is well above the Fermi momentum. The average value of the NN pair total momentum is around 250 MeV/c. This distribution falls rapidly, extending up to 600 MeV/c. The pair relative and total momentum distributions are very similar for both pp and pn pairs and for 2.2 and 4.4 GeV data. These observations supplement our correlation picture: we see pairs with large relative momentum and small total momentum with no isospin and little Q^2 dependence which indicates observation of NN correlations.

A pion production and reabsorption calculation fails to explain our data. This model produces events with one leading nucleon and two fast back-to-back nucleons, but the energy transfer in the reaction is too large and peaked in the delta region rather than in the quasielastic. The relative momentum distribution is too large since the minimum p_{rel} is determined by the pion mass. The cross section ratio of fast pp pairs to fast pn pairs are incorrect.

The data is very similar to PWIA calculations reduced by a factor of approximately $4-6$ to account for the continuum wave function of the outgoing NN pair. For both data and PWIA the cross section ratio of pp and pn pairs ($\approx 2-3$) is correct. Both data and PWIA drop by a factor of about 20 from $0.5 < Q^2 < 1$ GeV^2 (at 2.2 GeV) to $1 < Q^2 < 2$ GeV^2 (at 4.4 GeV).

Calculations by Glöckle at lower momentum transfer indicate that this reaction is primarily sensitive to the overlap integral between the NN continuum state and the same two nucleons in the bound state. It is entirely reasonable that the factor of 10 decrease in the cross section due to the the continuum state interaction of the outgoing NN pair that he found at lower q and p_{rel} is consistent with the factor of 6 difference between PWIA and our data.

Thus, experimental and theoretical evidence indicates that we have measured NN correlations in ^{3}He(e,e'pp)n by striking the third nucleon and detecting the spectator correlated pair. If so, this is the first measurement of two nucleon momentum distributions in nuclei.

BIBLIOGRAPHY

[1] S. Frullani and J. Mougey, Adv. Nucl. Phys. **14**, 1 (1984).

[2] J. Kelly, Adv. Nucl. Phys. **23**, 75 (1996).

[3] R. Machleidt, Phys. Rev. C **63**, 024001 (2001).

[4] R. B. Wiringa, V. G. J. Stoks, R. Schiavilla, Phys. Rev. C **51**, 38 (1995).

[5] V. G. J. Stoks *et al.*, Phys. Rev. C **49**, 2950 (1994).

[6] S. A. Coon *et al.*, Nucl. Phys. **A317**, 242 (1979).

[7] B. S. Pudliner *et al.*, Phys. Rev. C **56**, 1720 (1997).

[8] B.D. Serot, J.D. Walecka, Adv. Nucl. Phys. **16**, 1 (1986).

[9] A. Nogga, H. Kamada and W. Glöckle, Phys. Rev. Lett. **85**, 944 (2000).

[10] W. Glöckle *et al.*, Acta Phys. Polon. **B32**, 3053 (2001), nucl-th/0109070.

[11] J. Golak *et al.*, Phys. Rev. C **51**, 1638 (1995).

[12] H. Müther, A. Polls, Progress in Particle and Nucl. Phys. **45**, 243 (2000).

[13] M. Brack *et al.*, Phys. Rep. **124**, 275 (1985).

[14] J. Friedrich, P. Reinhard, Phys. Rev. C **33**, 335 (1986).

[15] H. Müther, A. Polls, Phys. Rev. C **61**, 014304 (2000).

[16] V.R. Pandharipande *et al.*, Rev. Mod. Phys. **69**, 981 (1997).

[17] K.A. Brueckner, Phys. Rev. **97**, 1353 (1955).

[18] H.A. Bethe, Ann. Rev. Nucl. Sci. **21**, 93 (1971).

[19] J.P. Jeukenne *et al.*, Phys. Rep. **25**, 83 (1976).

[20] H. Kümmel *et al.*, Phys. Rep. **36**, 1 (1978).

[21] W.H. Dickhoff, H. Müther, Reports on Progress in Physics **11**, 1947 (1992).

[22] R. B. Wiringa, V. Fiks, A. Fabrocini, Phys. Rev. C **38**, 1010 (1988).

[23] A. Akmal, V.R. Pandharipande, Phys. Rev. C **56**, 2261 (1997).

[24] K.E. Schmidt, D.M. Ceperley, in "Monte Carlo Methods III", ed. K Binder (Springer 1991)

[25] D.M. Ceperley, Rev. Mod. Phys. **C67**, 279 (1995).

[26] S. Janssen *et al.*, Nucl. Phys. **A672**, 285 (2000).

[27] C. Giusti and F.D. Pacati, Nucl. Phys. **A535**, 573 (1991).

[28] P. Wilhelm, J.A. Niskanen and H. Arenhövel, Nucl. Phys. **A597**, 613 (1996); Phys. Rev. Lett. **74**, 1034 (1995).

[29] S. Boffi, C. Giusti, F.D. Pacati and M. Radici, "Electromagnetic Response of Atomic Nuclei", Clarendon Press, Oxford, (1996).

[30] G. Orlandini and L. Sarra, 2nd Workshop on Induced Two Nucleon Emission, Gent, 1995.

[31] K. Egiyan *et al.*, Submitted to Phys. Rev. C (2002).

[32] J. Forest *et al.*, Phys. Rev. C **54**, 646 (1996).

[33] A. Antonov, P. Hodgson and I. Petkov, "Nucleon Momentum and Density Distributions in Nuclei", Clarendon Press, (1988).

[34] K. Dow *et al.*, Phys. Rev. Lett. **61**, 1706 (1988).

[35] L.L. Frankfurt, M.I. Strikman, D.B. Day, M.M. Sargsyan, Phys. Rev. C **48**, 2451, (1993).

[36] N. Liyanage *et al.*, Phys. Rev. Lett. **86**, 5670, (2001).

[37] J. Gao *et al.*, Phys. Rev. Lett. **84**, 3265 (2000).

[38] J. J. Kelly, Phys. Rev. C **60**, 044609 (1999).

[39] J. Ryckebusch *et al.*, Nucl. Phys. **A624**, 581 (1997).

[40] J. Ryckebusch *et al.*, Nucl. Phys. **A476**, 237 (1988).

[41] J. Ryckebusch *et al.*, Nucl. Phys. **A503**, 694 (1989).

[42] V. Van der Sluys *et al.*, Phys. Rev. C **55**, 1982 (1997).

[43] S. Janssen *et al.*, Nucl. Phys. **A672**, 285 (2000).

[44] J.P. Jeukenne and C. Mahaux, Nucl. Phys. **A394**, 445 (1983).

[45] A. Zondervan *et al.*, Nucl. Phys. **A587**, 697 (1995).

[46] L.J.H.M. Kester *et al.*, Phys. Rev. Lett. **74**, 1712 (1995).

[47] G. Onderwater *et al.*, Phys. Rev. Lett. **78**, 4893 (1997).

[48] G. Onderwater *et al.*, Phys. Rev. Lett. **81**, 2213 (1998).

[49] C. Giusti *et al.*, Phys. Rev. C **57**, 1691 (1998).

[50] G. Rosner, in Proc. Conf. on Perspectives in Hadronic Physics, Trieste 1997, ICTP/World Scientific, p. 185.

[51] R. Starink *et al.*, Phys. Lett. **B474**, 33 (2000).

[52] D. Groep *et al.*, Phys. Rev. Lett. **83**, 5443 (1999).

[53] D. Groep *et al.*, Phys. Rev. C **63**, 014005 (2000).

[54] G. Audit *et al.*, Phys. Lett. **B227**, 331 (1989).

[55] G. Audit *et al.*, Phys. Rev. C **44**, R575 (1991).

[56] J.M. Laget, Nucl. Phys. **A446**, 489c (1985).

[57] A.J. Sarty *et al.*, Phys. Rev. C **47**, 459 (1993).

[58] G. Audit *et al.*, Nucl. Phys. **A614**, 461 (1997).

[59] N.R. Kolb *et al.*, Phys. Rev. C **54**, 2175 (1996).

[60] T. Emura *et al.*, Phys. Rev. Lett. **73**, 404 (1994).

[61] T. Emura *et al.*, Phys. Rev. C **49**, R597 (1994).

[62] V. Blobel and CLAS software group, "The BOS System for CLAS Software", November 25, (1995).

[63] G. Adams *et al.*, "CLAS detector", Preprint submitted to Elsevier Science, July 15, (2002).

[64] M. D. Mestayer *et al.*, Nucl. Instr. and Meth. **A449**, 81 (2000).

[65] L. Qin *et al.*, CLAS-NOTE **1996-018** JLAB, (1996).

[66] G. Adams *et al.*, Nucl. Instr. and Meth. **A465**, 414 (2001).

[67] E. S. Smith *et al.*, Nucl. Instr. and Meth. **A432**, 265 (1999).

[68] M. Amarian *et al.*, Nucl. Instr. and Meth. **A460**, 239 (2001).

[69] R.M Gibbons, D.I Nathan, Thermodynamic Data of Helium-3, Tech. Report AFML-TR-67-175, Air Force Materials Laboratory, October 1967, Reproduced by U.S. Department of Commerce.

[70] Kim Egiyan, CLAS-NOTE **1999-007** JLAB, (1999).

[71] D. Protopopescu, Ph.D. Thesis, UNH, (2002).

[72] H. Egiyan, Ph.D. Thesis, WMU, (2001).

[73] B. Zhang, Ph.D. Thesis, MIT, (2002).

[74] D. Lawrence, M. Mestayer, CLAS-NOTE **1999-018** JLAB, (1999).

[75] C. Smith, EC Energy Calibration,
http://www.jlab.org/~lcsmith/EC_Energy_Calibration.html.

[76] M. Holtrop, CLAS GEANT Simulation,
http://improv.unh.edu/Maurik/gsim_info.html.

[77] A. Freyberg, CLAS REConstruction and analySIS framework,
http://www.jlab.org/~freyberg/recsis.html

[78] S. Stepanyan, "Simple Event Builder in the Framework of RECSIS", JLAB (private communication).

[79] D. Protopopescu *et al.*, CLAS-NOTE **2001-008** JLAB, (2001).

[80] D. Protopopescu, "Fiducial Cuts for CLAS at 4.4 GeV"
http://einstein.unh.edu/protopop/FiducialCuts/fc4E2.html.

[81] B. Zhang, "Positive Hadron Fiducial Cuts for E2 Run at 2.2 GeV"
http://www.jlab.org/Hall-B/secure/e2/bzh/pfiducialcut.html

[82] R. Niyazov, L. B. Weinstein, CLAS-NOTE **2001-013** JLAB, (2001).

[83] R. Niyazov, "Positive Hadron Fiducial Cuts for E2 Run at 4.4 GeV"
http://www.physics.odu.edu/~rust/clas/fidp.html

[84] Bob Michaels (private communication).

[85] Rolf Ent (private communication).

[86] D. Higinbotham, Proceedings of the International Symposium on Electro-magnetic Interactions in Nuclear and Hadronic Physics, ed. M. Fujiwara and T. Shima, p. 291, World Scientific, Singapore, (2002).

[87] A. Kievsky, E. Pace, G. Salme, and M. Viviani, Phys. Rev. C **56**, 64 (1997).

[88] M. Rvachev (private communication).

[89] J.M. Laget (private communication).

[90] D. H. Perkins, "Introduction to High Energy Physics", Cambridge University Press, (2000).

[91] M.M. Sargsian (private communication).

[92] E. Jans, *et al.*, Nucl. Phys. **A475**, 687 (1987).

[93] D. Drechsel, O. Hanstein, S.S. Kamalov, L. Tiator, Nucl. Phys. **A645** (1999).

[94] C.H. Oh, R.A. Arndt, I.I. Strakovsky, R.L. Workman, Phys. Rev. C **56**, 635 (1997).

[95] J.A. Niskanen, M. Vestama, Phys. Letters B**394**, 253 (1997).

[96] J. Franz, *et al.*, Physics Scripta T**87**, 14 (2000).

[97] T. Ericson and W.Weise, "Pions and Nuclei", Clarendon, Oxford, (1988).

[98] Fitting of Non-Equidistant Data Points
http://root.cern.ch/root/html/examples/Ifit.C.html

[99] J. Schwinger, Phys. Rev. **76**, 760 (1949).

[100] L.W. Mo and Y.S. Tsai, Rev. Mod. Phys. **41**, 205 (1969).

[101] Y.S.Tsai, Rev. Mod. Phys. **122**, 1898 (1961).

[102] Juncai Gao, Ph.D. Thesis, MIT (1999).

[103] H. Uberall, "Electron Scattering from Complex Nuclei", Academic Press, (1971).

APPENDIX A

ROOT TREE STRUCTURE

```
class THEADClass: public TObject{

 public:
   Int_t     Version;  // Version number from Recsis
   Int_t     Nrun;     // Run number for this run
   Int_t     Nevent;   // Event number for this run, starts with 1,
                       //increases with one for BOS each event in BOS file.
   Int_t     Time;     // Event Time as UNIX time.
   Int_t     Type;     // Event Type: 1-9 Physics event
//(2= sync, 4=level2 late fail) 10 Scaler event. < 0 Monte Carlo
   Int_t     Roc;
//=0 Sync status ok, >0 = bit pattern of offending ROC.
   Int_t     Evtclass;
// Event Classification from DAQ 0=special event,1-15 Physics
//event, 16 Sync Event, 17 Prestart, 18 Go, 19 Pause, 20 End.
   Int_t     Trigbits;// Level 1 Trigger Latch word.
 public:
   THEADClass(){};
   THEADClass(THEADClass *TmpHEAD);
   virtual ~THEADClass(){};
   void    Print();
   //
   ClassDef(THEADClass,1) //Header information for event
};


class THEADERClass : public TObject{

public:
   Int_t    NRun;      // Run number from HEAD bank.
   Int_t    NEvent;    // Event number from HEAD bank.
   Int_t    Time;      // Unix time from HEAD bank.
```

```
  Int_t    Type;       // Event type from HEAD bank.

  Int_t    ROC;        // ROC status from HEAD bank.

  Int_t    EvtClas;    // Event Type: 1-9 Physics event
//(2= sync, 4=level2 late fail) 10 Scaler event. < 0 Monte Carlo

  Int_t    TrigBits;   // Level 1 Trigger Latch word.

  Int_t    EStatus;    // Event status after reconstruction (HEVT)

  Int_t    TrgPrs;     // Trigger type*10000 +
//Prescale factor for that trigger (Event Class) (HEVT)

  Int_t    NPGP;       // Number of final reconstructed particles*100
//+ Number of geometrically reconstructed particles (HEVT)

  Float_t  FC;         // Faraday Cup (K) (HEVT)

  Float_t  FCG;        // Gated Faraday Cup (HEVT)

  Float_t  TG;         // Gated Clock (HEVT)

  Float_t  STT;        // Event start time (HEVT)

  Float_t  RF1;        // RF time (HEVT)

  Int_t    Latch1;// Trigger Latch from TGBI Bank (helicity info)

  Int_t    Helicity_Scaler; // Helicity scaler from TGBI Bank.

  Int_t    Interrupt_Time;
//Microsecond Interupt time from TGBI Bank.
}


class TEVNTClass: public TObject{


public:
  Int_t    Id;      // Particle Data Group ID (from SEB)

  Char_t   Charge;  // charge (from tracking)

  Float_t  Betta;   // Particle velocity in the units of c

  Float_t  Px;      // Momentum Vector X component.

  Float_t  Py;      // Momentum Vector Y component.

  Float_t  Pz;      // Momentum Vector Z component.

  Float_t  X;       // "Vertex" Vector X component.
      //The vertex is actually a projection onto a plane.
  Float_t  Y;       // "Vertex" Vector Y component.
      //The vertex is actually a projection onto a plane.
```

```
Float_t   Z;       // "Vertex" Vector Z component.
        //The vertex is actually a projection onto a plane.
UChar_t    Dcstat; // Index into the TDCPBClass array.
UChar_t    Ccstat; // Index into the TCCPBClass array.
UChar_t    Scstat; // Index into the TSCPBClass array.
UChar_t    Ecstat; // Index into the TECPBClass array.
UChar_t    Lcstat; // Index into the TLCPBClass array.
UChar_t    Status; // Status word
//(=0 for out of time particle)
};
class TDCPBClass: public TObject{


 public:
  Int_t     Sctr;  // 100*sector+track_ID in *BTR
  Float_t   X_sc;  // x coordinate of track intersection
//with SC plane
  Float_t   Y_sc;  // y coordinate of track intersection
//with SC plane
  Float_t   Z_sc;  // z coordinate of track intersection
//with SC plane
  Float_t   Cx_sc; // X dir cosine at (x_SC,y_SC,z_SC)
  Float_t   Cy_sc; // y dir cosine at (x_SC,y_SC,z_SC)
  Float_t   Cz_sc; // z dir cosine at (x_SC,y_SC,z_SC)
  Float_t   X_ec;  // vertex X after fiting to the beam position
  Float_t   Y_ec;  // vertex Y after fiting to the beam position
  Float_t   Z_ec;  // vertex Z after fiting to the beam position
  Float_t   Th_cc; //distance from production vertex to the beam.
  Float_t   Chi2;  //Chisquare of track fitting
  Int_t     Status;  // Status word
}
class TCCPBClass: public TObject{


 public:
  Int_t     Scsght; // 1000*sector+100*CC_segm_ID+Hit_ID in CCRC
```

```
    Float_t    Nphe;    // Number of photo-electrons
    Float_t    Time;    // Flight time relative to the evnt start time
    Float_t    Path;    // Path lenght from target
    Float_t    Chi2cc;  // Quality measure of geometrical matching
    Int_t      Status;  // Status word
}


class TSCPBClass: public TObject{


public:
    Int_t      Scpdht;  // 10000*sector+100*SC_PD_ID+Hit_ID in SCR
    Float_t    Edep;    // Deposited energy (dE/dX)
    Float_t    Time;    // Flight time relative to the evnt start time
    Float_t    Path;    // Path lenght from target
    Float_t    Chi2sc;  // Quality measure of geometrical matching
    Int_t      Status;  // Status word
}


class TECPBClass: public TObject{


public:
    Int_t      Scht;    // 100*sector+Whole_Hit_ID in ECHB
    Float_t    Etot;    // Reconstructed total energy
    Float_t    Ein;     // Inner energy
    Float_t    Eout;    // Outer energy
    Float_t    Time;    // Flight time relative to the evnt start time
    Float_t    Path;    // Path lenght from target
    Float_t    X;       // x coordinate of hit
    Float_t    Y;       // y coordinate of hit
    Float_t    Z;       // z coordinate of hit
    Float_t    M2_hit;  // second moment of _hit pattern
    Float_t    M3_hit;  // third moment of _hit pattern
    Float_t    M4_hit;  // forth moment of _hit pattern
    Int_t      Innstr;  // 10000*UI+100*VI+WI
```

```
     Int_t     Outstr;  // 10000*UO+100*VO+WO
     Float_t   Chi2ec;  // Quality measure of geometrical matching
     Int_t     Status;  // Status word
}


class TLCPBClass: public TObject{
 public:
     Int_t     Scht;    // 100*sector+Hit_ID in EC1R
     Float_t   Etot;    // Reconstructed total energy
     Float_t   Time;    // Flight time relative to the evnt start time
     Float_t   Path;    // Path lenght from target
     Float_t   X;       // x coordinate of the hit
     Float_t   Y;       // y coordinate of the hit
     Float_t   Z;       // z coordinate of the hit
     Float_t   Chi2lc;  // Quality measure of geometrical matching
     Int_t     Status;  // Status word
     Float_t   Ein;     // Reconstructed energy in the inner part
}


class TTRGSClass: public TObject{

 public:
     UInt_t    Clock_ug;    // Ungated Clock
     UInt_t    Fcup_ug;     // FCUP UNGATED
     UInt_t    Microsec;    // microsecond clock
     UInt_t    Mor_st;      // MOR.ST
     UInt_t    Mor_pc;      // MOR.PC
     UInt_t    Mor_ps;      // MOR.PS
     UInt_t    Mor_tac;     // MOR.TAC
     UInt_t    Mor;         // Master OR
     UInt_t    Pc;          // Pair Counter
     UInt_t    Ps;          // Pair Spectrometer
     UInt_t    Tac;         // Total Absorption Counter
     UInt_t    St;          // ST
```

```
UInt_t      Clock_ug_2;     // duplicate of channel 1
UInt_t      Fcup_ug_2;      // duplicate of channel 2
UInt_t      Clock_g1;       // Clock with run gatei
UInt_t      Fcup_g1;        // FCUP with Run Gate
UInt_t      Mor_st_rg;      // MOR.ST  with run gate
UInt_t      Mor_pc_rg;      // MOR.PC with run gate
UInt_t      Mor_ps_rg;      // MOR.PS with run gate
UInt_t      Mor_tac_rg;     // MOR.TAC with run gate
UInt_t      Mor_rg;         // MASTER_OR with run gate
UInt_t      Pc_rg;          // PC with run gate
UInt_t      Ps_rg;          // PS with run gate
UInt_t      Tac_rg;         // TAC with run gate
UInt_t      St_rg;          // ST  with run gate
UInt_t      Clock_g1_2;     // duplicate of channel 17
UInt_t      Fcup_g1_2;      // duplicate of channel 18
UInt_t      Clock_g2;       // CLOCK with Live gate
UInt_t      Fcup_g2;        // FCUP with Live gate
UInt_t      Mor_lg;         // MASTER_OR with Live gate
UInt_t      Clock_g2_2;     // duplicate of channel 33
UInt_t      Fcup_g2_2;      // duplicate of channel 34
UInt_t      Trig1_ug;       // Trigger 1 ungated, prescaled
UInt_t      Trig2_ug;       // Trigger 2 ungated, prescaled
UInt_t      Trig3_ug;       // Trigger 3 ungated, prescaled
UInt_t      Trig4_ug;       // Trigger 4 ungated, prescaled
UInt_t      Trig5_ug;       // Trigger 5 ungated, prescaled
UInt_t      Trig6_ug;       // Trigger 6 ungated, prescaled
UInt_t      Trig7_ug;       // Trigger 7 ungated, prescaled
UInt_t      Trig8_ug;       // Trigger 8 ungated, prescaled
UInt_t      Trig9_ug;       // Trigger 9 ungated, prescaled
UInt_t      Trig10_ug;      // Trigger 10 ungated, prescaled
UInt_t      Trig11_ug;      // Trigger 11 ungated, prescaled
UInt_t      Trig12_ug;      // Trigger 12 ungated, prescaled
UInt_t      Trig_or_ug;     // Trigger OR of 1-12 ungated,
UInt_t      L1accept;       // Level 1 accept
```

```
UInt_t      L2fail;           // Level2 fail
UInt_t      L2pass;           // Level2 pass
UInt_t      L2start;          // Level2 start
UInt_t      L2clear;          // Level2 clear
UInt_t      L2accept;         // Level2 accept
UInt_t      L3accept;         // Level3 accept
}


class TGSIMClass: public TObject{
public:
Int_t       Id;
Char_t      Charge;
Float_t     Betta;
Float_t     Px;
Float_t     Py;
Float_t     Pz;
Float_t     X;
Float_t     Y;
Float_t     Z;
Float_t     Weight;
UChar_t        Dcstat;
UChar_t        Ccstat;
UChar_t        Scstat;
UChar_t        Ecstat;
UChar_t        Lcstat;
UChar_t        Status;
}
```

APPENDIX B

CLAS FIDUCIAL ACCEPTANCE FUNCTIONS

B.0.1 Electron Fiducial Cut Function for 2.2 GeV Data

File ''EFid_2Gev_2250A.dat'':

62.2935, -92.5133, 87.0360, -38.4696, 6.3177, 0, 0, 0, 0,

78.5134, -58.5975, 3.30928, 77.4749, -64.3984, 14.4860, 0, 0, 0,

-140.845, 1381.30, -4499.99, 7557.27, -7140.27, 3828.75,

-1086.21, 126.468, 0, 497.951, -1846.42, 2759.58, -1634.71,

345.006, 0, 0, 0, 0, 9.40986, 180.752, -646.771, 1055.14,

-909.094, 424.435, -99.8368, 9.02086, 0, 288.485, -1016.03,

1463.72, -859.231, 185.976, 0, 0, 0, 0, 61.1474, -88.768,

82.6446, -36.2780, 5.92310, 0, 0, 0, 0, 78.5134, -58.5975,

3.30928, 77.4749, -64.3984, 14.4860, 0, 0, 0, 21.3087, 138.975,

-672.710, 1324.20, -1326.12, 714.866, -197.531, 21.9144, 0,

375.091, -1411.50, 2082.58, -1192.17, 239.685, 0, 0, 0, 0,

-121.816, 1182.59, -3800.98, 6319.82, -5937.33, 3179.37,

-903.954, 105.764, 0, -4781.96, 43165.9, -159567, 318502,

-376469, 271207, -116893, 27698.9, -2775.61, 61.1474, -88.7680,

82.6446, -36.2780, 5.92310, 0, 0, 0, 0, 73.7620, -34.6321,

-41.8796, 117.543, -81.2043, 17.1718, 0, 0, 0, 157.046, -765.472,

1735.21, -2053.86, 1371.34, -515.214, 101.081, -8.07402, 0,

-608.740, 4827.18, -13239.6, 17742.4, -12420.0, 4369.11,

-607.877, 0, 0, -274.278, 2380.63, -7560.19, 12582.3, -11924.5,

6464.66, -1863.44, 221.134, 0, -1240.72, 8096.04, -19407.0,

23942.9, -16052.3, 5559.32, -776.123, 0, 0, 61.1474, -88.7680,

82.6446, -36.2780, 5.92310, 0, 0, 0, 0, 78.5134, -58.5975,

3.30928, 77.4749, -64.3984, 14.4860, 0, 0, 0, -71.2528, 879.668,

-3027.37, 5226.61, -4999.19, 2689.35, -761.206, 88.1242, 0,

-1269.89, 9486.25, -26103.8, 35581.2, -25373.0, 9062.87,

-1277.60, 0, 0, -186.640, 1811.85, -6032.01, 10283.3, -9808.11,

5285.35, -1501.87, 174.799, 0, -530.826, 4643.56, -13864.2,

20580.2, -15898.0, 6106.69, -916.365, 0, 0, 61.6665, -90.4268,

84.5606, -37.2240, 6.09207, 0, 0, 0, 0, 78.5134, -58.5975,
3.30928, 77.4749, -64.3984, 14.4860, 0, 0, 0, -1.53910, 216.936,
-701.057, 1167.26, -1111.92, 615.364, -183.854, 22.8595, 0,
-19.7415, 454.317, -1250.51, 1512.52, -762.408, 137.695, 0, 0, 0,
-55.9612, 657.449, -2049.73, 3295.30, -2995.85, 1553.68,
-427.764, 48.4324, 0, -522.682, 3356.77, -7535.50, 8756.49,
-5518.61, 1795.60, -235.144, 0, 0, 61.1474, -88.7680, 82.6446,
-36.2780, 5.92310, 0, 0, 0, 0, 73.7620, -34.6321, -41.8796,
117.543, -81.2043, 17.1718, 0, 0, 0, -82.0368, 883.261, -2828.84,
4621.53, -4223.56, 2185.52, -598.218, 67.2908, 0, 608.323,
-2743.56, 4942.01, -4045.58, 1558.07, -226.240, 0, 0, 0, 4.07203,
138.882, -321.983, 282.702, -12.9566, -129.159, 74.5884,
-12.9994, 0, -866.737, 5984.13, -15129.6, 19134.6, -12757.7,
4276.79, -566.056, 0, 0 74.4893, -158.720, 251.241, -200.000,
52.2984, 25.4188, -18.8692, 3.27217, 90.8413, -226.800, 358.487,
-259.260, 30.9359, 68.7248, -38.9760, 6.47933, 117.102, -429.455,
1208.29, -1922.72, 1791.40, -965.135, 277.459, -32.8536, 55.0676,
91.0959, -444.252, 791.284, -717.492, 350.325, -87.3235, 8.68087
77.7940, -192.492, 361.852, -394.127, 246.499, -84.6133, 13.9182,
-0.713846, 41.2902, 110.603, -586.690, 1130.70, -1137.27,
633.345, -185.038, 22.1482 -12998.3, 57694.0, -109085, 114102,
-71303.6, 26616.9, -5494.45, 483.756, 17842.9, -74659.9, 133869,
-133170, 79380.0, -28352.3, 5617.88, -476.314, 65.5364, -99.8689,
88.5645, 24.8299, -121.327, 102.818, -37.8275, 5.28492, 66.4049,
-76.4096, -20.8674, 230.072, -318.905, 206.721, -66.3286,
8.48753, 100.262, -358.882, 957.267, -1495.42, 1396.73, -765.881,
226.791, -27.9341, 50.4447, 48.3032, -315.976, 580.141, -525.583,
252.075, -59.9294, 5.34805, 78.5845, -155.728, 320.528, -420.296,
341.899, -164.626, 42.5274, -4.50224, 95.9430, -221.787, 391.495,
-350.033, 131.391, 13.2965, -24.0460, 4.92253


```
C-------------------------------------------------------------

        SUBROUTINE ReadEFidPars
C-------------------------------------------------------------
```

```
c      read the parameters for electron fiducial cut
c      from the file EFid_2Gev_2250A.dat
c      which must be in current dir

       real par_phi(9,6,6)
       real par_the3(8,4)
       real par_the4(8,2)
       real par_the5(8,8)
       common /EFidPars/par_phi,par_the3,par_the4,par_the5

       open(unit=99,file="EFid_2Gev_2250A.dat",status="old")
       read (99,*) par_phi
       read (99,*) par_the3
       read (99,*) par_the4
       read (99,*) par_the5
       close(99)
       return
       end


C---------------------------------------------------------------
       SUBROUTINE EFiducialCut_2Gev_2250A(PX, PY, PZ, STATUS)
C---------------------------------------------------------------
c      electron fiducial cut for 2.2Gev 2250A
c      subroutine ReadEFidPars must be called before this subroutine
c      is called to get the parameters
c      input : real px py pz, three component of electron momentum
c output: int status, 1 means passing the cut, 0 means not passing

       real par_phi(9,6,6)
       real par_the3(8,4)
       real par_the4(8,2)
       real par_the5(8,8)
       common /EFidPars/par_phi,par_the3,par_the4,par_the5
```

```fortran
      real px, py, pz
      integer status, sector, ipar, dpar
      real p, theta, phi, tmptheta
      real con_phi(6)
      real con_the3(4)
      real con_the4(2)
      real con_the5(8)

      status = 1
      phi=atan2(py,px)*180./3.14159265
      if (phi.lt.-30) phi=phi+360
      sector=int((phi+30.)/60.)+1
      if (sector.lt.1) sector=1
      if (sector.gt.6) sector=6
      phi=phi-(sector-1)*60.
      theta=atan2(sqrt(px*px+py*py),pz)*180./3.14159265
      p=sqrt(px*px+py*py+pz*pz)
      do 771 ipar=1,6
         con_phi(ipar) = 0.0
         do 772 dpar=1,9
            con_phi(ipar) = con_phi(ipar)*p
     $              + par_phi(10-dpar,ipar,sector)
772      continue
771   continue
      if(phi.lt.0) then
         tmptheta=con_phi(1)-con_phi(4)/con_phi(3)
     $         +con_phi(4)/(con_phi(3)+phi)
         if(theta.gt.tmptheta.and.
     $         tmptheta.ge.con_phi(1).and.
     $         theta.lt.con_phi(2)) then
            status = 1
         else
            status = 0
         endif
```

```
          else
             tmptheta=con_phi(1)-con_phi(6)/con_phi(5)
     $             +con_phi(6)/(con_phi(5)-phi)
             if(theta.gt.tmptheta.and.
     $             tmptheta.ge.con_phi(1).and.
     $             theta.lt.con_phi(2)) then
                status = 1
             else
                status = 0
             endif
          endif


c     knockout bad sc paddles

          if(sector.eq.3) then
             do 661 ipar=1,4
                con_the3(ipar) = 0.0
                do 662 dpar=1,8
                   con_the3(ipar) = con_the3(ipar)*p
     $                   + par_the3(9-dpar,ipar)
662             continue
661          continue
             if(theta.gt.con_the3(1).and.
     $             theta.lt.con_the3(2)) status=0
             if(theta.gt.con_the3(3).and.
     $             theta.lt.con_the3(4)) status=0
          elseif(sector.eq.4) then
             do 551 ipar=1,2
                con_the4(ipar) = 0.0
                do 552 dpar=1,8
                   con_the4(ipar) = con_the4(ipar)*p
     $                   + par_the4(9-dpar,ipar)
552             continue
551          continue
```

```fortran
      if(theta.gt.con_the4(1).and.
$          theta.lt.con_the4(2)) status=0
    elseif(sector.eq.5) then
        do 441 ipar=1,8
          con_the5(ipar) = 0.0
          do 442 dpar=1,8
            con_the5(ipar) = con_the5(ipar)*p
$                  + par_the5(9-dpar,ipar)
442       continue
441     continue
        if(theta.gt.con_the5(1).and.
$          theta.lt.con_the5(2)) status=0
        if(theta.gt.con_the5(3).and.
$          theta.lt.con_the5(4)) status=0
        if(theta.gt.con_the5(5).and.
$             theta.lt.con_the5(6)) status=0
        if(theta.gt.con_the5(7).and.
$          theta.lt.con_the5(8)) status=0
    endif

    return
    end
C-----------------------------------------------
```

B.0.2 Electron Fiducial Cuts Function for 4.4 GeV Data

File ``EFid_4Gev_2250A.dat'':

0	1	24.0741	0.3956	0.0000	0.0000	0.0000	0.0000
1	1	6.4315	119.1049	-105.4670	39.4381	-7.0378	0.4891
10	1	35.0826	-14.0466	7.7426	-4.5093	2.5550	-0.4463
20	1	-45.5629	121.8945	-101.0246	38.3569	-6.9255	0.4866
11	1	37.6369	-16.6257	1.6594	0.7670	0.2638	-0.1023
21	1	-58.6417	150.6479	-114.5766	37.2221	-5.0617	0.1969
0	2	23.6692	0.3920	0.0000	0.0000	0.0000	0.0000
1	2	-0.1193	137.0834	-122.3934	46.8152	-8.5656	0.6108
10	2	29.2802	81.5290	-148.4241	93.9628	-24.8907	2.3643
20	2	15.5391	-67.2201	94.7798	-53.2652	13.1357	-1.1880
11	2	13.9977	39.5521	-51.6330	30.1618	-7.5100	0.6433
21	2	-11.5064	67.2117	-73.0534	34.0094	-7.3159	0.6019
0	3	23.9736	0.4161	0.0000	0.0000	0.0000	0.0000
1	3	1.9415	136.5231	-126.6265	49.9535	-9.3366	0.6735
10	3	51.2841	-63.0316	53.2926	-20.6212	4.1111	-0.3390
20	3	-41.8026	109.7667	-87.0272	30.4908	-4.7665	0.2574
11	3	56.5984	-70.1407	74.4999	-40.9315	11.0177	-1.1128
21	3	13.8989	-39.9438	51.9204	-27.7107	6.5402	-0.5703
0	4	24.0532	0.4014	0.0000	0.0000	0.0000	0.0000
1	4	-1.1383	135.4813	-117.8297	43.6276	-7.6775	0.5235
10	4	-16.5499	144.8553	-181.9218	99.2256	-24.1030	2.1425
20	4	-14.3965	40.1487	-10.1949	-9.7720	4.9530	-0.6104
11	4	0.1339	80.5209	-95.1136	52.0495	-12.8951	1.1852
21	4	-1.4177	18.7895	-11.3976	1.0894	0.6064	-0.1109
0	5	24.3039	0.4092	0.0000	0.0000	0.0000	0.0000
1	5	38.2610	34.5935	-20.2552	-0.8174	1.9360	-0.2740
10	5	42.5320	-34.9434	20.1032	-1.6946	-1.4179	0.2536
20	5	-74.5909	227.1844	-228.3079	105.7682	-23.0837	1.9285
11	5	-2.9526	105.1065	-138.4144	81.1844	-21.2689	2.0444
21	5	-33.3260	90.8762	-69.0875	22.4258	-3.0937	0.1310
0	6	23.7462	0.3907	0.0000	0.0000	0.0000	0.0000

```
 1  6   -6.6876 148.9805 -129.4038   48.1958   -8.5250   0.5849
10  6   -8.7005 112.6199 -137.9916   77.8463  -19.9898   1.8980
20  6   -8.8829  45.1467  -39.4914   14.1594   -2.1805   0.1131
11  6  116.1167-225.1722  200.6938  -82.9617   15.9407  -1.1413
21  6  -41.8961 145.5806 -153.8990   72.8448  -16.0143   1.3320


C---------------------------------------------------
      SUBROUTINE EFID_CUT_4GeV(PX, PY, PZ, STATUS)
C---------------------------------------------------
c     electron fiducial cuts for 4.461 GeV data
c     input real px, py, pz momentum components of electron
c     output int status 1 means passing, 0 means failure

      REAL T0_P(6,6)
      REAL T1_P(6,6)
      REAL B_P(6,2,6)
      REAL A_P(6,2,6)
      COMMON /EFID_PAR/T0_P, T1_P, B_P, A_P

      REAL PX, PY, PZ
      REAL P, TH,PHI
      REAL EN
      REAL phimin, phimax;
      REAL T0, T1, BP(2), AP(2)
      INTEGER SECTOR, K, I
      INTEGER STATUS

      STATUS = 0
      P = SQRT(PX*PX+PY*PY+PZ*PZ)
      PHI = ATAN2(PY,PX)*180./3.14159265
      IF (PHI.LT.-30) PHI=PHI+360.
      TH = ATAN2(SQRT(PX*PX+PY*PY),PZ)*180./3.14159265
      EN = P
```

```fortran
SECTOR = INT((PHI+30.)/60.)+1;


IF(SECTOR.LE.0) SECTOR = 1
IF(SECTOR.GT.6) SECTOR = 6


T0 =T0_P(SECTOR,1)/(EN**T0_P(SECTOR,2))
T1 = 0.
DO I=1,6
    T1 = T1 + T1_P(SECTOR,I)*(EN**(I-1))
ENDDO


DO I=1,2
    BP(I) = 0.
    AP(I) = 0.
    DO K = 1,6
        BP(I) = BP(I) + B_P(SECTOR,I,K)*(EN**(K-1))
        AP(I) = AP(I) + A_P(SECTOR,I,K)*(EN**(K-1))
    ENDDO
ENDDO


IF(T1.LT.45.)T1 = 45.
IF(T0.LT.TH.and.TH.LT.T1)THEN
    PHIMIN = 60.*(SECTOR-1) - BP(1)*(1.
&         - 1./((TH-T0)/(BP(1)/AP(1))+1.))
    PHIMAX = 60.*(SECTOR-1) + BP(2)*(1.
&         - 1./((TH-T0)/(BP(2)/AP(2))+1.))
ELSE
    PHIMIN = 60.*(SECTOR - 1)
    PHIMAX = 60.*(SECTOR - 1)
ENDIF


IF(PHIMIN.LT.PHI.and.PHI.LT.PHIMAX.and.TH.GT.15.
&      .and. EN .gt. 0.9)THEN
    STATUS = 1
```

```
        ENDIF
        END


C-------------------------------------------------------
        SUBROUTINE  INIT_FID_PARMS
C-------------------------------------------------------
C-    This Subroutine reads and fills
C-    Arrays with parameters for Fiducial Cuts.
C-    You have to first call this function once then call
C-    Fiducial cut function for every event.
C-
        REAL    T0_P(6,6)
        REAL    T1_P(6,6)
        REAL    B_P(6,2,6)
        REAL    A_P(6,2,6)
        COMMON /EFID_PAR/T0_P, T1_P, B_P, A_P
        INTEGER CI,PTYPE,K,I, ICOUNT


        REAL PARM(6)


        open(unit=99,file='EFid_4Gev_2250A.dat',status='old')


        ICOUNT = 0


 110    CONTINUE


C----DO I=1,6


        READ(99,*,end=111)PTYPE,CI,PARM(1),PARM(2),PARM(3),
     +      PARM(4),PARM(5),PARM(6)


        IF(PTYPE.EQ.0) THEN
            DO K = 1,6
                T0_P(CI,K) = PARM(K)
```

```
            ENDDO
         ENDIF


         IF(PTYPE.EQ.1) THEN
            DO K = 1,6
               T1_P(CI,K) = PARM(K)
            ENDDO
         ENDIF


         IF(PTYPE.EQ.10) THEN
            DO K = 1,6
               B_P(CI,1,K) = PARM(K)
            ENDDO
         ENDIF


         IF(PTYPE.EQ.11) THEN
            DO K = 1,6
               B_P(CI,2,K) = PARM(K)
            ENDDO
         ENDIF


         IF(PTYPE.EQ.20) THEN
            DO K = 1,6
               A_P(CI,1,K) = PARM(K)
            ENDDO
         ENDIF


         IF(PTYPE.EQ.21) THEN
            DO K = 1,6
               A_P(CI,2,K) = PARM(K)
            ENDDO
         ENDIF


         ICOUNT = ICOUNT + 1
```

```
            GOTO 110


111     CLOSE(99)


        WRITE(*,*) ICOUNT,'    parameters were read'



        END
C------------------------------------------------------
```

B.0.3   Proton Fiducial Cut Function for 2.2 GeV Data

File ''PFid_2Gev_2250A.dat'':

60.2165, -189.720, 446.990, -523.122, 320.721, -97.8518,

11.5258, -1457.16, 13814.2, -43182.7, 66646.0, -54355.1,

22423.5, -3683.76, 17.1086, 54.2974, -103.464, 111.325,

-70.7673, 27.2551, -5.02858, -2547.86, 22143.1, -66326.6,

101105.0, -82187.8, 33959.7, -5607.59, 65.7242, -246.922,

759.745, -1198.32, 1007.05, -428.060, 72.2644, 3384.16,

-19353.1, 54083.5, -79843.4, 63870.2, -26079.2, 4250.29,

85.2489, -441.821, 1327.52, -1978.53, 1567.84, -633.530,

102.928, 411.998, -533.572, 599.925, 2099.52, -5061.48,

3701.58, -891.843, 110.022, -558.044, 1512.96, -2098.53,

1579.55, -613.478, 96.3279, 3937.29, -23745.1, 59651.0,

-76988.6, 54276.0, -19900.2, 2974.95, 35.8488, -46.9595,

107.492, -93.9141, 10.5845, 26.1910, -9.89460, -326.838,

4634.99, -11155.2, 11811.4, -5405.80, 554.030, 175.526,

38.9338, -62.8663, 118.218, -56.6953, -40.5083, 46.1782,

-11.5822, 1864.83, -11735.6, 34175.4, -48928.5, 37315.8,

-14496.1, 2254.05, 23.6892, 9.69854, 94.4521, -270.119,

288.132, -140.031, 25.9272, -261.086, 4863.13, -11760.4,

13791.1, -8983.19, 3136.52, -457.183, -11.0252, 348.901,

-1172.63, 1980.73, -1759.08, 786.043, -139.299, -2231.41,

23477.1, -78229.3, 129238.0, -111761.0, 48561.4, -8370.65,

104.415, -548.464, 1506.70, -2064.10, 1507.55, -561.677,

83.9247, 1402.87, -9008.78, 25660.0, -37543.3, 29860.8,

-12238.4, 2019.03, 20.4577, 66.1373, -205.218, 372.864,

-366.625, 177.596, -33.1168, 2059.77, -14468.3, 46492.9,

-72168.2, 58275.9, -23615.8, 3800.60, -18.9897, 392.519,

-1234.31, 1950.24, -1623.01, 681.260, -113.806, -3478.50,

32840.9, -104381.0, 167656.0, -143070.0, 61909.3, -10690.1

110.007, 121.302, 97.8380, -1679.71, 4022.73, -3973.09,

1422.42, 69.7305, 359.843, -876.383, 649.612, 600.059,

-1155.43, 472.866, 13.9334, -236.587, 810.783, -1614.65,

1851.97, -1125.48, 280.069, 10.1644, 51.7943, -527.843,

2071.12, -3480.34, 2663.52, -768.498, 161.555, -263.801,

770.924, -902.814, 503.641, -319.619, 171.147, 154.660,

-619.711, 3444.65, -8994.29, 12253.9, -8439.82, 2321.14,

117.461, -1429.96, 6117.79, -13492.3, 16142.2, -9965.40,

2490.47, 7.77411, -17.3501, 279.462, -876.326, 1398.82,

-1137.49, 365.383, -31.1460, 1942.49, -9193.97, 21731.0,

-26961.3, 16701.7, -4067.85, 154.660, -654.420, 3774.08,

-9920.36, 13333.7, -8953.68, 2386.32, 63.2709, -867.859,

4000.97, -9557.57, 12215.1, -7926.91, 2052.90, -28.1127,

484.636, -2665.71, 7484.94, -10740.7, 7561.79, -2076.70,

172.853, -656.312, 3768.76, -10243.0, 14600.3, -10616.3,

3095.27, 270.076, -1938.46, 9276.01, -21861.1, 27363.7,

-17479.9, 4490.05, 32.2327, -432.593, 1666.57, -3491.43,

4031.58, -2406.30, 579.944, -44.9153, 638.112, -2971.77,

7223.13, -9328.99, 6080.46, -1576.13, 45.7403, 875.133,

-3646.85, 7848.52, -8905.36, 4914.78, -1010.91, 138.000,

-449.485, 2806.13, -7725.44, 10777.3, -7482.95, 2056.80,

72.7551, -944.002, 4200.92, -9776.76, 12316.6, -7955.78,

2066.50, -9.59531, 180.519, -795.797, 2124.85, -2978.29,

2040.14, -541.811, 77.5100, 494.571, -1625.99, 2397.48,

-1177.99, -574.604, 530.446, 117.869, -56.8761, 330.252,

-715.276, 807.257, -497.124, 133.989, 7.66164, -208.001,

996.883, -2772.33, 4100.81, -3008.90, 864.126, -25.3497,

346.501, -1458.46, 3513.62, -4625.70, 3088.01, -818.696

-28.1486, 425.124, -935.693, 1065.39, -608.526, 137.658,

-15.2084, 345.466, -697.657, 751.738, -419.288, 95.2206

17.1490, 294.605, -640.590, 707.758, -386.730, 83.2529,

35.9318, 204.580, -404.489, 413.240, -209.580, 41.7819,

47.6825, 274.777, -754.725, 1117.80, -846.816, 255.607,

44.7484, 344.543, -872.200, 1113.89, -694.736, 168.061,

-205.978, 828.617, -1199.65, 875.482, -317.846, 45.6938,

-240.595, 961.068, -1370.34, 977.625, -345.743, 48.3834,

-136.104, 479.276, -593.135, 374.730, -118.350, 14.7923,

-196.773, 700.974, -894.540, 577.460, -185.690, 23.6201

```
81.8115, 139.810, -445.130, 804.212, -821.194, 364.924,
79.5053, 317.287, -1582.80, 3987.05, -4880.55, 2305.63,
-137.480, 633.288, -954.383, 721.057, -269.140, 39.4822,
-145.605, 697.662, -1088.74, 853.855, -330.883, 50.3421
-29.9426, 370.963, -714.697, 707.343, -348.995, 67.7647,
-27.4173, 372.536, -693.341, 652.792, -302.559, 54.7761,
-47.1617, 132.967, -104.776, 41.7673, -7.68238, 0.404311,
-54.5895, 149.685, -111.590, 41.2556, -6.93943, 0.301087,
-79.1386, 275.678, -341.972, 218.907, -69.5520, 8.66381,
-97.5794, 352.616, -468.487, 322.829, -111.159, 15.0975,
22.5823, -182.064, 365.317, -294.653, 108.779, -15.2712,
-7.59521, 2.91795, 31.6773, -28.3085, 10.5943, -1.57966


C-------------------------------------------------------------
      SUBROUTINE ReadPFidPars
C-------------------------------------------------------------
c     read the parameters for proton fiducial cuts
c     from the file PFid_2GeV_2250A.dat
c     which must be in current dir

      real par_for(7,4,6)
      real par_bak(7,4,6)
      real par_pth2(6,2)
      real par_pth3(6,8)
      real par_pth4(6,4)
      real par_pth5(6,8)
      common /PFidPars/par_for,par_bak,par_pth2,
      par_pth3,par_pth4,par_pth5

      open(unit=99,file="PFid_2GeV_2250A.dat",status="old")
      read (99,*) par_for
      read (99,*) par_bak
      read (99,*) par_pth2
      read (99,*) par_pth3
```

```
read (99,*) par_pth4
read (99,*) par_pth5
close(99)
return
end


C----------------------------------------------------------
      SUBROUTINE PFiducialCut_2GeV_2250A(px, py, pz, status)
C----------------------------------------------------------
c     proton fiducial cuts for 2.2GeV 2250A data
c     subroutine ReadPFidPars must be called before this subroutine
c     is called for the first time to get the parameters
c     input : real px py pz, three components of proton momentum
c output: int status, 1 means passing the cut, 0 means not


      real par_for(7,4,6)
      real par_bak(7,4,6)
      real par_pth2(6,2)
      real par_pth3(6,8)
      real par_pth4(6,4)
      real par_pth5(6,8)
      common /PFidPars/par_for,par_bak,par_pth2,
      par_pth3,par_pth4,par_pth5


      real px, py, pz
      integer status, sector, ipar, dpar
      real p, p_for, p_bak, p_pth
      real theta0, theta, tmptheta
      real phi, phi_lower, phi_upper
      real con_for(4)
      real con_bak(4)
      real con_pth2(2)
      real con_pth3(8)
      real con_pth4(4)
```

```fortran
      real con_pth5(8)

      status = 1
      phi=atan2(py,px)*180./3.14159265
      if (phi.lt.-30) phi=phi+360
      sector=int((phi+30.)/60.)+1
      if (sector.lt.1) sector=1
      if (sector.gt.6) sector=6
      phi=phi-(sector-1)*60.
      theta=atan2(sqrt(px*px+py*py),pz)*180./3.14159265
      p=sqrt(px*px+py*py+pz*pz)

      p_for = p
      if (p_for.lt.0.3) p_for = 0.3
      if (p_for.gt.1.6) p_for = 1.6
      p_bak = p
      if (p_bak.lt.0.2) p_bak = 0.2
      if (p_bak.gt.1.0) p_bak = 1.0
      theta0 = 8.5
      phi_lower = -24.0
      phi_upper = 24.0

c     calculate the parameters for this momentum

      do ipar=1,4
         con_for(ipar) = 0.0
         con_bak(ipar) = 0.0
         do dpar=1,7
            con_for(ipar) = con_for(ipar)*p_for
     $              + par_for(8-dpar,ipar,sector)
            con_bak(ipar) = con_bak(ipar)*p_bak
     $              + par_bak(8-dpar,ipar,sector)
         enddo
      enddo
```

```
c       check forward region


        if(phi.lt.0) then
            tmptheta = theta0 - con_for(2)/con_for(1)
$               + con_for(2)/(con_for(1)+phi)
            if(theta.gt.tmptheta.and.
$               tmptheta.ge.theta0.and.
$               phi.ge.phi_lower) then
                status = 1
            else
                status = 0
                return
            endif
         else
            tmptheta = theta0 - con_for(4)/con_for(3)
$               + con_for(4)/(con_for(3)-phi)
            if(theta.gt.tmptheta.and.
$               tmptheta.ge.theta0.and.
$               phi.le.phi_upper) then
                status = 1
            else
                status = 0
                return
            endif
         endif


c     check backward region


        if(theta.gt.con_bak(1)) then
            status = 0
            return
        elseif(theta.gt.con_bak(2)) then
            if((phi-phi_lower)/(theta-con_bak(2)).ge.
```

```
$           (con_bak(3)-phi_lower)/(con_bak(1)-con_bak(2))
$           .and.(phi-phi_upper)/(theta-con_bak(2)).le.
$           (con_bak(4)-phi_upper)/(con_bak(1)-con_bak(2))) then
          status = 1
      else
          status = 0
          return
      endif
    endif


c     knock out bad sc paddles


    p_pth = p
    if (p_pth.lt.0.2) p_pth = 0.2
    if(sector.eq.2) then
        do ipar=1,2
            con_pth2(ipar) = 0.0
            do dpar=1,6
                con_pth2(ipar) = con_pth2(ipar)*p_pth
$                   + par_pth2(7-dpar,ipar)
            enddo
        enddo
        if(theta.gt.con_pth2(1).and.
$             theta.lt.con_pth2(2)) status = 0
     elseif(sector.eq.3) then
        do ipar=1,8
            con_pth3(ipar) = 0.0
            do dpar=1,6
                con_pth3(ipar) = con_pth3(ipar)*p_pth
$                   + par_pth3(7-dpar,ipar)
            enddo
        enddo
        if(theta.gt.con_pth3(1).and.
$             theta.lt.con_pth3(2)) status = 0
```

```
      if(theta.gt.con_pth3(3).and.
$          theta.lt.con_pth3(4)) status = 0
      if(theta.gt.con_pth3(5).and.
$          theta.lt.con_pth3(6)) status = 0
      if(theta.gt.con_pth3(7).and.
$          theta.lt.con_pth3(8)) status = 0
   elseif(sector.eq.4) then
      do ipar=1,4
         con_pth4(ipar) = 0.0
         do dpar=1,6
            con_pth4(ipar) = con_pth4(ipar)*p_pth
$                + par_pth4(7-dpar,ipar)
         enddo
      enddo
      if(theta.gt.con_pth4(1).and.
$          theta.lt.con_pth4(2)) status = 0
      if(theta.gt.con_pth4(3).and.
$          theta.lt.con_pth4(4)) status = 0
   elseif(sector.eq.5) then
      do ipar=1,8
         con_pth5(ipar) = 0.0
         do dpar=1,6
            con_pth5(ipar) = con_pth5(ipar)*p_pth
$                + par_pth5(7-dpar,ipar)
         enddo
      enddo
      if(theta.gt.con_pth5(1).and.
$          theta.lt.con_pth5(2)) status = 0
      if(theta.gt.con_pth5(3).and.
$          theta.lt.con_pth5(4)) status = 0
      if(theta.gt.con_pth5(5).and.
$          theta.lt.con_pth5(6)) status = 0
      if(theta.gt.con_pth5(7).and.
$          theta.lt.con_pth5(8)) status = 0
```

```
        endif


        return
        end
C-----------------------------------------------------
```

B.0.4 Proton Fiducial Cut Function for 4.4 GeV Data

File ''PFid_4Gev_2250A.dat'':

26.2564,0.441269,-29.7632,94.5137,7.71903,2.10915

29.7455,-0.826489,4.09596,91.8187,8.38108,1.5016

29.5399,-0.878321,43.1909,64.9772,11.1844,0.825411

28.5857,0.4061,98.6296,95.5022,13.7297,0.415071

31.9803,0.341766,257.124,103.504,14.2357,0.43387

29.2846,-0.257616,51.1709,84.3207,10.2963,1.69991

34.7359,-1.45301,660.653,-79.1375,11.3239,1.05352

30.6992,0.71858,442.087,4.20897,3.62722,3.35155

19.1518,3.71404,-197.134,177.828,9.63173,1.35402

23.9897,1.52101,23.9288,71.4476,8.89464,1.69512

22.6619,2.4697,-54.5174,112.22,11.2561,0.687839

20.9859,3.86504,-56.5229,230.635,13.6587,0.270987

24.683,0.470268,124.501,-9.04329,8.60129,1.66063

26.2736,-0.591497,182.954,-51.059,7.65701,2.29757

24.8681,1.15526,111.322,22.2304,9.46319,1.6834

29.3639,1.307,282.797,89.5863,11.7162,0.376266

36.8099,-0.785452,655.368,46.4935,12.0443,0.500522

25.8401,0.899645,141.723,27.6687,9.62103,1.7379

32.9905,-0.580968,464.263,30.5379,11.7414,0.320415

26.8867,0.748481,150.349,51.4182,8.70942,1.51013

26.0729,0.357197,136.456,24.1839,6.70568,0.820883

25.8339,1.018,149.648,38.7987,6.56928,0.527773

27.997,0.0685368,268.87,-45.3343,5.26386,3.08026

30.3568,1.60206,359.39,197.047,11.1523,0.451219

-24.4118,4.20154,-0.0480933,-0.0800641,0.000311929,0.000511191

-34.5523,8.81812,0.221281,-0.203846,-0.00115322,0.00119883

-29.4962,6.57417,0.0830637,-0.142094,-0.000271087,0.000801481

-29.5177,6.23458,0.183415,-0.160458,-0.00121912,0.0010282

-19.8091,4.37431,-0.046672,-0.124147,-7.21454e-05,0.000931229

-38.1865,10.6462,0.363126,-0.267793,-0.00212252,0.00162732

-15.6987,3.34818,-0.155291,-0.102923,0.000736214,0.000775517

-15.9442,1.75807,-0.196246,-0.0524198,0.00118102,0.000398854

```
-14.4453,1.65733,-0.269699,-0.0423913,0.00187485,0.000274252
-18.5972,1.41622,-0.144491,-0.0369631,0.000874762,0.000326006
-17.1008,0.577868,-0.173353,-0.021315,0.00108238,0.000189545
2.21904,-3.38706,-0.636698,0.0953525,0.0038789,-0.000559086
-13.7253,-1.53789,-0.296133,0.0648705,0.00269427,-0.000928492
-12.356,-2.62192,-0.366191,0.115155,0.0033624,-0.00137599
-2.52638,-9.6591,-0.743505,0.380195,0.0067055,-0.00369404
-34.5804,15.3815,0.417723,-0.489802,-0.00337546,0.00370894
1.87747,-7.70598,-0.919924,0.376373,0.00776553,-0.00354661
-12.3968,-2.37408,-0.367352,0.114661,0.00352523,-0.00148841
-29.5895,10.9088,0.248994,-0.326966,-0.00154954,0.00202508
-7.20087,-6.19132,-0.568426,0.257971,0.00476513,-0.00236084
-10.0076,-3.66545,-0.468027,0.163446,0.00421363,-0.00175242
-9.03582,-5.14009,-0.515592,0.221044,0.00482855,-0.00237549
-8.55955,-5.27785,-0.504058,0.201472,0.00404296,-0.00175892
-21.122,5.19264,-0.0761427,-0.0826774,0.0018747,-0.000390706
131.839,-6.64199,-22.8623,4.91185,126.5,20
132.055,-5.2283,2.20945,-1.57951,128.429,11.4286
137.945,-7.90553,-12.8716,3.94534,119.857,22.8571
124.743,-3.54503,-22.8263,5.62231,130.429,11.4286
136.455,-7.59559,-18.6847,4.52149,123.5,20
126.556,-4.02284,-22.2328,5.23298,124.857,22.8571
97.3917,2.99764,26.7715,-5.95695,126.5,20
132.154,-6.60261,0.000146616,1.53542,128.429,11.4286
113.746,-1.24667,32.0728,-9.35241,119.857,22.8571
118.596,-2.44983,22.2973,-5.40976,130.429,11.4286
125.129,-3.96273,21.6178,-5.86908,123.5,20
111.201,-0.178015,25.1267,-6.55928,124.857,22.8571


C-----------------------------------------------------------


File ''PFid_4Gev_2250A.inc'':


      real Pfidft1l(6,6)
```

```
      real Pfidft1r(6,6)
      real Pfidft2l(6,6)
      real Pfidft2r(6,6)
      real Pfidbt1l(6,6)
      real Pfidbt1r(6,6)
      real Pfidbt2l(6,6)
      real Pfidbt2r(6,6)
      real Pfidbl(6,6)
      real Pfidbr(6,6)
      parameter(pi     = 3.141592654)


      common /PFidPars/Pfidft1l Pfidft1r,Pfidft2l,Pfidft2r,
     x         Pfidbt1l,Pfidbt1r,Pfidbt2l,Pfidbt2r,Pfidbl,Pfidbr


C-----------------------------------------------------------
      SUBROUTINE ReadPFidPars
C-----------------------------------------------------------
c     call once before the first call of the fiducial cuts
c     to read the parameters
      include 'PFid_4Gev_2250A.inc'
      open(unit=99,file="PFid_4Gev_2250A.dat",status="old")


      read (99,*) Pfidft1l
      read (99,*) Pfidft1r
      read (99,*) Pfidft2l
      read (99,*) Pfidft2r


      read (99,*) Pfidbt1l
      read (99,*) Pfidbt1r
      read (99,*) Pfidbt2l
      read (99,*) Pfidbt2r


      read (99,*) Pfidbl
      read (99,*) Pfidbr
```

```
         close(99)

         return
         end

C-------------------------------------------------------------
         SUBROUTINE PFiducialCut_4GeV_2250A(px, py, pz, status)
C-------------------------------------------------------------
c        input real px py pz components of proton momentum
c        output int status 1 means pass, 0 means failure
         include 'PFid_4Gev_2250A.inc'

         real px,py,pz
         logical*4 status
         logical*4 forward
         logical*4 s1s4,s5,s6
         real p, theta, phi, tmptheta
         integer sector,ipar,jpar

         real parfidl(3)
         real parfidr(3)
         real parfidbl(2)
         real parfidbr(2)
         real cphil,cphir,phi45l,phi45r
         real phi60l,phi60r
         real thetamin,thetamax
         real thetab,pb
         real dl,el,dr,er


         phi=atan2(py,px)*180./pi
         if (phi.lt.-30) phi=phi+360
         sector=int((phi+30.)/60.)+1
         if (sector.lt.1) sector=1
```

```fortran
      if (sector.gt.6) sector=6
      phi=phi-(sector-1)*60.
      theta=atan2(sqrt(px*px+py*py),pz)*180./pi
      p=sqrt(px*px+py*py+pz*pz)
      WRITE(6,*) p,theta,sector,phi
      do ipar=1,3
         parfidl(ipar)=0.0
         parfidr(ipar)=0.0
      enddo
      do jpar=1,2
         parfidbl(jpar)=0.0
         parfidbr(jpar)=0.0
      enddo
      forward=.false.
      thateb=45.
      pb=0.575
      thetamax=140
      if (p.lt.0.2) p=0.2
      if (p.gt.4.4) p=4.4

      if(p.lt.0.6)thetamax=Pfidbl(5,sector)+ Pfidbl(6,sector)*p
      else thetamax=Pfidbl(5,sector)+ Pfidbl(6,sector)*pb
      forward=.true.

      if(p.lt.0.6) then
         do ipar=1,3
            jpar=2*ipar-1
            parfidl(ipar)=Pfidft1l(jpar,sector)+
     $         Pfidft1l(jpar+1,sector)/p;
            parfidr(ipar)=Pfidft1r(jpar,sector)+
     $         Pfidft1r(jpar+1,sector)/p;
         enddo
      else
         do ipar=1,3
```

```fortran
               jpar=2*ipar-1
               parfidl(ipar)=Pfidft2l(jpar,sector)+
     $             Pfidft2l(jpar+1,sector)/p;
               parfidr(ipar)=Pfidft2r(jpar,sector)+
     $             Pfidft2r(jpar+1,sector)/p;
           enddo
       endif


       phi45l=parfidl(1)*(parfidl(3)-45.)/(45.-parfidl(3)+
     $      (parfidl(2)/parfidl(1)))
       phi45r=-parfidr(1)*(parfidr(3)-45.)/(45.-parfidr(3)+
     $      (parfidr(2)/parfidr(1)))


       if(theta.gt.thetab) then
           if(theta.gt.140.) theta =140.
           if(p.gt.1)p=1.


           forward=.false.


       if(p.lt.0.6) then
           do ipar=1,3
               jpar=2*ipar-1
               parfidl(ipar)=Pfidbt1l(jpar,sector)+
     $             Pfidbt1l(jpar+1,sector)/p;
               parfidr(ipar)=Pfidbt1r(jpar,sector)+
     $             Pfidbt1r(jpar+1,sector)/p;
           enddo


           do ipar=1,2
               jpar=2*ipar-1
               parfidbl(ipar)=Pfidbl(jpar,sector)+
     $             Pfidbl(jpar+1,sector)/p;
               parfidbr(ipar)=Pfidbr(jpar,sector)+
     $             Pfidbr(jpar+1,sector)/p;
```

```
            enddo
        else
            do ipar=1,3
                jpar=2*ipar-1
                parfidl(ipar)=Pfidbt2l(jpar,sector)+
$                   Pfidbt2l(jpar+1,sector)/p;
                parfidr(ipar)=Pfidbt2r(jpar,sector)+
$                   Pfidbt2r(jpar+1,sector)/p;
            enddo

            do ipar=1,2
                jpar=2*ipar-1
                parfidbl(ipar)=Pfidbl(jpar,sector)+
$                   Pfidbl(jpar+1,sector)/pb;
                parfidbr(ipar)=Pfidbr(jpar,sector)+
$                   Pfidbr(jpar+1,sector)/pb;
            enddo
        endif
    endif

    if (forward) then
        if(p.lt.0.6) then
            thetamin=14
        else thetamin=11;
        endif
cphil=parfidl(1)*(parfidl(3)-theta)/(theta-parfidl(3)+
$           (parfidl(2)/parfidl(1)));
cphir=-parfidr(1)*(parfidr(3)-theta)/(theta-parfidr(3)+
$           (parfidr(2)/parfidr(1)));

    else
        phi60l=parfidl(1)+ parfidl(2)*60.+ parfidl(3)*3600.
        phi60r=-(parfidr(1)+ parfidr(2)*60.+ parfidr(3)*3600.)
        if(theta.lt.60) then
```

```
      cphil=parfidl(1)+ parfidl(2)*theta+parfidl(3)*theta*theta
      cphir=-(parfidr(1)+ parfidr(2)*theta+parfidr(3)*theta*theta)
        endif
        dl=parfidbl(1)
        el=parfidbl(2)
        dr=parfidbr(1)
        er=parfidbr(2)
        if(theta.gt.45.and.theta.lt.60) then
            if(cphil.gt.phi45l) cphil=phi45l
            if(cphir.lt.phi45r) cphir=phi45r
        endif
        if(theta.ge.60.and.theta.le.dl) cphil=phi60l
        if(theta.gt.dl.and.theta.le.thetamax) cphil=
$           (140-theta)*(phi60l-el)/(140-dl) +el
        if(theta.gt.thetamax) cphil=0

        if(theta.ge.60.and.theta.le.dr) cphir=phi60r
        if(theta.gt.dr.and.theta.le.thetamax) cphir=
$           (140-theta)*(phi60r-er)/(140-dr) +er
        if(theta.gt.thetamax) cphir=0

    endif

    if(phi.lt.0) status=(phi.gt.cphil)
    if(phi.ge.0) status=(phi.lt.cphir)

    if(theta.lt.thetamin) status=.false.
    if(forward.and.p<0.6.and.theta.lt.20.6-11.4*p)status=.false.
    s1s4=(theta.lt.11.7.and.(sector.eq.1.or.sector.eq.4))
    s5=(theta.lt.12.2.and.sector.eq.5)
    s6=(theta.lt.11.4.and.sector.eq.6)
    if(p.ge.0.6.and.p.lt.1.5.and.(s1s4.or.s5.or.s6))
    status=.false.
```

```
        return
        end
C----------------------------------------------------------------
```

APPENDIX C

4.4 GEV PROTON FIDUCIAL CUT

C.1 INTRODUCTION

The CEBAF Large Acceptance Spectrometer (CLAS) is designed to measure multi-particle final states [63]. It is based on six iron free superconducting coils that generate a toroidal magnetic field in between. Each of the six gaps between the coils is equipped with a set of drift chambers (DC) [64] and scintillator counters (SC) [67] from 10° to 145° in polar angle, Cerenkov counters (CC) [66] and electromagnetic calorimeters (EC) [68] from 10° to 45°. In electron scattering experiments with CLAS, the triggered event is accepted for physics analysis if the scattered electron and the other particles in event are identified. Due to the complicated readout structures (EC), (CC), detection and reconstruction efficiencies are not well understood in the regions close to the magnet, or close to any dead channels (DC,SC,CC,EC). In order to minimize systematic uncertainties in the physics analysis it is important to accept events in the fiducial region of the detector, where efficiencies are understood. The fiducial cut for electrons (for CLAS/E2) is discussed in [80]. We use the same data and the same method to derive fiducial cuts for positive hadrons (protons, pions), so we are going to follow the steps described in [80]. The Fiducial Cut Procedure is defined by three steps: 1. Applying cuts 2. Determining the flat acceptance regions in ϕ space for small bins of θ and momentum 3. Fitting the boundaries of the flat acceptance region as a function of θ and ϕ.

Web-based documentation that contains description of the procedure, plots, including a complete set of histograms and routines is given in [83].

C.2 SELECTING GOOD EVENTS

We applied cuts that helps to make better fit:
1. Selecting events with an electron and a good positive hadron (good DC, SC status).
2. Cut on χ^2 from DCPB bank. We cut out events with bad tracks (with $\chi^2 > 13.2$). That allows us to keep 99% of the integral of DC χ^2 distribution.
3. Cut on Energy transfer. We apply that cut to eliminate protons from quasi-free

TABLE XXIX. Momentum bins

Mom. Range MeV/c	Hadrons	Bin Size MeV/c	Number of Bins
0 − 600	p	50	12
600 − 1000	$p\,\pi$	50	8
1000 − 2000	$p\,\pi$	100	10
2000 − 4400	$p\,\pi$	200	12

reactions. These protons are not uniformly distributed in ϕ and could not be fit by the trapezoid method. The quasielastic peak results from the electron interacting with a single nucleon of mass m_N and knocking it out of the nucleus. The energy transfer for those events defined by:

$$\omega = \frac{Q^2}{2m_N} + \frac{\vec{q} \cdot \vec{p}}{m_N} \tag{60}$$

We cut out energy transfer in the range:

$$\frac{Q^2 - 2 \cdot q \cdot p_{init}}{2m_N} < \omega < \frac{Q^2 + 2 \cdot q \cdot p_{init}}{2m_N}; \tag{61}$$

where $p_{init} = 200$ MeV/c is the initial momentum of the struck nucleon. The 6 sectors (θ,ϕ) distribution plots with the quasielastic peak are shown in Figure 111.

C.3 FINDING THE FLAT ACCEPTANCE REGION

We divide the momentum range of the protons and pions in small bins and plot for each momentum bin a two-dimensional histogram of counts versus angles (θ and ϕ) for each sector. We use two momentum ranges $0.2 < p < 0.6$ GeV/c (protons only) and $0.6 < p < 4.4$ GeV/c (protons and pions). Table XXIX shows the momentum binning for our plots. Figure 112 shows some typical (θ,ϕ) plots for 6 sectors using E2 run ^{3}He data at 4.4 GeV.

The histograms in Figure 112 exhibit a well contoured semicircular region, surrounded by a fuzzy region. We want to select this solid area of the histogram, which is the flat acceptance region and discard the blurred area surrounding it. For this, we will fit its contour with a function $\Phi(\theta,p)$ for every sector. To define the flat area we slice the two-dimensional plots in theta bins of 2° at $11° < \theta < 45°$ (Forward region)

and $2 - 10°$ at $45° < \theta < 140°$ (Backward region). We fit each sliced histogram with a trapezoid + background function, defined by:

$$y = \begin{cases} p0, & \text{if } x < p2 - p1; \\ (p6 - p0) \cdot (x - p2 + p1)/p1 + p0, & \text{if } p2 - p1 < x < p2; \\ p6, & \text{if } p2 < x < p3; \\ (p6 - p5) \cdot (p3 + p4 - x)/p4 + p5, & \text{if } p3 < x < p3 + p4; \\ p5, & \text{if } x < p3 + p4. \end{cases} \qquad (62)$$

Each parameter is described in Figure 113. Some typical trapezoids (fitted θ slices) are shown in Figure 114. The plateau of the trapezoid (parameters $p2, p3$) defines our "flat" acceptance region. The automatic fitting procedure gives us reliable results in over 90% of the fits. Some of the "bad" θ slices are shown in Figure 115. Bad fits are "fixed" manually by increasing the error bar of the resulting parameters. The coordinates of the edges of the trapezoid plateau for each momentum bin and sector are written to a file and fitted with a function $\phi = \Phi(\theta, p)$ for every momentum bin and sector. The procedure is completely automatic. We use the CERN two-dimensional Minuit fit routine for fitting non-equidistant data points. We chose two different functions to fit the Forward and Backward regions and also we fit separately 2 momentum regions using the range of momenta $0.2 < p < 0.6$ GeV/c and $0.6 < p < 4.4$ GeV/C. For the Forward region we used a hyperbolic function for the theta dependence and a $1/p$ function for the momentum dependence:

For $\phi < 0$: $\Phi(\theta, p) = a \cdot (c - \theta)/(\theta - c + (b/a))$

For $\phi > 0$: $\Phi(\theta, p) = a' \cdot (\theta - c')/(\theta - c' + (b'/a'))$

where,

$$a = a_0 + a_1/p$$

$$b = b_0 + b_1/p$$

$$c = c_0 + c_1/p$$

and similarly for a', b' and c'. We divided the Backward region into two regions BackwardA ($45° < \theta < 60°$) and BackwardB ($60° < \theta < 140°$). For the BackwardA region we used a quadratic function and for the BackwardB region we used a constant ($60° < \theta < \theta_{flat}$) +straight line ($\theta_{flat} < \theta < \theta_{max}$) (see Fig. 116) with a $1/p$ function for the momentum dependence:

For $45° < \theta < 60°$:

$\phi < 0$: $\Phi(\theta, p) = (d + e \cdot \theta + f \cdot \theta^2)$

$$\phi > 0 : \quad \Phi(\theta, p) = -(d' + e' \cdot \theta + f' \cdot \theta^2)$$

where,

$$d = d_0 + d_1/p$$

$$e = e_0 + e_1/p$$

$$f = f_0 + f_1/p$$

and similarly for d', e' and f'.

For $60° < \theta < \theta_{flat}$:

$$\Phi(\theta, p) = \Phi(60°, p)$$

(no free parameters)

For $\theta_{flat} < \theta < \theta_{max}$:

$$\Phi(\theta, p) = (140° - \theta) \cdot (\Phi(60°, p) - \phi_{edge})/(140° - \theta_{flat}) + \theta_{flat}$$

where, θ_{flat} and ϕ_{edge} are determined from fitting and θ_{max} is determined visually from (θ, ϕ) distributions and parameterized using a linear function in p.

$$\theta_{flat} = g_0 + g_1/p;$$

$$\phi_{edge} = h_0 + h_1/p;$$

$$\theta_{max} = i_0 + i_1 \cdot p$$

BackwardB region parameters $\theta_{flat}, \phi_{edge}$ and θ_{max} are shown in Figure 116. These fits were necessary due to the lack of the data in the BackwardB region. For $p > 0.6$ GeV/c the $\theta_{flat}, \phi_{edge}$ and θ_{max} at $p = 0.575$ GeV/c were used (last momentum bin of $p < 0.6$ GeV/c region). To avoid discontinuity at $\theta = 45°$ we fit the BackwardA region θ range starting from $\theta = 30°$ instead of $\theta = 45°$. Also, we replace the $\Phi(40°, p)$ edge points with values defined from the Forward region fiducial function with error=0.05. That forced the BackwardA region curves to start from the end point of the Forward region curves. The list of fit parameters is given in Table XXX. Some typical plots of 2D fits of the data points with corresponding $\Phi(\theta, p)$ function for Forward and Backward regions are shown in Figures 117 and 118, respectively. The fitting procedure gives us the final set of parameters, that is included to the **PFiducialCut** subroutine of **E2AnaTool** package. Figure 119 shows the overall result of the fiducial cut as made by using the derived **PFiducialCut** function for 4.4 GeV data.

TABLE XXX. List of the fit parameters

P	ϕ	Forward $\theta < 45°$	BackwardA $45° < \theta < 60°$	BackwardB $60° < \theta < 140°$
$p < 0.6$	$\phi < 0$	$a_0, a_1, b_0, b_1, c_0, c_1$	$d_0, d_1, e_0, e_1, f_0, e_1$	$g_0, g_1, h_0, h_1, i_0, i_1$
	$\phi > 0$	$a'_0, a'_1, b'_0, b'_1, c'_0, c'_1$	$d'_0, d'_1, e'_0, e'_1, f'_0, e'_1$	$g'_0, g'_1, h'_0, h'_1, i'_0, i'_1$
$p > 0.6$	$\phi < 0$	$a_0, a_1, b_0, b_1, c_0, c_1$	$d_0, d_1, e_0, e_1, f_0, e_1$	
	$\phi > 0$	$a'_0, a'_1, b'_0, b'_1, c'_0, c'_1$	$d'_0, d'_1, e'_0, e'_1, f'_0, f'_1$	

C.4 SUMMARY

We determined the fiducial region for positive hadrons by the following techniques: We eliminated events with bad tracks and events that generate quasielastic peaks. We split the angle-momentum range into small bins and found the contour of the regions of CLAS where acceptance is flat. We get from this a set of curves. What is inside the contour passes as OK, what is out is discarded. We fit the parameters that define flat acceptance and insert them to **PFiducialCut**$(\vec{p})$ subroutine together with the functions that define the fiducial cut. The proton fiducial cut parameters and functions for 4.4 GeV data are given in Appendix B.0.4.
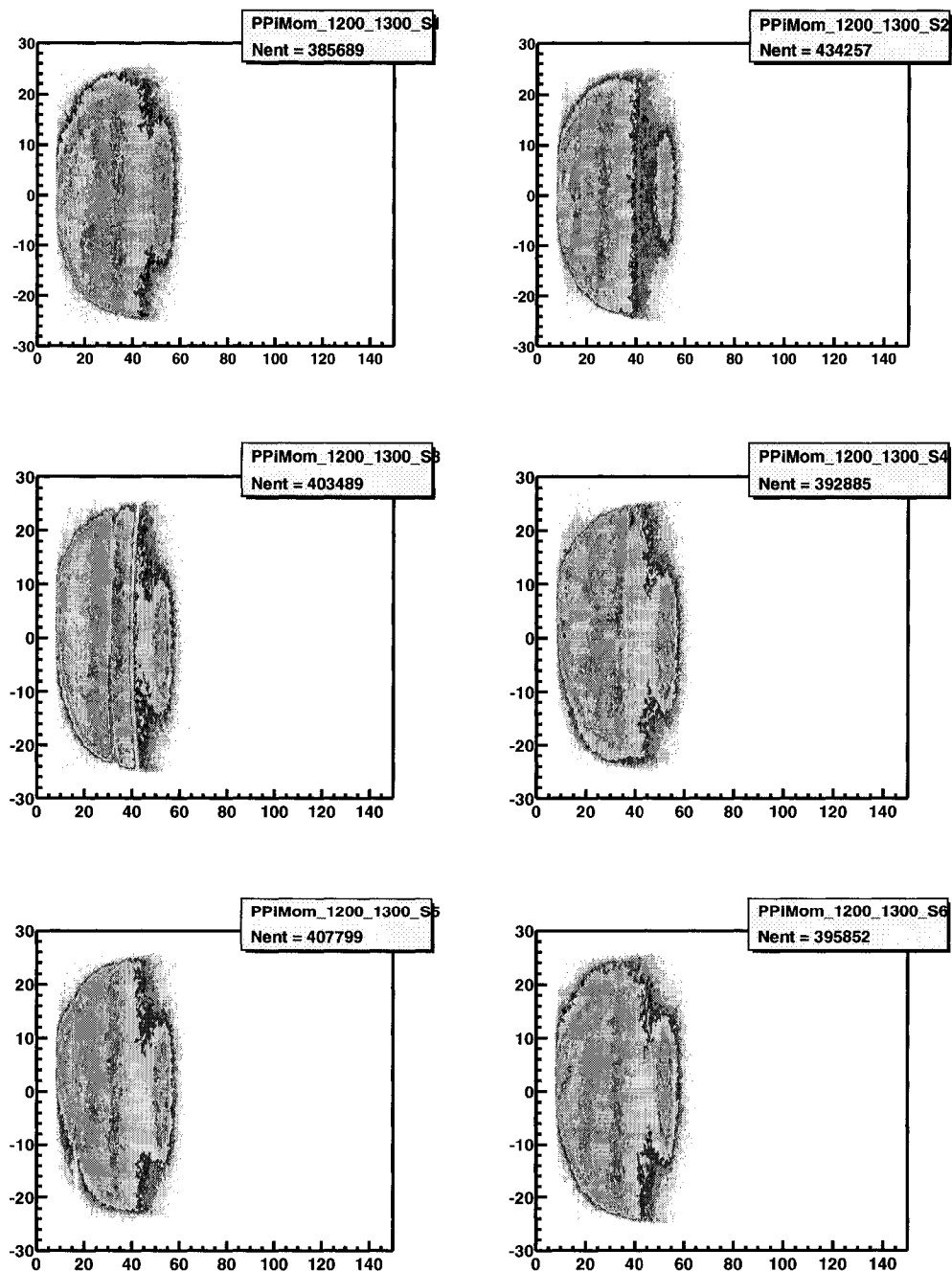
FIG. 111. Plots of (θ,ϕ) distribution with quasielastic peak. The peak is at $\theta = 50°$ at proton momentum (1200< p <1300 MeV/c). The 6 plots are for the 6 sectors. Vertical axis is ϕ, horizontal axis is θ.
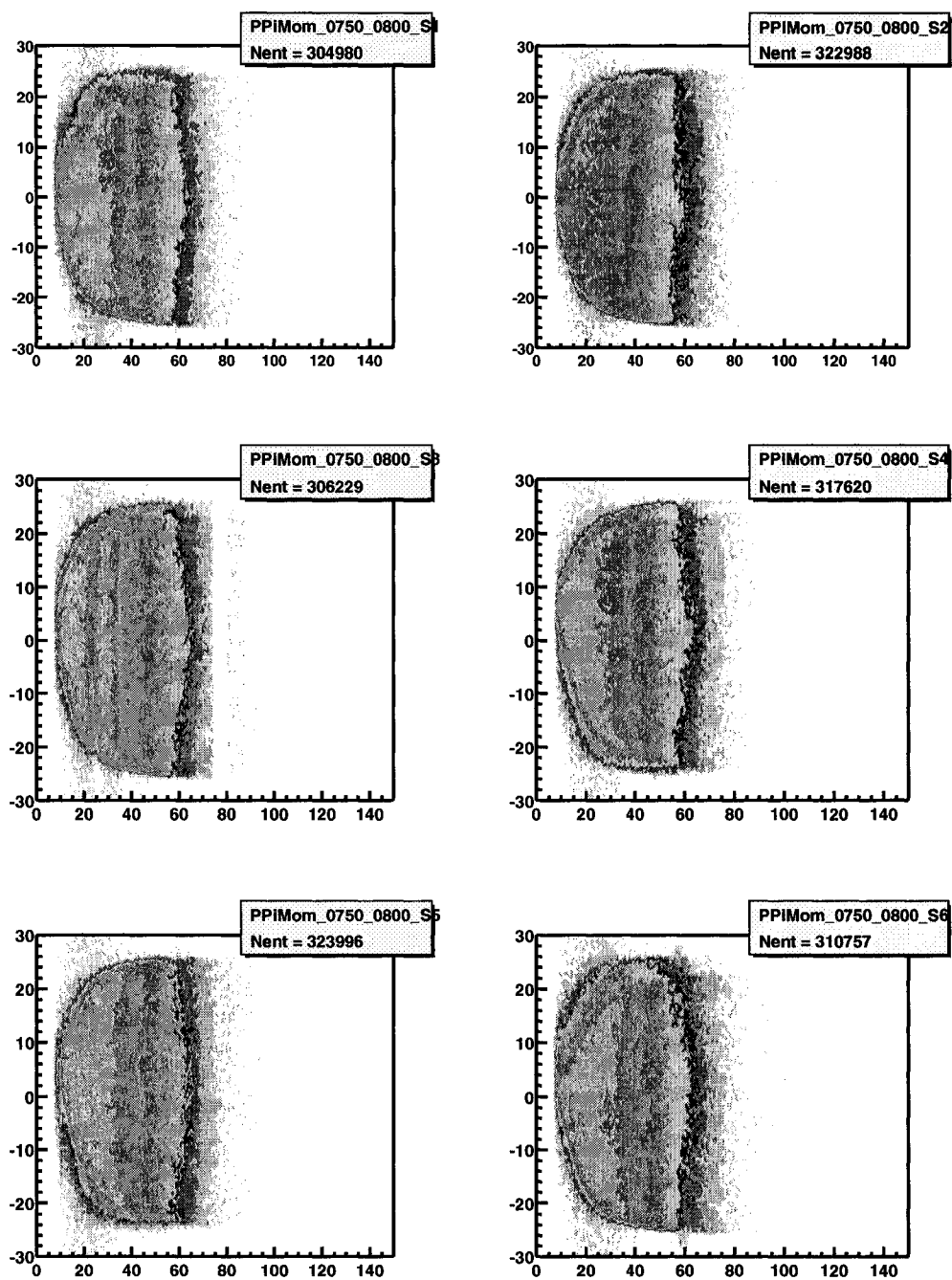
FIG. 112. Some typical plots of (θ,ϕ) distribution at $750< p <800$ MeV/c for all 6 sectors. Vertical axis is defined by ϕ, horizontal axis is defined by θ.
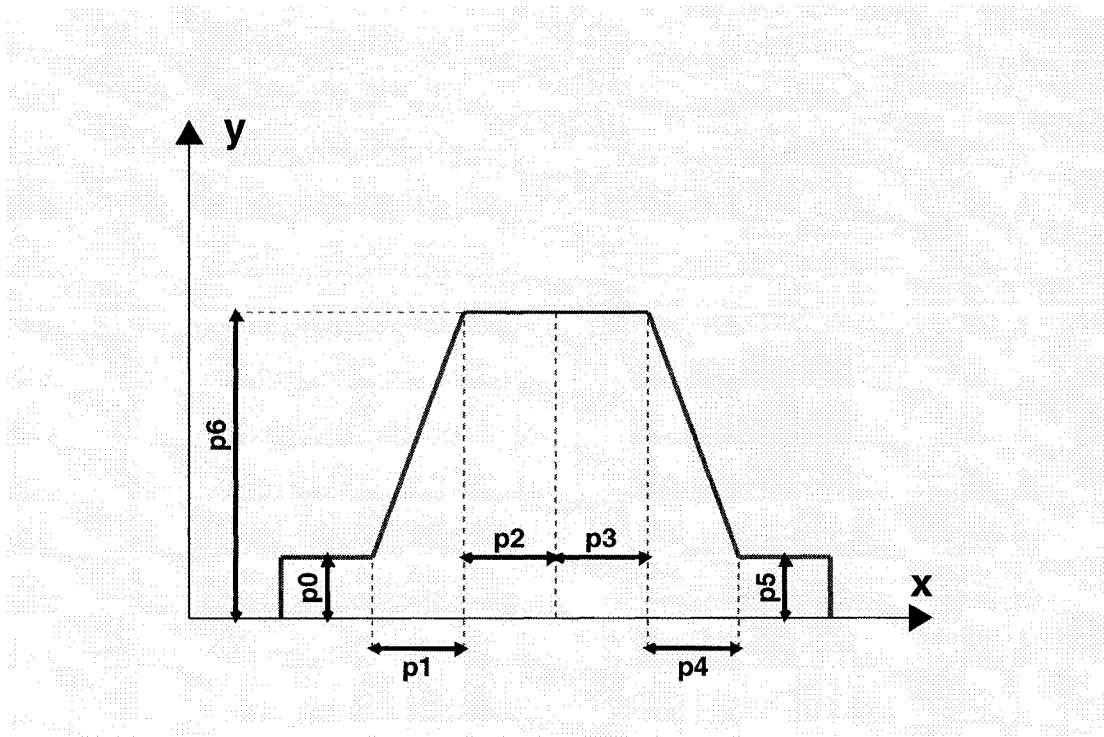
FIG. 113. Parameters used for fitting trapezoid+background function.
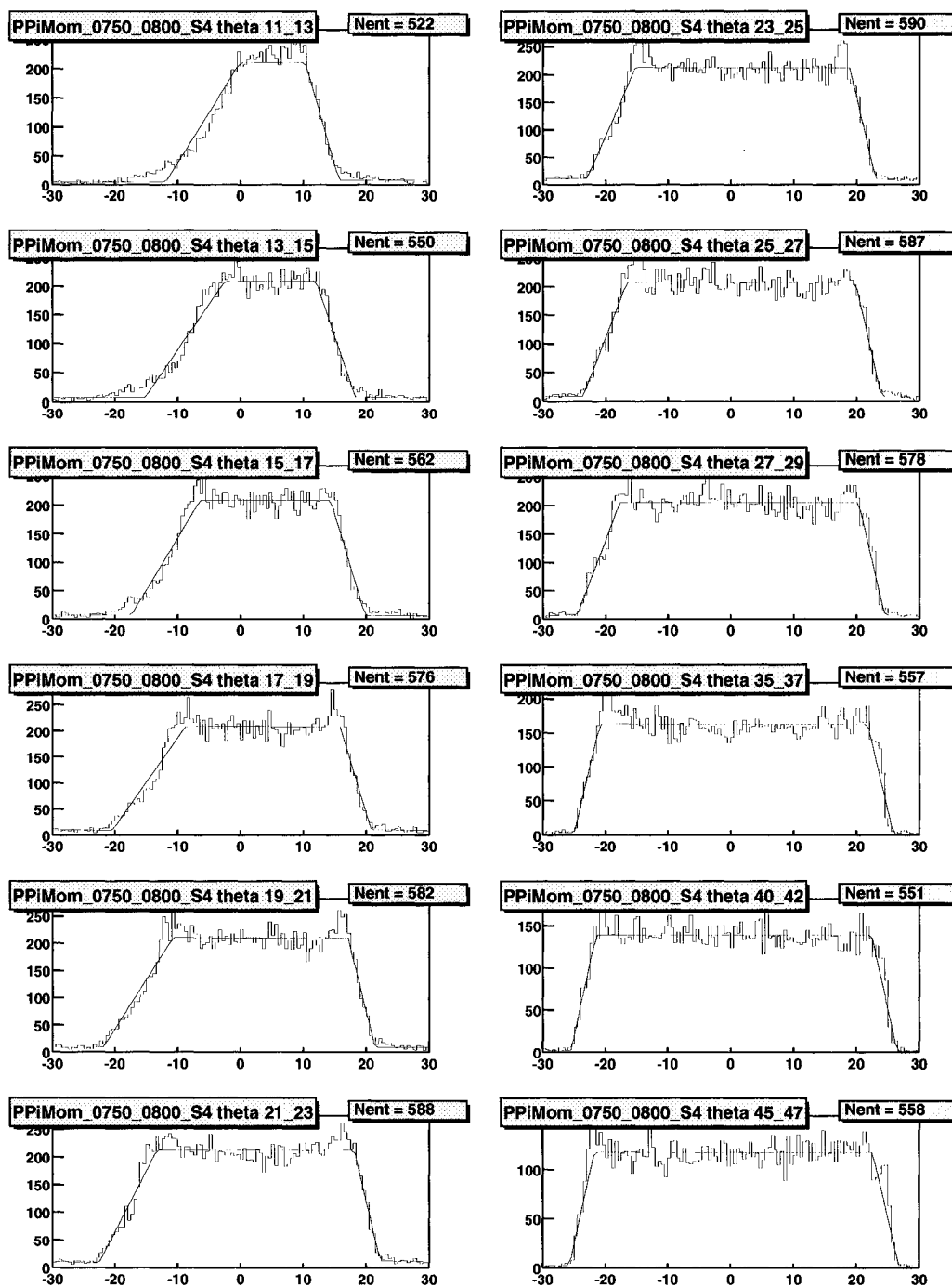
FIG. 114. Trapezoid+background function fitted on histogram counts vs ϕ angle. The top defines our "flat" region. These are for Sector 4, $750 < p < 800$ MeV/c.
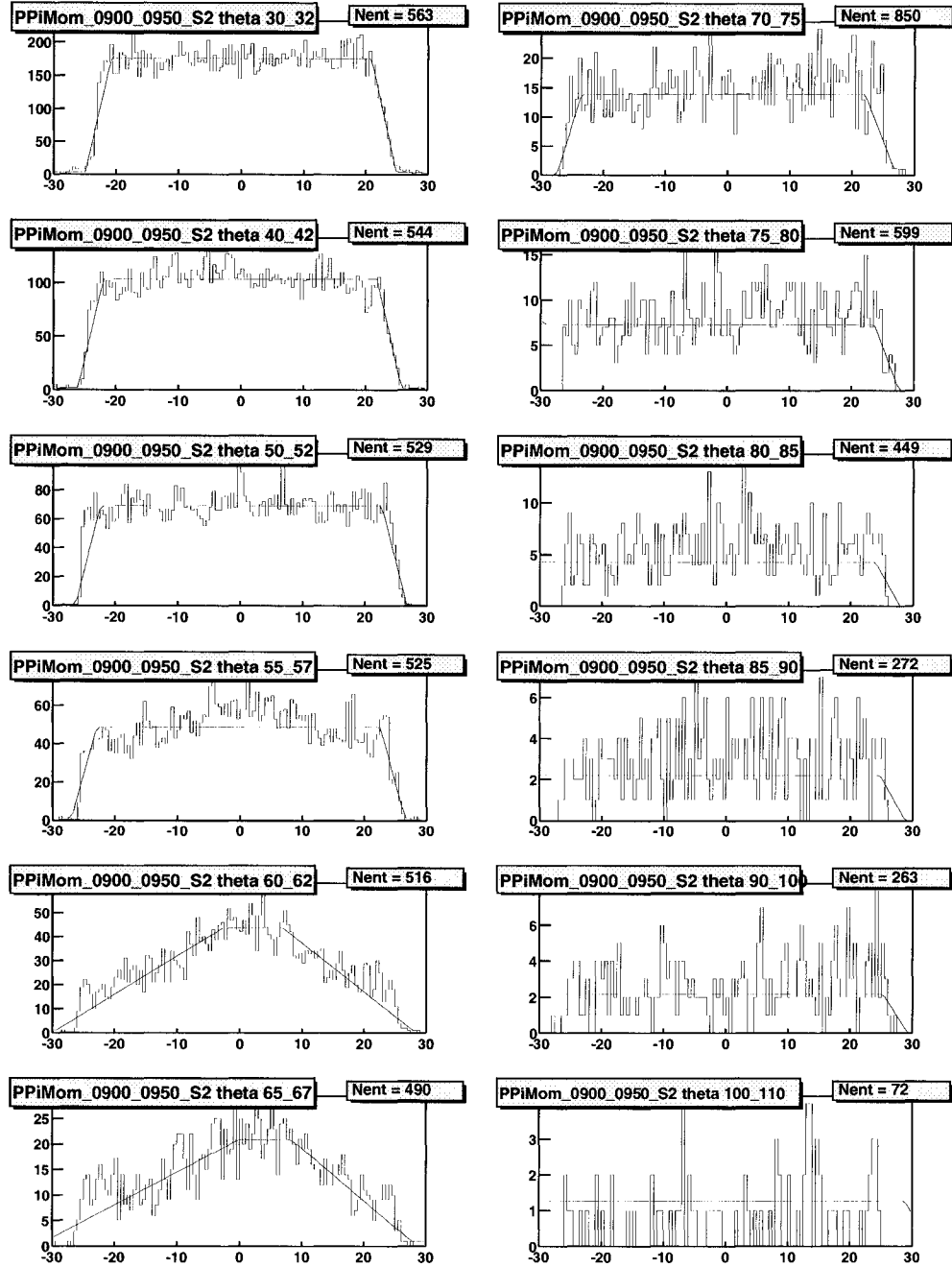
FIG. 115. Typical bad θ slice. These are for Sector 2, 900< p <950 MeV/c. Vertical axis is counts, horizontal axis is ϕ.
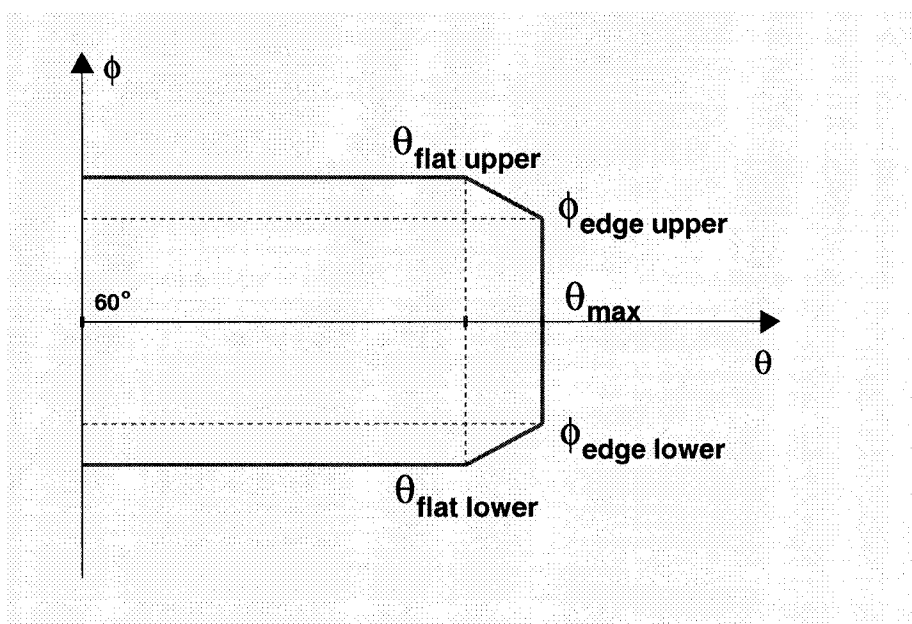
FIG. 116. Backward region parameters $\theta_{flat}, \phi_{edge}$ and θ_{max}.
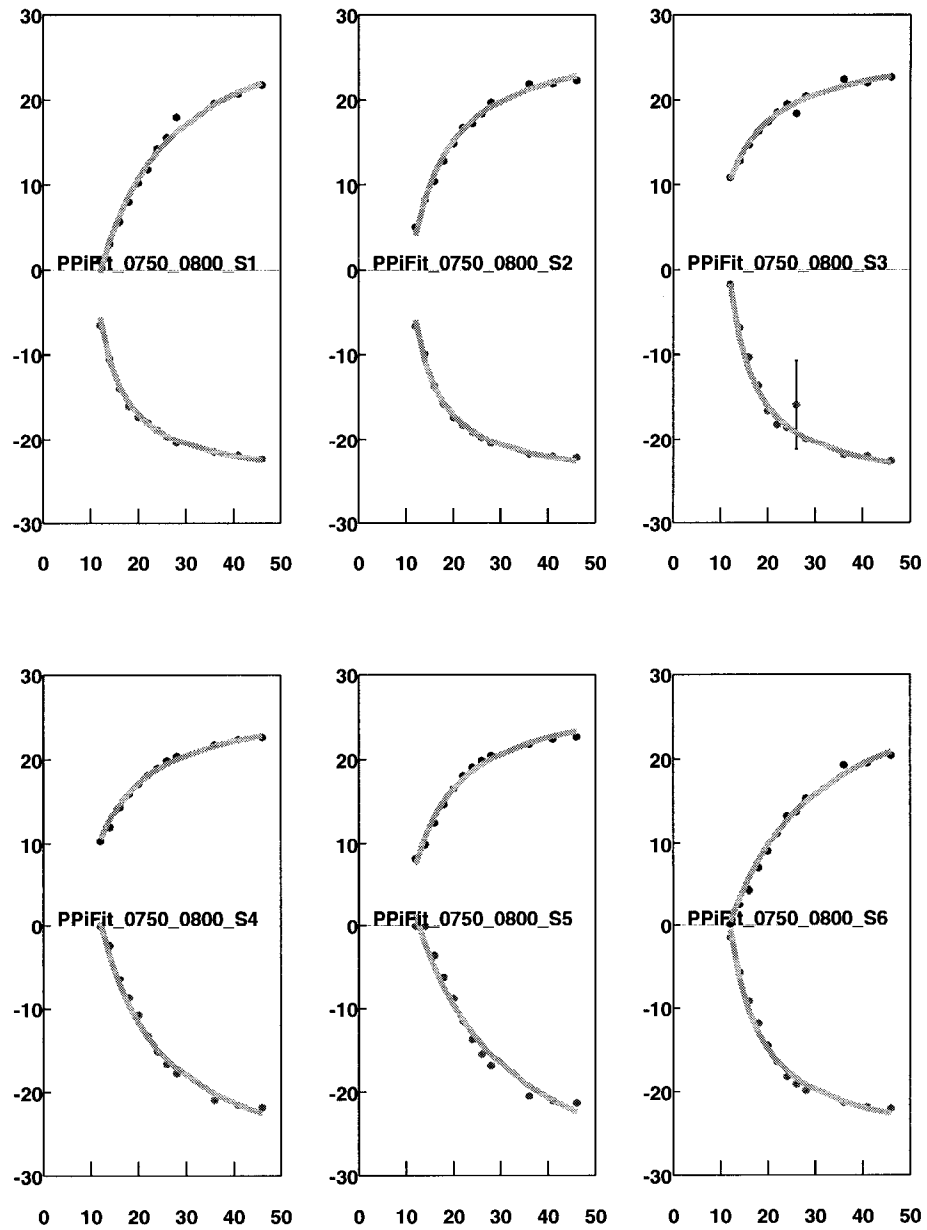
FIG. 117. Forward region $\Phi(\theta, p)$ fit at 750< p <800 MeV/c. Six graphs are for six sectors. Vertical axis is ϕ, horizontal axis is θ.
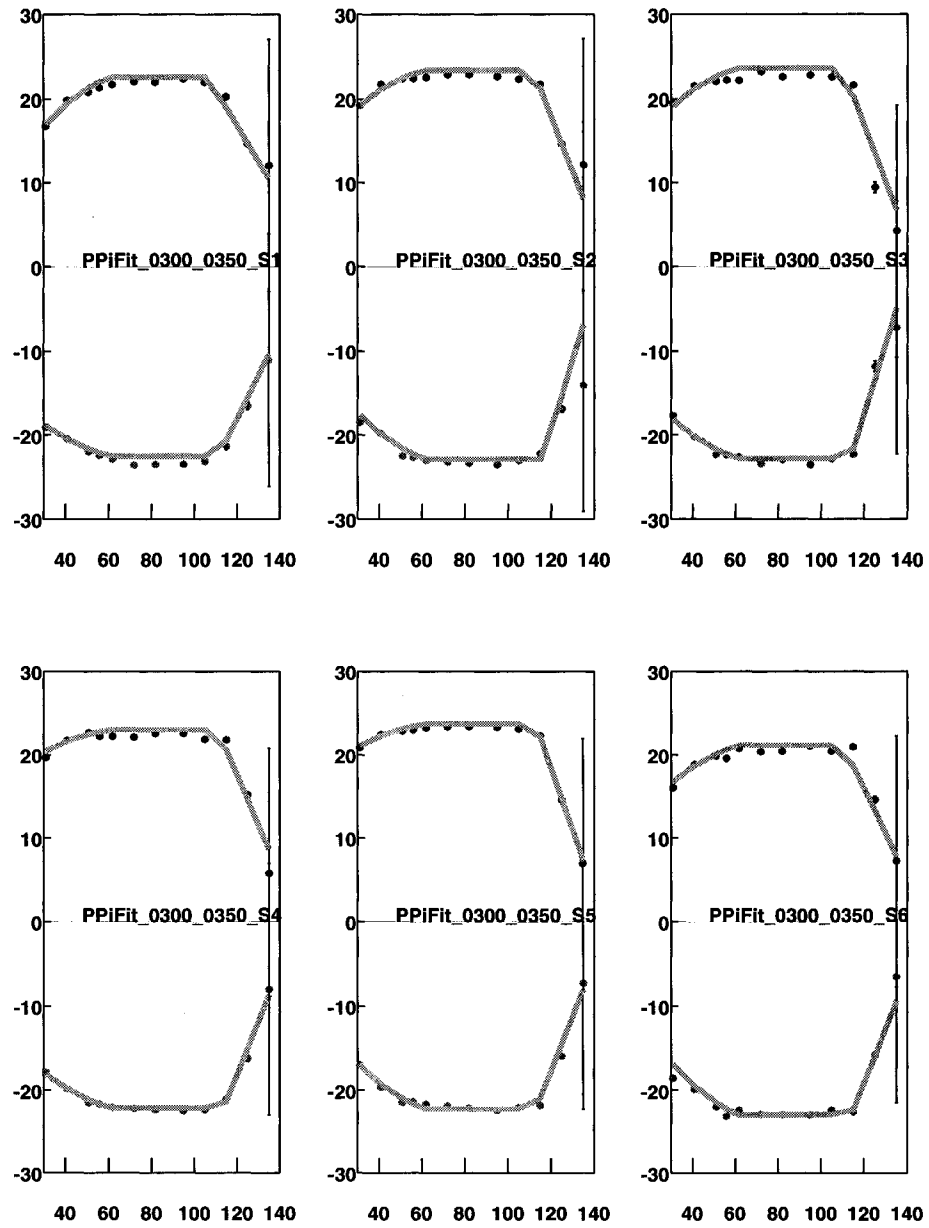
FIG. 118. Backward region $\Phi(\theta, p)$ fit at $300< p <350$ MeV/c. 6 graphs are for 6 sectors. Vertical axis is ϕ, horizontal axis is θ.

FIG. 119. Plots illustrating the result of the cut at 750< p <800 MeV/c for all 6 sectors. Vertical axis is ϕ, horizontal axis is θ.

APPENDIX D

(E,E′P) SYSTEMATIC UNCERTAINTY EVALUATION

We want to estimate systematic uncertainties due to the angular and momentum determination of electrons and protons with CLAS. The resolution of the charged particles in CLAS are $\Delta\theta \approx 1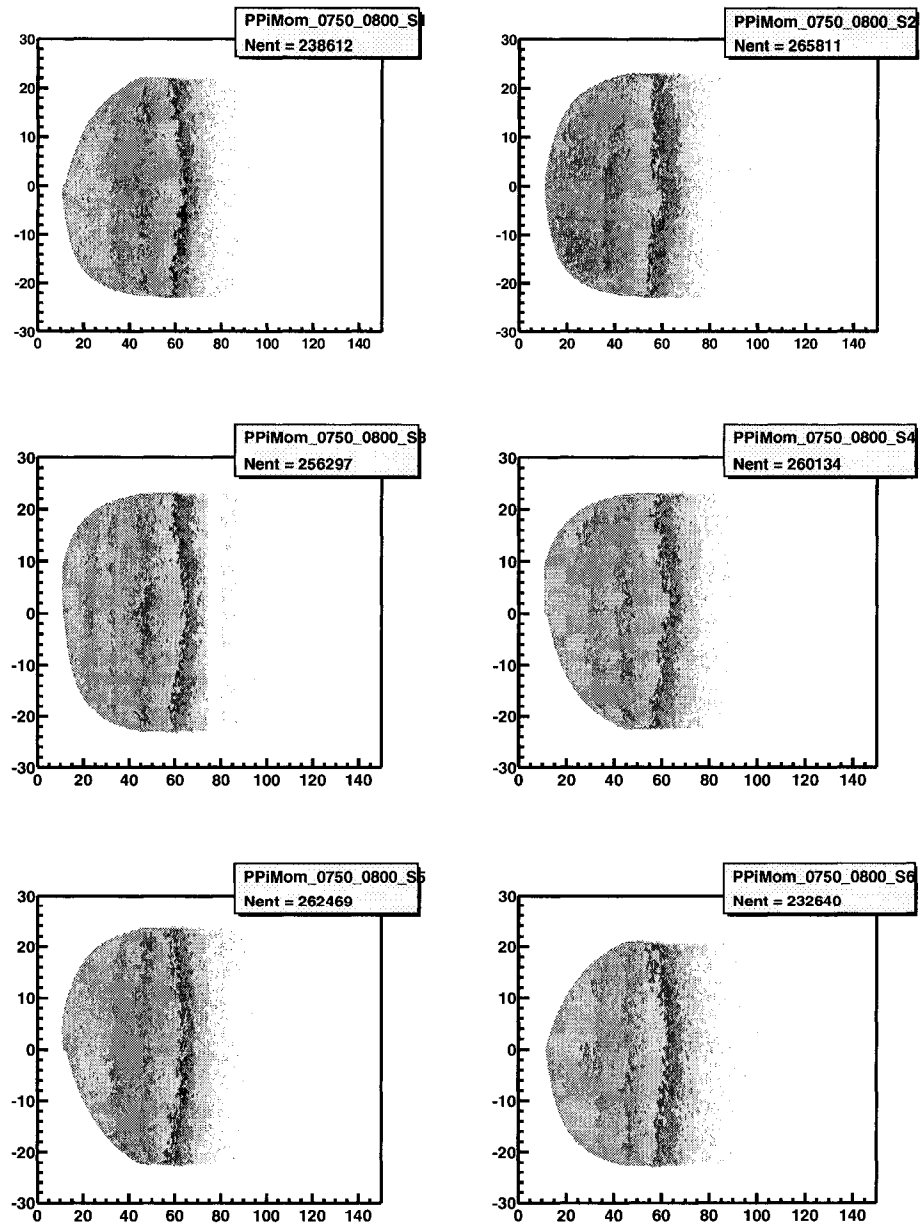$ mrad, $\Delta p/p \approx 0.5\%$ for $\theta \lesssim 30°$ and $\Delta p/p \approx (1\text{–}2)\%$ for $\theta \gtrsim 30°$ [63].

The kinematic quantities that correspond to Hall A measurements are given by: $|\vec{q}| = 1.5$ GeV/c, $\omega = 0.837$ GeV, $E_0 = 4.461$ GeV, $E'_e = E_0 - \omega = 3.624$ GeV, and $\theta_e = 17.8°$, where q and ω are momentum and energy transfer, E_0 and E'_e are the energy of incoming and outgoing electrons, and θ_e is the electron scattering angle.

From Figure 51 one can see that the cross section for our data increases by a factor of 100 in the interval $\Delta P_{miss} = 140$ MeV/c. This interval corresponds to the $\Delta\theta_{pq} = \Delta P_{miss}/q = 93$ mrad, where θ_{pq} is the outgoing proton angle with respect to $\vec{q}$. If CLAS can determine the electron and proton angles as $\Delta\theta_e = 1$ mrad and $\Delta\theta_p = 1$ mrad, then we can determine the cross section as $100^{\frac{1}{93}} \approx 1.05$ which gives $\frac{d[\sigma]}{d\theta_{pq}} \approx 5\%$ for both electrons and protons.

The momentum determination for electrons which is $\Delta p_e/p_e \approx 0.5\%$ is already included by the electron momentum correction procedure. For protons we use $\Delta p_p/p_p = 2$ % and also we estimate that we know the position of the centroid of the peak in our measurement 10 times better than the conservative estimation of $\Delta p_{miss}{=}3$ MeV/c at $p_p{=}1.5$ GeV/c. That gives $\frac{d[\sigma]}{dp_{miss}} = 10\%$. The systematic uncertainty for (e,e′p) measurement in Hall B is determined as $\sqrt{5^2 + 5^2 + 10^2} \approx 12\%$. We determined the contribution to systematic uncertainty from σ_{Mott}, R_L and R_T change for $\Delta\theta_e = 1$ mr to be 3%. We also include the 7% rms deviation contribution to the systematic uncertainty from the Hall A to Hall B data comparison (see Figure 51 b)), as well as the 15% contribution from three body strength subtraction (see Figure 50) which determines 3–5% uncertainty in determination of the remaining two body strength. These contributions to our systematic uncertainties are shown in Table XXXI.

TABLE XXXI. ^{3}He(e,e'p) systematic uncertainties for different values of missing momentum.

p_{miss} (GeV/c)	0.1	0.15	0.2
Kinematical uncertainties			
$\Delta\theta_e$	5	5	5
$\Delta\theta_p$	5	5	5
Δp_p	10	10	10
σ_{Mott}, R_L and R_T change (%)	3	3	3
2B fraction (%)	2.7	3.6	5.3
rms scatter of the ratio(%)	7	7	7
Total (%)	14.6	14.8	15.3

APPENDIX E

EVENT GENERATOR SUBROUTINE

```
Int_t TE2Func::GenEvent(Int_t ireg, Double_t E_beam,
TLorentzVector &V4ElScat, TLorentzVector &V4P1,
TLorentzVector &V4P2, TLorentzVector &V4P3,
TLorentzVector &V4P1qz, TLorentzVector &V4P2qz,
TLorentzVector &V4P3qz){

    // constants
    Double_t M1=0;Double_t M2=0;Double_t M3=0;
    Double_t Mp =0.9383;
    Double_t Mn =0.9396;
    Double_t  MTarget= 2.8092;
    if(ireg==22){M1=Mp;M2=Mp,M3=Mn;}
    if(ireg==21){M1=Mp;M2=Mn,M3=Mp;}
    if(ireg==12){M1=Mn;M2=Mp,M3=Mp;}


    // variables to be thrown randomly in a range specified

    Double_t E_e_out; //total energy of an outgoing electron
    Double_t phi_el,phi_elr,ctheta_el,theta_elr;
    Double_t Phi_1;  //azimuthal angles of outgoing nucleon 1
    Double_t Phi_2; //azimuthal angles of outgoing nucleon 2
    Double_t C_Theta_1; //polar angles of outgoing nucleon1
    Double_t C_Theta_2; //polar angles of outgoing nucleon2
    Double_t P1; // momentum of the first nucleon

    // calculated variables

    Double_t P2=0.; //momentum of a second nucleon
    Double_t P3x,P3y,P3z; //projection of the momentum of a neutron

    // intermediate variables
```

```
TVector3 V3q(0.,0.,0.);
TVector3 V3Z(0,0,1);
TVector3 V3qCrossZ;


Double_t A,B,C,D,x,y,z,xx,yy,zz,Det,Pmax1,Pmax2,Pm,Omega,Ep1,
   E,Theta_1,Theta_2,b,c;
Double_t random1,random2,random3,random4,random5,random6,
   random7,random8,ThetaQZ,P21,P22;
Double_t P1min=0.,P1max=0.;



//#################################################
//
// Randomly generating 8 variables in selected limits
//
//#################################################



// random numbers for later use
random1 = Rand->Rndm(1);
random2 = Rand->Rndm(1);
random3 = Rand->Rndm(1);
random6 = Rand->Rndm(1);


// generating variables
Double_t ElecThreshold=0;
if(E_beam>2&&E_beam<3) ElecThreshold=0.35;
if(E_beam>4&&E_beam<5) ElecThreshold=0.8;


E_e_out = ElecThreshold+(E_beam-ElecThreshold)*random1;
phi_el=-30. + 360. *random2;
//azimuthal angle of an outgoing electron
phi_elr = phi_el* TMath::Pi()/180.;
```

```
// [cos45,cos15] - cosine of polar angle of the outgoing electron
ctheta_el = cos(45./180.*TMath::Pi())+
  (cos(15./180.*TMath::Pi())-cos(45./180.*TMath::Pi()))*random3;


theta_elr = acos(ctheta_el);
C_Theta_1 = -1.+2.*random6;


    // preliminary calculations


Omega = E_beam - E_e_out; // energy transfer MeV
// momentum transfer
V3q.SetXYZ(-E_e_out*cos(phi_elr)*sin(acos(ctheta_el)),
-E_e_out*sin(phi_elr)*sin(acos(ctheta_el)),
E_beam-E_e_out*ctheta_el);


// Pmax calculation


x = pow(MTarget,2)+2.*MTarget*Omega+
pow(Omega,2)-M3*M3-2.*M3*M2-pow(V3q.Mag(),2);
  y = 2.*(MTarget+Omega);
  z = 2.*V3q.Mag()*C_Theta_1;


xx = z*z-y*y;
yy = 2.*x*z;
zz = x*x-y*y*M1*M1;


    // failure if the argument of determinant is less than 0
if ((yy*yy-4.*xx*zz)<0) return 0;


Det = sqrt(yy*yy-4.*xx*zz);


Pmax1 = (-yy-Det)/(2.*xx);
Pmax2 = (-yy+Det)/(2.*xx);
```

```
//generating P1 in the limits [Pmax1,Pmax2] if Pmax1 is positive
//and [0,Pmax2] if Pmax1 is negative

// first identifying the case

if(Pmax1<0&&Pmax2<0) return 0;
if(Pmax1>0) {
   if(Pmax2<0) {P1min=0;P1max=Pmax1;}
   if(Pmax2>0) {
      if(Pmax1<Pmax2) {P1min=Pmax1;P1max=Pmax2;} else
if(Pmax1>Pmax2) {P1min=Pmax2;P1max=Pmax1;} else
   if(Pmax1==Pmax2) return 0;
    }
 }
 if (Pmax1<0) {P1min=0;P1max=Pmax2;}

 random8 = Rand->Rndm(1);
 P1 = E_beam * random8;
 // throw P1 over entire range
 // not just the physical values
 if (P1 < P1min || P1 > P1max) return 0;// P1 out of range

 random4 = Rand->Rndm(1);
 random5 = Rand->Rndm(1);
 //  random6 = Rand->Rndm(1);
 random7 = Rand->Rndm(1);

 Phi_1 = 2.*TMath::Pi()*random4;
 //azimuthal angles of outgoing nucleon 1
 Phi_2 = 2.*TMath::Pi()*random5;
 //azimuthal angles of outgoing nucleon 2
 C_Theta_2 = -1.+2.*random7;
 //polar angles of outgoing nucleon 2
```

```
//#######################################
//
// Calculating remaining variables
//
//#######################################


// preliminary calculations

Ep1 = sqrt(M1*M1+P1*P1); // total energy of the 1st nucleon
E = MTarget+Omega-Ep1;
Pm = sqrt(pow(V3q.Mag(),2)+P1*P1-2.*V3q.Mag()*P1*C_Theta_1);
//missing momentum


// polinomial for T2 has a form
// A*T2^2+B*P2^2+C=0
// A,B,C are constants as defined bellow



Theta_1 = acos(C_Theta_1);
Theta_2 = acos(C_Theta_2);
b = 2.*(P1*(cos(Phi_1)*sin(Theta_1)*cos(Phi_2)*sin(Theta_2)+
sin(Phi_1)*sin(Theta_1)*sin(Phi_2)*sin(Theta_2)+
C_Theta_1*C_Theta_2)-V3q.Mag()*C_Theta_2);
c = Pm*Pm-E*E-M2*M2+M3*M3;
A = 4*E*E-b*b;
B = -2*c*b;
C = 4*E*E*M2*M2-c*c;


// solution of a polinomial
// calculating determinant

if((B*B-4.*A*C)<0) return 0;
D=sqrt(B*B-4.*A*C);
```

```
P21=(-B+D)/(2.*A);
P22=(-B-D)/(2.*A);


// choosing the solution for further calculations


if (P21<0&&P22<0) return 0;
if (P21<0&&P22>0) P2=P22;
if (P21>0&&P22<0) P2=P21;
if (P21>0&&P22>0)
  {
    P2=P21;
    if (Rand->Rndm(1)>0.5) P2=P22;
  }
// calculating components of P3


P3z = V3q.Mag()-P1*C_Theta_1-P2*C_Theta_2;
P3x = -P1*cos(Phi_1)*sin(acos(C_Theta_1))-
P2*cos(Phi_2)*sin(acos(C_Theta_2));
P3y = -P1*sin(Phi_1)*sin(acos(C_Theta_1))-
P2*sin(Phi_2)*sin(acos(C_Theta_2));


// filling in the output 4vectors


V4ElScat.SetPxPyPzE(E_e_out*cos(phi_elr)*sin(theta_elr),
E_e_out*sin(phi_elr)*sin(theta_elr),
E_e_out*cos(theta_elr),E_e_out);
V4P1.SetPxPyPzE(P1*cos(Phi_1)*sin(Theta_1),
P1*sin(Phi_1)*sin(Theta_1),P1*cos(Theta_1),sqrt(P1*P1+M1*M1));
V4P2.SetPxPyPzE(P2*cos(Phi_2)*sin(Theta_2),
P2*sin(Phi_2)*sin(Theta_2),P2*cos(Theta_2),sqrt(P2*P2+M2*M2));
V4P3.SetPxPyPzE(P3x,P3y,P3z,sqrt(P3x*P3x+P3y*P3y+P3z*P3z+M3*M3));


V4P1qz = V4P1;
V4P2qz = V4P2;
```

```
V4P3qz = V4P3;

TLorentzVector V4Sum = V4ElScat+V4P1+V4P2+V4P3;

// rotating hadrons back to original xyz (lab) system
V3qCrossZ = V3q.Cross(V3Z);
ThetaQZ = V3q.Angle(V3Z);
V4P1.Rotate(-ThetaQZ,V3qCrossZ);    //unrotate the hadrons
V4P2.Rotate(-ThetaQZ,V3qCrossZ);
V4P3.Rotate(-ThetaQZ,V3qCrossZ);

return 1;  // success
}
```

APPENDIX F

WEIGHTED BINOMIAL DISTRIBUTION

First we derive the mean and standard deviations for the unweighted binomial distribution: [1]

Suppose $x_i \sim \text{Binomial}(1, p)$, then

$E(x_i) = p$ – expected value,

$\text{var}(x_i) = p(1 - p)$ – variance,

and $SD(x_i) = \sqrt{p(1 - p)}$ – standard deviation.

Let $x_1, x_2, \ldots x_N$ be the observed values. Then

$$E\left(\sum_{i=1}^{N} x_i\right) = \sum_{i=1}^{N} E(x_i) = \sum_{i=1}^{N} p = Np \qquad (63)$$

$$var\left(\sum_{i=1}^{N} x_i\right) = \sum_{i=1}^{N} var(x_i) = \sum_{i=1}^{N} p(1 - p) = Np(1 - p) \qquad (64)$$

(All the covariance terms vanish because the samples $\{x_i\}$ are independent.) If we take

$$\hat{p} = \frac{\sum_{i=1}^{N} x_i}{N} = \frac{S}{N} = \frac{\text{no. of heads}}{\text{no. of tosses}} \qquad (65)$$

then from Equation 63 and 65

$$E(\hat{p}) = \frac{1}{N} E\left(\sum_{i=1}^{N} x_i\right) = \frac{Np}{N} = p \qquad (66)$$

from Equation 64 and 65

$$var(\hat{p}) = var\left(\frac{\sum_{i=1}^{N} x_i}{N}\right) = \frac{1}{N^2} var\left(\sum_{i=1}^{N} x_i\right) = \frac{1}{N^2} Np(1 - p) = p(1 - p)/N \qquad (67)$$

Hence the estimated

$$var(\hat{p}) = \frac{1}{N} \frac{S}{N} \frac{N - S}{N} \qquad (68)$$

and the estimated

$$SD(\hat{p}) = \sqrt{var(\hat{p})}. \qquad (69)$$

Note that estimated

$$var(\sum_{i=1}^{N} x_i) = var(S) = \frac{S(N - S)}{N}. \qquad (70)$$

---

[1] These notes are derrived by Dayanand Naik

Now we redo this for the weighted binomial distribution:

$$y_i = w_i x_i, \quad i = 1, 2, \ldots N$$

Using the results from Equation 66 and 67:

$$E(y_i) = E(w_i x_i) = p w_i \tag{71}$$

$$var(y_i) = var(w_i x_i) = w_i^2 var(x_i) = w_i^2 p(1 - p) \tag{72}$$

then

$$E\left(\sum_{i=1}^{N} y_i\right) = p \sum_{i=1}^{N} w_i \tag{73}$$

$$var\left(\sum_{i=1}^{N} y_i\right) = \sum_{i=1}^{N} var(y_i) = p(1 - p) \sum_{i=1}^{N} w_i^2 \tag{74}$$

Now we take the estimated weighted expected value:

$$\hat{p}_w = \frac{\sum_{i=1}^{N} y_i}{\sum_{i=1}^{N} w_i} = \frac{\sum_{i=1}^{N} x_i w_i}{\sum_{i=1}^{N} w_i} = \frac{S_w}{N_w} \tag{75}$$

Now we want to find the expectation and variance of $\hat{p}_w$: The expectation value is unchanged: $E(\hat{p}_w) = p$ The variance is:

$$var(\hat{p}_w) = var\left(\frac{\sum_{i=1}^{N} y_i}{\sum_{i=1}^{N} w_i}\right) = \frac{1}{(\sum_{i=1}^{N} w_i)^2} var\left(\sum_{i=1}^{N} y_i\right) = \frac{p(1 - p) \sum_{i=1}^{N} w_i^2}{(\sum_{i=1}^{N} w_i)^2} \tag{76}$$

If we define:

$$N_{eff} = \frac{(\sum_{i=1}^{N} w_i)^2}{\sum_{i=1}^{N} w_i^2} \tag{77}$$

therefore

$$var(\hat{p}_w) = \frac{p(1 - p)}{N_{eff}} \tag{78}$$

VITA

Rustam Niyazov

Department of Physics

Old Dominion University

Norfolk, VA 23529

Rustam A Niyazov is from Tashkent, Uzbekistan. In June 1986 he graduated from Minsk Radiotechnical Institute with radio-electronics engineering degree (M.S. equivalent). He started to work at Institute of Nuclear Physics in Tashkent as electronics engineer, but switched to physics by entering Tashkent State University, as a graduate student. His research project involved preparation, data taking and analysis of the nuclear spectroscopy experiments carried out at Joint Institute for Nuclear Research in Dubna, Russia. In 1995 he entered Old Dominion University graduate program. His research activity during graduate studies focused on electron scattering experiments. He participated in commissioning and testing, as well as the calibration of the drift chambers in Hall B, Jefferson Lab. He received his M.S. in physics in December 1997 and defended his thesis in November 2002.

Typeset using LaTeX.